




12-2013

## **Characterization Techniques and Electrolyte Separator Performance Investigation for All Vanadium Redox Flow Battery**

Zhijiang Tang

*University of Tennessee - Knoxville, ztang1@utk.edu*

Follow this and additional works at: [https://trace.tennessee.edu/utk\\_graddiss](https://trace.tennessee.edu/utk_graddiss)

 Part of the [Energy Systems Commons](#), [Membrane Science Commons](#), [Other Chemical Engineering Commons](#), [Physical Chemistry Commons](#), [Polymer Science Commons](#), and the [Transport Phenomena Commons](#)

---

### **Recommended Citation**

Tang, Zhijiang, "Characterization Techniques and Electrolyte Separator Performance Investigation for All Vanadium Redox Flow Battery. " PhD diss., University of Tennessee, 2013.  
[https://trace.tennessee.edu/utk\\_graddiss/2620](https://trace.tennessee.edu/utk_graddiss/2620)

This Dissertation is brought to you for free and open access by the Graduate School at TRACE: Tennessee Research and Creative Exchange. It has been accepted for inclusion in Doctoral Dissertations by an authorized administrator of TRACE: Tennessee Research and Creative Exchange. For more information, please contact [trace@utk.edu](mailto:trace@utk.edu).

To the Graduate Council:

I am submitting herewith a dissertation written by Zhijiang Tang entitled "Characterization Techniques and Electrolyte Separator Performance Investigation for All Vanadium Redox Flow Battery." I have examined the final electronic copy of this dissertation for form and content and recommend that it be accepted in partial fulfillment of the requirements for the degree of Doctor of Philosophy, with a major in Chemical Engineering.

Thomas A. Zawodzinski, Major Professor

We have read this dissertation and recommend its acceptance:

Matthew M. Mench, Stephen J. Paddison, Robert M. Counce

Accepted for the Council:

Carolyn R. Hodges

Vice Provost and Dean of the Graduate School

(Original signatures are on file with official student records.)

Characterization Techniques and Electrolyte  
Separator Performance Investigation for  
All Vanadium Redox Flow Battery

A Dissertation Presented for the  
Doctor of Philosophy  
Degree  
The University of Tennessee, Knoxville

Zhijiang Tang

December 2013

Copyright © 2013 by Zhijiang Tang  
All rights reserved.

## ACKNOWLEDGEMENTS

Firstly, I would like to thank my academic advisor Dr. Thomas Zawodzinski, for all of support and guidance throughout my entire doctoral study. His mentoring has largely helped me to grow to be a professional researcher in my fields. And I also want to give my gratitude to Dr. Alex Papandrew, who taught me a lot of lab skills and the philosophy to solve scientific problems in research, especially at the very beginning stage of my graduate study. I also would like to thank my committee members, Dr. Matthew Mench, Dr. Steve Paddison and Dr. Pete Counce for their professional advice and kind help.

The supporting from other members in Dr. Zawodzinski group, also helped me a lot in my research work at Tennessee. The atmosphere in Z group is full of friendliness, creativity, and cooperation, making my study and research very enjoyable. It was wonderful to work with colleagues Dr. Doug Aaron, Dr. Jamie Lawton and Dr. Che-Nan Sun in the battery team in Z group. The undergraduate research assistants, Rectal Svoboda, Michael Bright, Emma Hollmann and Christian Wilson, had helped me in experiments and data collection. Our lab manager, Dr. Gabriel Goenaga, can always keep the labs and research works in a good coordination to provide me good research environment. And he can entertain all the group members all the time. Our executive assistant Kat Forst helped us to organize well all the business outside the labs. And I appreciate the help and collaboration from all other Z group members. I also want to give my gratitude to Dr. Jihua Chen, who instructed and helped me to use transmission electron microscope in Center for Nanophase Material Research, Oak Ridge National Lab.

I appreciate the support from Dept. of Chemical and Biomolecular Engineering, and the University of Tennessee. My department and university offered me a valuable opportunity to study on a creative and friendly campus. Oak Ridge National Lab is also acknowledged for providing facility service.

Finally, I really want to express my gratitude to my family, my mother and father, who have been educating me to be an honest and kind person for twenty eight years. And they always support me to pursue my dream and work hard for it. Their supporting is the best comfort for me in undertaking the doctoral study in the University of Tennessee, far away from my homeland.

## ABSTRACT

The all-vanadium redox flow battery (VRFB) is an excellent prospect for large scale energy storage in an electricity grid level application. High battery performance has lately been achieved by using a novel cell configuration with advanced materials. However, more work is still required to better understand the reaction kinetics and transport behaviors in the battery to guide battery system optimization and new battery material development. The first part of my work is the characterization of the battery systems with flow-through or flow-by cell configurations. The configuration difference between two cell structures exhibit significantly different polarization behavior. The battery output can be increased by higher electrolyte feed rate, but electrolyte utilization was decreased correspondingly. The battery performance can be largely enhanced by non-wetproofed electrode material. The battery cell with higher vanadium crossover has lower energy efficiency and faster capacity decay in cycling test. Secondly, the state of charge (SOC) monitoring is of great importance for battery management. A SOC monitoring method is developed using UV-Vis spectrometric measurements on VRFB electrolyte solutions. The spectrum of the negative electrolyte is linearly dependent on its SOC. In the positive electrolyte, the nonlinear intensity dependence on SOC appears to be caused by formation of complex vanadium-oxygen ion. The characteristic molar UV-Vis spectrum of the complex vanadium-oxygen ion was separated from that of the pure positive vanadium electrolyte components. The SOC of the positive electrolyte can be then calculated from its UV-Vis spectrum by considering the complex vanadium ion equilibrium. Moreover, the understanding of ionic transport mechanism in the electrolyte

separator is critical to reduce internal resistance and vanadium crossover in the battery. The properties of Nafion and sulfonated Alder Diels poly(phelynene) (SDAPP) were investigated after equilibration with different electrolyte compositions. Both sulfuric acid and vanadium ion in the membrane can cause membrane conductivity loss. Vanadium-oxygen ion in membrane can slow down proton mobility via an unknown mechanism. Transmission electron microscope imaging showed that SDAPP is a more homogeneous ion exchange polymer with less phase separation than Nafion. The SDAPP membranes have better ion conducting properties than Nafion because of their higher ionic selectivity.



## TABLE OF CONTENTS

Chapter 1 Introduction and Literature Reviews .....	1
1.1 Background .....	1
1.2 The Fundamental of VRFB.....	4
1.3 The Development of VRFB Technique .....	8
1.3.1 New Cell Configuration.....	10
1.3.2 Carbon Electrode and Its Improvement .....	11
1.3.3 Electrolyte Separator (Membrane) Development .....	16
1.3.4 Effort for Electrolyte Improvement .....	28
1.4 Motivation and Goal of This Dissertation .....	30
Chapter 2 Polarization Curve Measurement and Cycling Test on All Vanadium Redox Flow Batteries .....	33
2.1 Introduction.....	33
2.2 Experiment.....	38
2.2.1 Battery Setup.....	38
2.2.2 Cell Designs .....	39
2.2.3 Electrochemical Tests .....	41
2.3 Results and Discussion .....	43
2.3.1 Flow-Through Cell Configuration .....	43
2.3.2 Vanadium Concentration Influence on Battery Performance .....	45
2.3.3 Electrolyte Feed Rate Effect on Cell's Output Performance .....	47
2.3.4 Properties of Electrode Material Impact on Battery Performance.....	53
2.3.5 Charging and Discharging Polarization Behavior at Various SoC .....	55
2.3.6 Battery Characterization by Cycling Test.....	59
2.4 Summary .....	64
Chapter 3 UV-Vis Spectroscopy Application in State of Charge Monitoring for VRFB	66
3.1 Background .....	66
3.2 Experimental .....	70
3.2.1 In-Line UV-Vis Spectroscopy Measurement.....	71
3.2.2 Electrospectrometry Measurement Setup .....	72

3.2.3 V <sup>4+</sup> /V <sup>5+</sup> Mixing Solution Spectrum Study .....	73
3.2.4 Vanadium Imbalance Monitoring In VRFB .....	73
3.3 Results and Discussion .....	74
3.3.1 Negative Electrolyte In-Line Spectrum .....	74
3.3.2 Positive Electrolyte UV-Vis Spectra Study .....	77
3.3.3 The equilibrium of V <sup>4+</sup> -V <sup>5+</sup> -V <sub>2</sub> O <sub>3</sub> <sup>3+</sup> in positive electrolyte .....	80
3.3.4 SoC of Positive Electrolyte Estimation by UV-Vis Spectrum .....	87
3.3.5 The Spectroscopic Monitoring On Negative Electrolyte Capacity Loss .....	91
3.4 Summary .....	94
Chapter 4 Composition and Conductivity of Membranes Equilibrated with Solutions of Sulfuric Acid and Vanadyl Sulfate .....	95
4.1 Introduction .....	95
4.2 Experiment .....	98
4.2.1 Membrane Preparation .....	98
4.2.2 Sulfuric Acid Uptake Measurement .....	99
4.2.3 Membrane Density Measurement .....	100
4.2.4 Vanadyl Uptake Measurement .....	100
4.2.5 Concentrated Vanadium/Sulfuric Acid Solution Preparation .....	101
4.2.6 Membrane Conductivity Measurement .....	101
4.3 Results and Discussion .....	102
4.3.1 Acid-Water Equilibrium in Nafion .....	102
4.3.2 Nafion Density After Sulfuric Acid Equilibration .....	107
4.3.3 VO <sup>2+</sup> Partitioning in Nafion .....	109
4.3.4 Sulfuric Acid Influence on Nafion Conductivity .....	112
4.3.5 VO <sup>2+</sup> Influence on Nafion Conductivity .....	118
4.3.6 Nafion Conductivity in Practical Electrolyte Conditions .....	124
4.4 Summary .....	127
Chapter 5 The Vanadium Cations Influence on Ion Transport in Ion Exchange Membrane .....	129
5.1 Introduction .....	129

5.2 Experimental .....	130
5.2.1 Membrane and Electrolyte Preparation .....	130
5.2.2 Membrane Equilibration and Conductivity Measurement.....	131
5.2.3 Electrolyte Species Contents in Membrane .....	131
5.3 Results and Discussion .....	132
5.3.1 Vanadium and Water Uptake in Nafion in Dilute HCl/VCl <sub>3</sub> Solutions .....	132
5.3.2 Conductivity of Nafion in Dilute HCl/VCl <sub>3</sub> Solutions .....	135
5.3.3 Conductivity of Nafion in Concentrated Vanadium/Sulfuric Acid Solutions	139
5.3.4 Uptakes in Nafion in Concentrated Vanadium/Sulfuric Acid Solutions .....	140
5.3.5 Analysis of Nafion Conductivity in Concentrated Equilibration Scenario....	143
5.4 Conclusion .....	149
Chapter 6 Sulfonated Diels Alder Poly(phenylene) Membrane Characterization as Electrolyte Separator for Vanadium Redox Flow Battery .....	150
6.1 Introduction.....	150
6.2 Experimental .....	152
6.2.1 Membrane Preparation and Characterization.....	152
6.2.2 Acid and Water Uptake after Equilibration in Aqueous Sulfuric Acid .....	153
6.2.3 Membrane Conductivity in Acidic Electrolyte .....	154
6.2.4 VO <sup>2+</sup> Permeation as a Function of Sulfuric Acid Concentration.....	155
6.2.5 VO <sup>2+</sup> Permeation as a Function of Temperature.....	156
6.2.6 Transmission Electron Microscopy .....	157
6.3 Results and Discussion .....	158
6.3.1 Membrane Characterization.....	158
6.3.2 Impact of Acid and Water Uptake after Equilibration.....	159
6.3.3 Sulfuric Acid Influence on Membrane Conductivity .....	165
6.3.4 VO <sup>2+</sup> Permeation across SDAPP Membranes .....	171
6.3.5 Morphology of SDAPP by TEM .....	175
6.4 Conclusion .....	179
Chapter 7 Recommendation for Future Work .....	181
Reference .....	189

VITA..... 205

## LIST OF TABLES

- Table 2-1. Comparison of theoretical and measured maximum current density and maximum electrolyte utilization on polarization curves with varying flow rates. Reynolds numbers of electrolyte flow are listed to compare flow regime in flow field. The battery cell is the FCB cell with Toray Carbon paper, with electrolyte solutions of  $1 \text{ mol}\cdot\text{dm}^{-3} \text{ V}^{\text{x}+}$  and  $5 \text{ mol}\cdot\text{dm}^{-3}$  total sulfate. 51
- Table 3-1. The parameters of the curve fitting for absorbance as a linear function of state of charge in negative electrolyte. 77
- Table 4-1. Conductivity and Equivalent ASR of Nafion 117 Equilibrated in Vanadium/Sulfuric Acid Solutions with Comparison to Internal Resistance of Nafion 117 Installed Battery Systems. 126
- Table 6-1. Density and water content in SDAPP and Nafion membranes at fully hydrated state, and calculated sulfonate concentration. 159
- Table 6-2. The pre-exponential factor and activation energy for SDAPP membranes and Nafion in Arrhenius kinetics theory. 175
- Table 6-3. Conductivity and  $\text{VO}^{2+}$  permeability comparison among SDAPPs and Nafion around  $20^\circ\text{C}$ . Membranes have been equilibrated in  $5 \text{ mol}\cdot\text{dm}^{-3} \text{ H}_2\text{SO}_4$ /sulfate solutions. SDAPPs have better conductivity to  $\text{VO}^{2+}$  permeability ratio than Nafion. 179

## LIST OF FIGURES

Figure 1–1. The sketch of a typical vanadium redox flow battery system. ....	5
Figure 1–2. The general structure of a VRFB cell with flow-through flow field. The cell includes a separator, electrodes and current collectors. (The electrode housing and end plate are not shown.) .....	7
Figure 1–3. Sketch of the novel non-gap VRFB cell configuration with a flow-by flow pattern. (Figure reproduced) <sup>34</sup> .....	11
Figure 1–4. A possible pathway for quaternary nitrogen to catalyze $\text{VO}^{2+}/\text{VO}_2^+$ redox reactions on nitrogen doped graphene electrode surface. (Figure reproduced) <sup>69</sup> ...	14
Figure 1–5. The synthesis of Nafion/ $\text{SiO}_2$ composite membrane with sol-gel method. (Figure reproduced) <sup>108</sup> .....	21
Figure 1–6. Nafion modification with multilayers of poly(diallyldimethylammonium chloride) and anionic poly(sodium styrene sulfonate) by self-assembly with interfacial polymerization. (Figure reproduced) <sup>104</sup> .....	24
Figure 1–7. The Donnan potential generated by the positively charged ionic group in the membrane can prevent vanadium permeation. <sup>128</sup> .....	28
Figure 2–1. The parts of polarization curve correspond to different sources of potential losses as varying current density. (Figure reproduced) <sup>33</sup> .....	37
Figure 2–2. The systematic sketch of the experimental VRFB setup with a battery cell, electrolyte transport and storage. ....	39
Figure 2–3. The raw and IR-corrected polarization curves tested on LA battery cell with $0.5 \text{ mol}\cdot\text{dm}^{-3} \text{ V}^{x+}/2.5 \text{ mol}\cdot\text{dm}^{-3}$ total sulfate electrolyte, at $30 \text{ ml}\cdot\text{min}^{-1}$ flow rate....	45
Figure 2–4. IR corrected polarization curves on FCB cell with carbon felt electrode with $0.5 \text{ mol}\cdot\text{dm}^{-3} \text{ V}^{x+}$ or $1 \text{ mol}\cdot\text{dm}^{-3} \text{ V}^{x+}$ in $5 \text{ mol}\cdot\text{dm}^{-3}$ total sulfate electrolyte solutions. The flow rate is $20 \text{ mL}\cdot\text{min}^{-1}$ . ....	46
Figure 2–5. The polarization curves measured on an FCB cell with Toray carbon paper (25% compression) electrode at varying electrolyte feed rate. The electrolyte solution contained $1 \text{ mol}\cdot\text{dm}^{-3} \text{ V}^{x+}$ and $5 \text{ mol}\cdot\text{dm}^{-3}$ total sulfate.....	49

Figure 2–6. The mass transport limiting current density and maximum electrolyte utilization in polarization curve measurement on FCB cell with Toray carbon paper (25% compression) electrode and electrolyte solution contained  $1 \text{ mol}\cdot\text{dm}^{-3} \text{ V}^{\text{x}+}$  and  $5 \text{ mol}\cdot\text{dm}^{-3}$  total sulfate at varying electrolyte feed rate. .... 53

Figure 2–7. The polarization curves on FCB cell with Toray or SGL 10AA carbon paper electrode. The electrolyte used was  $1 \text{ mol}\cdot\text{dm}^{-3} \text{ V}^{\text{x}+}$  and  $5 \text{ mol}\cdot\text{dm}^{-3}$  total sulfate. Toray carbon paper had a compression of 200/150  $\mu\text{m}$ , while 10AA was compressed to 300  $\mu\text{m}$  from 400  $\mu\text{m}$ . The electrolyte flow rates in both polarization testes were  $20\text{mL}\cdot\text{min}^{-1}$ . .... 55

Figure 2–8. The charging and discharging polarization curves at 90, 80, and 70% state of charge. Charging and discharging polarization curves overlap at kinetic control region for each SoC. The charging polarization curve deviates from the discharging one after  $15 \text{ mA}\cdot\text{cm}^{-2}$  due to several reasons. .... 58

Figure 2–9. The selected initial cycles in battery cycling tests on FCB cell with different membrane electrode combinations: A. Nafion 211 with 3 layers SGL 10AA carbon paper electrode (70% compression); B. Nafion 212 with 3 layers SGL 10AA carbon paper electrode (70% compression); C. Nafion 117 with 1 layer Toray carbon paper. Non-wetproof surface property of 10AA enables a much lower overpotential loss during both charging and discharging processes. .... 61

Figure 2–10. The coulombic efficiency (CE), voltage efficiency (VE) and energy efficiency (EE) of the FCB cell with different membrane electrode combinations: A. Nafion 211 with 3 layers SGL 10AA carbon paper electrode (70% compression); B. Nafion 212 with 3 layers SGL 10AA carbon paper electrode (70% compression); C. Nafion 117 with 1 layer Toray carbon paper. Thicker membrane in cell can bring up higher coulombic efficiency. Non-wet proofed electrode enables higher voltage efficiency. .... 63

Figure 3–1. The UV-Vis spectrometer setup built in a flow battery system. .... 72

Figure 3–2. The UV-Vis spectra of negative electrolyte solution (with  $1 \text{ mol}\cdot\text{dm}^{-3} \text{ V}^{2+}/\text{V}^{3+}$  and  $5 \text{ mol}\cdot\text{dm}^{-3}$  sulfate) at different states of charge. The spectra were taken on a flow cell with 1mm light path length. .... 75

Figure 3–3. The absorbance of  $V^{2+}/V^{3+}$  mixing electrolyte with  $1 \text{ mol}\cdot\text{dm}^{-3} V^{x+}$  in  $5 \text{ mol}\cdot\text{dm}^{-3}$  sulfate in flow cell (1mm) at 433nm, 600 nm and 750 nm. The strength of absorption at these wavelengths is mostly proportional to electrolyte’s state of charge..... 76

Figure 3–4. The UV-Vis spectra variation with state of charge change is not proportional to the  $V^{4+}/V^{5+}$  composition in the positive electrolyte solution. The excess absorbance happens when  $V^{4+}$  and  $V^{5+}$  coexist. .... 78

Figure 3–5. The  $V^{5+}$  reduction spectra variation in electrochromometry measurement. The electrolyte was  $80 \mu\text{L } 0.5 \text{ mol}\cdot\text{dm}^{-3} V^{4+}$  and  $5 \text{ mol}\cdot\text{dm}^{-3}$  sulfate solution. The lightpath length was 1 mm..... 79

Figure 3–6. At 600 and 760 nm, the excess absorbance of  $0.5 \text{ mol}\cdot\text{dm}^{-3} V^{4+}/V^{5+}$  and  $5 \text{ mol}\cdot\text{dm}^{-3}$  sulfate electrolytes is dependent on its state of charge as a parabolic function. .... 80

Figure 3–7. The normalized excess absorbance in  $V^{4+}/V^{5+}$  electrolyte solution with  $1 \text{ mol}\cdot\text{dm}^{-3} V^{x+}$  and  $5 \text{ mol}\cdot\text{dm}^{-3}$  total sulfate. The strength of excess absorbance is consistent with total vanadium concentration in solution..... 82

Figure 3–8. (a) The molar excess absorption coefficient of  $V^{4+}/V^{5+}$  mixed electrolyte,  $\epsilon_{ex}$ ; and (b) molar absorption coefficient of  $V_2O_3^{3+}$  in  $V^{4+}/V^{5+}$  mixed electrolyte,  $\epsilon_{V_2O_3^{3+}}$ . The electrolyte condition is  $0.08$  to  $1.2 \text{ mol}\cdot\text{dm}^{-3} V^{4+}/V^{5+}$  and  $5 \text{ mol}\cdot\text{dm}^{-3}$  sulfate/bisulfate..... 86

Figure 3–9. The SoC calculated from positive electrolyte total absorbance data at 765 nm wavelength with eq. 3-19. The state of charge can be directly calculated from the electrolyte absorbance spectrum and the total vanadium concentration. However, the calculation must be combined with some other method to rule out the imaginary root. .... 90

Figure 3–10. The charging and discharging capacity decay over 20 charging-discharging cycles. Capacity loss and low coulombic efficiency were both worsened by thin membrane utilization. .... 92



Figure 3–11. The UV-Vis absorbance of negative electrolyte after charging during the cycling test. The increased absorbance of electrolyte indicates lowered state of charge after charging. .... 93

Figure 4–1. Water and sulfuric acid uptake by Nafion 117 in aqueous sulfuric acid solutions within concentration range from 0 to 17.4 mol·kg<sup>-1</sup>. Acid existence can lead lowered water content in Nafion, and propel sulfuric acid overcome Donnan potential to enter membrane’s ionic domain..... 104

Figure 4–2. Water uptake in Nafion 117 vs. water activity in equilibrium between membrane and sulfuric acid solution. The water content dependence on water activity in sulfuric acid is very similar to that in water vapor.<sup>84,214</sup> ..... 105

Figure 4–3. Sulfuric acid concentration in the membrane versus sulfuric acid concentration in bathing solution. The ratio of membrane sulfuric acid to environmental sulfuric acid is roughly 1:2.5. .... 107

Figure 4–4. Measured density and calculated porosity of Nafion 117 with respect to sulfuric acid concentration in bathing solution. The declining density dependence on acid concentration in solution is indicating membrane deswells in acid solution. . 109

Figure 4–5. Water and vanadyl content in Nafion 117 equilibrated with vanadyl sulfate/sulfuric acid solutions of 0.1 mol·dm<sup>-3</sup> total sulfate background. Vanadyl presence in membrane has barely effect on membrane’s water content; Vanadyl is preferred by sulfonate to proton in Nafion. .... 111

Figure 4–6. Sulfuric acid presence in equilibrium can enhance membrane’s conductivity when sulfuric acid is no more concentrated than 5 mol·kg<sup>-1</sup> in environment; Acid can reduce membrane’s conductivity when its concentration is over 5 mol·kg<sup>-1</sup> in equilibrium..... 112

Figure 4–7. Calculated proton concentration and mobility are presented as functions of sulfuric acid concentration in bathing solution. By being exposed to acidic environment, membrane can gain an elevated proton concentration, but loss proton mobility. The two factors contribute comprehensively to enhanced or lowered membrane conductivity..... 115

Figure 4–8. Proton mobility relies on water/acid content ration in two different ways. At high water content, proton mobility is fairly constant; when water content is lower than 12 water molecules per acid, proton mobility decreases severely with decreasing water content in a linear pattern..... 117

Figure 4–9. In the Nafion membrane, proton mobility depends on water activity according to a power law,  $u_{H^+} = 7.61 \times 10^{-4} cm^2 \cdot V^{-1} \cdot s^{-1} \times a_{water}^{1.5}$ . The mobility dependence on water activity implies that proton transfer involves one to two water molecules. .... 118

Figure 4–10. Conductivity of Nafion 117 equilibrated with vanadyl sulfate/sulfuric acid solution with  $0.1 \text{ mol} \cdot \text{dm}^{-3}$  total sulfate background. The vanadyl has a decreasing effect on Nafion’s conductivity. .... 120

Figure 4–11. Measured conductivity for Nafion 117 with different vanadyl relative concentration in Membrane in comparison with predicted conductivity from ionic interaction model and fixed mobility model. The analysis illustrates that vanadyl has a much slower motion than proton in transferring inside Nafion, and it can also slow down proton’s transport in a linear relation of unrevealed mechanism..... 121

Figure 4–12. Nafion 117 conductivity upon equilibration in vanadyl sulfate/sulfuric acid solutions of 0 to  $1.75 \text{ mol} \cdot \text{dm}^{-3}$  vanadyl in  $5 \text{ mol} \cdot \text{dm}^{-3}$  sulfate background. .... 125

Figure 5–1. Normalized vanadium content in membrane with respect to normalized vanadium concentration in solution phase.  $V^{3+}$  and  $VO^{2+}$  have very close partitioning capability in Nafion; Both of  $V^{3+}$  and  $VO^{2+}$  are preferentially bonded by sulfonate in Nafion.  $VO^{2+}$  results are from literature.<sup>30</sup> ..... 134

Figure 5–2. Nafion conductivity loss is caused by vanadium ions presence in the environmental solution. The reduction caused by  $V^{3+}$  is lower than  $VO^{2+}$ . .... 136

Figure 5–3. Nafion conductivity is differently dependent on  $V^{3+}$  or  $VO^{2+}$  concentration in membrane phase.  $VO^{2+}$  can slow down proton motion in membrane to carry charge, while  $V^{3+}$  does not have such an impact on proton. Both  $V^{3+}$  and  $VO^{2+}$  have very low mobility compared to proton in a well hydrated membrane. .... 138

Figure 5–4. Nafion conductivity after being equilibrated in electrolyte solutions with vanadium in +3, +4 and +5 valence. The vanadium ion concentration in solutions is

0 to 2 mol·dm <sup>-3</sup> ; the total sulfuric acid/ bisulfate/ sulfate concentration is 5 mol·dm <sup>-3</sup> . .....	140
Figure 5–5. Water and sulfuric acid contents in Nafion equilibrated in concentrated electrolyte solutions (vanadium 0 to 2 mol·dm <sup>-3</sup> ; total sulfate 5 mol·dm <sup>-3</sup> ). The water and sulfuric acid contents are invariant with environmental vanadium concentration. .....	142
Figure 5–6. Vanadium ion content in Nafion being equilibrated in concentrated electrolyte solutions with V <sup>3+</sup> , VO <sup>2+</sup> or V <sub>2</sub> O <sub>3</sub> <sup>3+</sup> . V <sup>3+</sup> and VO <sup>2+</sup> have stronger partitioning in Nafion than V <sub>2</sub> O <sub>3</sub> <sup>3+</sup> . .....	143
Figure 5–7. Proton content and corrected water content in Nafion after equilibration. Proton is provided by sulfuric and sulfonic acid dissociation and reduced by vanadium replacement. Water content is corrected by vanadium aqua-coordination and extra sulfuric acid. ....	145
Figure 5–8. Proton transference number in Nafion with coexistence of vanadium ions (V <sup>3+</sup> , VO <sup>2+</sup> or V <sub>2</sub> O <sub>3</sub> <sup>3+</sup> ) in concentrated electrolyte equilibration. The proton mobility is assumed to be only dependent on membrane’s corrected water content. <sup>30</sup> .....	147
Figure 5–9. VO <sup>2+</sup> and V <sub>2</sub> O <sub>3</sub> <sup>3+</sup> can retard proton transfer in Nafion. V <sub>2</sub> O <sub>3</sub> <sup>3+</sup> has a stronger interference than VO <sup>2+</sup> on proton motion. ....	148
Figure 6–1. The molecular structures of SDAPP and Nafion. SDAPP is a short side-chained sulfonated poly(phenylene); Nafion is a long side-chained sulfonated tetrafluoroethylene based copolymer. ....	152
Figure 6–2. Sketch of VO <sup>2+</sup> diffusion across membrane monitored by UV-Vis spectrometer with temperature control. ....	157
Figure 6–3. Sulfuric acid (a) and water (b) contents in SDAPP membranes compared to Nafion 117. SDAPP membranes have both significantly higher sulfuric acid and water contents than Nafion in concentrated sulfuric acid environment. ....	161
Figure 6–4. SDAPP and Nafion have close water content after being equilibrated in sulfuric acid solutions. Sulfuric acid in the membrane ionic domain has similar hydration behavior to sulfonic acid group in SDAPP and Nafion. ....	162

Figure 6–5. Calculated sulfuric acid molality in membrane phase. Sulfuric acid can be more effectively excluded by Nafion than SDAPP. Donnan exclusion in SDAPP membrane is consistent with membrane ion exchange capacity. .... 164

Figure 6–6. Sulfuric acid uptake behavior in membrane is controlled by the degree of sulfonic acid group agglomeration and acidity (or dissociation). Nafion has high sulfonic acid group agglomeration and higher acidity; SDAPP has an even sulfonic acid group distribution and lower acidity. .... 165

Figure 6–7. Conductivity of SDAPP membranes after being equilibrated in sulfuric acid solutions with varying concentration. SDAPP membrane with higher IEC has higher conductivity. .... 166

Figure 6–8. Proton concentration (a) and mobility (b) in SDAPP membranes and Nafion with respect to the sulfuric acid concentration in the bathing environment. .... 169

Figure 6–9. Proton mobility in SDAPP is highly dependent on water content in membranes. Proton transport in SDAPP is favored by high availability of water molecules to serve as transport mediator. .... 171

Figure 6–10. Vanadium permeability across SDAPP membranes is sharply reduced by high sulfuric acid concentration in electrolyte environment..... 172

Figure 6–11. The logarithm of vanadyl diffusivity in SDAPP and Nafion is linearly dependent on  $1/T$ . The vanadyl diffusion in cation exchange membrane obeys classical Arrhenius kinetics..... 175

Figure 6–12.  $\text{Cs}^+$  stained TEM micrographs of SDAPP and Nafion 117 at 50 nm magnification. More homogeneous sulfonic acid group distribution is presented in SDAPP membranes with varying ion exchange capacity..... 177

Figure 6–13.  $\text{Cs}^+$  stained TEM micrograph of SDAPP and Nafion 117 at 5 nm magnification. The structure of SDAPP is highly homogeneous and the sulfonic acid group is evenly distributed in the polymer. .... 178

## CHAPTER 1

### INTRODUCTION AND LITERATURE REVIEWS

#### 1.1 Background

The vanadium redox flow battery (VRFB) is of significant potential in large scale energy storage to meet requirements for different applications. Currently, large scale energy storage systems (LSESS) are of great interest to improve the global energy economy, efficiency and sustainability. Generally, as a functional component of a future electrical grid, the LSESS can play three roles: as a grid demand-supply mismatch manipulation<sup>1-3</sup>, as a renewable energy output buffer<sup>4-9</sup> and for energy storage in small scale standalone micro-grids<sup>10,11</sup>.

The large scale energy storage system can improve the electrical grid's energy efficiency and economy.<sup>12</sup> The energy supply and demand are generally mismatched because the electricity generation tends to operate at its highest efficiency at steady state, but the demand for electricity can vary hourly due to regional day-night energy loading variation. High electricity demand happens during the day time due to the usage from commercial, industrial and residential customers. LSESS in the grid can play a role of energy buffering to save the high manufacturing and maintenance cost of adding peak plants kept idling and thus with continuous fuel usage.<sup>1,2</sup> With enough capacity in LSESS, only a base load power plant working at its highest efficiency is needed to meet average

demanded power for the grid.<sup>13</sup> Surplus energy generated on the grid can be stored into LSESS units during the low demand hours, and released to the user at peak hours. Finally, LSESS can respond to the emergent energy demands on the grid to keep its stable operation.

The LSESS is highly valuable to the electrical grid with high levels of integrated renewable energy resources.<sup>2,4-7,9</sup> For the purposes of reducing fossil fuel consumption and enhancing global energy sustainability, wind and solar energy are increasingly harvested and provided to electricity grid. However, these energy sources have strong intermittency due to daily and seasonal weather or sunlight variation. The significant intermittence of these energy sources introduces to the grid a highly variable and thus disruptive electricity feed which can cause frequency and voltage fluctuation on the grid, influencing stability of grid operation. With the integration of LSESS to buffer the electricity between stochastic power sources and the grid, the fluctuation of renewable energy sources can be filtered to avoid instability of the grid.

LSESS can also be used as an independent power source in a small standalone grid with a renewable power source or backup power source.<sup>10,11</sup> In a standalone grid, as discussed in the preceding paragraph, the intermittence of wind or solar source generates unstable electrical output. Energy storage can collect electricity from a local electricity generator and provide it to users on-demand. The same output strategy can be applied when the storage serves the backup power system.<sup>10</sup>

A vanadium redox flow battery is attractive for use in these applications due to its

characteristic property when compared to other technical competitors.<sup>2,3,14,15</sup> In contrast to traditional solid state batteries, such as lead acid or Ni-Cd, VRFB is a flowing electrochemical system similar to a fuel cell. One prominent feature of the VRFB is that its energy capacity and power capacity are separately related to different battery system components. The energy is carried by the vanadium redox couples in an electrolyte solution, while the energy can be converted at a demanded rate (power) by redox reaction in battery cells. The decoupled energy and power allows great flexibility in battery design and manufacturing to meet various requirements, especially to achieve systems with extremely high capacity and power. Because the electrode in VRFB cell is not involved directly in storing energy, problems such as material phase transformation and morphology changes that are observed in energy storage electrodes can be avoided to increase system durability and performance stability.<sup>3</sup>

Other advantages have also been well summarized in the literature.<sup>15</sup> Due to the decoupled power and capacity, modular battery cells and an essentially unlimited volume of liquid electrolyte make it relatively easy to build high power and capacity VRFB systems.<sup>2,3,16</sup> Several VRFB systems with MW level power output and MW·hr capacity have been established and are in operation in practical settings.<sup>17,18</sup> Because a long startup process is not needed in the VRFB system, the VRFB can respond instantly to input or output requirements at a very high speed (<1s).<sup>19</sup> Regarding the aspect of better durability, a large number of deep charge-discharge cycles (12000) has already been reported on a 20 kW battery module.<sup>20</sup> The high cycle number achieved can satisfy the requirement for over thirty years operational life span, given that the battery operation frequency is one

cycle per day. High energy efficiency (75-80%) has also been reported to be achieved with a VRFB at  $100 \text{ mA}\cdot\text{cm}^{-2}$  level operational current density.<sup>18-21</sup> The building cost of a VRFB system is very sensitive to its component price,<sup>22,23</sup> but competitive unit capital cost can be reached by using new materials with cheaper price and better performance and system optimization. These characteristics of VRFB technology make it a very competitive large scale energy storage technique to satisfy various application requirements.

## **1.2 The Fundamental of VRFB**

The vanadium redox flow battery was first developed by M. Skyllas-Kazacos group in the University of New South Wales<sup>24-27</sup>. A typical VRFB setup is presented in figure 1-1. Generally, the core parts of a VRFB include a battery cell or cell stack to serve as an electrochemical reactor, electrolyte solutions carrying vanadium redox couples to store energy, and auxiliary subsystems to seal and transport electrolyte solutions. A VRFB can operate over the temperature range from 10 to 40°C without temperature control<sup>15</sup>.



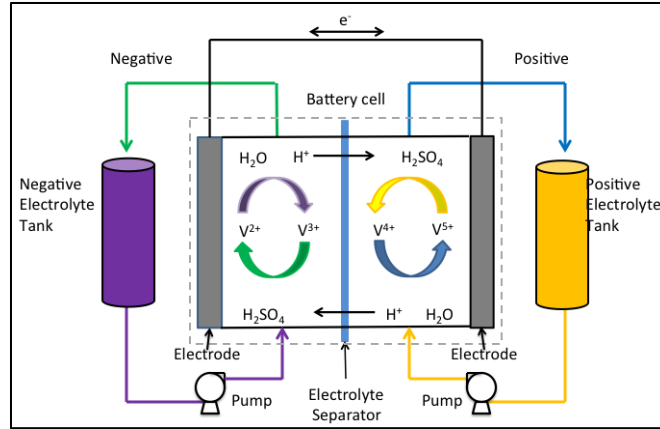
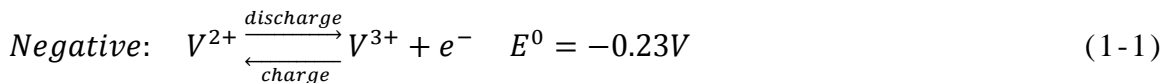
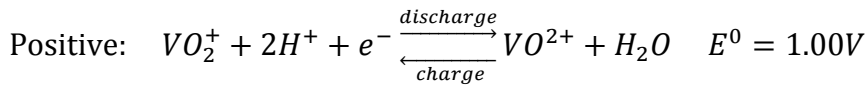


Figure 1–1. The sketch of a typical vanadium redox flow battery system.

The cell is the core part of VRFB. It conducts electrochemical reactions to interconvert energy between chemical and electrical forms. As is shown in Figure 1-2, the functional components of a battery cell are the separator (membrane), the electrodes and the current collector. In a VRFB, energy is carried by  $V^{2+}/V^{3+}$  and  $V^{4+}/V^{5+}$  (or  $VO^{2+}/VO_2^+$ ) redox couples in negative and positive electrolyte solutions, respectively. During battery operation, while electrolyte solutions are being pumped through electrodes in each half cell, redox reactions take place on the surface of electrode to store or release energy via the following reactions:



The function of each component in VRFB cell determines characteristic requirements for each component. The membrane separator in the cell separates

electrolyte to prevent direct contact and reaction between vanadium ions of varying redox states and minimizes unwanted mass transport. To conduct current, the separator should have high ion conductivity to minimize ohmic loss. A cation exchange membrane such as Nafion is commonly used as the electrolyte separator<sup>24,25,27-29</sup>. However, cation exchange membrane performance can be limited because of its conductivity decrease when in contact with vanadium-acid electrolyte and its low ion selectivity<sup>30-32</sup>. The electrode in a VRFB cell is generally a porous carbon material, which is electronically conductive and resistant to chemical and electrochemical corrosion in electrolyte<sup>24,25,33,34</sup>. The porous electrode structure can also provide relatively high surface area to support vanadium redox reactions and internal space for electrolyte convection to improve mass transport. The current collector (or bipolar plate in a cell stack) connects the electrode and external circuit to conduct electricity. In addition, the current collector should be impermeable to electrolyte solution and air to prevent electrolyte leakage and air penetration. Good resistance to electrolyte corrosion is also required to improve battery durability and reliability. In a flow-by battery cell architecture, flow channels are built into the current collector to distribute electrolyte solution into the electrodes<sup>33,34</sup>. In this case, the mechanical durability of the current collector is also of great importance to withstand any friction from electrolyte flow.

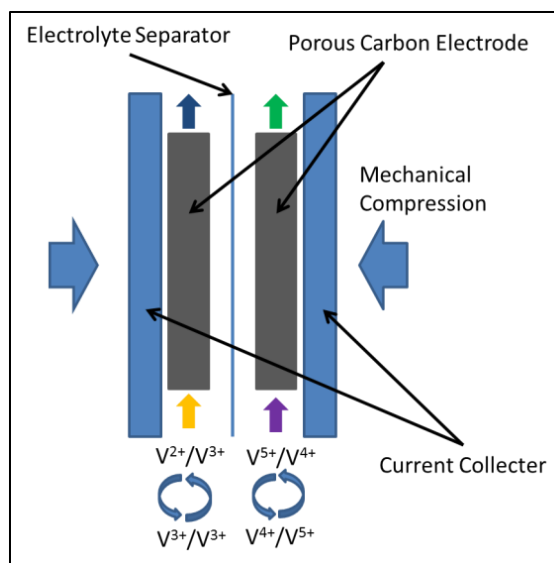


Figure 1–2. The general structure of a VRFB cell with flow-through flow field. The cell includes a separator, electrodes and current collectors. (The electrode housing and end plate are not shown.)

The electrolyte solution carries energy in the form of dissolved vanadium redox couples. Typically, the electrolyte solution is an aqueous solution of 1 to 2 mol·dm<sup>-3</sup> vanadium sulfate salt and excess sulfuric acid as supporting electrolyte<sup>21,25,33,34</sup>. The practical concentration of vanadium is limited by the stability of vanadium in electrolyte solution<sup>35</sup>. The sulfuric acid enhances vanadium solubility and conductivity. To achieve higher energy density and better electrochemical performance, several methods have been used to improve vanadium solubility and electrolyte stability.<sup>36,37</sup> More detailed discussion about electrolyte performance improvement will be presented in a later section.

The electrolyte storage and transport subsystem is a supporting part of the flow battery. Since  $V^{2+}$  is very sensitive to air oxidation, electrolytes, especially negative

electrolyte, must be stored and sealed in oxygen free containers and tubing/pipe with high resistivity to corrosive environment in electrolyte. Several kinds of polymeric materials, such as polypropylene (PP) and polytetrafluoroethylene (PTFE), are stable enough to contact the electrolyte. During operation, the electrolytes are continuously circulated by pumps between the reservoir and cells. The flow rate must be optimized by balancing battery performance and pump pressure loss.<sup>33</sup> To prevent battery capacity loss due to  $V^{2+}$  oxidation, a nitrogen atmosphere is usually kept in the electrolyte reservoir in lab setups.

### 1.3 The Development of VRFB Technique

The concept of redox flow battery (RFB) was initially proposed by National Aeronautic and Space Administration (NASA) to accomplish a battery system with several technical features.<sup>26</sup> Vanadium redox electrochemistry was first studied and applied in flow battery by the M. Skyllas-Kazacos group in the University of New South Wales.<sup>24,25,38,39</sup> Notable features making this system attractive are its simplicity in preventing cross contamination and its decent electrochemical performance. A pioneering 1 kW VRFB stack was built by the same group. 1.33 kW power and 72% energy efficiency were achieved on the battery stack at a current density  $80 \text{ mA}\cdot\text{cm}^{-2}$ , with  $1.5 \text{ mol}\cdot\text{dm}^{-3}$  vanadium in  $4 \text{ mol}\cdot\text{dm}^{-3}$  total sulfate electrolyte solutions at room temperature.<sup>27</sup> The stack showed steady voltage and coulombic efficiencies over 100 cycles without obvious capacity loss. Later, several other experimental kW-level VRFB stacks built by other researchers have been reported.<sup>20,29,40-42</sup> Over 80% energy efficiency

can be achieved in a current density range of 50 to 140 mA·cm<sup>-2</sup> on various systems. The 20 kW cell stack developed by Sumitomo Electric Industries (SEI) was reported to have lasted over 12,000 cycles with over 80% energy efficiency at 50 mA·cm<sup>-2</sup> current density.<sup>20</sup> The high cycle number achieved by the Sumitomo demonstration product proved the high durability and reliability of VRFB. Since the invention of VRFB, a number of practical VRFB systems, most of them at MW/MW·h power/capacity level, have been built and operated for different applications in many countries.<sup>17,18,43</sup>

Although great technical progress in VRFB development has been accomplished, there is still room for performance improvement. This is evident in comparison to proton exchange membrane (PEM) fuel cells which shares many common features, including flow pattern and the general cell structure. A PEM fuel cell can generally operate at 1 A·cm<sup>-2</sup> current density level with 0.1 Ω·cm<sup>2</sup> internal resistance level with a power output around 1 W·cm<sup>-2</sup>.<sup>44-48</sup> Although the operating voltage (1.2-1.6V)<sup>24,29</sup> of a VRFB is higher than that of PEM fuel cell, its typical current density (at 100 mA·cm<sup>-2</sup> level) can only support a power density at 100 mW·cm<sup>-2</sup> level. The internal resistance reported in the literature on VRFB stacks of roughly 1 Ω·cm<sup>2</sup> would severely reduce battery efficiency and power output at high current density. As has been pointed out by Zaffou et al.,<sup>28</sup> at 1 A·cm<sup>-2</sup> current density, 1 Ω·cm<sup>2</sup> leads to a 1 V ohmic potential loss, which is a tremendous voltage efficiency loss given a 1.5 V open circuit voltage. The low power output capacity and higher internal resistance are the primary targets for improving VRFB cell performance.

### ***1.3.1 New Cell Configuration***

Progress in lab scale system development is leading to VRFBs with  $\sim 1 \text{ W}\cdot\text{cm}^{-2}$  output power.<sup>34,49,50</sup> A new non-gap, flow-by battery cell architecture, shown in Figure 1-3, was applied to VRFB cell configuration in Mench and Zawodzinski Groups in the University of Tennessee and at Oak Ridge National Laboratory.<sup>33,34,49</sup> The limiting current density for such a structure is at least at the  $1 \text{ A}\cdot\text{cm}^{-2}$  level,<sup>34,49</sup> which is more similar to the mass transport limiting current density of PEM fuel cell.<sup>45,47</sup> The output capacity with the novel flow-by cell design is substantially higher than previous reported battery configurations,<sup>34</sup> in which cells were mostly flow-through designs.<sup>24,29,39,41</sup> 80% energy efficiency was reached in the cycling test with  $200 \text{ mA}\cdot\text{cm}^{-2}$  charging/discharging current density by Pezeshki et al. with the new cell design.<sup>51</sup> The operational current density with new cell design is about two times higher than that ( $\sim 100 \text{ mA}\cdot\text{cm}^{-2}$ ) of the reported demo stack setups. The internal resistance was also substantially reduced by the introduction of the new cell architecture. In a regular flow-through electrode battery, the internal resistance (IR) is generally at 1 to 4  $\text{ohm}\cdot\text{cm}^2$ .<sup>27,33,41</sup> In contrast, the new cell structure successfully brought the battery IR down to the  $0.5 \text{ ohm}\cdot\text{cm}^2$  level.<sup>33,34,49,50</sup>

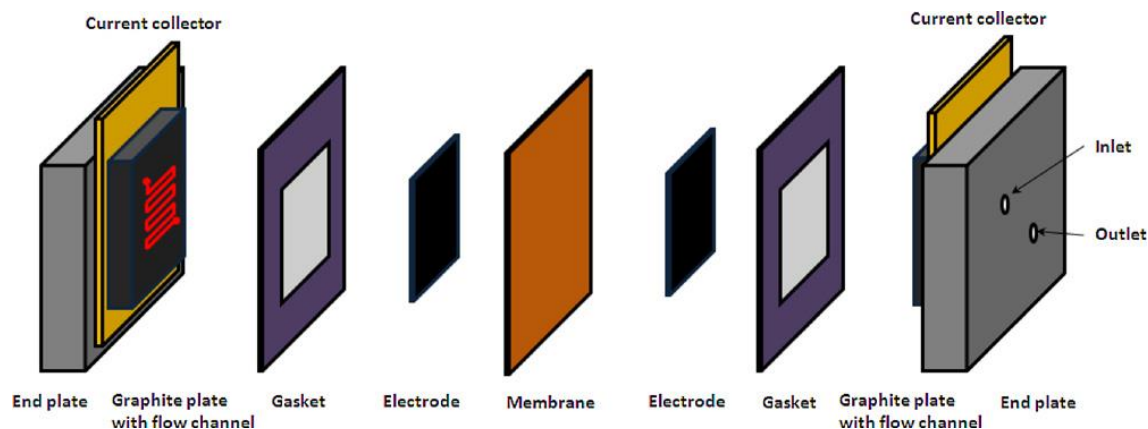


Figure 1–3. Sketch of the novel non-gap VRFB cell configuration with a flow-by flow pattern. (Figure reproduced)<sup>34</sup>

In addition to the progress achieved through improved cell configuration, effort has also been put into development of functional materials with higher performance.<sup>15,16,18,28,52</sup> The current state in development of each VRFB component is reviewed in the following sections. These components include carbon electrode material, electrocatalyst, electrolyte separator and electrolyte additives.

### ***1.3.2 Carbon Electrode and Its Improvement***

The function of electrode in VRFB requires its material to be electrically conductive, resistant to chemical and electrochemical corrosion in the electrolyte, to be porous to support facile transport of electrolyte and to provide active surface area to support redox reactions. Porous carbon was selected as the electrode material for both positive and negative electrodes, due to its conductivity and chemical stability, relatively low cost and porous structure.<sup>33,34,49,50,53–55</sup> Several carbon materials are available with highly variable

pore structure, surface chemistry, internal surface area and other properties. Graphite felt (Le Carbone) was firstly used as an electrode material in the early stage studies on vanadium redox flow battery cells.<sup>24</sup> The electrode material exhibited good stability over 2000 hours, and performed well in the battery system in which 70% energy efficiency can be reached at  $40 \text{ mA}\cdot\text{cm}^{-2}$  current density. Later, a comparative study was carried out to probe the suitability of various carbon-based electrode materials.<sup>54,56,57</sup> It was found that the average separation between carbon layers in the material and the functional groups on electrode surface can have significant effects on battery efficiency and resistance.<sup>57</sup> The carbon electrode corrosion caused by higher overpotential in acidic electrolyte was also reported for bulk graphite and fibrous carbon material.<sup>54</sup> Later, various porous carbon materials (graphite felt, carbon felt or graphite foil) were chosen as electrode materials in several literature reported VRFB setups.<sup>20,27,29,41,42</sup> Recently, hydrophilic SGL carbon papers which originally designed and manufactured for PEM fuel cell application, have been used as electrode materials in novel non-gap battery cell.<sup>34,49</sup> Compared to more traditional battery cell designs, high power output was achieved by the new cell configuration with these special electrode materials.

Various methods have been used to modify these porous carbon electrode materials to improve their performance. The effort to modify the surface of carbon electrode materials in VRFB mostly intends to increase its surface area, introduce more catalytic functional groups or decorate the catalyst to reduce activation loss in the battery. The primary strategies of electrode improvement include modification of existing electrode material, catalyst adoption and new electrode material development. These efforts are



briefly introduced in the following part of this section.

Chemical modification is a method to improve electrode material performance by introducing more active functional groups onto electrode surface or increase roughness of electrode surface. The oxygen or nitrogen containing functional groups on the electrode surface is believed to catalyze vanadium redox reaction. Sun et al. initially used boiling in concentrated sulfuric acid and 200 to 500°C heating in air to modify the surface of graphite felt for VRFB application.<sup>58,59</sup> Surface characterization by X-ray photoelectron spectroscopy showed that the prevalence of C-O and C=O bonds on the electrode surface was substantially increased by applying these two treatments. In battery tests with the treated graphite felt, enhanced battery energy efficiency and lowered internal resistance were observed. Similar strategies have also been utilized to modify carbon based electrode materials to introduce oxygen containing functional group onto material surface by many other research groups.<sup>60-64</sup> With the non-gap flow-by cell design, Pezeshki et al. reported 77% energy efficiency at 200mA·cm<sup>-2</sup> current density in a battery cycling test in a non-gap cell with Nafion 117 when employing SGL 10AA carbon paper heat-treated in 400°C air.<sup>64</sup> Electrode material modification by treatment in a NH<sub>3</sub> atmosphere at elevated temperature (220°C) has also been reported to improve electrode performance and thereby improve battery performance.<sup>61,65-69</sup> A detailed study on the properties of nitrogen-doped graphene suggested that the quaternary nitrogen is most stable in acidic electrolyte and active enough to catalyze VO<sup>2+</sup>/VO<sub>2</sub><sup>+</sup> redox reactions, as shown in Figure 1-4.<sup>69</sup> Some other methods for surface modification, such as plasma treatment, gamma ray irradiation,<sup>60</sup> and Fenton reagent oxidation,<sup>70</sup> were also utilized to treat electrode

materials. Another method to improve electrode performance is to increase the active surface area of the electrode. A nanoporous layer consisting of multilayers of carbon nanotubes was built on SGL 10AA carbon paper, and effectively increase the output of the battery.<sup>50</sup> Carbon felt decorated by reduced graphene oxide was also used in a VRFB to provide a finer degree of oxygen content control on the electrode surface.<sup>71</sup>

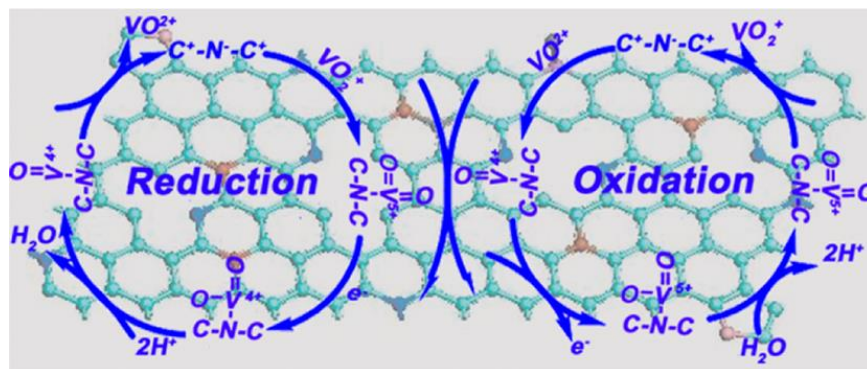


Figure 1–4. A possible pathway for quaternary nitrogen to catalyze  $\text{VO}^{2+}/\text{VO}_2^+$  redox reactions on nitrogen doped graphene electrode surface. (Figure reproduced)<sup>69</sup>

To improve the reaction kinetics for vanadium redox reactions, great amount of research attention has been paid to introducing a catalyst into a VRFB. Sun et al. did a wide range of screening work to evaluate the catalytic ability of several common catalysts impregnated in graphite fiber electrodes, including platinum, palladium, gold, manganese and iridium.<sup>72</sup> It was found that carbon fiber electrode with iridium had the best overall performance as a catalyst for various vanadium redox reactions, while precious metal can cause copious hydrogen evolution as a side-reaction, limiting its application in VRFB. Iridium-decorated carbon felt and iridium-decorated graphene

electrodes were respectively developed based on this observation.<sup>73,74</sup> With the Ir coated carbon felt electrode, it was reported that the reaction overpotential of  $\text{VO}^{2+}/\text{VO}_2^+$  couple was substantially reduced and cell internal resistance was lowered.<sup>73</sup> Graphene electrode with 3 nm Ir nanoparticle decoration was successfully synthesized.<sup>74</sup> It was observed that a Ir-decorated graphene electrode had a higher catalytic ability than graphene and Vulcan XC72 carbon to improve  $\text{VO}^{2+}/\text{VO}_2^+$  reaction kinetics.  $\text{Ti}/\text{IrO}_2:\text{Ta}_2\text{O}_5$  was synthesized and used as an electrode in vanadium system, and showed a higher electrochemical activity than graphite electrode.<sup>75</sup> Other catalytic electrodes have also been developed based on tungsten and bismuth. A tungsten trioxide/super active carbon ( $\text{WO}_3/\text{SAC}$ ) composite electrode and catalyst-coated membrane (CCM) were developed and adopted in a VRFB using a CCM configuration by Yao et al.<sup>76,77</sup> The  $\text{WO}_3/\text{SAC}$  promotes very high charge transfer rates within  $\text{VO}^{2+}/\text{VO}_2^+$  and  $\text{V}^{3+}/\text{V}^{2+}$  redox couples relative to pure SAC.<sup>76</sup> The cell with  $\text{WO}_3/\text{SAC}$  CCM performed at higher voltage and energy efficiencies (85.9% and 81.2%) than a regular cell (81.3% and 76.9%) at  $120 \text{ mA}\cdot\text{cm}^{-2}$  current density.<sup>77</sup> A carbon felt electrode decorated with nanoparticles of bismuth (Bi) has been developed as both positive and negative electrodes for VRFB.<sup>78,79</sup> It was found that the Bi nanoparticle doped graphite felt electrode had an 11% increase in battery energy efficiency at  $150 \text{ mA}\cdot\text{cm}^{-2}$  compared to untreated graphite felt electrode.  $\text{Mn}_3\text{O}_4$  has also been used as an electrocatalyst on carbon felt electrodes for VRFB.<sup>80</sup> Graphene-supported monometallic Platinum and bimetallic  $\text{CuPt}_3$  cubic catalysts have been developed for positive electrodes in VRFB.<sup>61,81</sup>

### ***1.3.3 Electrolyte Separator (Membrane) Development***

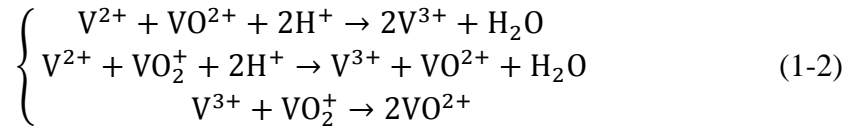
As a key component in the cell, the electrolyte separator physically separates liquid electrolyte compartments and provides an ionic connection between the positive and negative electrolytes to conduct current. The function of the electrolyte separator requires it to possess high ionic conductivity to minimize ohmic loss while simultaneously exhibiting low vanadium and water permeability to inhibit vanadium crossover and electrolyte imbalance.<sup>82</sup> Since the vanadium redox flow battery system has a very long lifetime target,<sup>20</sup> the separator needs to be very stable to withstand the highly acidic, oxidative and corrosive electrolyte solution. Finally, the membrane should be low cost to reduce the overall capital cost of battery system to enhance its marketing competitiveness.

Currently, several types of separator have been used or tested in VRFB system. A polymeric ion exchange membrane is commonly used as the electrolyte separator.<sup>82,83</sup> In reported scaled VRFB systems, Selemion CMV cation exchange membrane,<sup>27</sup> anion exchange membrane<sup>20</sup> and Nafion cation exchange membrane<sup>29,41</sup> were used as electrolyte separators and exhibited good durability in long term operation. The polymer ion exchange membrane, primarily the cation exchange membrane, such as Nafion, has several drawbacks as an electrolyte separator in electrolytes with high acid and vanadium cation concentration. Due to the relatively deep understanding of the property and performance of Nafion, which has been intensively studied as polymer electrolyte in PEM fuel cells, Nafion is widely used as a standard or reference membrane in VRFB research.

As a result of being exposed to electrolyte solutions, acid and vanadium ions are taken into the Nafion and they can drastically reduce the membrane conductivity in VRFB.<sup>30</sup> Although acid in the membrane can elevate its proton content to carry current, proton mobility in membrane is reduced. In the work reported below,<sup>30</sup> it is shown that the proton transport in sulfonated polymer ion exchange membranes is highly favored by high content and activity of water in the membrane.<sup>84,85</sup> The presence of acid in membrane can cause a major proton mobility loss due to water content reduction, which mainly contributes to conductivity loss in the membrane, compared to a water saturated membrane. In addition, vanadium ions can occupy sulfonic acid group sites in the ionic channel, leading to a lower proton concentration and less efficient charge conduction. With  $\text{VO}^{2+}$  in the membrane, proton motion can be slowed down via an unknown mechanism, leading to further proton mobility loss. Compared to the  $0.1 \sim 0.2 \text{ ohm}\cdot\text{cm}^{-2}$  area specific resistance (ASR) observed in a PEM fuel cell with similar membranes,<sup>86-88</sup> the internal resistance of non-gap battery cell with Nafion 117 is about  $0.4\sim 0.6 \text{ ohms}\cdot\text{cm}^{-2}$ ,<sup>33,34,49,50</sup> of which the major part is the resistance of separator.<sup>30,31</sup> The high internal resistance can cause significant efficiency loss, especially in a high performance battery cell with an operational current density at the  $1 \text{ A}\cdot\text{cm}^{-2}$  level.<sup>28</sup> For example,  $1 \text{ A}\cdot\text{cm}^{-2}$  current density on a battery cell with  $0.5 \text{ ohm}\cdot\text{cm}^2$  internal resistance leads to a  $0.5\text{V}$  ohmic loss, which is about equal to 30% efficiency loss with  $1.5\text{V}$  open circuit voltage.

High rates of permeation of vanadium and electrolyte across separator is another bottleneck limiting VRFB performance in long term operation.<sup>89-91</sup> During VRFB operation, vanadium ions can penetrate the separator and immediately react with

vanadium ions of separated valence state as indicated in the following formulas:



The vanadium crossover can reduce concentrations of reactive vanadium species,  $V^{2+}$  and  $V^{5+}$ , to bring down battery capacity. Self-discharge reactions can also bring down the battery energy efficiency by lowering both voltage and coulombic efficiencies. Water osmosis is another unfavorable mass transport process happening during battery operation.<sup>89,92</sup> Along with the charged species migration, water molecules can be dragged across the membrane by electro-osmosis. Water also can diffuse across membrane, driven by a water activity gradient between positive and negative electrolyte solutions. In long-term battery cycle test, it has been shown that the net water transport can cause electrolyte imbalance due to such electrolyte transfer.<sup>89</sup>

Stability of Nafion exposed to vanadium electrolyte solution is also a serious issue limiting its reliability in VRFB system.<sup>93-97</sup> Stability and lifetime tests have been carried out on several commercial ion exchange membrane and newly synthesized membrane by several groups. The strong oxidizing ability of  $V^{5+}$  ion is one of the main means of attack of the polymer structure in membrane.<sup>94,95,97,98</sup> Unfortunately, the long-term membrane stability in scaled battery setup has not been well studied. However, membrane stability is of great significance to improve VRFB's systematic reliability and overall maintenance cost.

Much effort has been devoted to develop alternative separators more suitable for

VRFB application. Several pathways, including hydrocarbon membrane, composite membrane, anion exchange membrane and nanofiltration membrane, have been taken to develop new materials for the VRFB separator. One strategy is to design and synthesize new ion exchange membranes with hydrocarbon polymer which can provide satisfactory transport properties and competitive cost.<sup>95,99-101</sup> Another strategy to improve membrane performance is to manufacture ionomer/functional component composite membrane.<sup>102-105</sup> In this type of membrane, the ionomer can maintain its conductivity, and the functional component (filling or polymer layer) is expected to reduce the unwanted transport across membrane. Anion exchange membranes have been used in running VRFB systems<sup>20</sup> and these are subjected to more fundamental research to develop its performance in VRFB.<sup>101,106,107</sup> In an anion exchange membrane, the cationic group site in membrane can establish a potential barrier to exclude vanadium cations. To somewhat extent, the vanadium crossover in battery can be suppressed.<sup>101</sup> Examples for these strategies are provided in following context.

#### 1.3.3.1 Nafion/Filler Hybrid Membranes

A Nafion/SiO<sub>2</sub> hybrid membrane was initially fabricated by In-Situ sol-gel method by Mauritz et al. to reduce methanol crossover in the direct methanol fuel cell.<sup>109</sup> This method introduces SiO<sub>2</sub> nanoparticles into nanopores in Nafion to impede methanol transport within the ionic cluster channel. The same strategy was borrowed by Xi et al. to manufacture Nafion/SiO<sub>2</sub> hybrid membrane for vanadium flow battery, as is presented in Figure 1-5.<sup>108</sup> The embedded nano-sized SiO<sub>2</sub> particles in micropores of Nafion were used to impede vanadium permeation. The Nafion/SiO<sub>2</sub> hybrid membrane was prepared

by the In-Situ sol-gel method, as for the DMFC. The weight fraction of SiO<sub>2</sub> in the hybrid membrane was roughly 9.2%. The membrane's fundamental properties were measured and compared to Nafion 117. The hybrid membrane thickness was 204 to 215 μm, close to that of Nafion 117. The hybrid membrane and Nafion 117 had very similar ion exchange capacity and conductivity, although water uptake by the hybrid membrane was apparently lower than that of pristine Nafion. The authors attributed lower water content in the hybrid membrane to decreased volume available in the ionic cluster as a consequence of SiO<sub>2</sub> occupation of space. In charge-discharge cycle tests, the setup with Nafion/SiO<sub>2</sub> hybrid membrane had a higher discharge capacity than Nafion 117, implying that vanadium crossover is lower in the Nafion/SiO<sub>2</sub> membrane than in unmodified Nafion. The battery voltage, coulomb and energy efficiencies are consistently higher with the Nafion/SiO<sub>2</sub> membrane, and open circuit voltage decay at 75% SoC in the battery with the hybrid membrane was three times slower than that in the battery with Nafion 117. The hybrid membrane also showed considerable stability in the battery cycling test, consistently showing 90% coulomb efficiency and 72% energy efficiency at 60 mA·cm<sup>-2</sup> after 100 cycles.



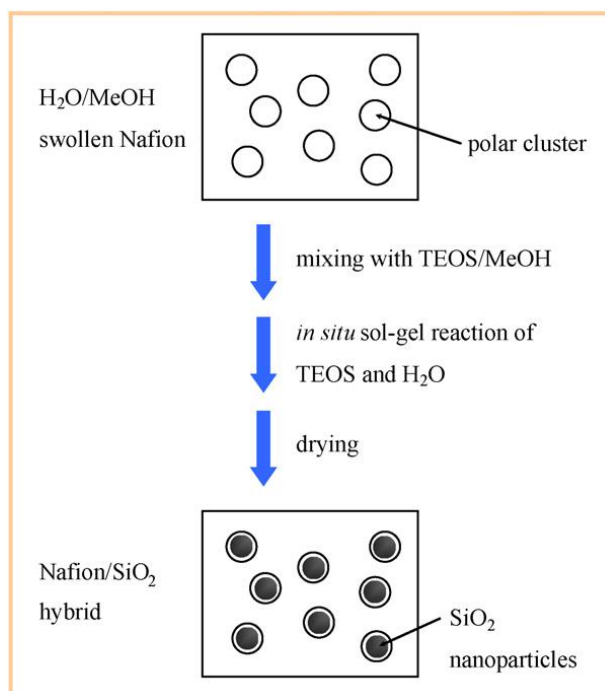


Figure 1–5. The synthesis of Nafion/SiO<sub>2</sub> composite membrane with sol-gel method. (Figure reproduced)<sup>108</sup>

More recently, some more detailed work has been done to extend the understanding on Nafion/SiO<sub>2</sub> hybrid membrane performance in VRFB.<sup>110,111</sup> The permeability of VO<sup>2+</sup> was measured with a counter diffusion measurement on Nafion/SiO<sub>2</sub> membrane of different SiO<sub>2</sub> fraction, including a comparison of pristine Nafion and recast Nafion membranes.<sup>110</sup> The measured Fickian diffusivities of VO<sup>2+</sup> and V<sup>3+</sup> across 5% (w/w) SiO<sub>2</sub> hybrid membrane were respectively reduced to  $0.068 \times 10^{-11} \text{m}^2 \text{s}^{-1}$  and  $0.095 \times 10^{-11} \text{m}^2 \text{s}^{-1}$  from  $0.293 \times 10^{-11} \text{m}^2 \text{s}^{-1}$  and  $0.33 \times 10^{-11} \text{m}^2 \text{s}^{-1}$  of Nafion 117. In a 20% (w/w) SiO<sub>2</sub> hybrid membrane,  $0.062 \times 10^{-11} \text{m}^2 \text{s}^{-1}$  to  $0.085 \times 10^{-11} \text{m}^2 \text{s}^{-1}$  VO<sup>2+</sup> diffusivity was observed. In the corresponding battery test, similar battery performance was achieved using composite

membranes with 5% (w/w) and 20% (w/w) SiO<sub>2</sub>. Spectroscopy work has been done on Nafion/SiO<sub>2</sub> hybrid membrane to investigate interactions among SiO<sub>2</sub>, polymer matrix and vanadium ions.<sup>111</sup> The results from spectroscopy suggested that SiO<sub>2</sub> nanoparticle does not irreversibly bind to the sulfonic acid group in ionic cluster channel in Nafion, but interacts via reversible water hydrogen binding. This finding provided insight on how to improve this strategy for fabricating better hybrid membranes.

Besides SiO<sub>2</sub>, some other materials have been embedded in Nafion polymeric matrix to form hybrid membranes for vanadium redox flow batteries. Nafion/TiO<sub>2</sub> hybrid membranes were fabricated and characterized with a similar method to the Nafion/SiO<sub>2</sub> hybrid membrane papers.<sup>105,110</sup> In counter diffusion measurements and battery tests, Nafion/TiO<sub>2</sub> hybrid membrane exhibited low vanadium permeability when compared to Nafion membranes, similar to the Nafion/SiO<sub>2</sub> hybrid membrane,. Since it was pointed out that TiO<sub>2</sub> was not stable enough in vanadium electrolyte solution, a Nafion/Si/Ti composite membrane was developed.<sup>105</sup> Authors used an in-situ gel-sol method with embedded dimethylsiloxane (DEDMS) and tetrabutyl titanate into Nafion framework to fabricate the Nafion/Si/Ti composite membrane. This membrane showed an eight times lower VO<sup>2+</sup> permeability than Nafion with a slightly lower conductivity. Also, this composite membrane did not show any apparent degradation after 100 charging-discharging cycles. Nafion/organically modified silicate hybrid membranes were prepared via in situ sol-gel reactions with mixtures of tetraethoxysilane (TEOS) and diethoxydimethylsilane (DEDMS), and compared with Nafion and Nafion/SiO<sub>2</sub>.<sup>105</sup>

### 1.3.3.2 Nafion Modification with Ion Exchange Polymer

Some researchers have been trying to combine the advantages of Nafion and some other polymers to meet the requirements for VRFB separator.<sup>103,104,112</sup> The purpose of this method is to build extra layer of polymer with positive charge to establish a positive charge barrier for vanadium ion crossover. Multilayers of functional polymers are polymerized on Nafion surface to improve its ionic selectivity and water osmosis, For example, the Nafion/PSS/PDDA composite membrane is shown in Figure 1-6. Electrolyte soaking, oxidation polymerization and electrodeposition were used to generate a vanadium diffusive barrier layer of polypyrrole on the surface of Nafion 117.<sup>112</sup> Compared to Nafion 117, the membrane modified by electro-deposition showed an obvious reduction in ionic permeability and water crossover, but without adversely affecting the membrane conductivity. A surface modification-adsorption method was utilized to introduce a layer of polyethylenimine (PEI) onto surface of Nafion 117 to form a cationic barrier to expel vanadium ions by the Donnan potential<sup>103</sup>. Although the membrane area specific resistance of Nafion with deposited PEI was slightly higher than Nafion 117, 1.24~1.34 ohm·cm<sup>2</sup> vs. 1.06 ohm·cm<sup>2</sup> in a battery test, the permeability of VO<sup>2+</sup> was reduced from 36.55×10<sup>-7</sup> cm<sup>2</sup>·min<sup>-1</sup> to 1.70~5.23×10<sup>-7</sup> cm<sup>2</sup>·min<sup>-1</sup>, in comparison to untreated Nafion. However, it was pointed out that ionic selectivity improvement did not effectively enhance battery system's energy efficiency, because increased membrane resistance brought down battery's voltage efficiency. Similarly, a multilayered modification was conducted on Nafion 117 to deposit multiple cationic poly(diallyldimethylammonium chloride) (PDDA) and anionic poly(sodium styrene

sulfonate) (PSS) microlayers on Nafion 117 surface by direct-soaking.<sup>104</sup> This multilayered Nafion exhibited significantly lowered vanadium permeability and also helped to increase the battery energy efficiency. A thin layer of Nafion was also cross-linked with sulfonated poly(ether ether ketone) to produce a dual-layered Nafion/SPEEK composite membrane.<sup>102</sup> This method provided a possibility to develop a suitable VRFB separator by enhancing the proton conductivity of some low-cost materials with good stability and low vanadium permeability.

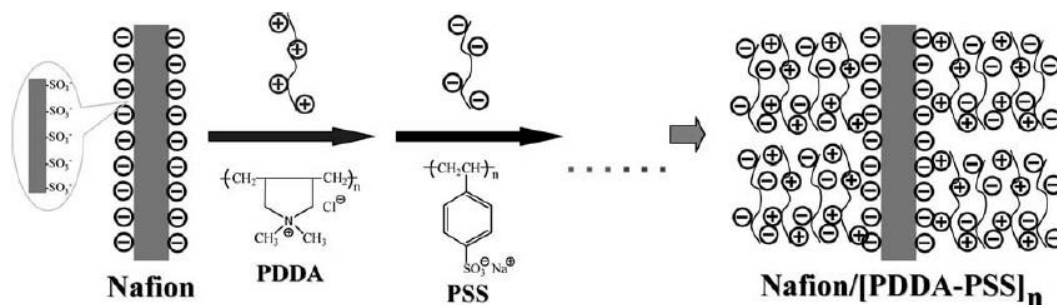


Figure 1–6. Nafion modification with multilayers of poly(diallyldimethylammonium chloride) and anionic poly(sodium styrene sulfonate) by self-assembly with interfacial polymerization. (Figure reproduced)<sup>104</sup>

### 1.3.3.3 Non Ion Exchange Polymer Modification

Introducing ion exchange material into a non-ion exchange membrane is another strategy to manufacture composite ion exchange membranes with good stability. Since polyvinylidene difluoride (PVDF) and ethylene tetrafluoroethylene (ETFE) have considerable chemical stability in extreme chemical environments, they have been tried

to develop new VRFB separators.<sup>113-115</sup> The essence of this strategy is to introduce ionomers into the pores of a framework polymer to form ionic channel to transport proton. Several ionomers, such as polystyrene sulfonic acid (PSSA) or dimethylaminoethyl methacrylate (DMAEMA), were grafted onto infrastructure of PVDF or ETFE and then sulfonated to introduce ionic conducting ability. These membranes demonstrated 20 to 40 times slower vanadium crossover in diffusion measurements and comparable conductivity to Nafion 117. Nafion was also incorporated into Daramic membrane pore to enhance its proton conducting ability, without consuming a large amount of Nafion.<sup>116</sup>

#### 1.3.3.4 Hydrocarbon Polymer

In recent years, non-fluorinated aromatic polymers have been used in the VRFB application because of their lower cost, tunable properties and good chemical and thermal stability.<sup>15,16,28,82,83</sup> Aromatic hydrocarbon cation exchange membranes are the primary alternative cation exchange membrane for PFSA cation exchange membrane in VRFB application because its performance is comparable to Nafion in electrochemical devices.<sup>117,118</sup> Such membranes are generally developed from thermoplastics by sulfonation, which results in high chemical/ thermal stability, good mechanical properties and low cost.<sup>119-121</sup> A series of sulfonated poly(ether ether ketone) (SPEEK) and modified SPEEK membranes have been manufactured and tested for VRFB applications.<sup>99,122-124</sup> These SPEEK membranes have different sulfonation degrees and various modifications, including SPEEK / heteropolyacid (PTA) / Polypropylene, or SPEEK / PTFE and SPEEK / polypropylene / Nafion composite membranes. Similarly, sulfonated poly(flourenyl ether ketone) (SPFEK) membranes and SPFEK/SiO<sub>2</sub> hybrid

membranes were fabricated by Chen et al.<sup>125,126</sup> Another series of membranes, sulfonated poly(arylene thioether ketone) (SPTK) and sulfonated poly(arylene thioether ketone ketone) (SPTKK) based on poly(arylene thioether) framework polymer, were synthesized and investigated.<sup>127</sup> Sulfonated poly(sulfone) (S-Radel) membrane has also been synthesized and subjected to VRFB testing by Kim et al.<sup>95,96</sup> The S-Radel membrane showed a comparable cycling performance to Nafion, and much lower vanadium permeability than for Nafion. However, S-Radel was chemically vulnerable in vanadium electrolyte, especially to highly oxidative  $V^{5+}$ . Recently, sulfonated Diels Alder poly(phenylene)s (SDAPP) membranes have been synthesized and tested for VRFB application by Fujimoto et al.<sup>100</sup> SDAPP membranes degrade faster than Nafion in  $V^{5+}$  containing electrolyte, and the degradation rate is proportional to the ion exchange capacity.

Good conductivity comparable to Nafion and low phenomenal vanadium ion permeability can both be achieved by most of the membranes mentioned above, but stability of these polymers in electrolyte solution still needs to be improved. Also, more insightful research is also required to establish a solid understanding of the relation between polymer structure and its performance in electrolyte conditions, especially the polymer property influence on membrane transport behavior and durability in the battery.

#### 1.3.3.5 Anion Exchange Membranes

Although anion exchange membranes have been used in commercial VRFB system for over ten years,<sup>20</sup> the research effort devoted to anion exchange membranes was

significantly less than that for cation exchange membrane. Due to the presence of cationic functional groups in the polymer backbone, the anion exchange membrane was proposed to reduce vanadium permeation in VRFB by Donnan exclusion (Figure 1-7). Crosslinked polysulfone anion exchange membranes were initially Crosslinked by accelerated electron beam irradiation.<sup>106</sup> The battery system using this membrane reached 80% energy efficiency in 8 cycles at  $60 \text{ mA}\cdot\text{cm}^{-2}$  current density. Another polysulfone based AEM was manufactured by functionalization with quaternary benzyl trimethylammonium groups (PSF-TMA<sup>+</sup>) by Jung et al.<sup>129</sup>. The PSF-TMA<sup>+</sup> membrane had good stability in  $1.5 \text{ mol}\cdot\text{dm}^{-3} \text{ V}^{5+}$  solution for over 90 days. A series of quaternized poly(phthalazinone ether sulfone) (QPPESE), quaternized poly(phthalazinone ether ketone) (QPPEK) and quaternized poly(phthalazinone ether ketone ketone) (QPPEKK) AEMs were synthesized and analyzed in a series of tests, including battery testing, by Jian et al.<sup>107,130,131</sup> Ethylene-tetrafluoroethylene (ETFE) based AEMs were also manufactured by grafting poly(methacryloxyethyl dimethyl ammonium chloride) (PMAOEDMAC)<sup>115</sup> and dimethylaminoethyl methacrylate (DMAEMA).<sup>132,133</sup> Quaternary ammonium functionalized Radel (QA-Radel) and quaternary ammonium functionalized poly(fluorenyl ether) (QA-PFE) were respectively synthesized and tested by Chen et al.<sup>128,134</sup>. In both of these AEMs, lower vanadium permeability was reflected by lower coulombic efficiency and slower capacity decay in the cycling tests. With QA-Radel, the battery system performed with higher power density and lower overpotential than Nafion 212.<sup>134</sup>

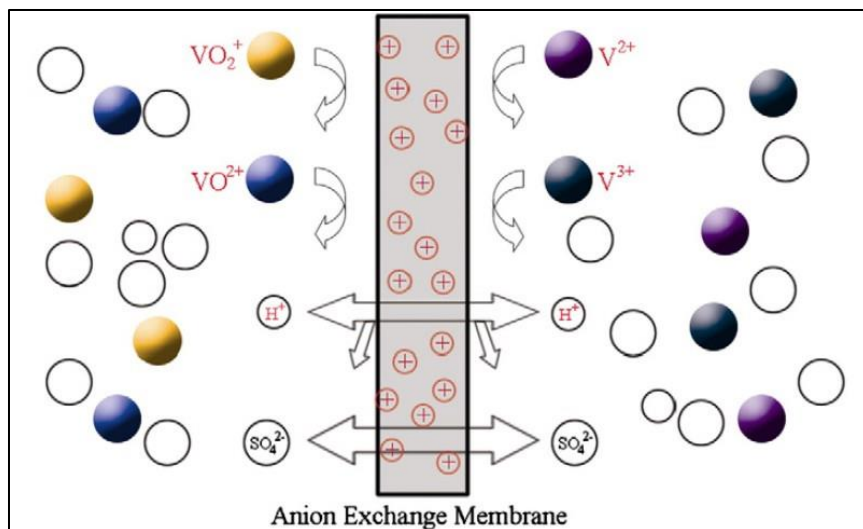


Figure 1–7. The Donnan potential generated by the positively charged ionic group in the membrane can prevent vanadium permeation.<sup>128</sup>

### 1.3.4 Effort for Electrolyte Improvement

Because the energy in VRFB is carried by the vanadium redox couple dissolved in electrolyte solution, the energy density of VRFB is favored by high concentration of vanadium salts in electrolyte. However, the solubility of vanadium in electrolyte was limited by several factors, leading to an electrolyte stability problem in battery operation.<sup>35,135</sup> It was pointed out that when the battery was operated with unstabilized electrolyte solution,  $V^{5+}$  and  $V^{3+}$  can respectively precipitate in the forms of  $V_2O_5 \cdot xH_2O$  and  $V_2(SO_4)_3 \cdot xH_2O$ .<sup>135</sup> To understand the stability of vanadium ions, as well as ionic structure features, research has been conducted to illustrate the state of vanadium ions in electrolyte solutions. A Raman spectroscopy investigation was conducted on the positive electrolyte solution with varying  $V^{5+}$  and sulfate concentration, state of charge and temperature by Kausar et al.<sup>136</sup>. Various  $V^{5+}$  ionic forms were suggested by the



spectroscopy work. It was concluded that the lack of  $H^+$  and sulfate supporting electrolyte was the main reason for  $V^{5+}$  precipitation at elevated temperature. Nuclear magnetic resonance (NMR) and density functional theory (DFT) simulation studies have been conducted to probe the vanadium ions (III, IV, V) in vanadium-sulfuric acid electrolyte.<sup>137-140</sup> The detailed mechanism of  $V^{5+}$  and  $V^{3+}$  precipitation was proposed on these works.<sup>138-140</sup> The precipitation of  $V^{5+}$  is caused by deprotonation and dehydration of its hydration structure.<sup>138,140</sup> The  $V^{3+}$  precipitation was caused by the nucleation in the  $V^{3+}$ -sulfate ion complex form by water-sulfate exchange in the hydration structure of  $V^{3+}$ .<sup>137,139</sup> Stability of electrolytes with practical vanadium concentration was also examined by researchers.<sup>35,135</sup> The stability of  $V^{5+}$  and  $V^{3+}$  was evaluated with respect to temperature, vanadium concentration and acid concentration. While high sulfuric acid concentration in the electrolyte can favor stabilization of  $V^{5+}$  in positive electrolyte, it would cause more severe  $V^{3+}$  precipitation in negative electrolyte.<sup>135</sup>

To improve the performance of vanadium-sulfuric acid electrolyte in VRFB, several methods were used to increase electrolyte stability and reaction kinetics. The effort was mainly focused on improvement of electrolyte thermal stability.<sup>36,37,141-143</sup> Several organic acid additives have been tested as positive electrolyte additive to stabilize  $V^{5+}$  to reduce its precipitation. These additives included polyacrylic acid and acetic acid mixture<sup>36</sup>, coultter dispersant<sup>141</sup>, inositol and phytic acid<sup>142</sup>, glycerin/n-propyl alcohol<sup>144</sup>, l-glutamic acid<sup>37</sup>, methanesulfonic acid (MSA) and aminomethylsulfonic acid<sup>143</sup>. Besides electrolyte stabilization, the electrolyte additive can also act as a catalyst to improve electrochemical reaction kinetics of vanadium redox couples on the electrode.<sup>37,142-144</sup>

The organic additives can introduce oxygen and nitrogen containing functional groups adsorbed on the electrode surface to catalyze vanadium redox reactions. The catalytic activity attributed to the additives is similar to that of carbon electrode surface heating treated in oxygen and ammonia atmosphere.

#### **1.4 Motivation and Goal of This Dissertation**

As reviewed above, a large of research effort has been devoted to develop VRFB systems and relevant materials, but thorough understanding of the battery system performance and components characterization has not been well established. A number of technical problems related to VRFB performance have been not solved or clarified by researchers. To improve the fundamental understanding of VRFB performance, the author has systematically investigated the performance of novel non-gap battery cell performance, the UV-Vis spectrometry of vanadium electrolytes and ionic transport behavior in perfluorinated sulfonic acid membrane (Nafion) and sulfonated Diels Alder poly(phenylene) membrane. In this dissertation relevant research is described to illustrate the performance characterization techniques for VRFB, state of charge monitoring by UV-Vis spectroscopy and ion exchange membrane characterization for electrolyte separator in VRFB.

The development of VRFB diagnostic technique and performance characterization are behind the development of new materials for VRFB. In chapter 2, the polarization curve measurement is coupled with high frequency resistance measurements and cycling

tests to reveal extensive information about battery performance loss. The principles and procedures of polarization curve measurements are presented to demonstrate the methodology of polarization curve tests in VRFB performance analysis as well. The polarization curve measurement can be used to illustrate the activation and mass transport loss, while the HFR measurement can reveal the ohmic loss during battery operation. The cycling test is able to show the long term capacity and efficiency loss due to self-discharge, while it can also partially reflect battery activation loss.

Since vanadium ions have characteristic UV-Vis spectra, it is plausible to monitor state of charge (SoC) by analyzing the UV-Vis spectra of  $V^{3+}/V^{2+}$  and  $V^{4+}/V^{5+}$  redox couples in positive and negative electrolytes. In chapter 3, a SoC monitoring method was developed on the basis of vanadium UV-Vis spectroscopy. In acidic electrolyte environment, it is found that complex ion  $V_2O_3^{3+}$  can be formed by the coexistence of  $V^{4+}$  and  $V^{5+}$ . The UV-Vis characteristic spectrum of  $V_2O_3^{3+}$  was successfully separated from the spectra of positive electrolyte. The equilibrium constant of the  $V_2O_3^{3+} - V^{4+} - V^{5+}$  system was calculated from spectral analysis on the positive electrolyte.

In VRFB, because the sulfuric acid and vanadium ions can enter micropore in the separator, for example Nafion, the polymer-acid-cation balance in the separator can have a strong influence on ion transport in the separator. In chapters 4 and 5, to illustrate the effect of sulfuric acid and vanadium cations on ionic transport in Nafion, Nafion conductivity was measured and analyzed together with the sulfuric acid and vanadium uptake. It is found that sulfuric acid can increase the proton concentration in the membrane for carrying charge, but also cause a decrease in proton mobility. The

vanadium ions generally have much lower mobility than protons, and  $\text{VO}^{2+}$  and  $\text{VO}_2^+$  can also slow down proton motion. Low conductivity in Nafion can be increased by taking advantage of the acid and vanadium ion partitioning.

Sulfonated Diels Alder Poly(phenylene) (SDAPP) is a newly synthesized hydrocarbon cation exchange membrane and was recently used in VRFBs as an electrolyte separator. In chapter 6, SDAPP was characterized using a series of methods to evaluate its ionic conductivity,  $\text{VO}^{2+}$  permeability, equilibrium with electrolyte and polymer morphology. By tuning the ion exchange capacity in SDAPP, conductivity higher than Nafion can be obtained with SDAPP equilibrated in sulfuric acid. A higher conductivity to vanadium permeability ratio was measured on SDAPP membranes at various IEC than that for Nafion, suggesting that SDAPP has higher ionic selectivity. Transmission electron microscope imaging showed that SDAPP is a more homogeneous polymer than Nafion, which presents a manifest phase separation.

**CHAPTER 2**

**POLARIZATION CURVE MEASUREMENT AND CYCLING TEST ON  
ALL VANADIUM REDOX FLOW BATTERIES**

**2.1 Introduction**

The performance characterization methods are of great importance to VRFB development.<sup>5,8,9,11,145,146</sup> In electrochemical device development, diagnostic methods are used to clarify limiting factors (activation, ohmic or mass transport) in device performance. However, diagnostic techniques or characterization methods have not been well developed for VRFB cells or stacks. In contrast, a relatively comprehensive diagnostic technique system has been developed for proton exchange membrane fuel cells to aid understanding the fundamental aspects of fuel cell, including electrochemical reactions, fluid dynamics and thermodynamics etc..<sup>46,147-151</sup> The primary electrochemical diagnostic methods for PEM fuel cells includes polarization curve, current interruption and electrochemical impedance spectroscopy measurements.<sup>147</sup> The polarization curve is a plot of battery potential (or any other electrochemical cell) vs. its current density under given operating conditions. Combining theoretical or semi-empirical mathematical modeling analysis, analysis of the shape of polarization curve can provide straightforward information about reaction kinetics and mass transport.<sup>150-153</sup> The fundamental theory of the polarization curve and its experimental and analytical methodology will be described in the later context with more detail. Current interruption is a method to isolate the ohmic loss from other losses in electrochemical devices.<sup>154,155</sup> The principle of this method is to

measure the different vanishing rates of overpotentials due to internal resistance and activation after a current interruption. The ohmic overpotential disappears immediately after the current is turned off, while the overpotential caused by the electrochemical reaction needs a significantly longer time to fade out.<sup>156</sup> Electrochemical impedance spectroscopy (EIS, or AC impedance) is another commonly used diagnostic method to characterize fuel cells or flow batteries.<sup>149,157-159</sup> During an EIS measurement, small AC perturbation/signals (potential or galvanic) of varying frequency are applied to the electrochemical device. The resulting ratios of voltage to current are determined and plotted as implicit functions of signal frequency. Performance information about the electrochemical cell is obtained by quantitative analysis of the shape (arc heights or length) and position of impedance spectra (in Nyquist or Bode plots). Some other diagnostic methods based on physical or chemical methodology have been developed to investigate performance related problems in fuel cells,<sup>148</sup> such as neutron imaging<sup>160-162</sup> and current mapping<sup>163-166</sup>. These methods can significantly enhance the information content of the electrochemical methods mentioned above to more accurately identify and quantify the factors causing performance loss in the fuel cell. Many of the diagnostic methods developed for fuel cell applications can be utilized in VRFB research because of similarity between fuel cells and flow batteries.

Several electrochemical diagnostic methods have been utilized in vanadium redox flow battery research. Currently, the charge-discharge cycling test is the most widely used technique to evaluate VRFB performance. In the battery community, the cycling test is a standard measurement to illustrate a secondary battery's overall performance under

specific operation conditions. Primarily, cycling test can provide performance information including capacity, voltage and energy efficiencies in VRFBs.<sup>21,27,29</sup> The battery capacity decay can further provide information about imbalanced vanadium permeation across the membrane.<sup>100,167</sup> However, the cycling test is limited to identify the factors causing performance loss in a VRFB system. As has just been discussed, the polarization curve is a commonly utilized method in electrochemical system performance characterization. This experimental protocol has been used recently to evaluate new battery cell architectures,<sup>33,34</sup> optimize cell configurations<sup>49</sup> and investigate vanadium reaction kinetics<sup>168,169</sup>. The polarization curve measurement on a novel battery cell showed that the battery cell can achieve remarkable battery output performance with its zero-gap configuration, flow-by flow field and non-wetproofed carbon paper electrode.<sup>33,34,49</sup> The low current polarization measurement was carried out to study the vanadium reaction kinetics on carbon paper surface.<sup>168,169</sup> The results of polarization tests suggested that  $V^{5+}/V^{4+}$  couple has significantly faster reaction kinetics than the  $V^{2+}/V^{3+}$  couple. The future catalyst development effort for VRFBs should primarily focus on the negative electrode which is dominating activation overpotential loss. Besides polarization curve tests, electrochemical impedance spectroscopy was also used to investigate VRFB's performance.<sup>170</sup> The result of EIS investigations also indicated that the negative electrode, or  $V^{2+}/V^{3+}$  couple, is the main source of activation overpotential in VRFB, contributing about 80% of the overpotential loss during a battery discharging polarization test. However, it should be noted that this test was done under operating conditions deliberately chosen to allow rigorous identification of the origin of some cell features and may not be indicative of the ultimate performance losses in a high performance cell.

The general procedure of polarization curve measurement includes stepwise galvanic or potential polarization and coupled impedance measurement. The polarization is to trigger redox reaction and collect battery potential or current response; the impedance measurement is to determine battery internal resistance under the reaction condition. The polarization curve coupled with internal resistance measurement is capable of distinguishing activation, ohmic and mass transport loss across the battery cell, as can be seen in Figure 2-1. The kinetic loss of the electrochemical reaction comes from the energy barrier to electron transfer and mass transport at the electrode-electrolyte interface, represented by the overpotential loss at low current density. The ohmic loss includes internal resistance (IR) loss and ‘pseudo-IR’ loss. IR loss is the overpotential loss caused by charge conduction resistance and includes ionic resistance in electrolytes and membrane separator, contact resistances between cell components and electronic resistance in electrodes. Pseudo-IR loss is associated with mass transfer of redox-active species within electrode diffusion layers. Mass transport loss is caused by concentration polarization and ohmic loss within the electrode, controlled by transport resistance of active species towards electrode surface. All these types of performance losses happen simultaneously during battery operation, but each of them dominates a different section on the polarization curve. The ohmic loss is represented by a linear overpotential loss corresponding to increasing current density. The ohmic loss can be theoretically removed by potential loss due to internal resistance, or  $IR$  in which  $I$  is the passing current and  $R$  is the DC resistance determined by the high frequency resistance (HFR). The impedance of mass transport loss can be excluded from DC resistance or HFR, because electrode is electronically shorted by DC or high frequency signal. However, polarization behavior in



ohmic region can still result in a nonhorizontal pattern, after  $IR$  correction. The mass transport loss is brought up by reactant depletion on the electrode surface due to the high consumption rate at high current density. The mass transport limiting current density is reached when the reactant on electrode surface was completely converted. The amplitude of the limiting current density can reflect the mass transport resistance for reactive species within flow field and electrode.

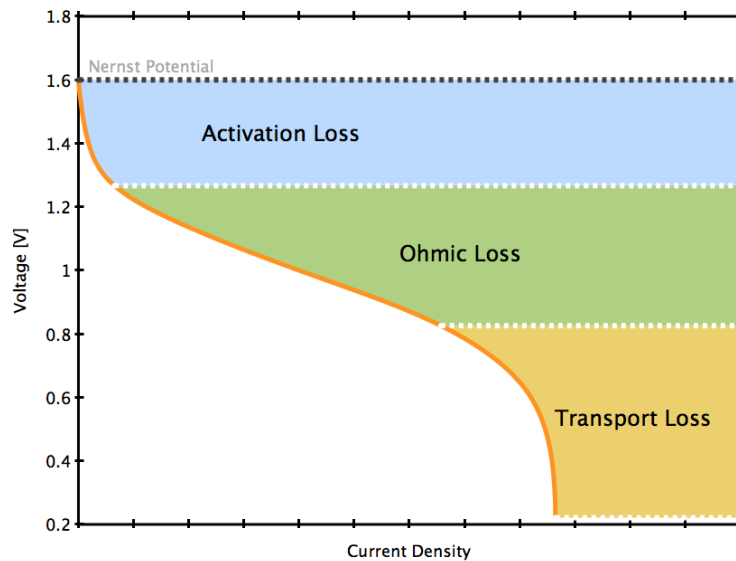


Figure 2–1. The parts of polarization curve correspond to different sources of potential losses as varying current density. (Figure reproduced)<sup>33</sup>

In following part of this chapter, I will present a protocol for polarization measurements as well as battery cycling. Part of the work in this chapter has already been published.<sup>33</sup> The purpose of the combination of these diagnostic technique is to develop a characterization methodology to analyze the battery performance in different aspects.

Polarization curve analysis conducted on two flow battery setups is presented, respectively with one lab-assembled battery cell of a flow through flow field, and one modified direct methanol fuel cell with flow-by flow field. We also conduct polarization curve measurements on the fuel cell battery setup with different commercial electrode materials to investigate electrode material influence on battery output performance. Battery cycling was also carried out on battery setup with modified DMFC cell to quantify battery's efficiency and capacity loss due to vanadium crossover.

## **2.2 Experiment**

### ***2.2.1 Battery Setup***

The key components of the battery setup includes a battery cell, electrolyte solution reservoirs and pumps circulating the electrolytes, as is shown in Figure 2-2. Positive and negative electrolyte solutions were respectively contained in two Corning Pyrex 250 mL glass reagent bottles. Electrolyte solutions were circulated between the battery cell and reservoirs within 1/8" or 1/4" outside diameter polyethylene tubing by two KNF Stepdos 08 dosing pumps. The electrolyte separators used in all following measurements included Nafion 117, 211 and 212 membranes, purchased from Ion Power Inc. Their dry thicknesses were 180, 25 and 50  $\mu\text{m}$  respectively. Before being installed in battery cell, the membrane was cut into a size fitting in the cells and pretreated with the protocol described elsewhere.<sup>84</sup>

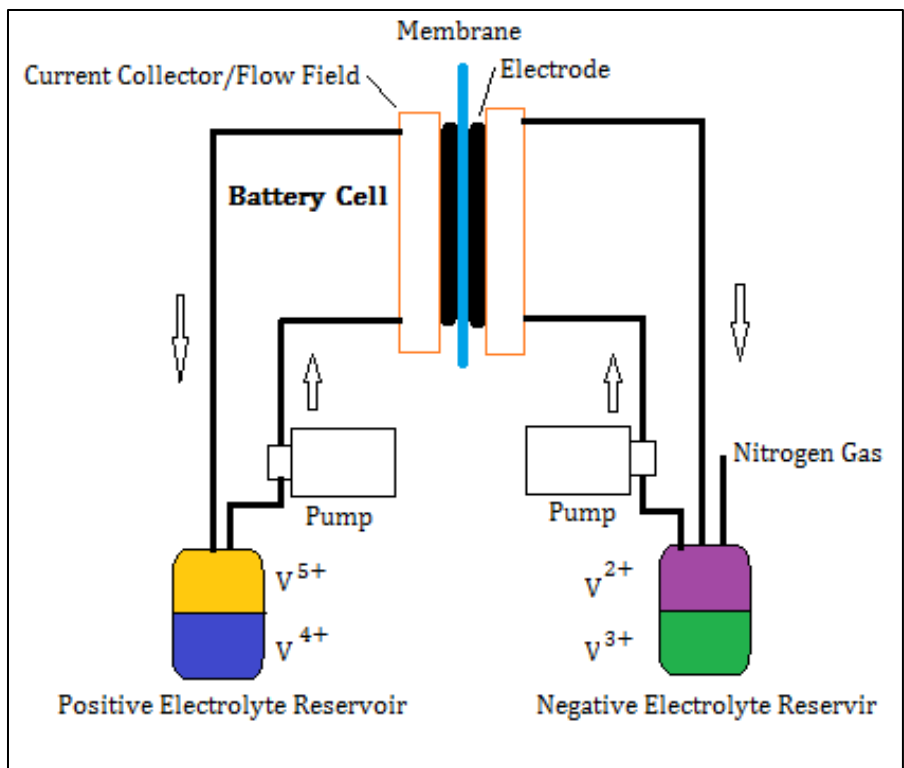


Figure 2–2. The systematic sketch of the experimental VRFB setup with a battery cell, electrolyte transport and storage.

### 2.2.2 Cell Designs

Two battery cells of distinct configurations were tested in this work. One battery cell was lab-assembled with a flow-through electrode pattern, referred as LA cell in future discussion. The membrane electrode assembly (MEA) consisted of one Nafion 117 cation exchange membrane and two layers of graphite carbon felt (Cera Material, 1.27 cm thick,  $0.12 \Omega\cdot\text{cm}$  uncompressed through-plane resistivity). On each side of the cell, two layers of carbon felt were housed in a  $5\times 5$  cm square PVC tube of 2 cm length, with 20% compression. The cross sectional area of battery was  $20 \text{ cm}^2$ , controlled by the size of

window on Viton gaskets between membrane and PVC housing. Two polypropylene 1/8" NPT to 1/4" tube fittings were diagonally placed on the walls of the housing to be inlet and outlet of electrolyte solutions. The MEA and PVC housing were compressed by two 7.5×7.5×1.27cm PVC endplate tightened by four 1/4" bolts. One platinum wire was fixed through each endplate to serve as current collector on each side.

The other battery cell tested in this work was modified from a 5 cm<sup>2</sup> direct methanol fuel cell (Fuel Cell Technology Inc.), referred to as fuel cell battery (FCB). In this cell, a flow-by flow pattern was introduced by graphite current collectors with serpentine flow channels (0.787 mm wide and 1.02 mm deep). The membrane used in this cell was a pretreated Nafion membrane. Several electrode materials were tested with FCB cell, including carbon felt (2.5mm), Toray TGP-H-060 carbon paper (200μm) (referred as Toray in future) and SGL 10AA (400μm) (referred as 10AA in future). During battery operation, the MEA was confined by glass fiber gaskets and compressed by graphite flow fields.

The electrolyte solutions were originally made from VOSO<sub>4</sub>·xH<sub>2</sub>O (Alfa Aesar, x=3.23, 99.9%), H<sub>2</sub>SO<sub>4</sub> (Alfa Aesar, 96~98%) and deionized water (Milli Q, 18MΩ·cm). All electrolyte solutions were charged from VOSO<sub>4</sub>/H<sub>2</sub>SO<sub>4</sub> solutions made from the reagents. Electrolyte solutions of two concentration levels were prepared: 0.5M VOSO<sub>4</sub>/2M H<sub>2</sub>SO<sub>4</sub> and 1M VOSO<sub>4</sub>/4M H<sub>2</sub>SO<sub>4</sub>. To prepare electrolyte solutions for the battery, electrolyte solutions were charged in a two-step charging protocol. The solutions were charged by a 1.8V constant voltage across the battery to prevent overcharge. In the first charging step, VOSO<sub>4</sub> solutions of the same volume were placed on both sides of the

battery.  $V^{3+}$  and  $VO_2^+$  were obtained respectively on negative side and positive side of the battery. The positive electrolyte containing  $VO_2^+$  was then replaced by fresh  $VOSO_4$  solution of the same volume to reach a fully discharged state in battery. Then one more charging step was conducted to charge the battery to a fully charged state and  $V^{5+}$  ( $VO_2^+$ ) and  $V^{2+}$  were obtained on the positive and negative sides respectively. During battery operation, nitrogen was pumped into the negative electrolyte solution to protect  $V^{2+}$  from oxidation of air.

### ***2.2.3 Electrochemical Tests***

All electrochemical experiments, including battery charging, were conducted with a Bio-Logic HCP803 high current potentiostat. The high performance potentiostat consists of a basic potentiostat with 400mA current capacity and a booster with 80A current capacity. During battery charging or testing, the working electrode probe of the potentiostat was connected to the positive electrode ( $V^{5+}/V^{4+}$  side) of the battery cell and the counter electrode probe was attached to negative electrode ( $V^{2+}/V^{3+}$  side), while the reference electrode probe was connected to battery's negative electrode. The battery was regarded as fully charged after being charged constantly at 1.8V until the current density dropped to 2 mA/cm<sup>2</sup>.

Polarization curve measurement was the main electrochemical characterization carried out in this work. A potential-control polarization measuring protocol was applied to avoid reaching high potentials under current control and thereby damaging the carbon electrode and graphite flow field. A stepwise increasing or decreasing battery voltage

from the open circuit voltage was set across battery cell to trigger electrochemical reactions at varying over potential. For each polarization step, a constant voltage was applied to the battery for 30 seconds to reach a steady state and to provide a data point on the polarization curve. Then, battery rested at open circuit voltage (OCV) for 120 seconds to refresh electrolyte in the electrode. The flow rate was controlled by the setting of dosing pumps, ranging from 0.5 to 45 mL/min. All measurements were carried out at 22°C ambient temperature, without temperature control on the battery system. Because the temperature difference between electrolyte inlet and outlet of battery cell was no more than 1°C at maximum power, we assumed that all measurements were at constant temperature. The battery internal resistance was measured by determining high frequency resistance (HFR) of the battery from electrochemical impedance spectrum (EIS). The EIS was conducted with potential-controlled electrochemical impedance spectroscopy (PEIS) over an AC frequency range of 100 kHz to 1Hz and with 10mV perturbation amplitude. To correct ohmic loss (IR loss) of the polarization curve, the voltage of the raw polarization curve was adjusted by the product of current and HFR.

Battery cycling was carried out on the FCB battery setups with the same test equipment. The FCB cell was installed with three membrane-electrode combinations: A. Nafion 211+3 layers 10AA (70% compression); B. Nafion 212+3 layers 10AA (70% compression); C. Nafion 117+one layers Toray (70% compression). The cycling current densities were 80 mA·cm<sup>-2</sup> for battery A and B, and 120 mA·cm<sup>-2</sup> for setup C. The charging and discharging limits for battery A and B are 1.8V and 0.8V; the charging and discharging limits for battery C are 2.4V and 0.4V. The voltage efficiency (CE) of the

battery during a cycling process is defined as:

$$VE = \frac{E_{Discharging}}{E_{Charging}}.$$

And the coulombic efficiency (CE) of the battery is

$$CE = \frac{Q_{Discharging}}{Q_{Charging}}$$

Here,  $E$  and  $Q$  are the voltage and capacity of an individual discharging or charging step. The energy efficiency (EE) equals the product of VE and CE.

## 2.3 Results and Discussion

### 2.3.1 Flow-Through Cell Configuration

The raw and IR corrected polarization curves measured on the LA cell with  $0.5 \text{ mol}\cdot\text{dm}^{-3} \text{ V}^{\text{x+}}$  and  $2.5 \text{ total mol}\cdot\text{dm}^{-3} \text{ SO}_4^{2-}$  electrolyte solutions are presented in Figure 2-3. The cross battery internal resistance determined by impedance measurement was  $4.57 \text{ ohm}\cdot\text{cm}^2$ . The IR correction resulted in a flattened IR free polarization curve pattern. This implies that there are very low kinetic and pseudo-ohmic losses in the LA cell setup. Because the surface area of the carbon felt is high enough due to the large volume of carbon felt electrode in the LA cell, activation loss can be largely avoided given the low local current density on electrode surface. In the LA cell, the contact resistance is the primary source of battery internal resistance. It has been proved that an ion exchange membrane can have lower conductivity in the electrolyte environment due to sulfuric acid

and vanadium ions entering and dehydrating the membrane.<sup>30</sup> However, in electrolyte with  $1 \text{ mol}\cdot\text{dm}^3 \text{ V}^{x+}$  and  $5 \text{ mol}\cdot\text{dm}^3$  total sulfate, the membrane can only account for  $0.4 \text{ ohm}\cdot\text{cm}^2$  resistance which is an order of magnitude lower than the observed ASR of the LA cell. In the half cell compartment, two pieces of carbon felt electrodes were compressed from 2.5 cm to 1.8 cm, but good contact between electrode and membrane cannot be achieved because they were just loosely pressed together. The edge of carbon felt can be separated from the membrane by the sealing rubber gasket. Another significant factor in high internal resistance is the contact between electrode and platinum wire current collector. The platinum wire was simply inserted into the carbon electrode to collect current, without tight contact to carbon fibers. The loose contact between platinum wire and carbon material can lead to significant contact resistance, or even an electrolyte gap between the platinum wire and carbon fiber in electrode. We conclude that the contact resistance is the primary resistance source in LA cell, leading to significant ohmic loss in the polarization curve.



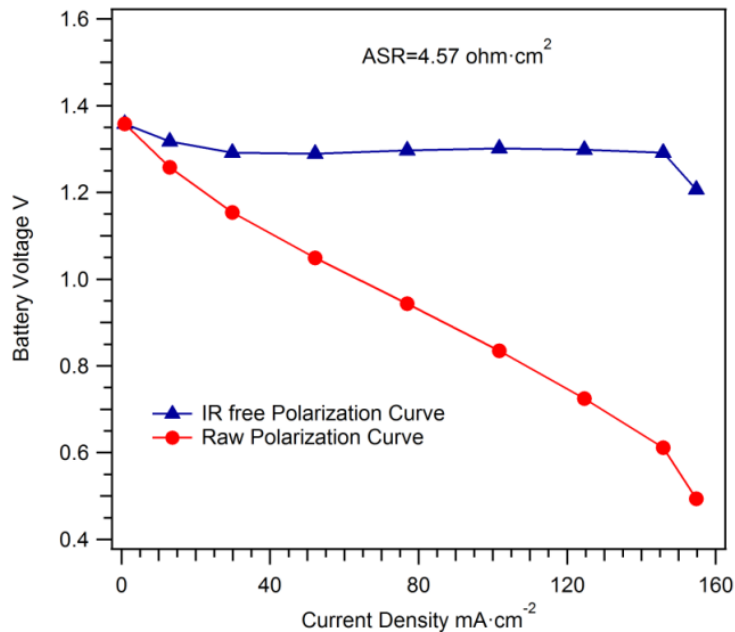


Figure 2–3. The raw and IR-corrected polarization curves tested on LA battery cell with  $0.5 \text{ mol}\cdot\text{dm}^{-3} \text{ V}^{x+}/2.5 \text{ mol}\cdot\text{dm}^{-3}$  total sulfate electrolyte, at  $30 \text{ ml}\cdot\text{min}^{-1}$  flow rate.

### 2.3.2 Vanadium Concentration Influence on Battery Performance

To compare the vanadium concentration influence on cell performance, polarization curves were measured on an FCB cell with  $0.5 \text{ mol}\cdot\text{dm}^{-3} \text{ V}^{x+}$  or  $1 \text{ mol}\cdot\text{dm}^{-3} \text{ V}^{x+}$  in  $5 \text{ mol}\cdot\text{dm}^{-3}$  total sulfate electrolyte solutions. The electrode in the battery was 2.5 mm thick carbon felt, compressed to 0.5 mm thickness. The flow rate in this measurement was 20 mL/min. Due to the high compression of the electrode and the diffusive resistance in the flow-by pattern, low limiting current density, about  $90 \text{ mA}/\text{cm}^2$ , was achieved on both polarization curves with different vanadium concentrations. Obviously, the vanadium concentration has a strong influence on the mass transport during the battery operation. In

the mass transport controlled region, a polarization curve with 0.5 mol/L flow rate of vanadium shows less performance than that for 1 mol/L. Interestingly, in the kinetic region and higher end of ohmic region, the two polarization curves perfectly overlap each other. This means that the kinetics of the vanadium redox reaction on carbon felt are not influenced by the concentration change.

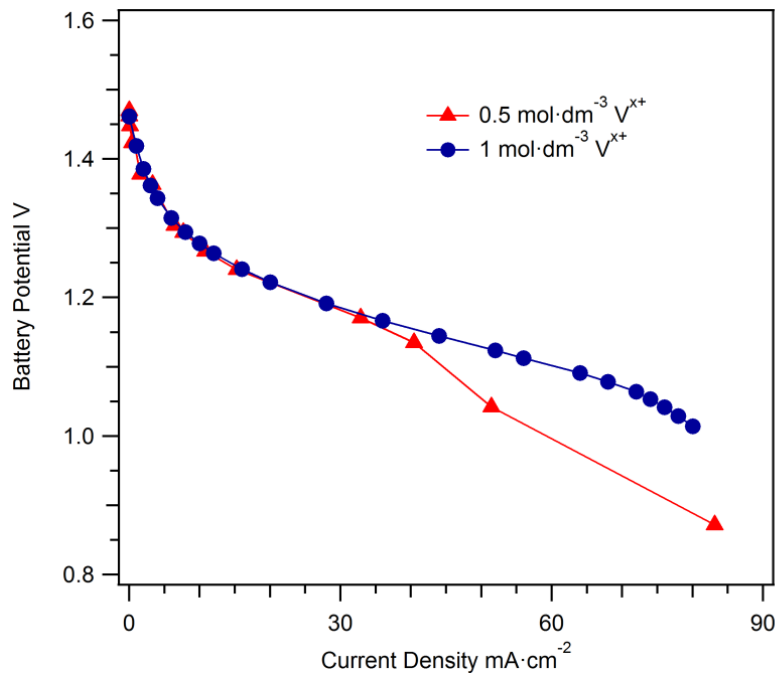


Figure 2-4. IR corrected polarization curves on FCB cell with carbon felt electrode with 0.5 mol·dm<sup>-3</sup> V<sup>x+</sup> or 1 mol·dm<sup>-3</sup> V<sup>x+</sup> in 5 mol·dm<sup>-3</sup> total sulfate electrolyte solutions. The flow rate is 20 mL·min<sup>-1</sup>.

The kinetic polarization difference between the FCB cell and LA cell is a result of cell architecture difference. Distinct IR-free polarization curves can be observed on LA

and FCB cells, as can be seen in Figure 2-3 and 2-4. The higher electrode surface area in LA cell can effectively reduce activation loss during battery operation. Because the electrode uncompressed thickness of the carbon felt electrode in LA cell is 2.53 cm, about ten times thicker than that of the carbon felt electrode in FCB cell, the LA cell can have a ten times larger electrode surface area than FCB cell. At a given current density across the battery, the high surface area in LA cell can effectively reduce the local current density on the surface of electrode. The lower current density at the electrode surface would lead to lowered activation overpotential loss, which was shown by the flat IR free polarization curve in Figure 2-3. In contrast, the activation loss on the FCB cell is manifest, because the surface area of the electrode is limited. Similar observations, i.e. that a thicker electrode can effectively reduce activation loss in VRFB, were made elsewhere.<sup>34,49</sup>

### ***2.3.3 Electrolyte Feed Rate Effect on Cell's Output Performance***

High feed rate of electrolyte solutions into both sides in battery cell can immediately increase output capacity of the battery. The FCB cell with Toray carbon paper electrode (25% compression) polarization curves at varying flow rates are presented in Figure 2-5. The electrolyte solution contained  $1 \text{ mol}\cdot\text{dm}^{-3} \text{ V}^{x+}$  and  $5 \text{ mol}\cdot\text{dm}^{-3}$  total sulfate. High electrolyte feed rate can obviously improve mass transport in electrodes. The mass transport limiting current density increases corresponding to the growth of feed rate. It is reasonable that higher flow rate into the cell can bring more active species onto the electrode surface to support the redox reaction to generate higher current density. In the

mass transport region of polarization curves with high feed rate 16 to 40 mL/min, these polarization curves show a hooking tail bending back towards lower current density. This could be caused by the circulating operation mode of the tested experimental battery setup. During the polarization curve measurement, because the electrolyte solutions were constantly circulated between battery cell and electrolyte reservoir, the battery state of charge would be reduced during the battery test, especially at the high current density (mass transport loss region). This is consistent with the hooked polarization curve at the low voltage end of polarization curve.

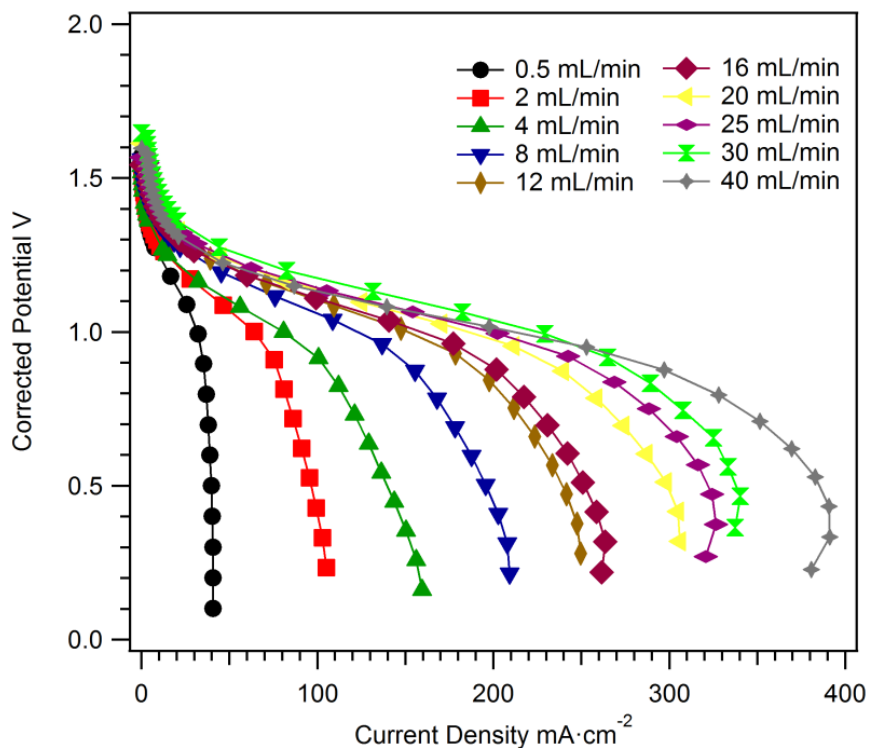


Figure 2–5. The polarization curves measured on an FCB cell with Toray carbon paper (25% compression) electrode at varying electrolyte feed rate. The electrolyte solution contained  $1 \text{ mol}\cdot\text{dm}^{-3} \text{ V}^{x+}$  and  $5 \text{ mol}\cdot\text{dm}^{-3}$  total sulfate

Although battery performance can be directly improved by elevating electrolyte feed rate, several other factors manifest themselves in limiting battery performance. As can be seen in Table 2-1, the mass transport limiting current density in FCB increases with the increase of flow rate, but it is also increasingly lower than the theoretical maximum current density that calculated from the flow rate. The maximum theoretical current density in the FCB is calculated by:

$$i_{max}^{theoretical} = \frac{Q_{feed}c_{V^{x+}}F}{A} \quad (2-1)$$

Here,  $Q_{feed}$  is the electrolyte flow rate;  $c_{V^{x+}}$  is the concentration of reactive vanadium ion  $V^{2+}$  or  $VO_2^+$ ,  $1 \text{ mol}\cdot\text{dm}^{-3}$ ;  $F$  is Faraday constant;  $A$  is the sectional area of FCB cell,  $5 \text{ cm}^2$ . The maximum electrolyte utilization is defined as  $i_{max}^{measured}/i_{max}^{theoretical}$ . In Table 2-1,  $i_{max}^{measured}$  increases with flow rate increase, but is increasingly lower than  $i_{max}^{theoretical}$ , leading to a decreasing electrolyte utilization. 25% maximum vanadium utilization was achieved at  $0.5 \text{ mL}\cdot\text{min}^{-1}$  flow rate, but only  $40 \text{ mA}\cdot\text{cm}^{-2}$  limiting current density was reached. At  $40 \text{ mL}\cdot\text{min}^{-1}$  flow rate,  $390 \text{ mA}\cdot\text{cm}^{-2}$  limiting current density can be achieved, but it only corresponds to 3.0% vanadium utilization. There is a balance between electrolyte feed rate and electrolyte utilization, or between pump load and battery output. Since the battery output growth decreases with flow rate increase, elevating flow rate is not always economical to increase battery performance because the battery output harvest by higher flow rate is traded off by higher pump load by increasing flow rate.

Table 2-1. Comparison of theoretical and measured maximum current density and maximum electrolyte utilization on polarization curves with varying flow rates. Reynolds numbers of electrolyte flow are listed to compare flow regime in flow field. The battery cell is the FCB cell with Toray Carbon paper, with electrolyte solutions of  $1 \text{ mol}\cdot\text{dm}^{-3} \text{V}^{\text{x+}}$  and  $5 \text{ mol}\cdot\text{dm}^{-3}$  total sulfate.

Flow rate mL/min	Theoretical Maximum Current Density mA/cm <sup>2</sup>	Observed Maximum Current Density mA/cm <sup>2</sup>	Maximum Electrolyte Utilization %	Reynolds Number
0.5	160.8	40.6	25.2	29.9
2	643.3	105.1	16.3	119.9
4	1286	159.3	12.3	239.8
8	2573	209	8.12	479.7
12	3860	249.6	6.46	719.6
16	5146	263.5	5.11	959.5
20	6433	305.8	4.75	1199
25	8041	326.5	4.06	1499
30	9650	340.4	3.52	17994
40	12866	390.7	3.03	2398

The mass transport in the flow field and carbon electrode and reaction on the surface of electrode are of great complexity in the FCB cell. As presented in Figure 2-6, the mass transport limiting current density and maximum electrolyte utilization are coincidentally power functions of flow rate. Although the numerical fitting is in good agreement with the original experimental data, the simple algebraic equation cannot directly illustrate the essence of mass transport and electrochemical reactions in battery. Because of the high complexity of mass transport and reaction processes in battery cell,<sup>171-173</sup> it is not easy to clarify the detailed mechanism between flow rate change and battery performance. However, the flow rate change is directly related to mass transport in the flow field. To

evaluate the flow regime impact on battery performance, the Reynolds number of electrolyte flow in the graphite flow field is calculated for each flow rate, as is listed in Table 2-1. The density and viscosity of electrolyte solution were adopted from literature in the Reynolds number calculation.<sup>32</sup> As flow rate increases in battery cell, the flow in flow field channel begins to be more turbulent, considering the interference from the rough surface of the electrode. The active vanadium species diffusion in the porous electrode or at the electrode-flow field interface might be limited or disturbed by the turbulent flow. Moreover, with increasing flow rate in battery, the electrolyte flow might creep out of the flow channel into the flow field plate and bypass the flow field.<sup>174,175</sup> This effect would bring reactant vanadium directly onto the electrode surface by convection, but some reaction area can be bypassed due to the long diffusive distance from the electrolyte bypass flow. A dilemma similar to the flow-through flow field would be caused by limiting reactant feed to part of reaction area and shortening electrolyte resident time.



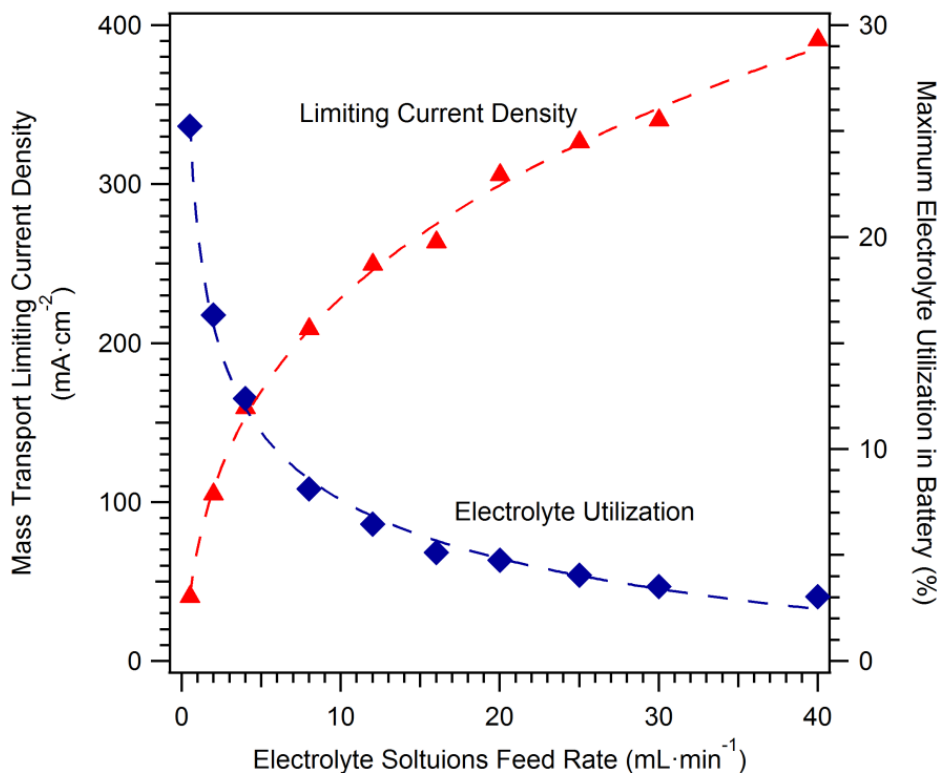


Figure 2–6. The mass transport limiting current density and maximum electrolyte utilization in polarization curve measurement on FCB cell with Toray carbon paper (25% compression) electrode and electrolyte solution contained  $1 \text{ mol}\cdot\text{dm}^{-3} \text{ V}^{\text{x}+}$  and  $5 \text{ mol}\cdot\text{dm}^{-3}$  total sulfate at varying electrolyte feed rate.

### 2.3.4 Properties of Electrode Material Impact on Battery Performance

Battery performance is strongly dependent on electrode material. In Figure 2-7, the *IR* corrected polarization curves of FCB cell with SGL 10AA and Toray TGP-H-060 show that 10AA has better performance than Toray carbon paper. Toray and 10AA were respectively compressed from  $200\mu\text{m}$  and  $400 \mu\text{m}$  original thickness to  $150\mu\text{m}$  and  $300 \mu\text{m}$ . The electrolyte solution was  $1 \text{ mol}\cdot\text{dm}^{-3} \text{ V}^{\text{x}+}$  and  $5 \text{ mol}\cdot\text{dm}^{-3}$  total sulfate. The flow

rates in both polarization tests were  $20 \text{ mL}\cdot\text{min}^{-1}$ . As is presented in Figure 2-7, the polarization curve of 10AA has a more flattened kinetic region and higher limiting current density. At  $10 \text{ mA}\cdot\text{cm}^{-2}$  current density, the overpotential loss in cell with 10AA was just about 0.04 V, while the overpotential loss with Toray reached 0.2 V. The mass transport limiting current densities were respectively 754 and  $305 \text{ mA}\cdot\text{cm}^{-2}$  for 10AA and Toray. 10AA overwhelms Toray in both kinetic and mass transport aspects. One significant performance difference source is the coating structure of this carbon paper. Because Toray carbon paper is originally manufactured as a gas diffusion electrode for proton exchange membrane fuel cells, a PTFE hydrophobic layer is coated on the surface of carbon fiber to prevent water flooding. The PTFE layer on electrode surface can reduce contact area between carbon surface and electrolyte solutions. Because PTFE is not conductive, it cannot provide surface to efficiently support redox reaction on its surface and it impedes surface wetting. The carbon surface reduction caused by PTFE coating directly leads to higher kinetic overpotential loss due to higher surface current density. By contrast, without PTFE coating, SGL 10AA has more hydrophilic surface structure to make good contact between carbon substrate and electrolyte solutions to utilize internal carbon surface. The hydrophobic coating on the carbon surface can also impede electrolyte transport within the pore of electrode. The hydrophobic effect on the PTFE layer provides a strong repulsive barrier for electrolyte convection in Toray carbon paper<sup>176</sup> leading to a much lower limiting current density in the cell. In addition, the thickness of the carbon paper can also contribute to cell performance differences. Although the electrochemical surface areas for both Toray and 10AA are not known, the increased thickness of 10AA can expose more surface area due to the PTFE coating in

Toray.

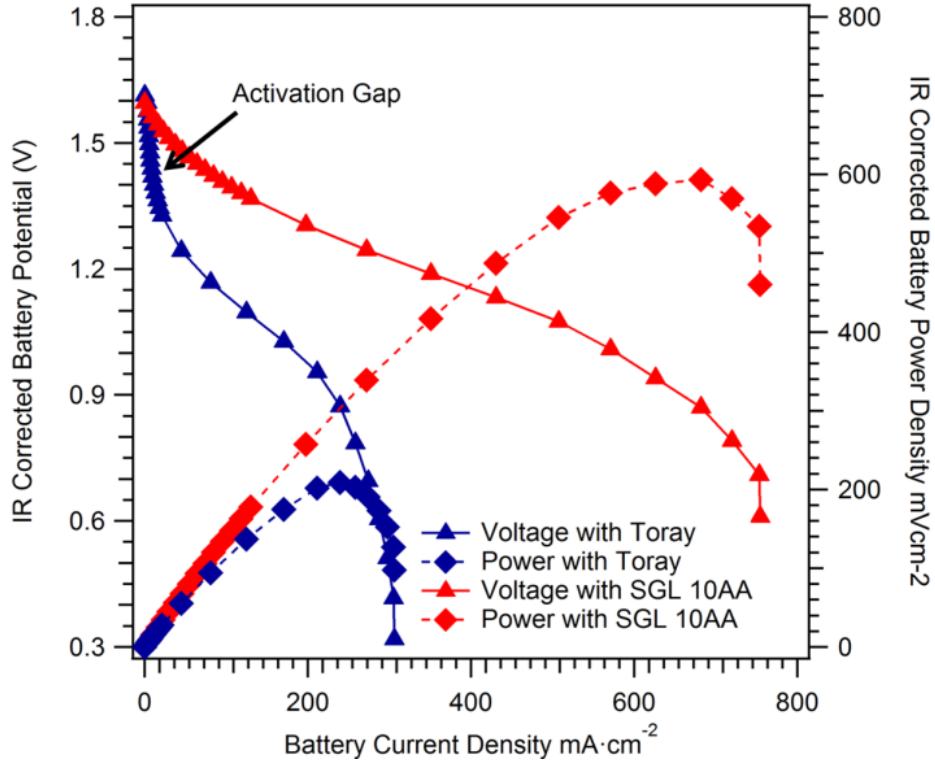


Figure 2–7. The polarization curves on FCB cell with Toray or SGL 10AA carbon paper electrode. The electrolyte used was  $1 \text{ mol}\cdot\text{dm}^{-3} \text{ V}^{\text{x}+}$  and  $5 \text{ mol}\cdot\text{dm}^{-3}$  total sulfate. Toray carbon paper had a compression of  $200/150 \text{ }\mu\text{m}$ , while 10AA was compressed to  $300 \text{ }\mu\text{m}$  from  $400 \text{ }\mu\text{m}$ . The electrolyte flow rates in both polarization testes were  $20\text{mL}\cdot\text{min}^{-1}$ .

### 2.3.5 Charging and Discharging Polarization Behavior at Various SoC

The charging and discharging polarization curves at lower state of charge were also measured to illustrate battery performance under practical conditions. In Figure 2-8,

charging and discharging polarization curves of FCB with Toray were measured respectively at 90%, 80% and 70% states of charge. The electrolyte flow rate was 20 mL·min<sup>-1</sup>. The electrolyte composition was 1 mol·dm<sup>-3</sup> V<sup>x+</sup> and 5 mol·dm<sup>-3</sup> total sulfate. To avoid electrode and flow-field being damaged by high voltage during charging polarization, the maximum current density was limited at 80 mA·cm<sup>-2</sup>. To better compare polarization behaviors of charging and discharging, the overpotential was plotted vs. current density. For all states of charge, the kinetic regions (0 to 15 mA·cm<sup>-2</sup>) of charging and discharging polarization curves highly overlap. The similar activation losses means activation loss in the battery is not strongly related to battery state of charge or the relative concentrations of corresponding active species. This consistency suggests that the mass transport to the electrode surface, rather than charge transfer, is the dominating factor to the activation loss. Because Toray carbon paper used in this measurement has a PTFE coating on the surface, this layer can strongly impede vanadium transfer between electrolyte solution and carbon surface to cause large mass transport activation loss. When the current density exceeds 15 mA·cm<sup>-2</sup>, the charging polarization gradually deviates from discharging polarization curve, with higher overpotential. The deviation was mainly contributed by pseudo-IR, because the reactant vanadium species concentrations in the charging polarization test were lower than those in discharging test at the given experimental state of charge. Higher mass transport overpotential is required to drive reactant vanadium transport in the carbon-electrolyte interface during the charging polarization curve measurement. As can be seen in Figure 2-8, at a higher SoC, there is a wider overpotential gap between charging and discharging polarization curves.

With higher SoC the charging needs larger overpotential to drive mass transport and discharging needs less overpotential to distribute reactive vanadium into electrode. For the charging polarization measurement, the battery voltage is significantly higher than the electrochemical window of water which equals 1.23V and side reactions (oxygen on positive electrode and hydrogen on negative electrode) might contribute to battery current as well.

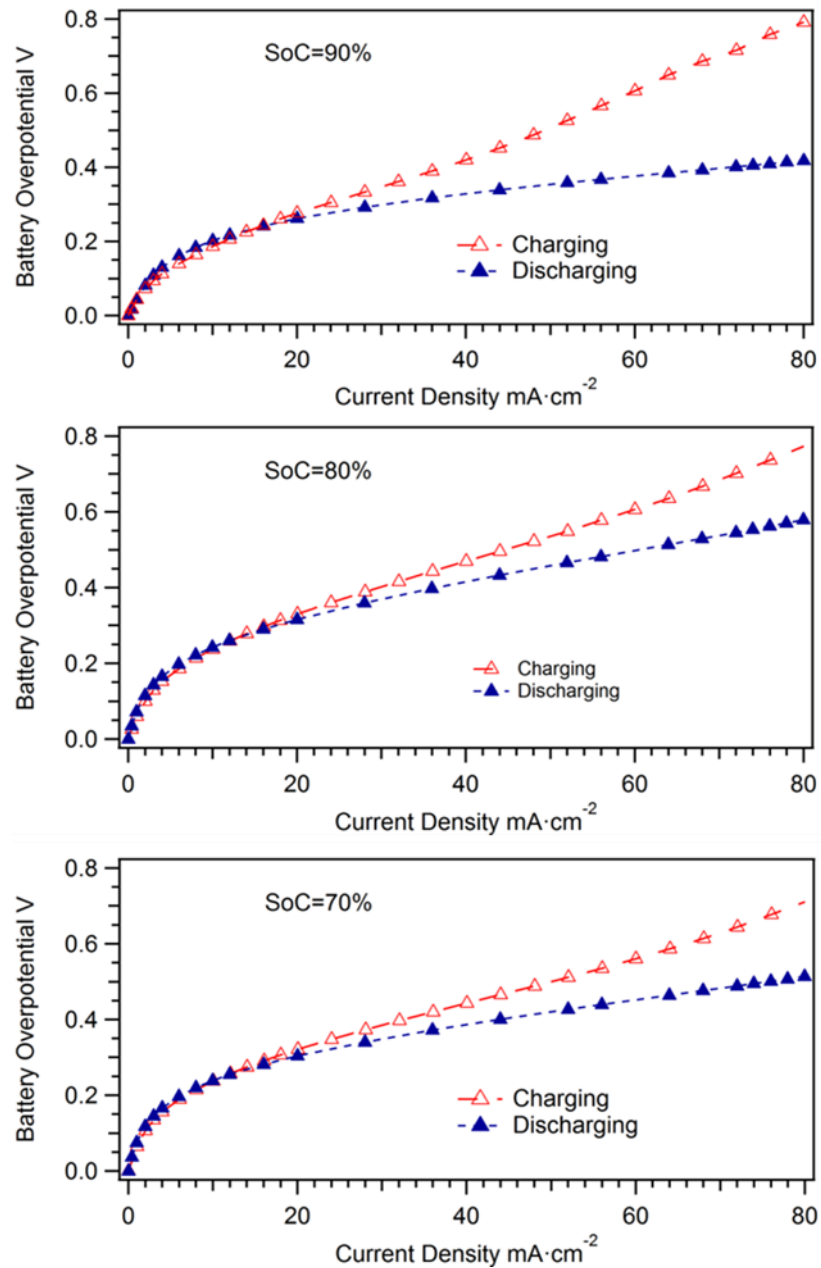


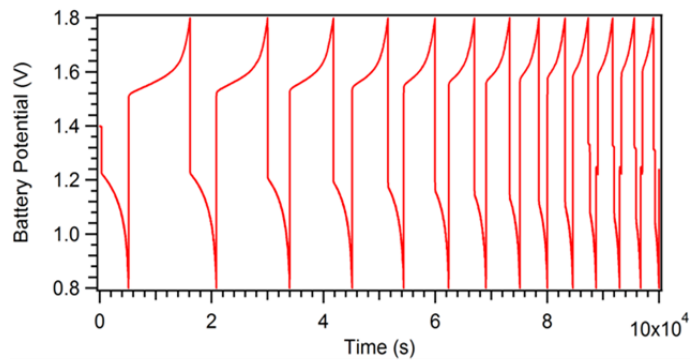
Figure 2–8. The charging and discharging polarization curves at 90, 80, and 70% state of charge. Charging and discharging polarization curves overlap at kinetic control region for each SoC. The charging polarization curve deviates from the discharging one after 15  $\text{mA}\cdot\text{cm}^{-2}$  due to several reasons.

### **2.3.6 Battery Characterization by Cycling Test**

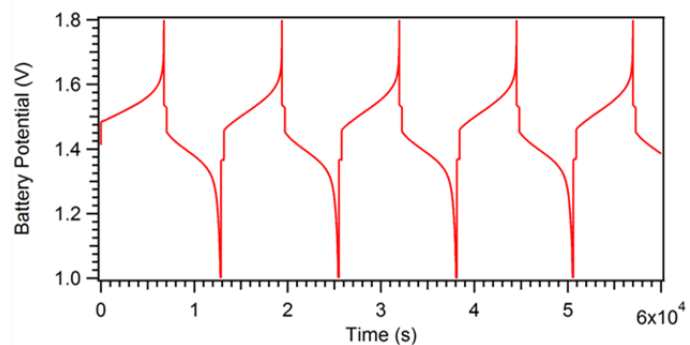
The cycling test is able to illustrate long term operation stability, which cannot be provided by polarization curve measurement. In this work, cycling tests were carried out on FCB cell with three membrane electrode combinations: A. Nafion 211 + three layers of SGL 10AA (70% compression); B. Nafion 212 + three layers of SGL 10AA (70% compression); C. Nafion 117 + one layer Toray carbon paper. The current densities applied in these cycling tests were respectively: A.  $80 \text{ mA}\cdot\text{cm}^{-2}$ ; B.  $80 \text{ mA}\cdot\text{cm}^{-2}$ ; C.  $120 \text{ mA}\cdot\text{cm}^{-2}$ . The potential window of the cycling test A and B was 0.8 to 1.8 V, while potential window for C was 0.4 to 2.4 V. The first few cycles of this cycling are presented in Figure 2-9. With the cell using Nafion 211 as separator, original discharging and charging battery capacity faded 83% and 82% during 13 cycles in 27 hours. In contrast, in 50 cycles, the battery with Nafion 212 only lost 6.4% and 2.1% in its charging and discharging capacities, and no obvious capacity decay was observed in the battery with Nafion 117. The capacity fade rates in the three battery setups are consistent with the thicknesses of membranes in their cells. In addition, the battery with the thinner membrane also showed lower coulombic efficiency, as is presented in Figure 3-10. The battery with Nafion 211 has 50% coulombic efficiency which is much lower than 96% for Nafion 212 and near 100% for Nafion 117. The rapid capacity decay and low coulombic efficiency in battery A was caused by fast vanadium crossover during its operation. As has been shown, the positive and negative electrolyte can become unbalanced due to vanadium crossover and water osmosis.<sup>89</sup> Since the thickness of Nafion 211 (25  $\mu\text{m}$ ) is substantially lower than Nafion 212 (50  $\mu\text{m}$ ) and Nafion 117 (180

$\mu\text{m}$ ), fast vanadium permeation can happen in Nafion 211. The rapid vanadium crossover can change the vanadium composition at membrane-electrode interface, leading to lowered battery open circuit potential.<sup>49</sup> Side reactions caused by vanadium crossover can lead to lower discharging capacity and higher charging capacity in battery, and thus lowered coulombic efficiency. Since vanadium ions have different permeability and water electro-osmotic ability,<sup>89</sup> the long term unbalanced vanadium crossover can cause vanadium imbalance in the electrolyte solution, leading to capacity decay in long operation. Briefly, the low ionic selectivity or high vanadium permeability in membrane can cause both efficiency and capacity loss in battery, due to rapidly unbalanced vanadium crossover.

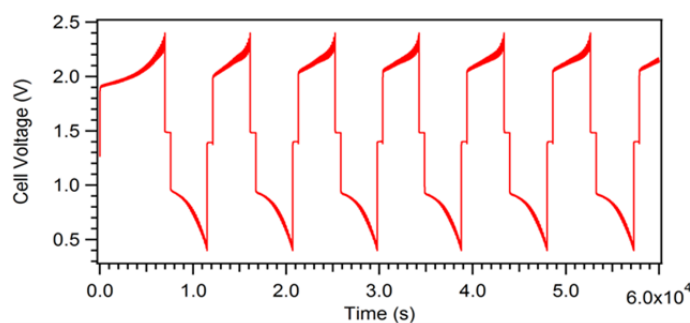




A. Nafion 211+3SGL 10AA,  $80 \text{ mA}\cdot\text{cm}^{-2}$



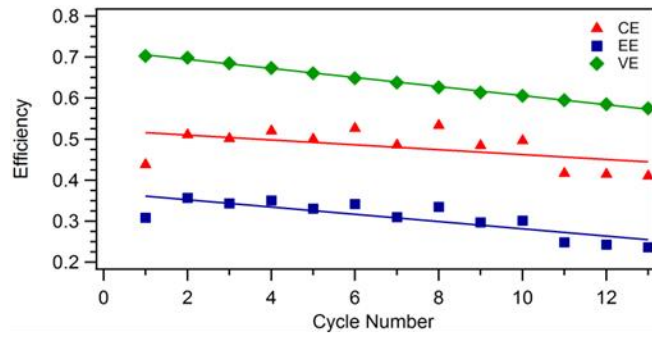
B. Nafion 212+3 SGL 10AA,  $80 \text{ mA}\cdot\text{cm}^{-2}$



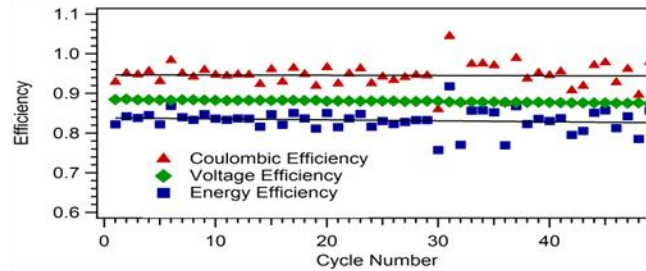
C. Nafion 117+1 Toray,  $120 \text{ mA}\cdot\text{cm}^{-2}$

Figure 2–9. The selected initial cycles in battery cycling tests on FCB cell with different membrane electrode combinations: A. Nafion 211 with 3 layers SGL 10AA carbon paper electrode (70% compression); B. Nafion 212 with 3 layers SGL 10AA carbon paper electrode (70% compression); C. Nafion 117 with 1 layer Toray carbon paper. Non-wetproof surface property of 10AA enables a much lower overpotential loss during both charging and discharging processes.

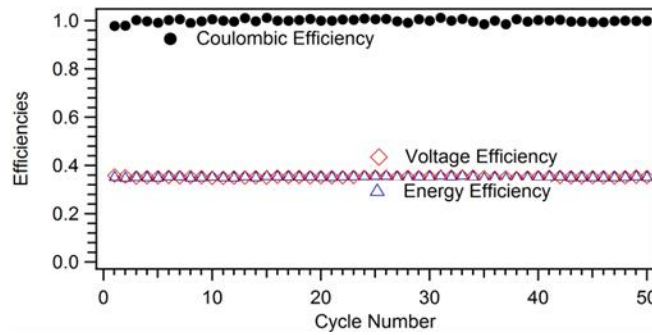
Specific information about kinetics and efficiency can also be extracted from battery cycling. For battery C, although high coulombic efficiency was achieved with a thick membrane minimizing vanadium crossover, the energy efficiency was significantly lowered by very low voltage efficiency compared to battery B. The lowered voltage efficiency was caused by high overpotential loss in charging and discharging cycles. The high overpotential loss should mainly be attributed to the PTFE-coated electrode surface on Toray. As has been discussed in previous section, the hydrophobic and nonconductive coating layer on carbon paper can impede mass and charge transfer during battery running, and cause higher activation and mass transport losses. Although the higher operation current density in battery A ( $120 \text{ mA}\cdot\text{cm}^{-2}$ ) can generate higher overpotential loss, the efficiency loss should mainly be attributed to hydrophobic surface of the electrode. In contrast, battery B has three layers of 10AA carbon paper as electrodes on both sides. These are favorable for electrolyte transport and charge transfer, due to its hydrophilic surface and the three layer electrode can also provide a higher surface area for redox reaction to bring down reaction current density on electrode surface, and thus activation overpotential loss.



A. Nafion 211 + 3 SGL 10AA, 80 mA·cm<sup>-2</sup>



B. Nafion 212 + 3 SGL 10AA, 80 mA·cm<sup>-2</sup>



C. Nafion 117 + 1 Toray, 120 mA·cm<sup>-2</sup>

Figure 2–10. The coulombic efficiency (CE), voltage efficiency (VE) and energy efficiency (EE) of the FCB cell with different membrane electrode combinations: A. Nafion 211 with 3 layers SGL 10AA carbon paper electrode (70% compression); B. Nafion 212 with 3 layers SGL 10AA carbon paper electrode (70% compression); C. Nafion 117 with 1 layer Toray carbon paper. Thicker membrane in cell can bring up higher coulombic efficiency. Non-wet proofed electrode enables higher voltage efficiency.

## 2.4 Summary

Polarization curve and cycling test protocols were developed and successfully carried out on vanadium redox flow batteries with a lab-assembled flow-through cell configuration and a modified direct methanol fuel cell. Multiple membrane and electrode materials were installed and tested in battery cells to compare their properties influence on battery performance. The performance of flow battery systems can be characterized by polarization curve measurements and cycling test to reveal different aspects.

The limiting factors for battery performance loss (activation loss, ohmic loss and mass transport loss) in each battery cell can be identified by polarization curve tests combined with high frequency impedance measurements. In a battery setup with LA cell, the activation loss was largely prevented by large surface area on 2.5 cm thick carbon felt electrode. However, the high contact resistance ( $4.6 \text{ ohm}\cdot\text{cm}^2$ ) and mass transport resistance (limiting current density  $160 \text{ mA}\cdot\text{cm}^{-2}$ ) were substantially limiting the performance of the LA cell. In FCB cell, since the good mechanical contact among electrode, membrane and current collector was provided by good compression, contact resistance and electronic resistance were significantly reduced. Most of the ohmic loss in the FCB cell can be compensated by IR correction except for pseudo-IR loss which is related to mass transport issues. The activation loss in the battery cell was largely controlled by the electrode surface area (LA vs. FCB) and electrode surface structure (PTFE coated or non-wetproofed). The vanadium concentration in the electrolyte solution has little effect on activation loss on carbon felt electrode. The mass transport loss in FCB

cell was impacted by both the electrolyte flow rate and electrode surface structure. Higher flow rate of electrolyte can allow better mass transfer, reflected by a higher mass transport limiting current. However, the output gain by increasing electrolyte flow rate is lower than the corresponding growth of electrolyte flow rate, or pump load. The hydrophilic surface of carbon paper electrode material can also improve electrolyte mass transport in the flow field and porous electrode.

Cycling tests can provide battery performance stability and efficiency evaluation. The cycling test was carried out on a battery setup with FCB cells with different membrane and electrode material. Vanadium permeability across the membrane is critical to the capacity and coulombic efficiency, since fast battery capacity decay and low coulombic efficiency were observed on battery setup with Nafion 211 with thickness of 25  $\mu\text{m}$ , the thinnest membrane used in this test. The electrode properties strongly influence battery voltage efficiency. The voltage efficiency of a battery with Nafion 117 and Toray TGP-H-060 carbon paper only reached 40%, while high overpotential loss was caused in charging and discharging process by the PTFE coated surface.

**CHAPTER 3**  
**UV-VIS SPECTROSCOPY APPLICATION IN**  
**STATE OF CHARGE MONITORING FOR VRFB**

**3.1 Background**

State of charge (SoC) is a significant indicator to provide direct information on the remaining capacity in a battery for battery management. During the operation of a VRFB, the SoC is defined as the concentration fraction of  $V^{5+}$  and  $V^{2+}$  respectively in positive and negative electrolytes:  $SoC_{positive} = n_{V^{5+}} / (n_{V^{5+}} + n_{V^{4+}})$  and  $SoC_{negative} = n_{V^{2+}} / (n_{V^{2+}} + n_{V^{3+}})$ . Real time state of charge monitoring can immediately feed the available amount of active vanadium species in electrolyte back to the battery management system to aid the future operation. In addition, the state of charge can also reflect the system health by analyzing vanadium consumption on each side and concentration variation.<sup>177</sup> The charging and discharging reactions should lead to equal vanadium consumptions in both sides of VRFB. However, several other factors can cause malign vanadium concentration change, leading to imbalanced electrolyte and faded battery capacity.<sup>177</sup> Factors leading to active vanadium loss or electrolyte imbalance are listed as below:

1. Gas generation side reactions. Hydrogen and oxygen can be generated on electrodes during the battery charging process, in which high overpotential is necessary. Although the carbon electrode utilized in VRFB is not highly catalytic for the proton reduction reaction, hydrogen evolution is highly favored in thermodynamics because the

standard potential of  $H^+/H_2$  (0 V) is higher than  $V^{3+}/V^{2+}$  (-0.23 V).<sup>178</sup> The side reaction in VRFB can cause unbalanced vanadium consumption (mainly excess reaction on the positive side to support hydrogen evolution on negative side) in the cell.

2. Carbon oxidation reaction in the electrode. During the charging process, the carbon material on positive electrode can be etched by the acidic electrolyte in an electro-corrosion side reaction.<sup>179,180</sup> The carbon corrosion reaction can generate part of operational current, leading to a lowered  $V^{4+}$  charging efficiency.

3.  $V^{2+}$  oxidation by oxygen.  $V^{2+}$  can be oxidized by oxygen penetrated into electrolyte transport or storage.  $V^{2+}$  oxidation can reduce SoC in the negative electrolyte.

4. Asymmetric vanadium crossover. The vanadium concentration in positive and negative electrolytes can be unbalanced by the vanadium crossover because vanadium ion at different valence states have varying permeability across separator<sup>89</sup> and the unique direction of vanadium migration is driven by the battery potential difference.

5. Water and sulfuric acid crossover. Water and sulfuric acid transport across the separator can be caused by concentration or hydraulic osmosis or electroosmosis. This transport would not influence the state of vanadium charge, but it can interfere with accurate measurement of vanadium concentration and will cause concentration differences to develop.

For traditional batteries, like lead acid and lithium ion batteries, a series of state of charge estimation methods have been thoroughly developed.<sup>181-185</sup> Generally, these methods for state of charge monitoring can be categorized into directly experimental

methods and modeling analysis methods. One branch of experimental method is comprised of electrochemical methods. The electrochemical experimental SoC monitoring strategy include discharging test, ampere counting, open circuit voltage,<sup>186</sup> electrochemical impedance spectroscopy<sup>181,183</sup> and D.C internal resistance measurements.<sup>182</sup> Another experimental method for state of charge is to estimate SoC by measuring battery component physical or chemical properties. The SoC modeling analysis, such as linear model or artificial neural network<sup>187</sup>, estimates battery SoC by collecting and analyzing real time performance (current density and voltage), given that a complete performance database of the battery has been well established<sup>182</sup>. Kalman filter has also been used widely used to analyze battery SoC by simulating the battery via a dynamic algorithm.<sup>186-188</sup>

Considerable effort has been devoted to develop spectroscopy based techniques to measure electrolyte SoC in VRFB. Because of the characteristic UV-Vis absorption of each vanadium ion,<sup>189</sup> UV-Vis spectrometry has been utilized in measurement of state of charge in VRFB electrolytes.<sup>177,190-194</sup> In the negative electrolyte, because the spectra of  $V^{2+}$  and  $V^{3+}$  are explicitly additive to each other, the SoC of negative electrolyte can be calculated in a straightforward manner from the absorbance in the isosbestic points' vicinity on its UV-Vis spectrum.<sup>177,192-194</sup> Due to the existence of  $V_2O_3^{3+}$  during the coexistence of  $V^{4+}$  and  $V^{5+}$  in acidic environment,<sup>195,196</sup> strong excess absorbance can take place in positive electrolyte at intermediate SoC, leading to isosbestic point absence in the spectra of positive electrolyte. The strong UV-Vis absorption also caused difficulty to directly calculate solution concentrations of  $V^{4+}$ ,  $V^{5+}$  and  $V_2O_3^{3+}$  from the positive



electrolyte absorbance spectrum. Transmittance spectrum analysis coupled with an intensity corrected correlation coefficient (ICCC) algorithm was conducted to measure both positive and negative electrolyte solution state of charge.<sup>190,191</sup> The SoC of electrolyte solution was calculated from its UV-Vis transmittance by fitting it into the premeasured SoC-transmittance database. Besides UV-Vis spectroscopy, infrared spectroscopy was used to measure SoC in VRFB. Similar to the algorithm of UV-Vis method, the concentrations of vanadium ions in each electrolyte solution were calculated from electrolyte IR absorption signal collected by a precalibrated IR detector coupled with a VRFB setup.

Some methods other than spectroscopy were also developed to measure electrolyte state of charge in VRFBs. The state of charge of each electrolyte solution can be determined by its conductivity because the conductivities of vanadium electrolyte solutions have been shown to be linear function of their SoC.<sup>177</sup> The open circuit voltage (OCV) of the battery was also used to indicate the state of charge in battery.<sup>192,194,197</sup> However, because the detailed reaction mechanism has not been clarified for vanadium redox reaction on both electrodes, the OCV calculated by the Nernst equation cannot provide sufficiently accurate SoC estimation for battery management. To enhance SoC estimation from battery OCV, an equivalent electrical circuit model was established for a VRFB setup and Kalman filter dynamic analysis was carried out to reinforce the SoC analysis<sup>188</sup>.

In this chapter, I will present my work on utilization of UV-Vis spectroscopy in VRFB state of charge monitoring and electrolyte imbalance study. The UV-Vis

absorbance spectrum of negative and positive electrolytes was measured at different states of charge. The spectrum of negative electrolyte proportionally consists of characteristic spectra of  $V^{2+}$  and  $V^{3+}$ . The state of charge in the negative electrolyte can be calculated by the analysis of the absorbance in the vicinity of isosbestic points in the spectra. In the positive electrolyte, the  $V^{4+}$ - $V^{5+}$ - $V_2O_3^{3+}$  equilibrium can generate strong excess absorbance to impede direct SoC calculate by isosbestic point analysis. By analysis of  $V^{4+}/V^{5+}$  mixing electrolyte at different SoC and overall vanadium concentration, the equilibrium constant for  $V^{4+}$ - $V^{5+}$ - $V_2O_3^{3+}$  system was calculated. And the molar UV-Vis absorption spectrum of  $V_2O_3^{3+}$  was successfully separated from the spectrum of positive electrolyte solution. The state of charge of positive electrolyte can be calculated by a mathematical analysis incorporating the equilibrium of  $V^{4+}$ - $V^{5+}$ - $V_2O_3^{3+}$ . The UV-Vis spectrometry measurement coupled with cycling tests suggests that  $V^{4+}$  loss in the positive electrolyte is the main reason for charging capacity loss during VRFB operation.

### 3.2 Experimental

Two experimental protocols were developed to take UV-Vis spectroscopy measurements in-line or ex-situ. The in-line spectroscopy measurement was applied to directly record UV-Vis spectra in electrolyte solutions to develop a method to monitor their state of charging. The ex-situ measurement was developed to investigate vanadium ion spectral changes more precisely during redox reaction, or with their valence states changing. The electrolyte preparation process has already been described in the last

chapter.

### ***3.2.1 In-Line UV-Vis Spectroscopy Measurement***

The spectrometer was coupled with an operational flow battery system, via a UV-Vis flow cell built into electrolyte tubing line in the battery system, as is shown in Figure 3-1. The flow battery setup is a regular battery set up with a 25 cm<sup>2</sup> modified direct methanol fuel cell and 100 mL electrolyte solution on each side of the battery. The separator used was pretreated Nafion 117, and the electrode was SGL 10AA. The battery was started at 0 SoC with 1 mol·dm<sup>-3</sup> V<sup>3+</sup> / 5 mol·dm<sup>-3</sup> sulfate solution on negative side and 1 mol·dm<sup>-3</sup> V<sup>4+</sup> / 5 mol·dm<sup>-3</sup> sulfate solution on positive side. While the battery was in operation, the electrolyte solution of interest was constantly pumped through the UV-Vis flow cell by a KNF STEPDOS 08 dosing pump. The light path length in the spectrometer flow cell was 1 mm. The spectrum of the electrolyte solution was recorded by an ALS-Japan SEC2000 UV-Vis spectrometer-light source setup. Chronoamperometry at 1.8V was carried out on the battery to charge it up to 100% SoC, and then the spectrum at varying SoC was simultaneously recorded by the spectrometer. The flow battery was controlled by a Bio-Logic HCP803 high current potentiostat.

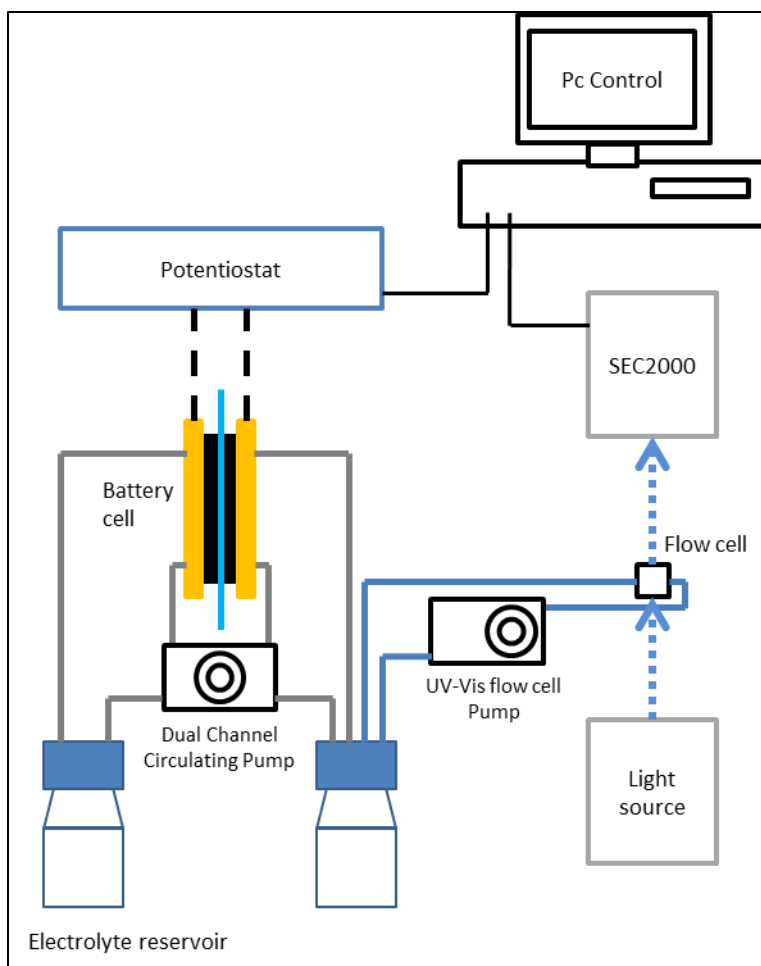


Figure 3–1. The UV-Vis spectrometer setup built in a flow battery system.

### 3.2.2 *Electrospectrometry Measurement Setup*

One electrospectrometer setup was used to acquire vanadium ions ( $V^{4+}/V^{5+}$ ) spectra variation according to state of charge change. The experiment was carried out in a quartz electrochemical cuvette with a platinum mesh working electrode and a platinum counter electrode. This cuvette with electrodes was supplied by ALS-Japan as well. The path length of the quartz cell was 1 mm. The cuvette was mounted on a cuvette holder

assembled with the ALS-Japan SEC2000 spectrometer and light source. Chronopotentiometry was carried out to reduce 80  $\mu\text{L}$   $0.5 \text{ mol}\cdot\text{dm}^{-3} \text{ V}^{5+} / 5 \text{ mol}\cdot\text{dm}^{-3}$  sulfate solution in the cuvette with 2 mA current generated by a Bio-Logic SP200 potentiostat.

### **3.2.3 $\text{V}^{4+}/\text{V}^{5+}$ Mixing Solution Spectrum Study**

To better investigate the spectrum of  $\text{V}^{4+}/\text{V}^{5+}$  mixed solution, the UV-Vis spectrum of the mixed solutions of different concentrations was measured by the SEC2000 spectrometer. The  $\text{V}^{4+}/\text{V}^{5+}$  mixed solutions of total vanadium concentrations 0.08 to 1.2  $\text{mol}\cdot\text{dm}^{-3}$  in  $5 \text{ mol}\cdot\text{dm}^{-3}$  total sulfate background were prepared from  $2 \text{ mol}\cdot\text{dm}^{-3} \text{ V}^{4+} / 5 \text{ mol}\cdot\text{dm}^{-3}$  total sulfate solution,  $2 \text{ mol}\cdot\text{dm}^{-3} \text{ V}^{5+} / 5 \text{ mol}\cdot\text{dm}^{-3}$  total sulfate solution and  $5 \text{ mol}\cdot\text{dm}^{-3} \text{ H}_2\text{SO}_4$ . The SoC of these electrolyte solutions ranges from 0 to 100%. The spectra of these solutions were taken by the same spectrometer setup mentioned above, with a 0.5 mm, 1 mm or 1 cm quartz cuvette.

### **3.2.4 Vanadium Imbalance Monitoring In VRFB**

One vanadium imbalance monitoring experiment was carried out on a battery-spectrometer setup similar to the one in Figure 3-1. A  $5 \text{ cm}^2$  cell with one layer of pretreated Nafion 211 and one layer of SGL 10AA electrode (400 $\mu\text{m}$ , 25% compression) on each side was used as the battery. The battery initially contained 100 mL  $1 \text{ mol}\cdot\text{dm}^{-3} \text{ V}^{3+} / 5 \text{ mol}\cdot\text{dm}^{-3}$  sulfate solution on negative electrode and 100 mL  $1 \text{ mol}\cdot\text{dm}^{-3} \text{ V}^{4+} / 5 \text{ mol}\cdot\text{dm}^{-3}$  solution on positive electrode, with 0% beginning state of charge. The battery

was operated in a chronoamperometry cycling test with the following procedure: 5 hours constant voltage charging at 1.8 V; 1 hour open circuit voltage; 5 hours constant voltage discharging at 1.0 V; 1 hour open circuit voltage. The spectrum of the negative electrolyte was recorded by the spectrometer with the in-line flow cell.

### **3.3 Results and Discussion**

#### ***3.3.1 Negative Electrolyte In-Line Spectrum***

The spectrum of the negative electrolyte can directly reflect the state of charge variation during battery operation. The UV-Vis spectra of negative electrolyte at SoC 0 to 100% are presented in Figure 3-2. Clearly, at SoC=0 or SoC=100%, the spectrum of the negative electrolyte is a spectrum with obvious  $V^{3+}$  or  $V^{2+}$  characteristic peaks at 620 nm and 430 nm or 580 nm and 430 nm. At state of charge between 0% and 100%, the negative electrolyte spectrum varies linearly from the spectrum of  $V^{3+}$  or  $V^{2+}$ . This characteristic variation suggests that the spectrum of negative electrolyte at a given SoC is an additive combination of the spectra at 0 and 100% SoC, or a function proportional to  $V^{3+}/V^{2+}$  composition in solution. This dependence provides a potential method to indicate negative electrolyte state of charge by its UV-Vis spectrum analysis.

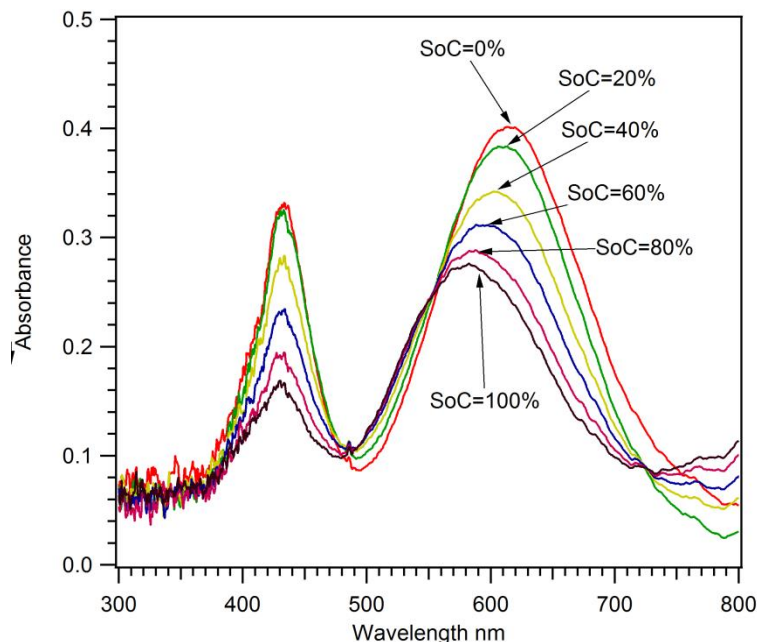


Figure 3–2. The UV-Vis spectra of negative electrolyte solution (with  $1 \text{ mol}\cdot\text{dm}^{-3} \text{ V}^{2+}/\text{V}^{3+}$  and  $5 \text{ mol}\cdot\text{dm}^{-3}$  sulfate) at different states of charge. The spectra were taken on a flow cell with 1mm light path length.

In Figure 3-2, there are three isosbestic points at 485nm, 720 nm and 553 nm, where these spectra intersect at these three points for all states of charge. The spectrum in the vicinity of these isopiestic points changes linearly with SoC change. In addition, there is a characteristic peak at 433 nm for both  $\text{V}^{3+}$  and  $\text{V}^{2+}$ , but of different magnitudes. This feature can also be used as  $\text{V}^{3+}/\text{V}^{2+}$  relative composition gauge to monitor the state of charge in negative electrolyte. In Figure 3-3, absorbance of negative electrolyte at 433, 600, 750 nm is presented as a function of state of charge in the solution. Clearly, the absorbance at these wavelengths is a linear function of SoC of negative electrolyte. This observation is consistent with observation reported in literature.<sup>177</sup> The linear dependence

of absorbance on the chosen wavelength suggests that it can be easily used as SoC gauge for negative electrolyte solution during battery operation. The state of charge can be fitted as a linear function of the absorbance at selected wavelengths:

$$\text{SoC} = kI_{\text{selected}} + n \quad (3-1)$$

The fitted parameters are listed in Table 3-1.

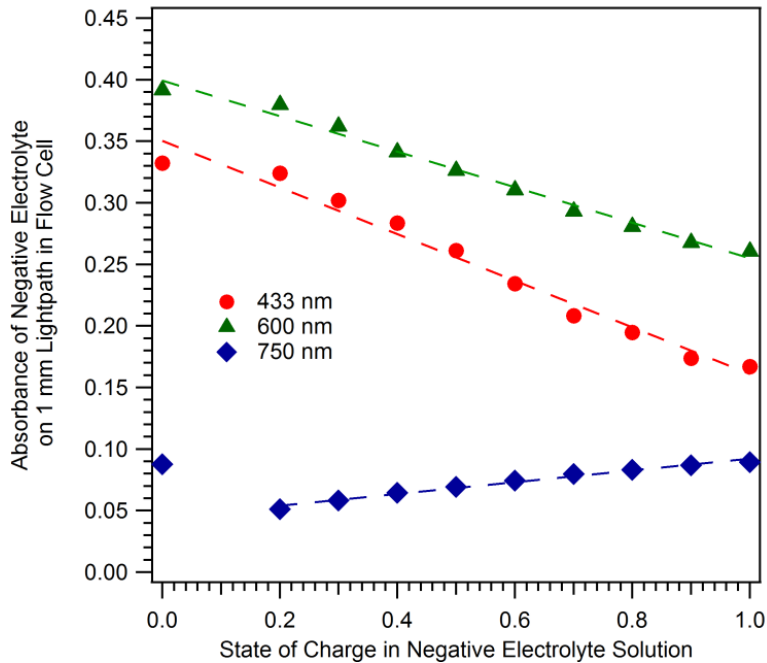


Figure 3–3. The absorbance of  $V^{2+}/V^{3+}$  mixing electrolyte with  $1 \text{ mol}\cdot\text{dm}^{-3} V^{x+}$  in  $5 \text{ mol}\cdot\text{dm}^{-3}$  sulfate in flow cell (1mm) at 433nm, 600 nm and 750 nm. The strength of absorption at these wavelengths is mostly proportional to electrolyte's state of charge.



Table 3-1. The parameters of the curve fitting for absorbance as a linear function of state of charge in negative electrolyte.

Wavelength nm	k	n
750	18.5	-0.74
600	-6.62	2.65
433	-4.85	1.75

### 3.3.2 Positive Electrolyte UV-Vis Spectra Study

Excess absorbance can be produced by the coexistence of  $V^{4+}$  and  $V^{5+}$  in the acidic environment. In Figure 3-4, the spectra during the charging of  $1 \text{ mol}\cdot\text{dm}^{-3} V^{4+}$  and  $5 \text{ mol}\cdot\text{dm}^{-3}$  sulfate electrolyte solution in an operating flow battery were presented. The spectrum of positive electrolyte is not proportional to the vanadium composition in positive vanadium electrolyte. Most of the UV-Vis absorbance of the positive electrolyte with an intermediate SoC, especially 500 to 800 nm, is substantially higher than the absorbance of individual vanadium valence state. The nonlinear spectral response to  $V^{4+}/V^{5+}$  composition changes suggests there is an interaction between  $V^{4+}$  and  $V^{5+}$  in the electrolyte environment.

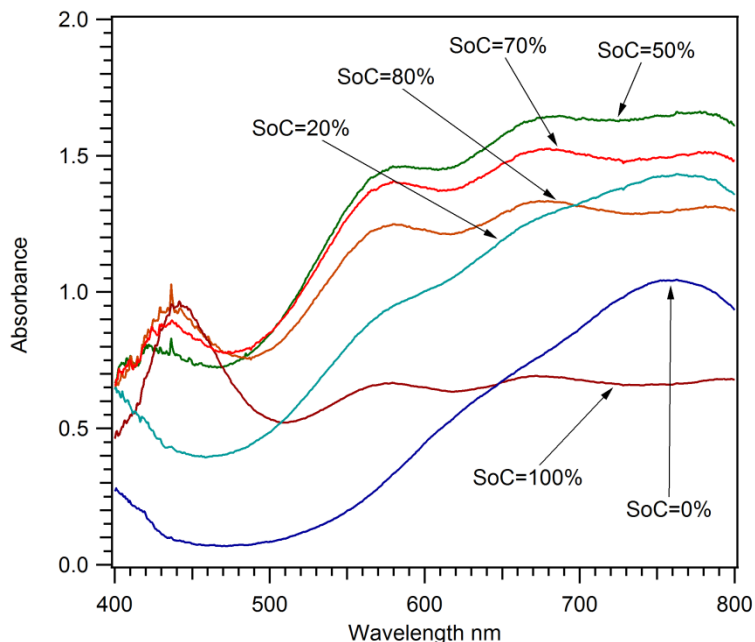


Figure 3–4. The UV-Vis spectra variation with state of charge change is not proportional to the  $V^{4+}/V^{5+}$  composition in the positive electrolyte solution. The excess absorbance happens when  $V^{4+}$  and  $V^{5+}$  coexist.

The increased UV-Vis absorption of  $V^{4+}/V^{5+}$  interaction was repeated in ex-situ electrochromometry experiment. In Figure 3-5, the vanadium spectra were taken during reduction of  $80 \mu\text{L } 0.5 \text{ mol}\cdot\text{dm}^{-3} V^{4+}$  and  $5 \text{ mol}\cdot\text{dm}^{-3}$  sulfate electrolyte solution in the UV-Vis electrochemical cell. By comparing the spectra change in the in-line measurement and electrochromometry measurement, it is obvious that the excess absorbance of intermediate SoC is lower than that in in-line measurement. The absorbance relative magnitude difference between these two measurements can be caused by the total vanadium concentration difference.

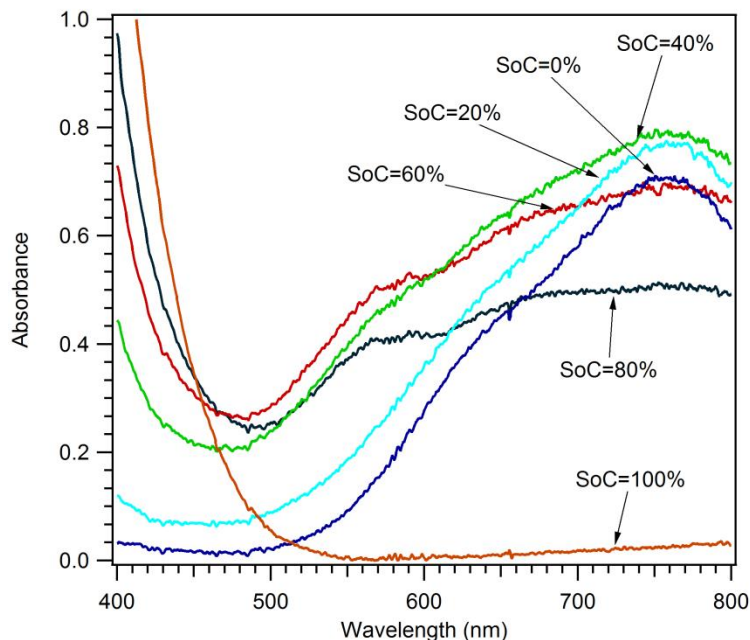


Figure 3–5. The  $V^{5+}$  reduction spectra variation in electrochromometry measurement. The electrolyte was  $80 \mu\text{L } 0.5 \text{ mol}\cdot\text{dm}^{-3} V^{4+}$  and  $5 \text{ mol}\cdot\text{dm}^{-3}$  sulfate solution. The lightpath length was 1 mm.

A third vanadium ion species ( $V_2O_3^{3+}$ ) can be formed by the coexistence of  $V^{4+}/V^{5+}$  in acidic environment, leading strong excess UV-Vis absorption.  $V_2O_3^{3+}$  has been proved to exist in acidic environment by UV-Vis spectroscopy and later with vanadium-51 NMR,<sup>195,196</sup> formed by one  $V^{4+}$  and one  $V^{5+}$ . To separate the absorbance of  $V_2O_3^{3+}$  from the total absorbance of electrolyte solution, the excess absorbance of  $0.5 \text{ mol}\cdot\text{dm}^{-3} V^{4+}/V^{5+}$  and  $5 \text{ mol}\cdot\text{dm}^{-3}$  sulfate electrolyte in an electrochromometry test was calculated according to the definition and shown in Figure 3-6:

$$I_{ex} = I_{total} - I_{SoC=0}(1 - SoC) - I_{SoC=1}SoC \quad (3-2)$$

Here  $I_{ex}$  is the excess absorbance of  $V^{4+}/V^{5+}$  electrolyte at intermediate SoC;  $I_{SoC=0}$  and  $I_{SoC=1}$  are the absorbances at SoC=0 and SoC=1, representing the electrolyte spectra with all  $V^{4+}$  or  $V^{5+}$ . The curve pattern of excess absorbance of the  $V^{4+}$  and  $V^{5+}$  mixing electrolyte has an obvious parabolic character with the maximum excess absorbance around SoC=0.5. The parabolic dependence of excess absorbance on SoC is consistent with that has been reported by Blanc et al.<sup>195</sup>

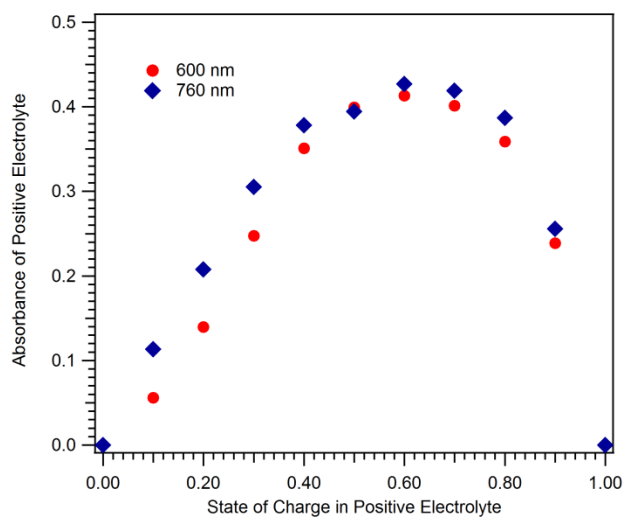


Figure 3–6. At 600 and 760 nm, the excess absorbance of  $0.5 \text{ mol}\cdot\text{dm}^{-3} V^{4+}/V^{5+}$  and  $5 \text{ mol}\cdot\text{dm}^{-3}$  sulfate electrolytes is dependent on its state of charge as a parabolic function.

### 3.3.3 The equilibrium of $V^{4+}-V^{5+}-V_2O_3^{3+}$ in positive electrolyte

To quantitatively investigate the equilibrium of  $V^{4+}-V^{5+}-V_2O_3^{3+}$  system in the positive electrolyte, the spectra of a series of positive electrolyte solutions with different

total vanadium concentrations and state of charge were measured by UV-Vis spectrometer. In positive electrolyte with 0.08 to 1.2 mol·dm<sup>-3</sup> total vanadium concentration, the normalized excess absorbance, or molar excess absorption coefficient,  $\epsilon_{ex}$  at 600 nm and 760 nm are respectively presented in Figure 3-7. The normalized excess absorbance has an analogous definition to molar absorption coefficient:

$$I_{ex}^{nor} = \frac{I_{ex}}{[V^{x+}]L} \quad (3-3)$$

Here,  $[V^{x+}]$  is total vanadium concentration in solution, equals  $[V^{4+}] + [V^{5+}]$ ;  $L$  is the path length of the cuvette. Clearly, after concentration and path length correction, the excess absorbance strength is highly consistent with the overall vanadium concentration of the solution. This consistency suggests that the existence of  $V_2O_3^{3+}$  is prompted by the concentrated vanadium. The strength of excess absorbance is closely dependent on SoC in a parabolic function.

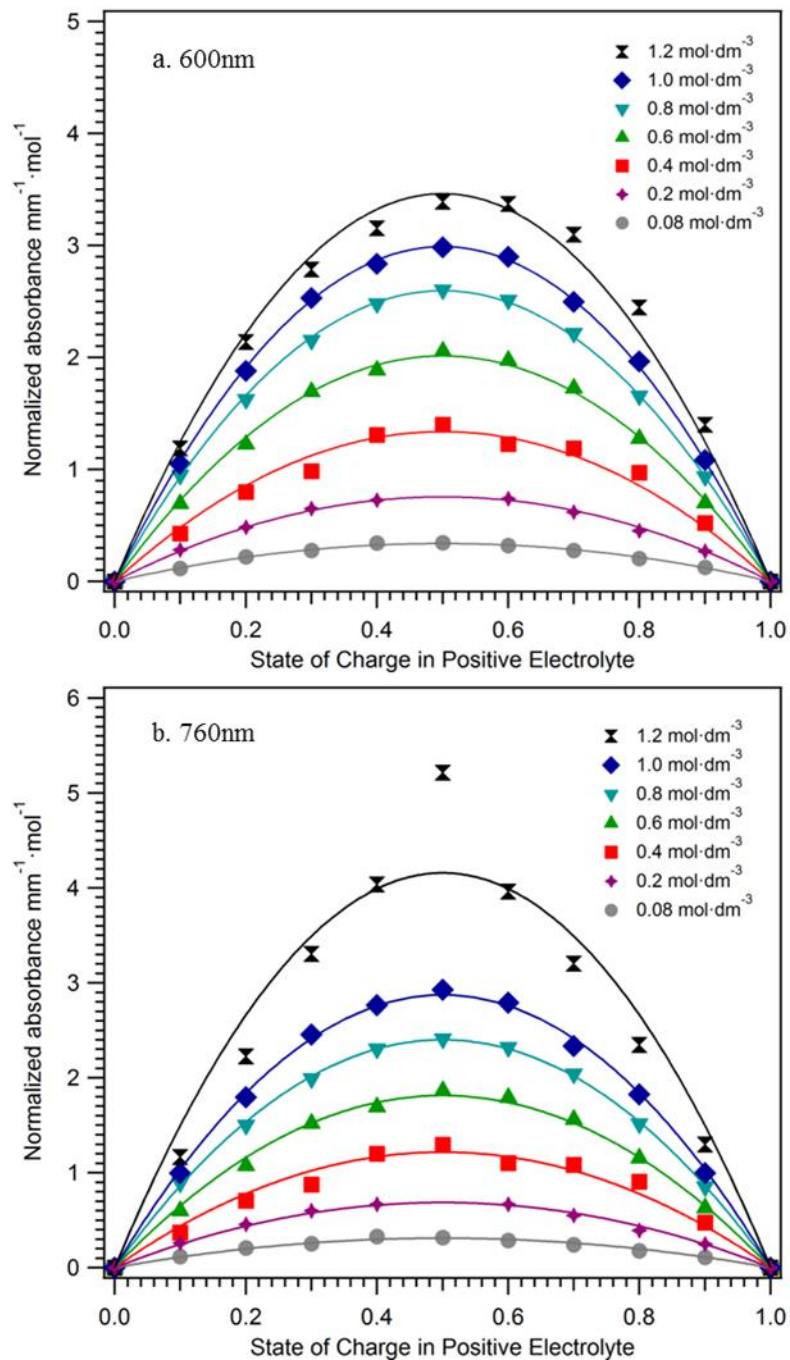


Figure 3-7. The normalized excess absorbance in  $V^{4+}/V^{5+}$  electrolyte solution with 1 mol·dm<sup>-3</sup>  $V^{x+}$  and 5 mol·dm<sup>-3</sup> total sulfate. The strength of excess absorbance is consistent with total vanadium concentration in solution.

To clarify the equilibrium among  $V^{4+}$ ,  $V^{5+}$  and  $V_2O_3^{3+}$  and the equilibrium's influence on the UV-Vis absorption of the positive electrolyte, we combine chemical equilibrium to spectrum analysis to conduct a modeling analysis. This work was partially inspired by work of Gao et al.<sup>193</sup>, but more thorough analysis was conducted to obtain equilibrium constant for  $V_2O_3^{3+}$  balance with  $V^{4+}$  and  $V^{5+}$  and its molar absorbance spectrum. Since  $V_2O_3^{3+}$  is the most significant vanadium complex ion in the system,<sup>193,195,196</sup> it is assumed that  $V^{4+}$ ,  $V^{5+}$ ,  $V_2O_3^{3+}$  are the only vanadium ions existing in the system. During coexistence of  $V^{4+}$  and  $V^{5+}$ ,  $V_2O_3^{3+}$  forms instantly, so that the ionic system was always in balance during spectroscopic measurement:



The balance  $V^{4+}$ ,  $V^{5+}$  and  $V_2O_3^{3+}$  can be described by the first order equilibrium through the equilibrium constant:

$$K = \frac{[V_2O_3^{3+}]}{[VO^{2+}][VO_2^+]} \quad (3-5)$$

By considering the vanadium balance during battery operation:

$$\begin{cases} [VO^{2+}] + [V_2O_3^{3+}] = [V^{x+}](1 - SoC) \\ [VO_2^+] + [V_2O_3^{3+}] = [V^{x+}]SoC \end{cases} \quad (3-6)$$

After solving equation 3-5 and 3-6, the concentration of  $V_2O_3^{3+}$  can be calculated:

$$[V_2O_3^{3+}] = \frac{[V^{x+}]}{2} \left\{ \left( 1 + \frac{1}{K[V^{x+}]} \right) - \sqrt{\left( 1 + \frac{1}{K[V^{x+}]} \right)^2 - 4SoC(1 - SoC)} \right\} \quad (3-7)$$

In equation 3-7, the concentration of  $V_2O_3^{3+}$  is directly determined by the total vanadium concentration in electrolyte and its state of charge, as is demonstrated in Figure 3-7. To ease future mathematical derivation, equation 3-7 can be simplified by defining

$$B = 1 + \frac{1}{K[V^{x+}]} = \frac{K[V^{x+}] + 1}{K[V^{x+}]}$$

$$[V_2O_3^{3+}] = \frac{[V^{x+}]}{2} \{B - \sqrt{B^2 - 4SoC(1 - SoC)}\} \quad (3-8)$$

The overall absorbance of positive electrolyte solution consists of absorbance of  $VO^{2+}$ ,  $VO_2^+$  and  $V_2O_3^{3+}$ :

$$I_{total} = I_{VO^{2+}} + I_{VO_2^+} + I_{V_2O_3^{3+}} \quad (3-9)$$

According to the definition of excess absorbance, equation 3-2 can be expressed in a more precise formula:

$$I_{ex} = I_{total} - \varepsilon_{VO^{2+}}[V^{x+}](1 - SoC) \cdot L - \varepsilon_{VO_2^+}[V^{x+}]SoC \cdot L \quad (3-10)$$

$\varepsilon_{VO^{2+}}$  and  $\varepsilon_{VO_2^+}$  are molar absorption coefficient arrays of  $VO^{2+}$  and  $VO_2^+$ . The excess absorbance can also be broken down into effects of individual vanadium ion species, by combining 3-9 and 3-10:

$$\begin{aligned} I_{ex} &= I_{total} - \varepsilon_{VO^{2+}}[V^{x+}](1 - SoC) \cdot L - \varepsilon_{VO_2^+}[V^{x+}]SoC \cdot L \\ &= L \left\{ \varepsilon_{VO^{2+}}[VO^{2+}] + \varepsilon_{VO_2^+}[VO_2^+] + \varepsilon_{V_2O_3^{3+}}[V_2O_3^{3+}] - \varepsilon_{VO^{2+}}[V^{x+}](1 - SoC) - \varepsilon_{VO_2^+}[V^{x+}]SoC \right\} \\ &= L \left\{ \varepsilon_{VO^{2+}}[VO^{2+}] + \varepsilon_{VO_2^+}[VO_2^+] + \varepsilon_{V_2O_3^{3+}}[V_2O_3^{3+}] - \varepsilon_{VO^{2+}}[VO^{2+}] - \varepsilon_{VO_2^+}[VO_2^+] - \varepsilon_{V_2O_3^{3+}}[V_2O_3^{3+}] \right\} \end{aligned}$$



$$= L(\varepsilon_{V_2O_3^{3+}} - \varepsilon_{VO^{2+}} - \varepsilon_{VO_2^+})[V_2O_3^{3+}] \quad (3-11)$$

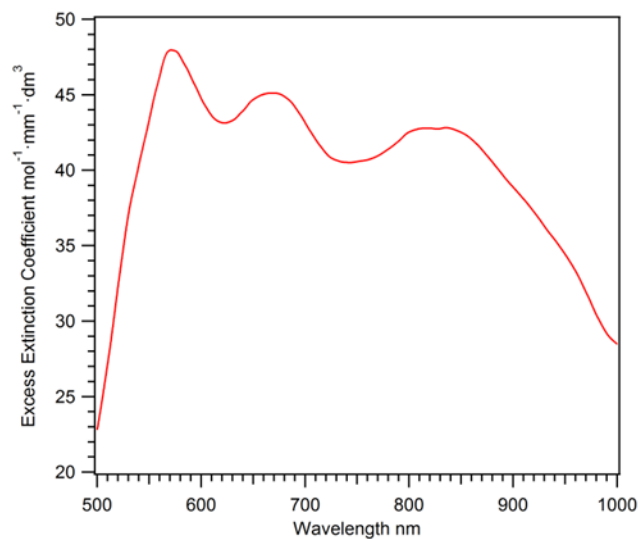
$$= L\varepsilon_{ex}[V_2O_3^{3+}] \quad (3-12)$$

Here, it is clear that the strength of excess absorbance is dependent on light-path length and concentration in the Beer-Lambert law. By introducing  $[V_2O_3^{3+}]$ , equation 3-8, into equation 3-12, the excess absorbance is correlated to total vanadium concentration and state of charge:

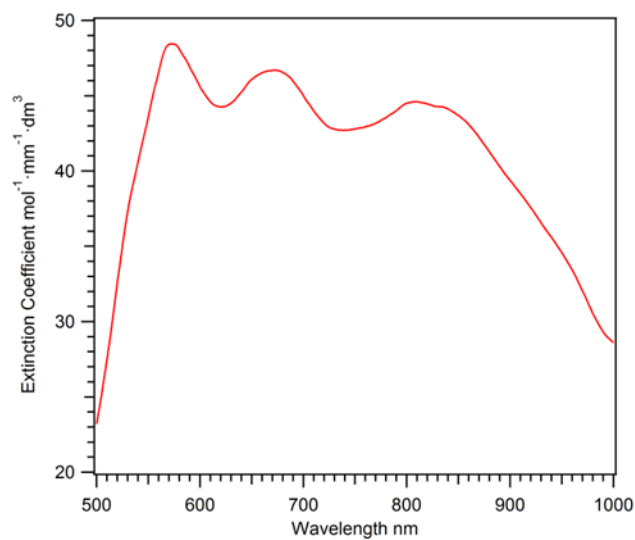
$$I_{ex} = \frac{L\varepsilon_{ex}[V^{x+}]}{2} \{B - \sqrt{B^2 - 4SoC(1 - SoC)}\} \quad (3-13)$$

$$I_{ex}^{nor} = \frac{I_{ex}}{[V^{x+}]_L} = \frac{\varepsilon_{ex}}{2} \{B - \sqrt{B^2 - 4SoC(1 - SoC)}\} \quad (3-14)$$

By fitting the spectral data in Matlab,  $\varepsilon_{ex}$  and  $K$  can be calculated from the normalized excess absorption data for positive electrolyte solution at various vanadium concentration and  $SoC$ . For vanadium equilibrium in equation 3-4, the calculated equilibrium constant  $K$  is  $0.379 \text{ dm}^{-3} \cdot \text{mol}$ .  $\varepsilon_{ex}$  is presented in Figure 3-8(a), and  $\varepsilon_{V_2O_3^{3+}}$  is accordingly corrected with  $\varepsilon_{VO^{2+}}$  and  $\varepsilon_{VO_2^+}$  and presented in 3-8(b). The absorption strength of  $V_2O_3^{3+}$  is an order of magnitude higher than that of  $VO^{2+}$  and  $VO_2^+$ . The absorption coefficient of  $VO^{2+}$  at its absorption peak at 765nm is  $1.7 \text{ L} \cdot \text{mol}^{-1} \cdot \text{mm}^{-1}$ , while  $VO_2^+$  has no significant absorption with 500 to 1000 nm region which is the wavelength range most excess absorption takes place.



a.



b.

Figure 3–8. (a) The molar excess absorption coefficient of  $V^{4+}/V^{5+}$  mixed electrolyte,  $\epsilon_{ex}$ ; and (b) molar absorption coefficient of  $V_2O_3^{3+}$  in  $V^{4+}/V^{5+}$  mixed electrolyte,  $\epsilon_{V_2O_3^{3+}}$ . The electrolyte condition is 0.08 to 1.2 mol·dm<sup>-3</sup>  $V^{4+}/V^{5+}$  and 5 mol·dm<sup>-3</sup> sulfate/bisulfate.

### 3.3.4 SoC of Positive Electrolyte Estimation by UV-Vis Spectrum

The state of charge of positive electrolyte can be determined by its spectrum. The overall absorbance of positive electrolyte consists of absorbance of  $V^{4+}$  and  $V^{5+}$  and  $V_2O_3^{3+}$  in the solution, as is presented in equation 3-15.

$$I_{total} = I_{ex} + \varepsilon_{VO^{2+}}[V^{x+}](1 - SoC) \cdot L + \varepsilon_{VO_2^+}[V^{x+}]SoC \cdot L \quad (3-15)$$

By introducing equation 3-13, the total absorbance can be expressed in a more detailed pattern:

$$I_{total} = \frac{L\varepsilon_{ex}[V^{x+}]}{2} \left\{ B - \sqrt{B^2 - 4SoC(1 - SoC)} \right\} + \varepsilon_{VO^{2+}}[V^{x+}](1 - SoC) \cdot L \\ + \varepsilon_{VO_2^+}[V^{x+}]SoC \cdot L \quad (3-16)$$

Then, 3-16 can be simplified as:

$$\frac{I_{total}}{L[V^{x+}]} - \varepsilon_{VO^{2+}} - \frac{B\varepsilon_{ex}}{2} - SoC(\varepsilon_{VO_2^+} - \varepsilon_{VO^{2+}}) = -\frac{\varepsilon_{ex}}{2} \sqrt{B^2 - 4SoC(1 - SoC)} \quad (3-17)$$

To simplify the solution of equation 4-17, it is defined that  $D = \frac{I_{total}}{L[V^{x+}]} - \varepsilon_{VO^{2+}} - \frac{B\varepsilon_{ex}}{2}$ .

Then a concise version of 3-17 is obtained:

$$D - SoC(\varepsilon_{VO_2^+} - \varepsilon_{VO^{2+}}) = -\frac{\varepsilon_{ex}}{2} \sqrt{B^2 - 4SoC(1 - SoC)} \quad (3-18)$$

Then SoC can directly be calculated by solving equation 3-18:

$$SoC = \frac{2D(\varepsilon_{VO_2^+} - \varepsilon_{VO^{2+}}) - \varepsilon_{ex}^2 \pm \left\{ [\varepsilon_{ex}^2 - 2D(\varepsilon_{VO_2^+} - \varepsilon_{VO^{2+}})]^2 - 4 \left( D^2 - \frac{\varepsilon_{ex}^2 B^2}{4} \right) [(\varepsilon_{VO_2^+} - \varepsilon_{VO^{2+}})^2 - \varepsilon_{ex}^2] \right\}^{1/2}}{2 \{ (\varepsilon_{VO_2^+} - \varepsilon_{VO^{2+}})^2 - \varepsilon_{ex}^2 \}} \quad (3-19)$$

By solving eq. 3-19, the state of charge in positive electrolyte can be calculated from the UV-Vis absorbance of the electrolyte (included in variable  $D$  in eq. 3-19) and the overall literal concentration of  $V^{4+}/V^{5+}$  couple (included in variable  $B$ ). The SoC calculated from the absorbance data at 765 nm in electrolytes at different overall vanadium concentrations is presented in Figure 3-9. Due to the parabolic response of the absorbance to SoC, eq. 3-19 can give two roots for SoC to a given absorbance. One of these two roots is physically meaningless, because the absorbance is a function of SoC. For low vanadium concentration in the positive electrolyte ( $0.08 \text{ mol}\cdot\text{dm}^{-3}$ ), one root of eq. 3-19 (b) is highly consistent with the state of charge, and the other root is entirely negative which is of no physical meaning in this discussion. Then the state of charge in positive electrolyte can be simply calculated by 3-19 (b) from absorbance and total vanadium concentration at this vanadium concentration. For higher concentration, the roots from eq. 3-19 (a) and (b) can intersect at an intermediate SoC. The intersection suggests that neither eq.3-19 (a) nor (b) can solely provide a complete solution for state of charge. But parts of roots of eq. 3-19 (a) and (b) can respectively provide two parts of an accurate solution for SoC. The root of eq. 3-19 (a) is good at low SoC, while root of eq. 3-19 (a) is good to match actual SoC on the higher end. Accordingly lower SoC part in roots of 3-19 (a) adjunct higher SoC part in roots of 3-19 (b) can make up a complete match to SoC. The solution of eq. 3-19 provides a very accurate solution for state of

charge in the positive electrolyte from its UV-Vis absorbance. However, due to the dual roots of eq. 3-19, a more sophisticated method is needed to rule out the physically meaningless root. The high match of a root of eq. 3-19 to the real SoC suggests the analysis conducted in this section is valid with the assumptions and calculation approach.  $V_2O_3^{3+}$  is produced by the coexistence of  $V^{4+}/V^{5+}$  couple, and their balance obeys the first order equilibrium in eq. 3-4.

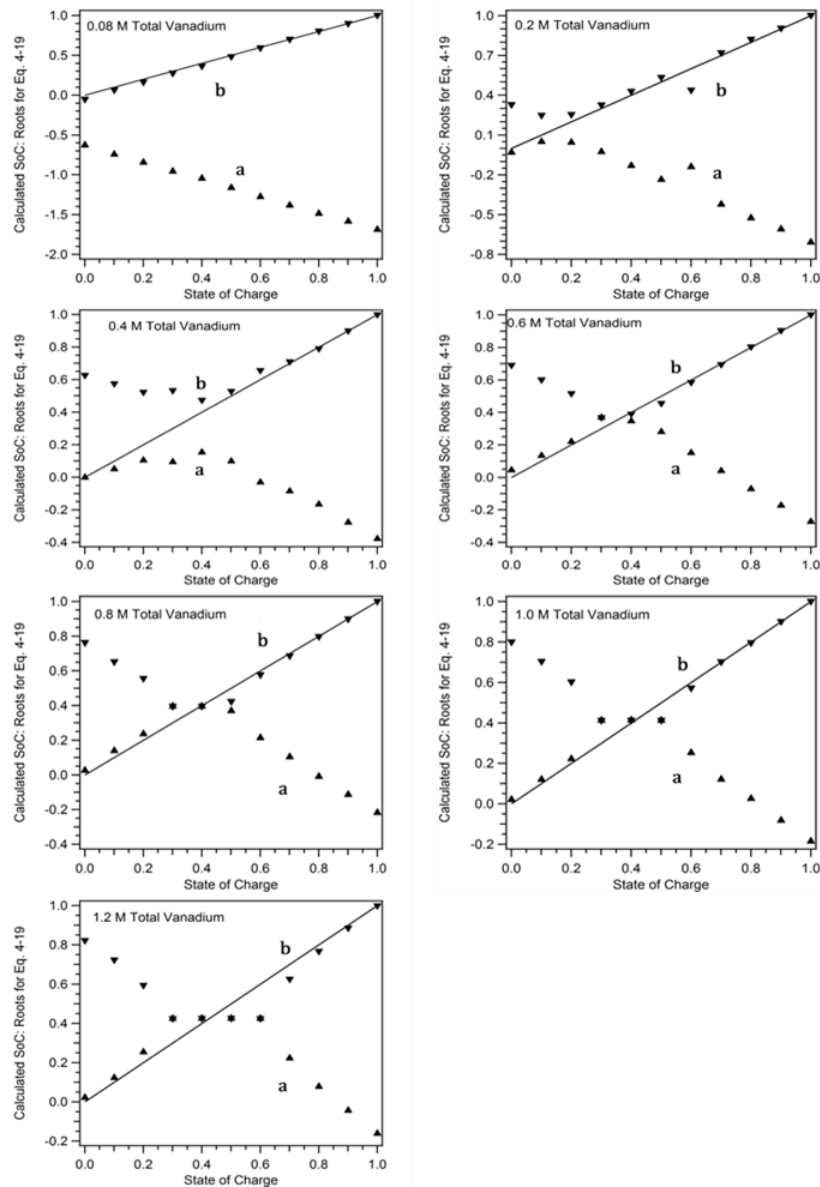


Figure 3-9. The SoC calculated from positive electrolyte total absorbance data at 765 nm wavelength with eq. 3-19. The state of charge can be directly calculated from the electrolyte absorbance spectrum and the total vanadium concentration. However, the calculation must be combined with some other method to rule out the imaginary root.

### ***3.3.5 The Spectroscopic Monitoring On Negative Electrolyte Capacity Loss***

The electrolyte imbalance can be monitored by UV-Vis spectrometer. By using a thin membrane, Nafion 211, the capacity decay in VRFB was effectively accelerated in the chronoamperometry cycling test. By setting the battery to operate between 1.0 to 1.8 V, the battery was expected to cycle within the SoC range 0 to 100%. As is presented in Figure 3-10, 75% of the original charging capacity and 82% of the discharging capacity decayed in 20 cycles (240 hours). Correspondingly, the state or charge fade in the negative electrolyte can be reflected by its UV-Vis absorbance. In Figure 3-11, after charging, the UV-Vis absorbance of the negative electrolyte at 433 and 600 nm increased significantly during the cycling test. According to the observation of the negative SoC monitoring, the increased absorbance at these two wavelengths means that decreased SoC in the negative electrolyte had been achieved by charging. This is obvious evidence of vanadium imbalance: the capacity of the positive electrolyte faded, leading to limited  $V^{4+}$  availability to store charge. Meanwhile, abundant  $V^{3+}$  was collected in the negative electrolyte, reflected by the decreased SoC of the negative electrolyte after charging. The vanadium imbalance should be caused by both vanadium diffusion and migration. Due to the voltage across the battery, vanadium migration can happen constantly across the separator to transport  $V^{4+}$  and  $V^{5+}$  into negative electrolyte to generate a large amount of  $V^{3+}$ .

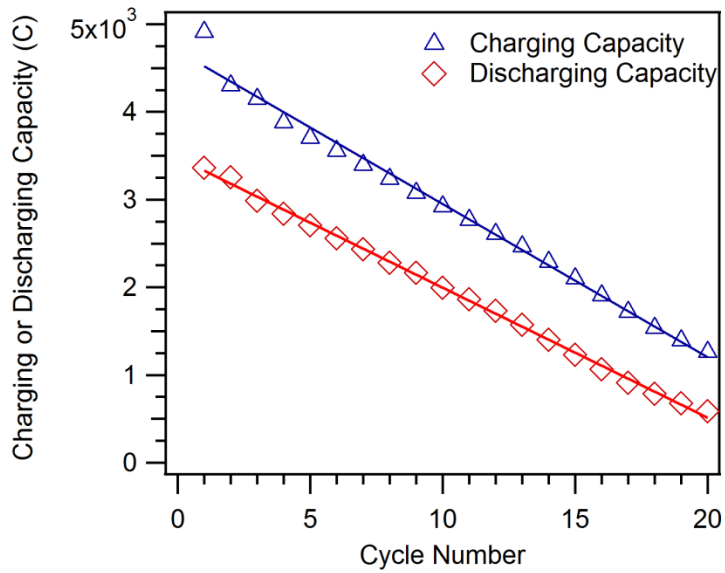
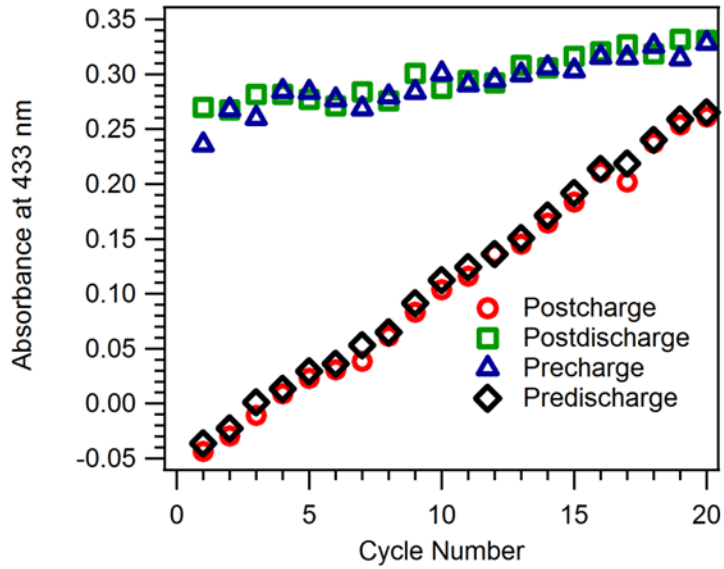
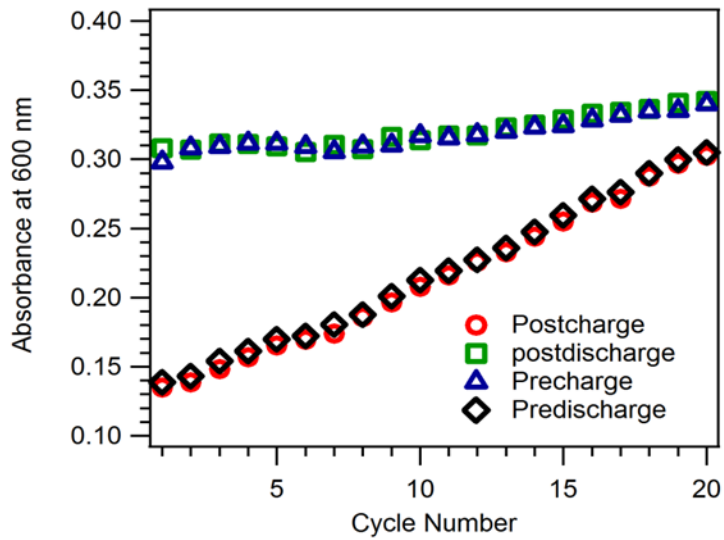


Figure 3–10. The charging and discharging capacity decay over 20 charging-discharging cycles. Capacity loss and low coulombic efficiency were both worsened by thin membrane utilization.





a. 433nm



b. 600 nm

Figure 3–11. The UV-Vis absorbance of negative electrolyte after charging during the cycling test. The increased absorbance of electrolyte indicates lowered state of charge after charging.

### 3.4 Summary

The UV-Vis provides a powerful tool to explore the operation of the vanadium redox flow battery. Both negative and positive electrolyte state of charge can be determined by their UV-Vis spectrum. The state of charge in the negative electrolyte can be directly calculated from its UV-Vis absorbance. For the positive electrolyte, due to the existence of the complex ion  $V_2O_3^{3+}$ , its state of charge cannot be directly estimated from its UV-Vis spectrum by isosbestic analysis. However, the characteristic spectrum of  $V_2O_3^{3+}$  was successfully separated from the spectrum of  $V^{4+}/V^{5+}$  mixed electrolyte solution. The state of charge can be calculated from the absorbance spectrum of  $V^{4+}/V^{5+}$  mixed electrolyte by incorporating  $V^{4+}-V^{5+}-V_2O_3^{3+}$  equilibrium. The UV-Vis technique can also be utilized to conduct vanadium transport analysis to diagnose the factors for battery capacity loss.

**CHAPTER 4**

**COMPOSITION AND CONDUCTIVITY OF MEMBRANES EQUILIBRATED  
WITH SOLUTIONS OF SULFURIC ACID AND VANADYL SULFATE**

**4.1 Introduction**

Cation exchange membranes, such as Nafion, are widely used in proton exchange membrane fuel cells, which have a similar cell structure to the VRFB cell.<sup>17,25,28,83</sup> Nafion and other perfluorosulfonic acid polymers exhibit high conductivity when they are well hydrated and possess excellent chemical and mechanical stability. Nafion has also been introduced into the VRFB system as an electrolyte separator. However, reports in the literature suggest an area specific resistance, or ASR of 0.5 to 6  $\Omega\cdot\text{cm}^2$  in VRB cell, in contrast to typical ASR values of 0.05~0.18  $\Omega\cdot\text{cm}^2$  with Nafion in PEMFC.<sup>27,33,44,198,199</sup> While much of this can be ascribed to contact resistance and aspects of cell design,<sup>33</sup> the membrane resistance must also be considered.

Recently, significant VRFB performance improvement has been achieved using a zero-gap battery cell design in combination with Nafion membranes.<sup>28,33,34,49</sup> A maximum limiting current density, 994mA $\cdot\text{cm}^{-2}$  was reported on a battery using a Nafion 115 membrane, accompanied by areal specific resistance of 399-467m $\Omega\cdot\text{cm}^2$ .<sup>49</sup> In this cell, the membrane is the primary source of ASR. Such a high internal resistance significantly limits battery performance at high current density; this ASR entails voltage losses of roughly 400 to 500 mV at 1 A $\cdot\text{cm}^{-2}$ .<sup>28</sup>

In a VRFB, the membrane is exposed to a much more complicated working environment than that in a PEMFC. During battery operation, the membrane is directly exposed to electrolyte solutions that contain sulfuric acid and vanadium ions concentrated at  $1 \text{ mol}\cdot\text{dm}^{-3}$  level. For Nafion, this is substantially higher than the effective anion concentration range for anion equilibrium dominated by Donnan-exclusion, generally  $0.1 \text{ mol}\cdot\text{dm}^{-3}$  level or lower.<sup>200,201</sup> In such an equilibrium, anion can be effectively kept out of membrane by electrostatic force from negatively charged sulfonate, as referred Donnan-exclusion.<sup>202</sup> Thus all of the electrolyte species can enter the nanopores in the membrane and can alter the microenvironment for proton and cation transport.<sup>31,200,203</sup> Furthermore, the electrolyte composition ensures ‘concentrated solution’ behavior, and thus a complex transport regime and a situation in which the activity coefficients of all species, including water, vary substantially. Clearly, we must quantitatively describe the uptake of species into the membrane and, eventually, how this depends on membrane composition as well as how it affects transport.

Though there are several ‘practical’ studies of the properties of membranes in the presence of VRB electrolyte components, those studies fail to identify and isolate critical contributors to observable membrane performance. Furthermore, there is not an extensive body of literature describing the behavior of ion exchange membranes under conditions of exposure to high acid or transition metal ion concentration. Some literature regarding the influence of the presence of acid on membrane performance has been published in the context of PEMFC performance. Verbrugge et al. studied the impact of sulfuric acid on Nafion properties experimentally and mathematically.<sup>204,205</sup> With exposure to sulfuric

acid solution, Nafion can suffer remarkable de-swelling and, it is proposed, ionic cluster channel compression, leading to lowered membrane porosity. Acid uptake by membranes can also contribute to significant water loss with equilibration in concentrated sulfuric acid solution. The influence of temperature on Nafion's ionic transport properties was also investigated in a similar experimental and theoretical framework.<sup>206</sup> The transport behavior of different acids in Nafion and other alternative membranes has been studied by several groups.<sup>200,201,203,207</sup> Although acid uptake and dissociation in Nafion can be significant enough to influence its conductivity, the anion transference number was no more than 0.016 when the external equilibrating sulfuric acid concentration was elevated to  $4 \text{ mol}\cdot\text{dm}^{-3}$ .<sup>200</sup> In addition, phosphoric acid and sulfuric acid dissociation can be constrained in membrane nanopores because of the presence of sulfonic acid groups and limited amount of water. Lawton *et al.* found vanadyl diffusivity in Nafion to be controlled by the sulfuric acid concentration in electrolyte solutions.<sup>32</sup>

Due to the slow motion of metal cations in Nafion membranes, cationic contaminants can severely affect transport properties, reducing membrane conductivity even under well hydrated conditions.<sup>208-212</sup> Membrane sulfonic acid groups demonstrated a high preference to interact with some cations other than protons,<sup>212</sup> and cationic occupancy on sulfonates can result in a reduced proton concentration. Some transition metal ions, such as  $\text{Fe}^{3+}$ , lower proton mobility by an unknown interaction with protons.<sup>212</sup> Nevertheless, water is the most important mediator for proton transport in sulfonated membranes.<sup>84,85</sup> Equilibration in dilute acid with some cations, such as  $\text{K}^+$ ,  $\text{Cs}^+$ ,  $\text{Ni}^{2+}$  and  $\text{Fe}^{3+}$ , can cause water content loss in Nafion, because their

hydration energy is lower than that of a proton.<sup>209–211,213,214</sup> All these observations cited above are helpful for understanding proton exchange membrane performance in vanadium redox flow batteries, but a definitive understanding of membrane-electrolyte interactions in VRFBs is still not available.

To provide a solid basis in physical principles for membrane development in redox flow batteries, we have undertaken a systematic study of composition and transport in membranes exposed to the environment of the VRFB. Here, a study of uptake behavior of vanadium/sulfuric acid electrolyte solutions in Nafion is reported, as well as the influence of bathing solution composition on membrane conductivity. The dependence of the sulfuric acid and vanadyl ion uptake by the membrane on electrolyte solution condition is described. A correlation between Nafion conductivity and composition is built on a basis of component and thermodynamic analysis. This work is partly based on previous reports of thermodynamics of water uptake and conductivity in Nafion.<sup>31</sup> Finally, the membrane resistance upon equilibration in electrolyte solutions is also compared to the measured internal resistance of several recently reported batteries.

## **4.2 Experiment**

### ***4.2.1 Membrane Preparation***

Nafion 117 supplied by Ion Power Inc. was treated to obtain uniform initial conditions prior to all experiments reported below. The as-received membrane was cut into 1×5 cm strips. The as-received membranes were sequentially boiled in 3% hydrogen

peroxide (Fisher Scientific), deionized water (Milli Q, 18.2 M $\Omega$ ·cm), 1 mol·dm<sup>-3</sup> sulfuric acid and deionized (DI) water for at least 1 hour each step at 85°C. The sulfuric acid was prepared from 96% concentrated sulfuric acid (Alfa Aesar). After membrane pretreatment, the membrane samples were stored in DI water for future use.

#### ***4.2.2 Sulfuric Acid Uptake Measurement***

Before the water and sulfuric acid uptake and conductivity measurements, pretreated membrane samples were soaked in sulfuric acid solutions with concentration ranging from 0.5 to 17.4 mol·kg<sup>-1</sup> for 72 hours to achieve water and sulfuric acid equilibration at room temperature (22°C). After equilibration with aqueous sulfuric acid solutions, membrane samples were taken out of bathing solutions, liquid droplets were removed from the surface with Kimwipes and the ‘soaked’ weight of membrane,  $m_1$ , was measured. This step was performed very quickly to avoid weight change caused by fast water exchange between membrane and air. Here,  $m_1$  includes the mass of the dry membrane, water and sulfuric acid. To remove imbibed sulfuric acid, the acid-equilibrated membrane was boiled in DI water for at least 1 hour. The amount of acid removed into the water was determined by titration with a Mettler Toledo DL 15 auto-titrator using 0.01 mol·dm<sup>-3</sup> NaOH aqueous titrant. The weight of the dry membrane was determined by measuring the membrane weight after dehydration in a vacuum oven at 90°C for at least 3 hours after boiling in DI water. Water weight inside the membrane then can be calculated by subtracting weights of sulfuric acid and membrane from  $m_1$ :

$$m_{\text{water}} = m_1 - m_{\text{acid}} - m_{\text{membrane}} \quad (4-1)$$

#### ***4.2.3 Membrane Density Measurement***

The membrane density was measured using a Micromeritics AccuPyc 1340 pycnometer and Sartorius CPA224s analytical balance. The principle of this method is reported in literature in more detail.<sup>215</sup> Before the density measurement, the membrane was soaked in electrolyte solution with the same protocol mentioned in membrane uptake measurement section. Sample weight was measured using the analytical balance immediately after emersion and surface liquid removal. The volume of the membrane sample was measured using a pycnometer with helium. Sample density was calculated by using the measured sample volume and sample weight.

#### ***4.2.4 Vanadyl Uptake Measurement***

The sample equilibrating method applied to vanadium uptake measurements was identical to that used for the acid uptake measurement. Pretreated membrane samples were equilibrated in  $\text{VO}_2\text{SO}_4/\text{H}_2\text{SO}_4$  solutions with  $0.1 \text{ mol}\cdot\text{dm}^{-3}$  total sulfate/bisulfate concentration. We expect that  $0.1 \text{ mol}\cdot\text{dm}^{-3}$  total sulfate and bisulfate concentration is low enough to prevent substantial anion uptake given the Donnan potential effect in Nafion<sup>202</sup>. After solution equilibration, the membrane was removed, blotted and weighed. Then the membrane was immersed into 20 mL 3% (v/v) nitric acid to extract vanadyl ions for no less than 72 hours. The vanadyl content in nitric acid was measured using a Perkin Elmer 2100DV inductively couple plasma optical emission spectrometer (ICP-OES) relative to vanadium calibration standards (Ricca Chemical). After nitric acid soaking, the membrane was boiled in DI water to remove all residual vanadyl and acid.



The membrane weight was measured after at least 3 hours dehydration in a vacuum oven at 90°C. Water content in the membrane can be calculated as above. To illustrate vanadyl's relative concentration in the membrane or solution phase, its content fraction is expressed as  $x_{VO^{2+}} = \frac{2c(VO^{2+})_{membrane}}{c(-SO_3H)}$  or  $c(VO^{2+})/c(SO_4^{2-})$ .

#### ***4.2.5 Concentrated Vanadium/Sulfuric Acid Solution Preparation***

Concentrated vanadium/sulfuric acid solutions were used to simulate the electrolyte solution environment for the membrane in a vanadium redox flow battery. 1 mol·dm<sup>-3</sup> VO<sup>2+</sup> and 5 mol·dm<sup>-3</sup> SO<sub>4</sub><sup>2-</sup> solution was first made from VOSO<sub>4</sub> · xH<sub>2</sub>O powder and 96% sulfuric acid supplied by (Alfa Aesar). V<sup>3+</sup> and VO<sub>2</sub><sup>+</sup> solutions were prepared by electrolysis of 1 mol·dm<sup>-3</sup> VO<sup>2+</sup> and 5 mol·dm<sup>-3</sup> SO<sub>4</sub><sup>2-</sup> solution with a 5 cm<sup>2</sup> battery setup and method described in chapter 2.<sup>33</sup>

#### ***4.2.6 Membrane Conductivity Measurement***

Membrane resistance was measured on a four electrode conductivity cell by electrochemical impedance spectroscopy with a Bio-Logic SP200 potentiostat. The same membrane equilibration strategy as above was used in conductivity sample preparation before conductivity measurement. After wiping liquid droplets from the surface, each membrane sample was mounted onto the four-point conductivity cell. The EIS spectrum of the equilibrated membrane was taken from 200 kHz to 1 Hz with a 30 mV potential amplitude at 22°C. The membrane resistance between two sense electrodes was determined from the high frequency intercept of the impedance curve with the real

impedance axis in a Nyquist plot. Membrane conductivity was calculated from measured membrane resistance and the length between the two sense electrodes:

$$\sigma = \frac{L}{RW\delta} \quad (4-2)$$

$R$  is the measured membrane resistance between two electrodes;  $L$  is the distance between the electrodes;  $W$  and  $\delta$  are width and thickness of the membrane sample, respectively measured by a Fisher Scientific digital caliper and Mitutoyo 543-696 micrometer after impedance taking.

## 4.3 Results and Discussion

### 4.3.1 Acid-Water Equilibrium in Nafion

As is shown in Figure 4-1, the presence of a high concentration of sulfuric acid in the bathing electrolyte solution causes significant reduction in membrane water content. This is caused by several factors. In aqueous sulfuric acid solution, the water concentration and activity are reduced as acid concentration increases. The water content of Nafion as parameterized by  $\lambda = n(\text{H}_2\text{O})/n(-\text{SO}_3\text{H})$ , is known to depend on the water activity with equilibration in water vapor.<sup>84,214</sup> Upon equilibration with aqueous sulfuric acid, the water content in Nafion shows a dependence on water activity similar to that observed with water vapor equilibration, though the data for the solution equilibration shows a systematically larger magnitude of  $\lambda$  (Figure 4-2). Considering the presence of sulfuric acid in the membrane, another water content indicator  $\lambda'$  can be defined as

$\lambda' = n(\text{H}_2\text{O}) / (n(-\text{SO}_3^-) + n(\text{HSO}_4^-))$  based on the total amount of sulfonic acid group and sulfuric acid. By incorporating the sulfuric acid content in the membrane into the determination of  $\lambda'$ , the water content in Nafion with sulfuric acid equilibration is much closer to the  $\lambda$ - $a_w$  relation in water vapor equilibrated Nafion. That suggests that sulfuric acid and the sulfonic acid group have similar hydration behavior in the ionic clusters, channels and/or pores of the membrane. The inflated water content in the membrane was brought up by water associated with sulfuric acid. In both water vapor and sulfuric acid equilibrations, two distinct regions of water uptake can be observed, discriminated by an activity less or greater than approximately 0.8. When water activity is below 0.8, membrane water content is roughly linearly proportional to water activity. Once water activity exceeds 0.8, substantial increase in the water uptake per fractional increase in activity occurs in the membrane. In general, the water uptake at low water activity is usually associated with water of hydration of fixed acid sites in the membrane<sup>216</sup>. At high water activity, the chemical energy provided is sufficient to partly overcome the restoring force associated with the polymer matrix, resulting in extra membrane swelling associated with micropore expansion<sup>84</sup>. Within water activity range  $0 < a_{\text{water}} < 1$ , water content difference between acid equilibrated membrane and water vapor equilibrated membrane might be attributed to Schroeder's paradox, based on the experimental observation that polymers take up less water from water vapor than liquid phase.<sup>217,218</sup>

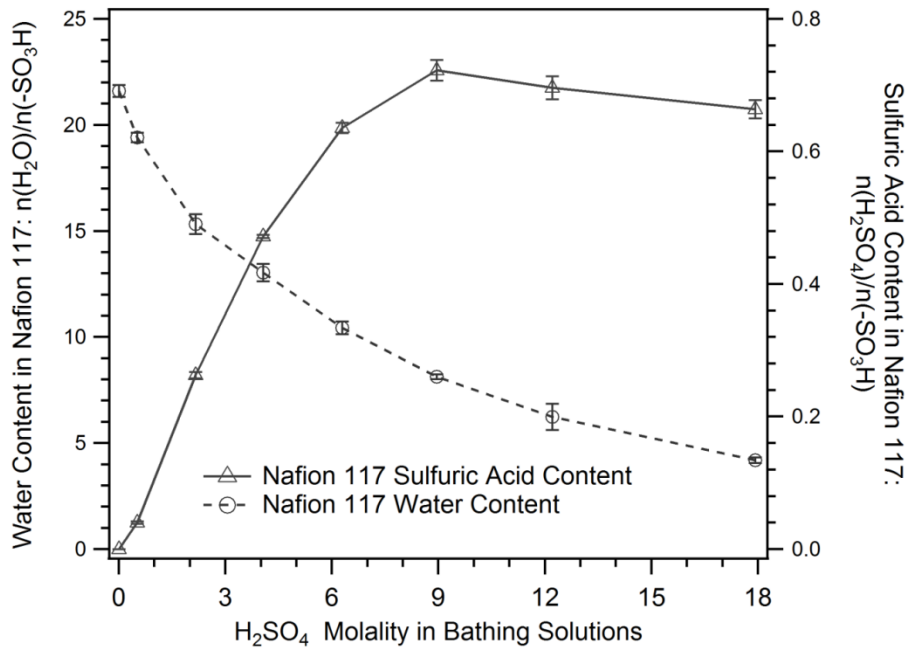


Figure 4–1. Water and sulfuric acid uptake by Nafion 117 in aqueous sulfuric acid solutions within concentration range from 0 to 17.4 mol·kg<sup>-1</sup>. Acid existence can lead lowered water content in Nafion, and propel sulfuric acid overcome Donnan potential to enter membrane’s ionic domain.

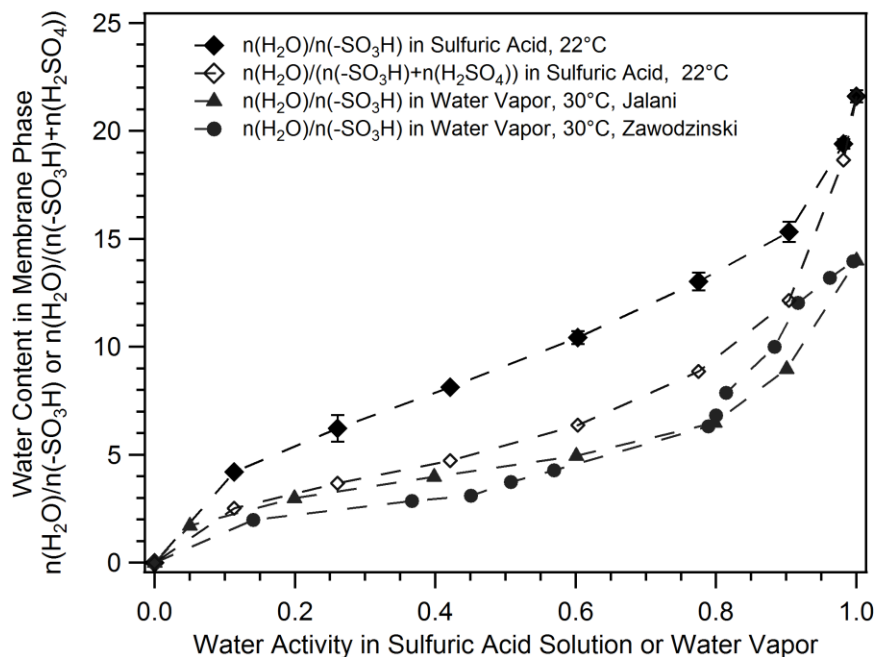


Figure 4–2. Water uptake in Nafion 117 vs. water activity in equilibrium between membrane and sulfuric acid solution. The water content dependence on water activity in sulfuric acid is very similar to that in water vapor.<sup>84,214</sup>

In Figure 4-1, the acid uptake in Nafion 117 shows very different response to acid concentration variation when equilibrating acid molality is above or below  $9 \text{ mol}\cdot\text{kg}^{-1}$ . The acid content in Nafion is roughly linearly dependent on acid concentration for acid concentrations lower than  $9 \text{ mol}\cdot\text{kg}^{-1}$ . In this concentration range, the acid uptake by the membrane is simply dominated by the acid concentration difference between the solution phase and membrane phase. Once acid concentration exceeds  $9 \text{ mol}\cdot\text{kg}^{-1}$ , acid content in the membrane slightly decreases with increasing solution acid concentration. However, this may be an artifact of the way the data are represented in Figure 4-2. As shown in Figure 4-3, the ratio of acid to water content in the membrane, i.e. the sulfuric acid

molality inside the membrane, is proportional to the acid concentration in the equilibrating solution. Sulfuric acid molality inside membrane is calculated from uptake data in Figure 4-1:

$$m_{\text{H}_2\text{SO}_4, \text{membrane}} = \frac{n(\text{H}_2\text{SO}_4)}{n(-\text{SO}_3\text{H})} / \lambda \times \frac{1000}{18} \quad (4-3)$$

This suggests that the solution is simply imbibed into the membrane, albeit with some degree of exclusion of acid. Although the acid concentrations used in this research are mostly beyond the concentration limit of Donnan exclusion, fixed sulfonic acid groups still create a barrier to uptake of sulfuric acid or sulfate anions, thereby lowering their content inside membrane. A concentration ratio about 1 to 2.5 was observed between sulfuric acid concentrations inside the membrane compared to that in solution.

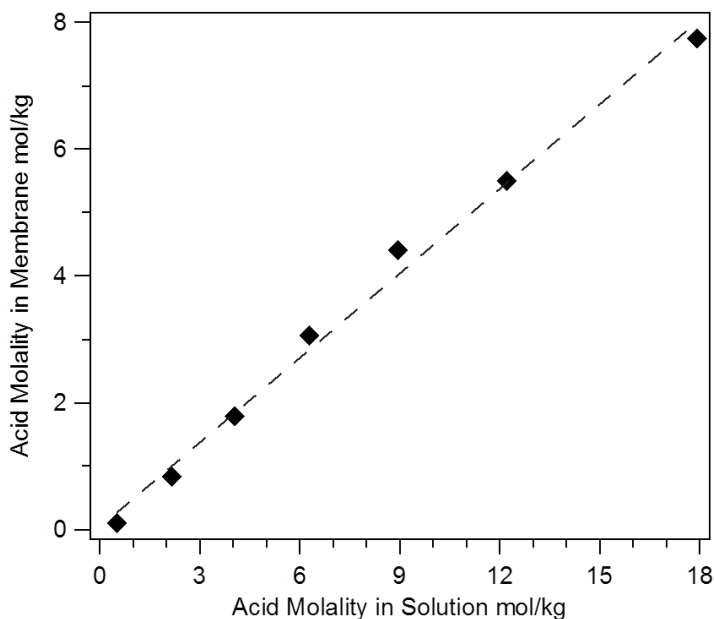


Figure 4–3. Sulfuric acid concentration in the membrane versus sulfuric acid concentration in bathing solution. The ratio of membrane sulfuric acid to environmental sulfuric acid is roughly 1:2.5.

#### ***4.3.2 Nafion Density After Sulfuric Acid Equilibration***

Analysis on membrane density after sulfuric acid soaking illustrates that Nafion suffers severe deswelling while being exposed to concentrated acid environment. The density measurement results in Figure 4-4 clearly show a monotonic increasing in density upon equilibration with increasingly concentrated sulfuric acid. The measured density of dehydrated Nafion 117 was  $2.10 \pm 0.10 \text{ g} \cdot \text{cm}^{-3}$ . Verbrugge and Hill suggested that Nafion 117's porosity can decrease from 30% to 15% upon equilibration with sulfuric acid over the concentration range  $0.001$  to  $10 \text{ mol} \cdot \text{dm}^{-3}$  by experiment<sup>204</sup>. The porosity is calculated by:

$$\theta = \frac{V_{wet} - V_{Dry, H^+}}{V_{wet}} \quad (4-4)$$

Where  $V_{wet}$  and  $V_{Dry, H^+}$  are membrane volume per mole of sulfonic acid group, respectively in sulfuric acid equilibrated state and dehydrated state in proton form.  $V_{wet}$  is calculated from water and acid contents in membrane and measured membrane density, by:

$$V_{wet} = (EW + 18\lambda + 98 \frac{n_{H_2SO_4}}{n_{-SO_3H}}) / \rho_{Membrane} \quad (4-5)$$

The calculated Nafion porosity is presented in Figure 4-4 as well, showing a good agreement in general trend over the acid concentration range with porosity reported in reference.<sup>204</sup> The porosity loss in Nafion after being exposed to acidic solution illustrates that acidic environment can lead significant deswelling on Nafion. The internal pore space reduction in concentrated acid is also coincident with the species uptake reduction discussed above.



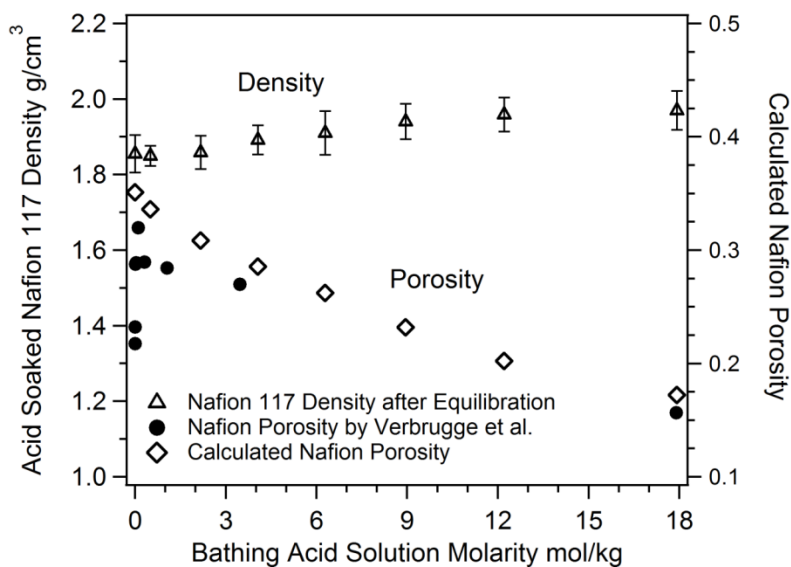


Figure 4–4. Measured density and calculated porosity of Nafion 117 with respect to sulfuric acid concentration in bathing solution. The declining density dependence on acid concentration in solution is indicating membrane deswells in acid solution.

### 4.3.3 $VO^{2+}$ Partitioning in Nafion

$VO^{2+}$  and water uptake for membranes exposed to vanadium/acid solutions are shown in Figure 4-5. In this experiment, the total sulfate concentration was maintained at  $0.1 \text{ mol}\cdot\text{dm}^{-3}$  and the vanadium to proton mole fraction was varied. The water content in the membrane was not strongly related to the vanadium concentration in the equilibrating solutions. Neither vanadyl nor sulfuric acid concentration was high enough to reduce water activity in the equilibrium. The high water activity in the membrane results in high and fairly constant water content in the equilibrated membrane with varying vanadyl/sulfate fraction. The vanadyl fraction in the membrane phase was typically

higher than its fraction in the solution phase, i.e. vanadyl preferentially was taken into the membrane relative to protons. The membrane has a stronger affinity to vanadyl most likely because vanadyl is a divalent ion which can have a stronger electrostatic attraction with sulfonic acid group than a monovalent ion. Although it has been proved that several factors more than ionic valence can influence ion partitioning in Nafion<sup>219-221</sup>, especially when high surface charge density monovalent ion exists in system, the vanadyl/proton partitioning observed in this study behaved more similar to the partitioning competition between low surface charge density monovalent ion and divalent, such as  $\text{Li}^+/\text{Ni}^{2+}$  pair in reference<sup>220</sup>. The surprise here is the lack of a concomitant decrease in the water content expected if the vanadyl is strongly ion pairing with the sulfonate<sup>211,212</sup>. Nafion's hydration level highly relies on the hydration energy of the cation<sup>209,214</sup>. Since the vanadium atom in a vanadyl-aqua complex has +4 valence, its electrostatic attraction to water molecules should be stronger than cations with lower valence to maintain a more stable water shell over the entire vanadyl content range.

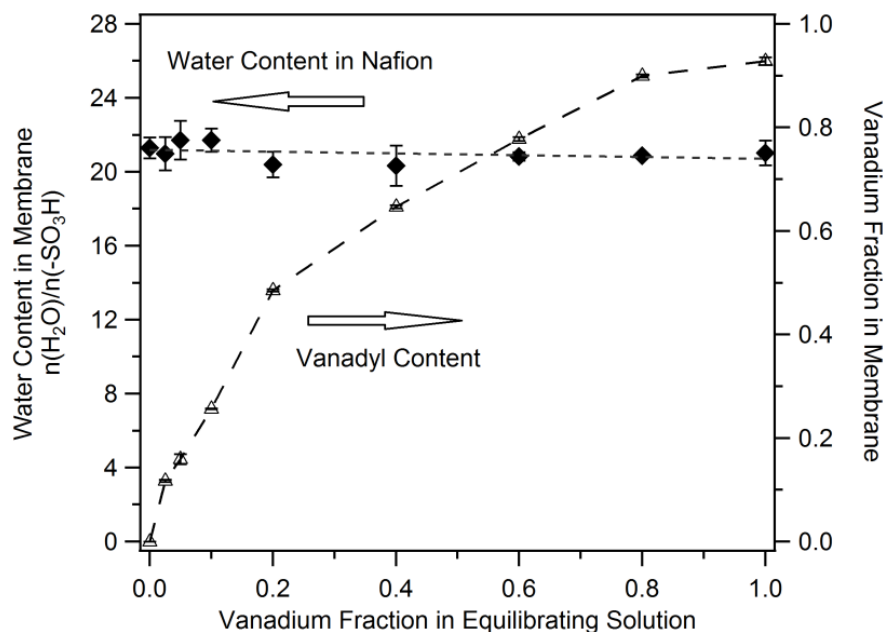


Figure 4–5. Water and vanadyl content in Nafion 117 equilibrated with vanadyl sulfate/sulfuric acid solutions of  $0.1 \text{ mol}\cdot\text{dm}^{-3}$  total sulfate background. Vanadyl presence in membrane has barely effect on membrane’s water content; Vanadyl is preferred by sulfonate to proton in Nafion.

In the real battery environment, other oxidation states, including  $\text{V}^{3+}$ , also can enter the membrane and bond to sulfonic acid groups, possibly with an even stronger electrostatic attractive force because of their high charge. Further investigation of the partitioning competition among vanadium ions and proton is needed but that is beyond the scope of the present work, which focuses on vanadyl ions.

#### 4.3.4 Sulfuric Acid Influence on Nafion Conductivity

The conductivity of the membrane as a function of concentration of bathing sulfuric acid solution is shown in Figure 4-6. The data shows a change in conductivity behavior between low and high acid concentrations. The membrane conductivity enhancement or reduction can be considered as a trade-off between proton concentration increase and proton mobility loss caused by acid presence in environment. In membrane, the sulfuric acid can provide excess protons by its ionization, while it also reduces membrane's water content.

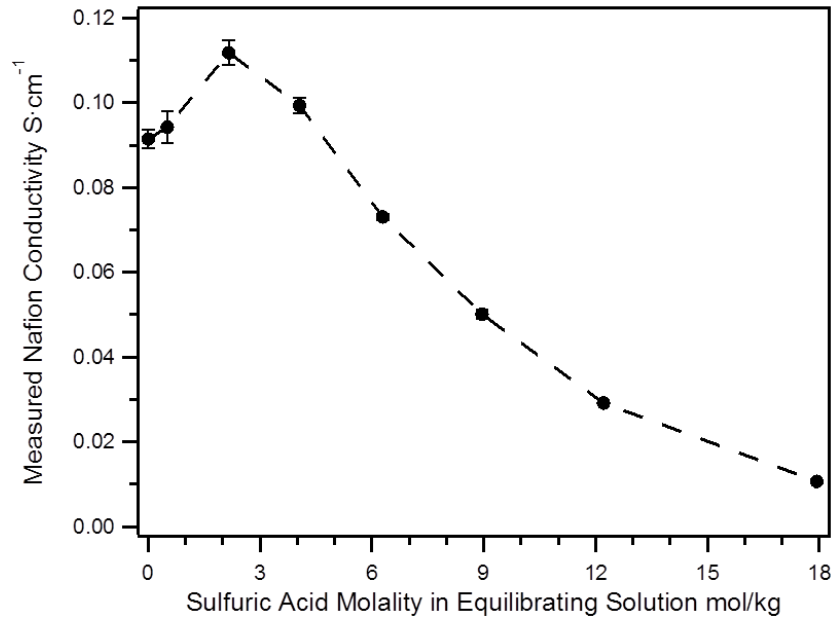


Figure 4–6. Sulfuric acid presence in equilibrium can enhance membrane's conductivity when sulfuric acid is no more concentrated than 5 mol·kg<sup>-1</sup> in environment; Acid can reduce membrane's conductivity when its concentration is over 5 mol·kg<sup>-1</sup> in equilibrium.

To qualitatively analyze the impact of sulfuric acid uptake on proton concentration and mobility in the membrane, a model was developed based on measured Nafion uptake and conductivity results. In sulfuric acid solutions with concentration up to  $40 \text{ mol}\cdot\text{kg}^{-1}$ , all sulfuric acid molecules in solution can complete their first dissociation<sup>222,223</sup>. Sulfonic acid groups in Nafion also have been shown to be dissociated even at low hydration level<sup>216,224</sup>. We propose a simple model of Nafion conductivity with sulfuric acid equilibrium under the assumption that all sulfonic acid groups dissociate and sulfuric acid molecules accomplish their first dissociation. By assuming a bisulfate dissociation constant ( $\text{pK}_{\text{a},2}$ ) of 2,<sup>225</sup> it is straightforward to balance proton, bisulfate and sulfate in a dissociation equilibrium:

$$n(\text{H}^+)n(\text{SO}_4^{2-})/n(\text{HSO}_4^-) = K_{\text{a},2} \quad (4-6)$$

The total concentration of bisulfate and sulfate equals the measured concentration of sulfuric acid in the membrane:

$$n(\text{SO}_4^{2-}) + n(\text{HSO}_4^-) = n(\text{H}_2\text{SO}_4)_{\text{measured}} \quad (4-7)$$

The membrane proton concentration is balanced by ionic electrical neutrality inside the membrane:

$$n(\text{H}^+) = n(-\text{SO}_3^-) + n(\text{HSO}_4^-) + 2n(\text{SO}_4^{2-}) \quad (4-8)$$

By solving equations 4-6 to 4-8, the proton content in the membrane is proved to be equal to the total amount of sulfonic acid group and imbibed sulfuric acid. Dissociated sulfuric acid in the membrane is able to provide abundant additional protons for carrying charge.

Extra protons in the membrane are overwhelmingly generated by sulfuric acid molecule ionization rather than dissociation of bisulfate, because bisulfate's dissociation is completely suppressed by the high proton concentration from ionization of both sulfuric acid molecules and sulfonic acid groups. Combining the density and uptake measurements presented above, the actual sulfonate concentration can be calculated and proton concentration can be derived:

$$c_{-\text{SO}_3\text{H}} = \rho_{\text{membrane}} / \left[ \text{EW} + 18\lambda + \frac{98n(\text{H}_2\text{SO}_4)}{n(-\text{SO}_3\text{H})} \right] \quad (4-9)$$

$$c_{\text{H}^+} = \frac{n(\text{H}^+)}{n(-\text{SO}_3\text{H})} c_{-\text{SO}_3\text{H}} = \frac{n(-\text{SO}_3\text{H}) + n(\text{H}_2\text{SO}_4)}{n(-\text{SO}_3\text{H})} c_{-\text{SO}_3\text{H}} \quad (4-10)$$

The proton mobility can be precisely estimated from membrane conductivity and the calculated proton concentration in the membrane, by assuming that bisulfate contribution is trivial to the membrane conductivity. Based on previous findings in the literature, the anion transference number is extremely low compared to that of the proton.<sup>200,201</sup> Accordingly, our assumption is safe and proton mobility can be determined by the relation:

$$\sigma_{\text{membrane}} = z_{\text{H}^+} F u_{\text{H}^+} c_{\text{H}^+} \quad (4-11)$$

The calculated proton concentration and mobility with respect to the bathing sulfuric acid concentration are presented in Figure 4-7. A significant amount of excess protons in the membrane can be generated by sulfuric acid molecule dissociation, while the proton mobility appears to be drastically reduced. Since the first dissociation of sulfuric acid dominates excess proton generation, excess proton concentration is proportional to acid

uptake. The peak in membrane conductivity observed in Figure 4-6 is thus a consequence of the simultaneous increase in proton availability combined with the corresponding decrease in proton mobility.

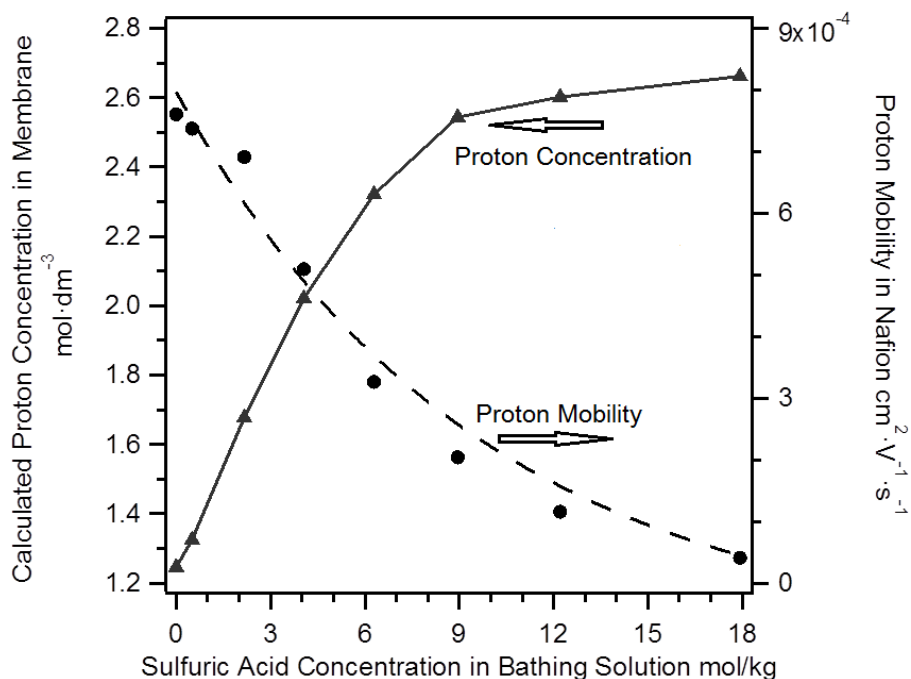


Figure 4–7. Calculated proton concentration and mobility are presented as functions of sulfuric acid concentration in bathing solution. By being exposed to acidic environment, membrane can gain an elevated proton concentration, but loss proton mobility. The two factors contribute comprehensively to enhanced or lowered membrane conductivity.

Proton mobility in Nafion is highly dependent on water content. Water is the most important proton transport mediator in acid equilibrated membrane as well as hydrated Nafion.<sup>84,85,226</sup> In the presence of sulfuric acid, proton mobility increases with membrane

water content in two different regimes, demarcated by  $\lambda' = 12$  (Figure 4-8). The turning point of proton mobility dependence on water content at  $\lambda' = 12$  suggests that the membrane, sulfuric acid and water reach a critical equilibrium for proton transport at this point. At this equilibrium, water is present in a favorable quantity amount to facilitate effectively the proton transport. At this level of water content, proton transport in Nafion is benefitted by Grotthus mechanism that can provide relatively fast proton diffusion across the water network.<sup>84,226</sup> Although the membrane still suffers water loss when  $\lambda' > 12$ , bisulfate could facilitate proton transfer by providing additional connection among sulfonates. In these cases, proton mobility is not sensitive to modest water content variations in membrane. Below the critical point, significant proton mobility loss is caused by severe water-sulfuric acid content change. At low hydration level, the proton 'hopping' probability is further reduced because of lower water availability to serve as proton transfer mediator. Facilitation from bisulfate can no longer enhance proton mobility, or may even become an adverse effect. According to Lawton's observations on sulfuric acid influence on ion transport in Nafion and expectations based on classic diffusion theory, ion transport can be slowed down due to increased solution viscosity which is primarily contributed by sulfuric acid.<sup>32</sup>



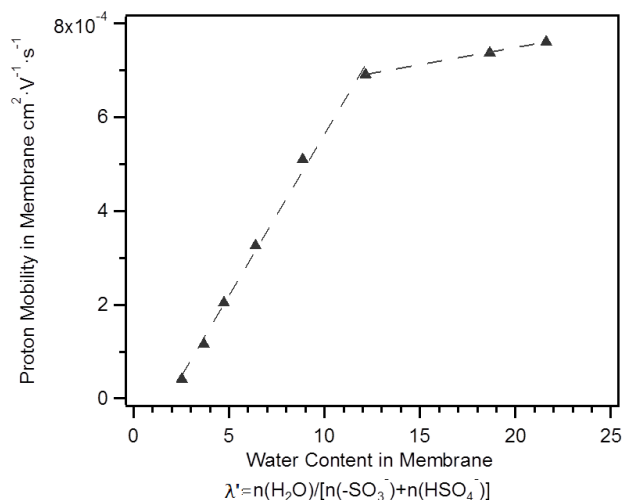


Figure 4–8. Proton mobility relies on water/acid content ratio in two different ways. At high water content, proton mobility is fairly constant; when water content is lower than 12 water molecules per acid, proton mobility decreases severely with decreasing water content in a linear pattern.

In Figure 4-9, we show that proton mobility in acid-equilibrated membranes can be represented by a power law dependence on water activity given by  $u_{\text{H}^+} = 7.61 \times 10^{-4} \text{ cm}^2 \cdot \text{V}^{-1} \cdot \text{s}^{-1} \times a_{\text{water}}^{1.5}$ . Water activity in the membrane is determined by the sulfuric acid concentration with the activity-concentration relationship in aqueous sulfuric acid solution recommended by Staples.<sup>227</sup> With equilibration in water vapor, membrane conductivity is a function of water activity.<sup>84,228,229</sup> In the membrane-water-sulfuric acid equilibrium, proton mobility dependence on water activity is similar to its conductivity dependence on water activity with equilibration in water vapor. In both cases, higher water activity can guarantee a larger quantity of water molecules that can participate in proton transport.

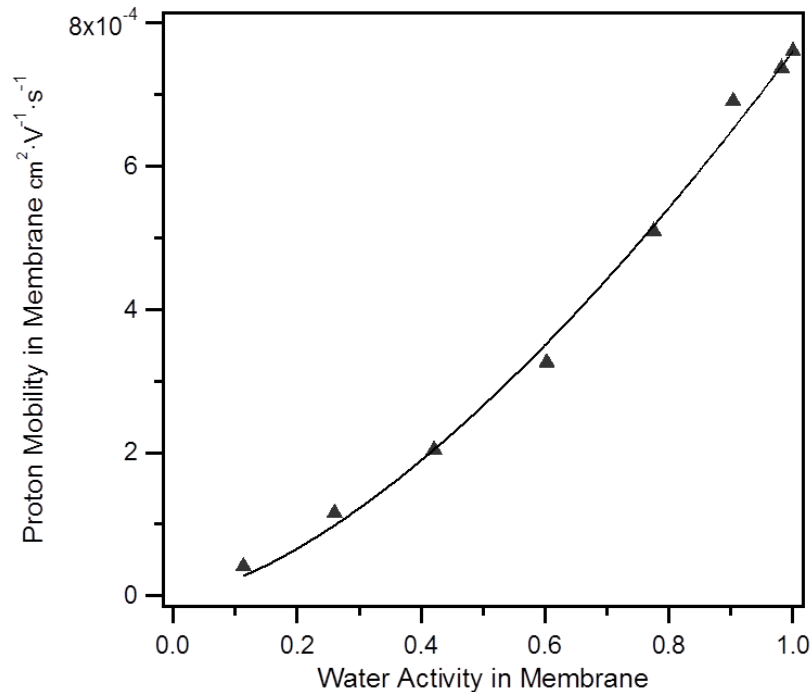


Figure 4-9. In the Nafion membrane, proton mobility depends on water activity according to a power law,  $u_{H^+} = 7.61 \times 10^{-4} \text{ cm}^2 \cdot \text{V}^{-1} \cdot \text{s}^{-1} \times a_{\text{water}}^{1.5}$ . The mobility dependence on water activity implies that proton transfer involves one to two water molecules.

#### 4.3.5 $\text{VO}^{2+}$ Influence on Nafion Conductivity

The conductivity of Nafion was measured after membrane samples were equilibrated in  $0.1 \text{ mol} \cdot \text{dm}^{-3}$  total sulfate solutions of different vanadyl/proton fractions (Figure 4-10). Clearly, with increasing vanadyl fraction in the bathing solution and thus the membrane, decreased conductivity suggests that vanadyl ion most likely has a substantially lower mobility than the proton. Since the total concentration of sulfate and bisulfate in this set of solutions was  $0.1 \text{ mol} \cdot \text{dm}^{-3}$ , i.e. not high enough to overcome the

Donnan potential of the membrane, only a trace amount of anion can get into the membrane. Thus, the influence of sulfuric acid on membrane conductivity can be neglected. As is presented in Figure 4-5, the water content of Nafion equilibrated with the different acid-salt compositions was essentially constant. Therefore, water content variation in the membrane should not be a factor influencing membrane conductivity. In Figure 4-11, a strong decrease of membrane conductivity is observed upon vanadium uptake into the membrane. Since the concentrations of vanadyl ions and protons in the membrane are balanced by the number of sulfonic acid groups, uptake of vanadyl can reduce the proton concentration. Because metallic cations have much lower mobility than protons in fully hydrated Nafion, membranes containing cations generally have much lower conductivity than unexchanged proton-form membranes.<sup>211,212</sup> In Figure 4-11, the measured membrane conductivity is obviously lower than the conductivity projected from proton-form and fully exchanged vanadyl-form membrane conductivity based on a linear interpolation with the assumption of fixed proton and vanadyl mobility. This deviation suggests that there must be some interaction between protons and vanadyl ions to slow their motion in the membrane.

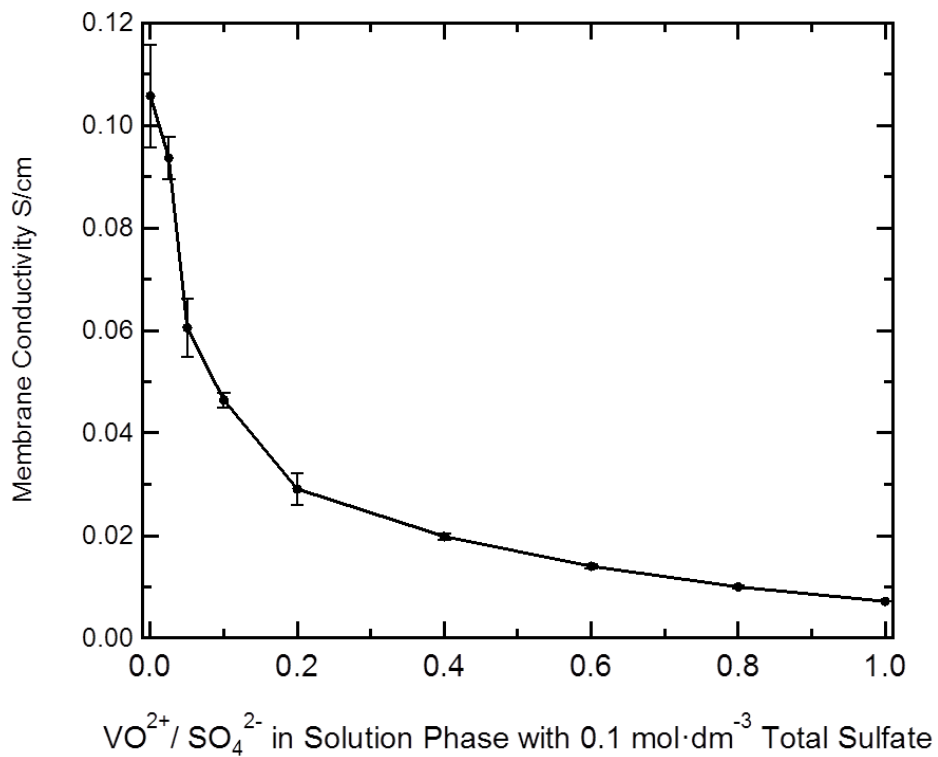


Figure 4–10. Conductivity of Nafion 117 equilibrated with vanadyl sulfate/sulfuric acid solution with  $0.1 \text{ mol} \cdot \text{dm}^{-3}$  total sulfate background. The vanadyl has a decreasing effect on Nafion's conductivity.

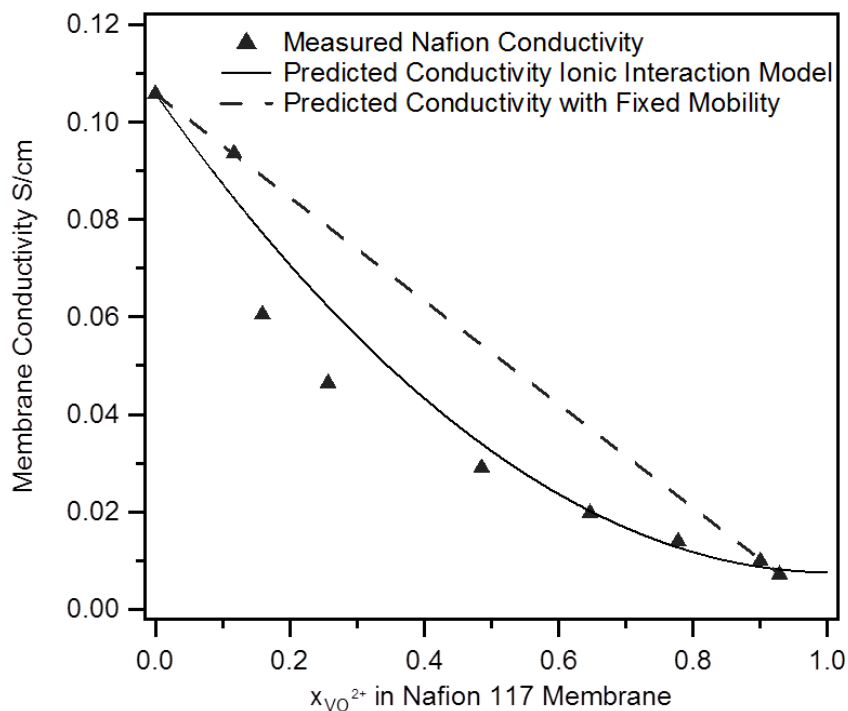


Figure 4–11. Measured conductivity for Nafion 117 with different vanadyl relative concentration in Membrane in comparison with predicted conductivity from ionic interaction model and fixed mobility model. The analysis illustrates that vanadyl has a much slower motion than proton in transferring inside Nafion, and it can also slow down proton’s transport in a linear relation of unrevealed mechanism.

To quantify the vanadyl ion influence on proton mobility and membrane conductivity, a model was constructed based on an ionic interaction hypothesis. In our system, since vanadyl-Nafion was as well hydrated as it was fully saturated by pure water, we expect that the Grotthus mechanism dominates proton transport through the hydration networks in ionic cluster channels. Some transition metals have been shown to interact with protons in membranes causing proton mobility reductions without a significant

change in the mobility of the metallic ion.<sup>212</sup> To achieve a concise model, it is assumed that vanadyl has a constant mobility while proton mobility is changed by vanadyl. Using the Nernst-Einstein equation, the conductivity of Nafion in mixed vanadyl/proton form is a function of mobility and concentration of vanadyl and proton in membrane:

$$\sigma_{\text{membrane}} = F(z_{\text{H}^+}c_{\text{H}^+}u_{\text{H}^+} + z_{\text{VO}^{2+}}c_{\text{VO}^{2+}}u_{\text{VO}^{2+}}) \quad (4-12)$$

Here,  $\sigma_{\text{membrane}}$  is the membrane's conductivity;  $F$  is the Faraday constant,  $96500 \text{ C}\cdot\text{mol}^{-1}$ ;  $z$ ,  $c$  and  $u$  are the respective charge number, concentration and mobility of proton and vanadyl. Because of electrical neutrality in membrane, proton and vanadyl concentrations are balanced by the sulfonic acid group concentration in membrane, as presented in eq.4-13:

$$z_{-\text{SO}_3\text{H}}c_{-\text{SO}_3\text{H}} + z_{\text{H}^+}c_{\text{H}^+} + z_{\text{VO}^{2+}}c_{\text{VO}^{2+}} = 0 \quad (4-13)$$

To simplify our analysis process, we define proton and vanadyl relative concentration in the membrane as  $x_{\text{H}^+} = z_{\text{H}^+}c_{\text{H}^+}/z_{-\text{SO}_3\text{H}}c_{-\text{SO}_3\text{H}}$  and  $x_{\text{VO}^{2+}} = z_{\text{VO}^{2+}}c_{\text{VO}^{2+}}/z_{-\text{SO}_3\text{H}}c_{-\text{SO}_3\text{H}}$ . Then eq.4-13 was reduced to  $x_{\text{H}^+} + x_{\text{VO}^{2+}} = 1$ . With definitions introduced, eq.4-12 can also be simplified as:

$$\sigma_{\text{membrane}} = Fc_{-\text{SO}_3\text{H}}(x_{\text{H}^+}u_{\text{H}^+} + x_{\text{VO}^{2+}}u_{\text{VO}^{2+}}) \quad (4-14)$$

The sulfonic acid group concentration is estimated from the water-saturated Nafion 117 density and equivalent weight and water uptake:  $c_{-\text{SO}_3\text{H}} = \frac{\text{EW}+18\lambda}{\rho_{\text{Nafion,Water}}} = 1.25 \times 10^{-3} \text{ mol}\cdot\text{cm}^{-3}$ . Because the constant water content implies only minor membrane deswelling

caused by vanadyl uptake, it is proper to assume a constant sulfonate concentration for different proton/vanadyl ratios. Here, proton mobility loss is assumed to be proportional to vanadyl concentration in membrane:

$$u_{H^+} = u_{H^+}^* - kx_{VO^{2+}} \quad (4-15)$$

Where  $k$  is an undetermined coefficient and  $u_{H^+}^*$  is proton mobility in fully saturated H-form Nafion. Its value is  $8.79 \times 10^{-4} \text{ cm}^2 \cdot \text{s}^{-1} \cdot \text{V}^{-1}$ , calculated from water saturated Nafion 117 conductivity. By combining eq. 4-14, eq.4-15 can be derived as:

$$\frac{\kappa_{\text{membrane}}}{F \cdot c_{-\text{SO}_3\text{H}}} - u_{H^+}^* = kx_{VO^{2+}}^2 + (u_{VO^{2+}} - k - u_{H^+}^*)x_{VO^{2+}} \quad (4-16)$$

Then  $k$  and  $u_{VO^{2+}}$  can be calculated from the polynomial coefficients of quadratic curve by fitting the left side of eq. 4-16 as a function of  $x_{VO^{2+}}$ . The quadratic curve was fitted by least square polynomial fitting from measured conductivity-vanadyl content data presented in Figure 4-11. The results are  $k=8.04 \times 10^{-4} \text{ cm}^2 \cdot \text{s}^{-1} \cdot \text{V}^{-1}$  and  $u_{VO^{2+}}=6.28 \times 10^{-5} \text{ cm}^2 \cdot \text{s}^{-1} \cdot \text{V}^{-1}$ . Compared to proton mobility in H-form Nafion, the vanadyl ion exhibits more than 10 times slower mobility, comparable to mobility of  $\text{Fe}^{3+}$ ,  $5.3 \times 10^{-5} \text{ cm}^2 \cdot \text{s}^{-1} \cdot \text{V}^{-1}$ .<sup>1,212</sup> In Figure 4-11, the predicted conductivity for Nafion 117 by the ionic interaction model is in qualitative agreement with measured conductivity.

The agreement of modeled and experimental conductivity implies that there is a decrease in proton mobility caused by the presence of the vanadyl ion in the membrane. Proton mobility decreases in proportion to the vanadyl content inside the membrane. This result is similar to the iron-proton interaction reported by Okada etc., although vanadyl

does not lead to a water content loss in Nafion.<sup>212</sup> As has been stated previously,<sup>212</sup> the cation-proton interaction is implemented through the cation constraint on water molecule self-exchange to participate in proton hopping processes near the cation exchange site, rather than direct cation-cation interaction. The vanadyl ion has a very stable hydration shell, which seems to be maintained even in the presence of the anions of this system. The strong constraint on water in the vanadyl-aqua complex can restrict coordinated water motion and availability for proton hopping. By this means, the presence of vanadyl ion promotes a higher barrier to proton transport than would be expected at the given water content.

#### ***4.3.6 Nafion Conductivity in Practical Electrolyte Conditions***

In Figure 4-12, the Nafion 117 conductivity after one-day equilibration in solutions of  $5 \text{ mol}\cdot\text{dm}^{-3}$  total sulfate and varying vanadyl concentration is presented. This is a typical composition of the VRB feed. With more concentrated acid in electrolyte solution, the inhibitive effect of vanadyl on membrane conductivity was less than observed in a low concentration measurement. Even though the concentration of vanadyl in the equilibration solution increased from  $0.25$  to  $1.75 \text{ mol}\cdot\text{dm}^{-3}$ , the Nafion conductivity only decreased from  $0.051$  to  $0.34 \text{ S}\cdot\text{cm}^{-1}$ . Only a 30% conductivity loss on Nafion 117 was brought about by an increase of seven times the vanadyl concentration in these high vanadyl/acid concentration solutions. In the lower concentration investigation described above, membrane conductivity was reduced from  $0.60$  to  $0.20 \text{ S}\cdot\text{cm}^{-1}$ , with the same vanadyl/sulfate concentration ratio elevation. The conductivity reduction caused by the



presence of vanadyl was partly inhibited by the presence of concentrated sulfuric acid in the electrolyte solution. The lowered vanadyl uptake impact on Nafion's conductivity indicates that there is a more complicated situation for equilibrium amongst vanadyl, sulfuric acid and sulfonic acid groups under these conditions of high concentrations of all components, with a substantial effect of ion 'competition' for partitioning into the Nafion.

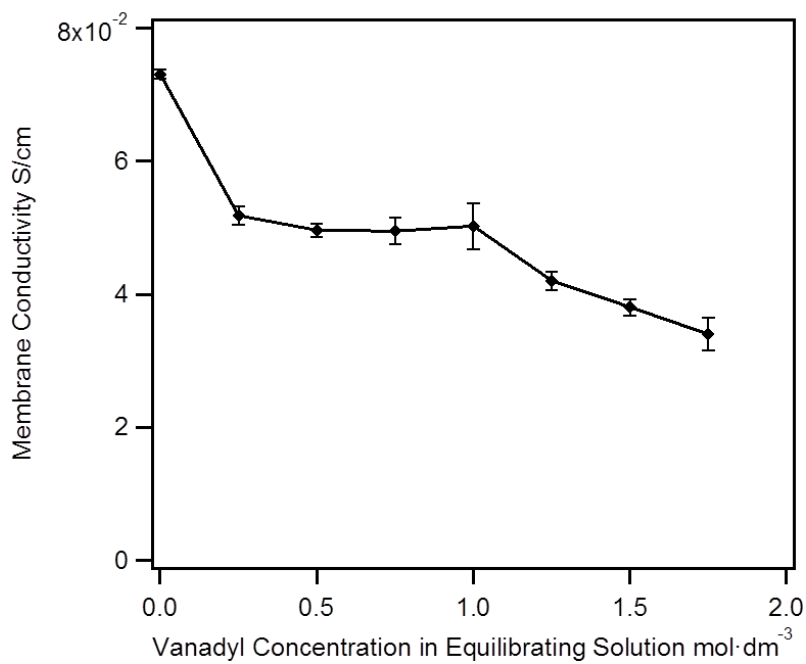


Figure 4–12. Nafion 117 conductivity upon equilibration in vanadyl sulfate/sulfuric acid solutions of 0 to 1.75 mol·dm<sup>-3</sup> vanadyl in 5 mol·dm<sup>-3</sup> sulfate background.

As a component of the measured internal resistances of non-gap battery system, membrane resistance contributes significantly to battery internal resistance. The equivalent areal specific resistance of a single layer Nafion 117 equilibrated with 1

$\text{mol}\cdot\text{dm}^{-3}$  vanadium /  $5 \text{ mol}\cdot\text{dm}^{-3}$  sulfate with valence states of +3 to +5 was circa 0.37 to  $0.40 \Omega\cdot\text{cm}^{-2}$ . Several measured internal areal specific resistances of non-gap architecture batteries employing a single layer of Nafion 117 are also listed in Table 4-1, ranging from 0.5 to  $0.687 \Omega\cdot\text{cm}^{-2}$ . The internal resistance of the battery cell reported here includes the resistance of every cell component and contact resistance on respective interface. The equivalent ASR of equilibrated Nafion 117, which is much higher than any other contributor to IR loss, can be up to 50 to 80% of battery IR loss. To remedy this, we must understand fully the implications of studies such as that described above.

Table 4-1. Conductivity and Equivalent ASR of Nafion 117 Equilibrated in Vanadium/Sulfuric Acid Solutions with Comparison to Internal Resistance of Nafion 117 Installed Battery Systems.

Test Type	Electrolyte	Electrode (compression)	Conductivity $\text{S}\cdot\text{cm}^{-1}$	ASR $\text{ohm}\cdot\text{cm}^{-2}$	Reference
Conductivity test	$5 \text{ mol}\cdot\text{dm}^{-3}$ Sulfuric acid	—	0.073	0.27	
Conductivity test	$1 \text{ mol}\cdot\text{dm}^{-3} \text{ V}^{3+}$ $5 \text{ mol}\cdot\text{dm}^{-3}$ sulfate	—	0.055	0.37	
Conductivity test	$1 \text{ mol}\cdot\text{dm}^{-3} \text{ V}^{4+}$ $5 \text{ mol}\cdot\text{dm}^{-3}$ sulfate	—	0.050	0.40	
Conductivity test	$1 \text{ mol}\cdot\text{dm}^{-3} \text{ V}^{5+}$ $5 \text{ mol}\cdot\text{dm}^{-3}$ sulfate	—	0.054	0.37	
Non-gap Battery	$1 \text{ mol}\cdot\text{dm}^{-3} \text{ V}^{x+}$ $5 \text{ mol}\cdot\text{dm}^{-3}$ Sulfate	Toray carbon paper 200 $\mu\text{m}$ (25%)	—	0.63~0.65	33
Non-gap Battery	$1 \text{ mol}\cdot\text{dm}^{-3} \text{ V}^{x+}$ $5 \text{ mol}\cdot\text{dm}^{-3}$ Sulfate	SGL 10AA CP 400 $\mu\text{m}$ (19-25%)	—	0.5	34
Non-gap Battery	$1 \text{ mol}\cdot\text{dm}^{-3} \text{ VO}\text{SO}_4$ $5 \text{ mol}\cdot\text{dm}^{-3} \text{ H}_2\text{SO}_4$	SGL 10AA CP 400 $\mu\text{m}$ (20%)	—	0.606~0.68 7	49

As has been discussed above, electrolyte species in the vanadium redox flow battery can affect Nafion properties as an electrolyte separator. The membrane conductivity can be enhanced or reduced by sulfuric acid in electrolyte, depending on the surrounding concentration. Vanadium ion in the electrolyte is another essential factor leading to lowered Nafion conductivity in a VRFB. When vanadium displaces protons in the membrane, conductivity can be reduced by both lowered proton concentration and slowed proton motion. Vanadyl in an electrolyte with high acid concentration can also enter membrane and cause conductivity reduction. We have conclusively shown that the membrane can lose its conductivity upon exposure to concentrated electrolyte which is necessary to improve battery energy density. Moreover, high membrane resistance also decreases high battery efficiency, especially in the recently achieved high operating current density.<sup>28</sup> To optimize battery system performance, membrane performance and electrolyte composition, or battery energy density should be well balanced in battery design. Our observations also support new electrolyte separator development based on cation exchange polymer membrane. Sulfuric acid and vanadium uptake should be suppressed to keep high proton concentration and mobility to maintain conductivity in future sulfonated polymer electrolyte separator.

#### **4.4 Summary**

The membrane-electrolyte equilibrium and its impact on ionic transport in Nafion have been discussed. Uptake behavior of the membrane in contact with sulfuric acid is comprehensively dependent on the equilibrium between sulfuric acid solution and

membrane. From our sulfuric acid influence study, sulfuric acid is concentrated enough to overcome Donnan exclusion to enter nanopores in the membrane. Low water activity in membrane-electrolyte equilibrium can lead lowered membrane water content. Membrane dehydration caused by low water activity in the equilibrating solution can prevent incremental acid uptake by the membrane at a relatively high acid concentration. Sulfuric acid in the membrane can have an enhancing or reducing impact on membrane conductivity, depending on acid and water contents in membrane. Acid in the membrane can enhance membrane conductivity by increasing proton concentration in membrane. However proton mobility can significantly decrease with water loss from the membrane caused by the low water activity of bathing solutions with high sulfuric acid concentration. When vanadyl ion is present in the membrane equilibrated in dilute acid, it can reduce membrane conductivity by reducing proton concentration and mobility. Two effects contribute to this: vanadyl mobility is much lower than that of proton in membrane, and it can slow down the proton dynamics in spite of the fact that it does not reduce membrane water content. In a membrane with equilibration in electrolyte with practical composition for VRFB operation, vanadyl and acid also contribute to a reduction of membrane conductivity, but not to the extent observed in the case of the vanadyl/proton form Nafion formed upon equilibration with dilute solutions. This suggests a more complicated equilibrium and partitioning competition between protons and vanadyl for a membrane soaked in concentrated electrolyte.

**CHAPTER 5**  
**THE VANADIUM CATIONS INFLUENCE ON ION TRANSPORT IN ION**  
**EXCHANGE MEMBRANE**

**5.1 Introduction**

The electrolyte separator, or membrane, is one main factor limiting VRFB development.<sup>28</sup> There are several membrane problems strongly influencing VRFB's systematic performance. Membranes can lose conductivity due to being exposed to the electrolyte solution, especially acidic solution.<sup>30,31,200,201,207</sup> Battery capacity and efficiency losses are caused by vanadium permeation across the membrane<sup>32,89</sup>. Membrane durability is also an important factor limiting battery performance, especially for hydrocarbon membranes.<sup>100</sup>

The aim of work in this chapter is try to understand equilibrium between Nafion membrane and ionic solutions, and its impact on proton's transport in membrane. Elemental analysis combined with gravimetric analysis was used to study ionic equilibrium in membranes equilibrated in electrolyte solutions. Electrochemical impedance spectroscopy was utilized to measure membrane's conductivity after equilibration in electrolyte solutions of varying conditions. A simple modeling analysis was carried out based on the measurement of conductivity and membrane water and ion uptake behavior.

## 5.2 Experimental

### 5.2.1 Membrane and Electrolyte Preparation

Nafion 117 used in this work was purchased from Ion Power Inc., referred as Nafion in future description. Before being subjected to test conditions, Nafion has been pretreated in a standard procedure from the literature. Nafion was pretreated in 3% H<sub>2</sub>O<sub>2</sub> (Fisher Scientific), deionized water, 1 mol·dm<sup>-3</sup> H<sub>2</sub>SO<sub>4</sub> (Alfa Aesar) and DI water respectively for one hour at 90°C. The DI water (18.2 MΩ·cm) used in this study was generated by MilliQ water purification system. After pretreatment, each membrane sample was stored in DI water for future use.

Electrolyte solutions of two concentration levels were prepared to achieve different membrane-electrolyte equilibriums. The dilute VCl<sub>3</sub>/HCl solutions were prepared from VCl<sub>3</sub> powder (99%, Sigma Aldrich) and HCl (1 mol·dm<sup>-3</sup>, Alfa Aesar). The total chloride concentration in solutions was controlled at 0.1 mol·dm<sup>-3</sup> to prevent chloride entering micropores in membrane, according to Donnan exclusion.<sup>202</sup> More concentrated electrolyte was prepared to achieve equilibrium including co-ions in the membrane's ionic domain. The raw electrolyte solution containing 2 mol·dm<sup>-3</sup> VOSO<sub>4</sub> and 3 mol·dm<sup>-3</sup> H<sub>2</sub>SO<sub>4</sub>, was firstly made from VOSO<sub>4</sub>·xH<sub>2</sub>O (99.9% Alfa Aesar) and H<sub>2</sub>SO<sub>4</sub> (96%, Alfa Aesar). Electrolyte solutions containing 2 mol·dm<sup>-3</sup> V<sup>3+</sup> or VO<sub>2</sub><sup>+</sup> were made by electrolysis from the raw electrolyte. Electrolyte solutions with 2 mol·dm<sup>-3</sup> V<sup>x+</sup> (V<sup>3+</sup>, VO<sup>2+</sup> or VO<sub>2</sub><sup>+</sup>) were dilute by 5 mol·dm<sup>-3</sup> H<sub>2</sub>SO<sub>4</sub> to make solutions with 0.25, 0.50, 0.75, 1.00, 1.25, 1.50 and 1.75 mol·dm<sup>-3</sup> vanadium and 5 mol·dm<sup>-3</sup> total sulfate or bisulfate.

### ***5.2.2 Membrane Equilibration and Conductivity Measurement***

Nafion conductivity was measured after membrane samples were equilibrated in electrolyte solutions to investigate influence of the electrolyte on proton transport in the membrane. Before conductivity measurement, pretreated Nafion samples (1 × 5 cm) were soaked in respective electrolyte solution for 72 hours to achieve electrolyte partitioning equilibrium. After equilibration, the membrane was taken out from electrolyte solution, and wiped with a Kimwipe to remove all liquid droplets on the surface. The membrane was mounted on a four-electrode conductivity cell to measure the high frequency resistance between. Membrane conductivity can be calculated from this measured high frequency resistance and its dimensions:

$$\sigma = \frac{l}{R \cdot \delta \cdot W} \quad (5-1)$$

$R$  is measured membrane's high frequency resistance between two electrodes;  $l$  is membrane's length between two reference electrodes;  $\delta$  is membrane thickness;  $W$  is membrane width.

### ***5.2.3 Electrolyte Species Contents in Membrane***

Electrolyte species contents in Nafion were measured after membrane had been equilibrated in the same protocol described in previous section. To record the membrane's total weight after equilibration, membrane's weight,  $m_{total}$  was measured by an analytical balance (Sartorius CPA224S) after liquid droplets on membrane surface was removed by Kimwipe. Each membrane sample then was soaked in 20 mL 3% nitric

acid (Fisher Scientific) for at least 72 hours to extract vanadium ions and sulfuric acid. After extraction, sulfuric acid and vanadium concentrations in nitric acid were measured by a Perkin Elmer 2100DV inductively couple plasma optical emission spectrometer (ICP-OES). The equipment was calibrated by a standard solutions series made from a vanadium standard (1000ppm,  $V_2O_5$  in 2%  $HNO_3$ , Ricca Chemical), a sulfur standard (1000ppm,  $(NH_4)_2SO_4$  in  $H_2O$ , Ricca Chemical) and nitric acid (Fisher Scientific). An extracted membrane was boiled in DI water to remove remaining vanadium and sulfuric acid, and then dehydrated in a vacuum oven at  $90^\circ C$  for at least 12 hours. The membrane dry weight was recorded as  $m_{membrane}$ . Water content in membrane in equilibrium can be calculated:

$$m_{H_2O} = m_{total} - m_{V^{x+}} - m_{H_2SO_4} \quad (5-2)$$

## 5.3 Results and Discussion

### 5.3.1 Vanadium and Water Uptake in Nafion in Dilute $HCl/VCl_3$ Solutions

$V^{3+}$  and water content in Nafion equilibrated in dilute  $VCl_3/HCl$  solutions are presented in Figure 5-1, with comparison to  $VO^{2+}$  partitioning and corresponding water content reported in the literature.<sup>30</sup> Since the environmental  $Cl^-$  concentration is just  $0.1 \text{ mol}\cdot\text{dm}^{-3}$ , it was assumed that there was at most a trace amount of  $Cl^-$  entering membrane because of Donnan exclusion<sup>202</sup>.  $V^{3+}$  content in membrane is higher than expected based on its proportion of the solution concentration. This indicates that  $V^{3+}$  has partitioning behavior stronger than proton in Nafion, as high as reported for  $VO^{2+}$ . High  $V^{3+}$



partitioning suggests that sulfonate in membrane has a higher preference for  $V^{3+}$  than proton. This phenomenon is consistent with the general reported observation that multivalent cations have stronger partitioning than proton in membrane.<sup>30,212,230,231</sup> The cause of this higher preference for multivalent cations can be explained by the electrostatic force between sulfonate and cations.<sup>30,212,230,231</sup> Since electrostatic attraction between multivalent cations and sulfonate is stronger than that of proton, multivalent cations bind with sulfonate more favorably than protons. Although it has been demonstrated that factors, other than valence, e.g. ionic size, can influence the cation partitioning competition in Nafion, valence state is more significant for multivalent cations than monovalent cations.<sup>220,221</sup> In Figure 5-1, the relative content of  $V^{3+}$  and  $VO^{2+}$  in membrane,  $x_{VM} = z(V^{x+})n(V^{x+})/n(-SO_3H)$ , are very close in the trend and magnitude corresponding to vanadium relative content in solution phase. Partitioning behavior of  $V^{3+}$  is not substantially stronger than  $VO^{2+}$ , although  $V^{3+}$  has higher ionic charge than  $VO^{2+}$ . Because the vanadium atom has +4 valence in  $VO^{2+}$ , the attractive force between  $VO^{2+}$  and sulfonate can be strong enough to maintain its partitioning effect as high as  $V^{3+}$ . More plausible is the fact that  $V^{3+}$  has a more strongly held and saturated first hydration shell than does  $VO^{2+}$ .

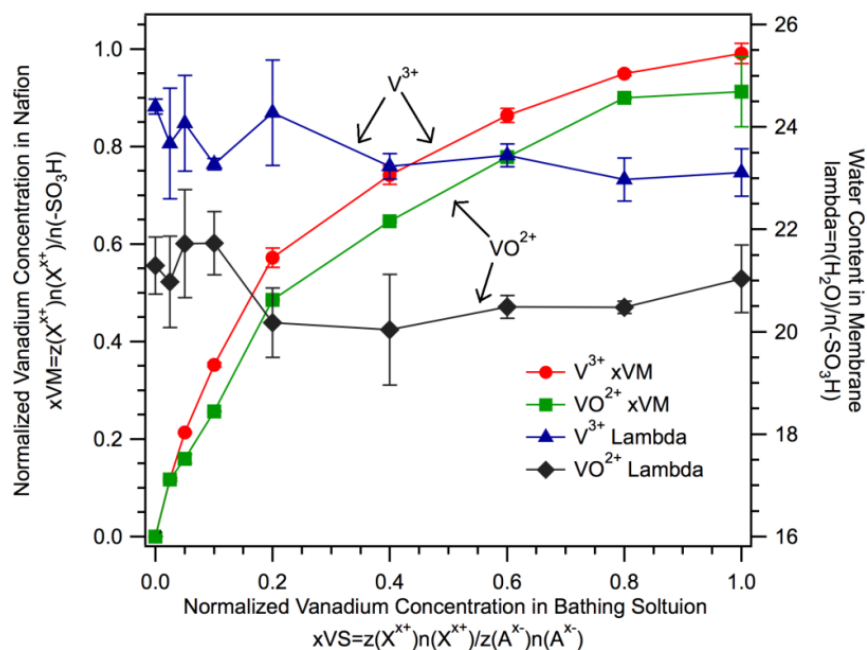


Figure 5–1. Normalized vanadium content in membrane with respect to normalized vanadium concentration in solution phase.  $V^{3+}$  and  $VO^{2+}$  have very close partitioning capability in Nafion; Both of  $V^{3+}$  and  $VO^{2+}$  are preferentially bonded by sulfonate in Nafion.  $VO^{2+}$  results are from literature.<sup>30</sup>

$V^{3+}$  presence in Nafion has limited influence on water content in membrane, as is seen in Figure 5-1. The indicator used to quantify water content in membrane is  $\lambda = n_{H_2O}/n_{-SO_3H}$ . Both  $V^{3+}$  and  $VO^{2+}$  has high affinity for sulfonate in membrane, but they do not significantly reduce membrane water content.<sup>30</sup> The low water reduction extent and high affinity for Nafion of vanadium ions is contradictory to the observation that water content loss is accordant to cation affinity to membrane.<sup>211,212,232</sup> This contradiction suggests that cationic affinity to membrane is not the only dominating factor to determine water uptake of the membrane in the cation form. Although less pore volume in the

membrane might result from deswelling due to partitioning of multivalent cations,  $V^{3+}$  and  $VO^{2+}$  have the ability to maintain a high hydration level inside membrane.<sup>233</sup> Since  $V^{3+}$  and  $VO^{2+}$  have +3 and +4 valence on the core vanadium atom, a strong electrostatic force of cation-water dipole attraction in the vanadium aqua complex can help to maintain high water content in the membrane.

### ***5.3.2 Conductivity of Nafion in Dilute HCl/VCl<sub>3</sub> Solutions***

After being equilibrated in dilute  $VCl_3/HCl$  solutions, Nafion conductivity was sharply reduced by  $V^{3+}$  presence in equilibrium, as is shown in Figure 5-2. With  $V^{3+}$  concentration increasing in the bathing electrolyte solutions, Nafion loses its conductivity sharply, as is the case with  $VO^{2+}$  in the environment.<sup>30</sup> Since the water content in the membrane was not changed by the presence of  $V^{3+}$ , proton and cation mobility cannot be directly reduced by loss of water content. The conductivity loss caused by  $V^{3+}$  is lower than the loss caused by  $VO^{2+}$  in the environment. The difference between vanadium ions effect of lowering membrane conductivity is due to different patterns of vanadium ions influencing proton motion.<sup>30</sup> The detail is going to be discussed below.

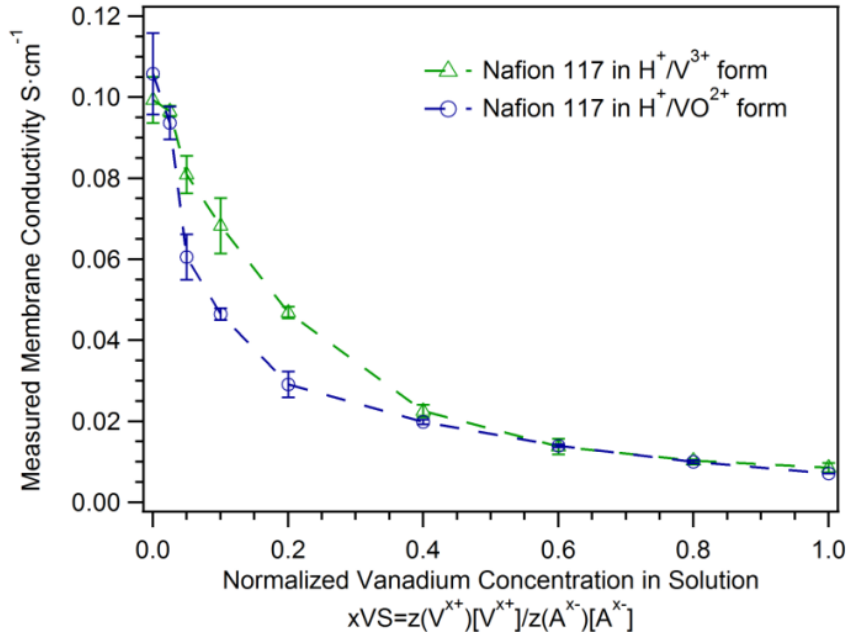


Figure 5–2. Nafion conductivity loss is caused by vanadium ions presence in the environmental solution. The reduction caused by V<sup>3+</sup> is lower than VO<sup>2+</sup>.

The conductivity loss is caused by the lowered proton concentration and slow proton motion in membrane. In Figure 5-3, Nafion conductivities are plotted vs. vanadium contents in membrane. As has been proved, proton mobility in Nafion can be linearly reduced by VO<sup>2+</sup> presence in membrane, so Nafion conductivity is dependent on VO<sup>2+</sup> content in a concave pattern<sup>30</sup>. Nafion conductivity is linearly dependent on V<sup>3+</sup> content in membrane, so it is reasonable to assume that both proton and V<sup>3+</sup> have constant mobility in the H<sup>+</sup>/V<sup>3+</sup> form Nafion. Membrane's conductivity consists of transference of proton and V<sup>3+</sup>:

$$\sigma = F(z_{\text{H}^+}c_{\text{H}^+}u_{\text{H}^+} + z_{\text{V}^{3+}}c_{\text{V}^{3+}}u_{\text{V}^{3+}}) \quad (5-3)$$

Here,  $F$  is Faraday Constant,  $96500\text{C}\cdot\text{mol}^{-1}$ ;  $z$  is charge number;  $c$  is concentration in membrane phase,  $\text{mol}\cdot\text{cm}^{-3}$ ;  $u$  is mobility,  $\text{cm}^2\cdot\text{V}^{-1}\cdot\text{s}^{-1}$ . The normalized content fraction  $x_M = z_M c_M / c_{-SO_3H}$  is introduced into equation 5-3:

$$\sigma = F c_{-SO_3H} (x_{H^+} u_{H^+} + x_{V^{3+}} u_{V^{3+}}) \quad (5-4)$$

$c_{-SO_3H}$  is calculated from the density measurement of fully hydrated proton form Nafion, and assumed to be invariant with vanadium content.<sup>30</sup> Mobilities of proton and  $V^{3+}$  can be calculated from membrane conductivity and uptake measurement:  $u_{H^+} = 8.23 \times 10^{-4} \text{cm}^2 \cdot \text{V}^{-1} \cdot \text{s}^{-1}$  and  $u_{V^{3+}} = 6.36 \times 10^{-5} \text{cm}^2 \cdot \text{V}^{-1} \cdot \text{s}^{-1}$ .  $V^{3+}$  mobility is very similar to  $VO^{2+}$  mobility reported in previous work,<sup>30</sup>  $u_{VO^{2+}} = 6.28 \times 10^{-5} \text{cm}^2 \cdot \text{V}^{-1} \cdot \text{s}^{-1}$ . The modeled Nafion conductivity from the calculated mobilities has good consistency with measured results, as is shown in Figure 5-3.

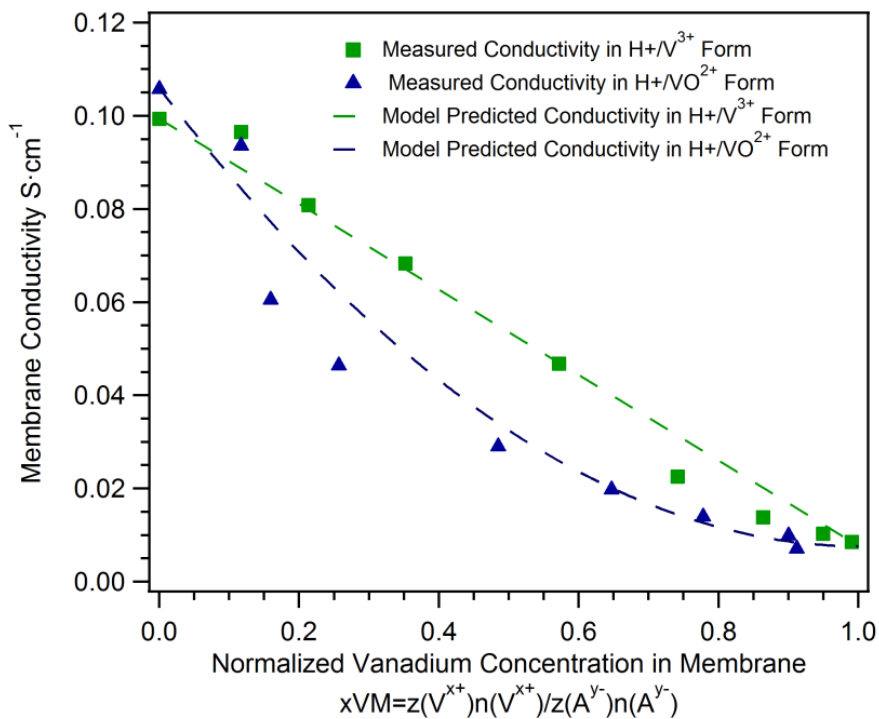


Figure 5–3. Nafion conductivity is differently dependent on  $V^{3+}$  or  $VO^{2+}$  concentration in membrane phase.  $VO^{2+}$  can slow down proton motion in membrane to carry charge, while  $V^{3+}$  does not have such an impact on proton. Both  $V^{3+}$  and  $VO^{2+}$  have very low mobility compared to proton in a well hydrated membrane.

The water structure in hydration shells of vanadium ions is of great interest to clarify the higher water content in  $V^{3+}$  and  $VO^{2+}$  form Nafion and  $VO^{2+}$  interference on proton transport in membrane. The reason for the different cation-proton interactions has not been satisfactorily explained yet, but it should be related to the cation interference on state of water in ionic domain. It has been suggested that proton transport in Nafion was facilitated by the fast water self-exchange in the primary hydration shell on the cations.<sup>212</sup>  $V(H_2O)_6^{3+}$  has water self-exchange rate constant about  $5 \times 10^2 \text{ s}^{-1}$ , which is close to that of

$\text{Fe}(\text{H}_2\text{O})_6^{3+}$ ,  $1.6 \times 10^2 \text{ s}^{-1}$ ,<sup>212,234</sup> but  $\text{Fe}^{3+}$  has severe decelerating effect on proton, while  $\text{V}^{3+}$  has no interference on proton transport. In  $\text{VO}(\text{H}_2\text{O})_5^{2+}$ , because water has self-exchange rate constant  $5 \times 10^2 \text{ s}^{-1}$  on the equatorial positions and  $\sim 10^9 \text{ s}^{-1}$  on the axial position, the overall water self-exchange is faster than that in  $\text{V}(\text{H}_2\text{O})_6^{3+}$ . So the water self-exchange kinetic in the first hydration shell of cation is not the main reason for the cation slowing down proton transport in Nafion. It has been demonstrated that high valence cations, like  $\text{Al}^{3+}$ , can form stable hydration shells beyond the first hydration shell by H-bonding.<sup>235–</sup>  
<sup>237</sup> Cations with higher valence can have more ordered hydration shells and stronger restriction on water molecules in hydration shell. It has been proved that water in the hydration shells of multivalent cation is more condensed than bulk water.<sup>237</sup> With high valence state,  $\text{V}^{3+}$  and  $\text{VO}^{2+}$  can constraint water in its hydration shell strongly enough to overcome the deswelling effect caused by cation uptake, thereby maintaining a higher hydration level in membrane. The water molecules in hydration shells around  $\text{VO}^{2+}$ , especially outer ones, would have lowered availability to favor proton transport, because of the high valence state in  $\text{VO}^{2+}$ .

### ***5.3.3 Conductivity of Nafion in Concentrated Vanadium/Sulfuric Acid Solutions***

Vanadium ions can reduce the membrane conductivity in the equilibrium including membrane, water, sulfuric acid and vanadium ions. Nafion conductivity after being equilibrated in concentrated electrolyte is presented in Figure 5-4, showing a descending trend with increasing vanadium concentration in solution. The vanadium ( $0\text{--}2 \text{ mol}\cdot\text{dm}^{-3}$ ) and sulfuric acid ( $5 \text{ mol}\cdot\text{dm}^{-3}$ ) were concentrated enough to overcome Donnan exclusion

for anion to form a polymer-vanadium-sulfuric acid equilibrium in membrane phase. Nafion samples show similar conductivity at a given vanadium concentration of the bathing electrolyte solutions regardless of the different valence state. Although this coincidence could be a comprehensive result of several factors, it can still provide great convenience to rapidly estimate Nafion conductivity in VRFB system, according to electrolyte conditions.

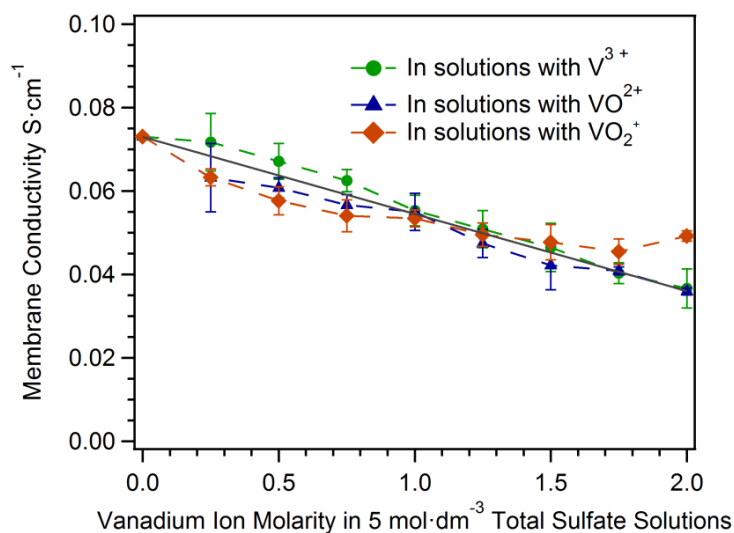


Figure 5–4. Nafion conductivity after being equilibrated in electrolyte solutions with vanadium in +3, +4 and +5 valence. The vanadium ion concentration in solutions is 0 to 2 mol·dm<sup>-3</sup>; the total sulfuric acid/ bisulfate/ sulfate concentration is 5 mol·dm<sup>-3</sup>.

### 5.3.4 Uptakes in Nafion in Concentrated Vanadium/Sulfuric Acid Solutions

The water and sulfuric acid contents in Nafion equilibrated concentrated electrolyte solutions are very consistent with vanadium concentration results. The measured water



and sulfuric acid content in concentrated electrolyte equilibrated samples are shown in Figure 5-5. As has been proved, membrane water and sulfuric acid content are largely controlled by the acid concentration in the electrolyte environment.<sup>30,200,201,203</sup> In dilute electrolyte equilibration,  $\text{VO}^{2+}$  and  $\text{V}^{3+}$  cannot significantly change water content in membrane.<sup>30</sup> In the concentrated electrolyte scenario, the consistent water and sulfuric acid contents corresponding to changing vanadium concentration suggest that vanadium ions do not affect membrane deswelling in the presence of large amount of sulfuric acid. This is consistent with the observation on vanadium concentration influence on vanadium permeation across Nafion.<sup>32</sup> It was illustrated that vanadium permeation, or diffusion, is mainly controlled by sulfuric acid concentration in the electrolyte.<sup>32</sup> These behaviors are suggesting that sulfuric acid is the primary factor determining Nafion deswelling, which in turn controls the size of ionic clusters controlling uptake of electrolyte species and vanadium crossover. The extent of the vanadium effect on membrane swelling is similarly weak as its effect on crossover, and can be explained by sulfuric acid.

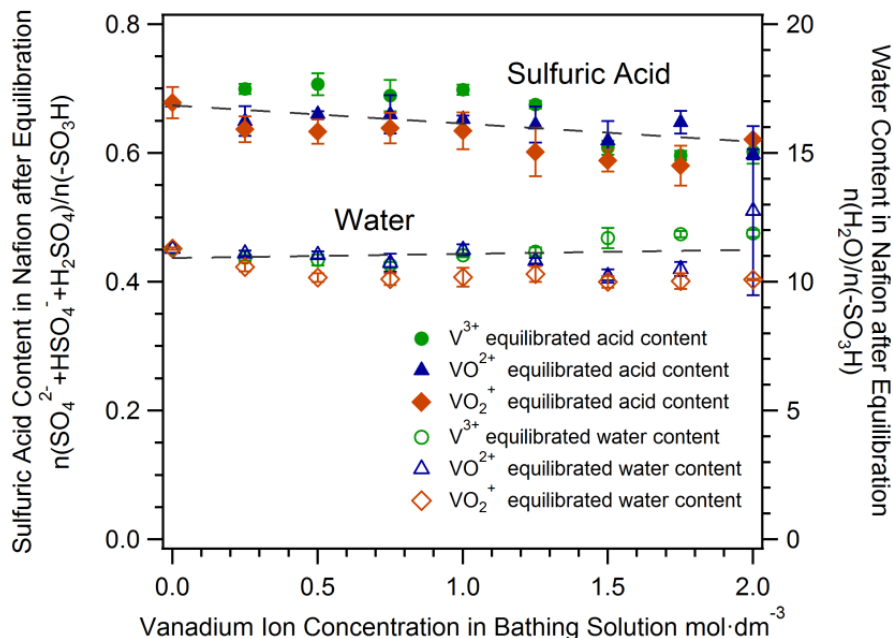


Figure 5–5. Water and sulfuric acid contents in Nafion equilibrated in concentrated electrolyte solutions (vanadium 0 to 2 mol·dm<sup>-3</sup>; total sulfate 5 mol·dm<sup>-3</sup>). The water and sulfuric acid contents are invariant with environmental vanadium concentration.

Vanadium ion partitioning in Nafion is highly dependent on the apparent charge number of the cation. The vanadium ion content in Nafion equilibrated in concentrated electrolyte is presented in Figure 5-6. All three vanadium ion contents in Nafion are nearly proportional to vanadium concentration in the electrolyte solutions. V<sup>3+</sup> and VO<sup>2+</sup> have similar partitioning extents in Nafion, both stronger than VO<sub>2</sub><sup>+</sup>. V<sup>3+</sup> and VO<sup>2+</sup> have higher partitioning in Nafion than VO<sub>2</sub><sup>+</sup> because cations with higher valence usually has higher affinity to sulfonate in membrane.<sup>212,220,221,232</sup> V<sup>3+</sup> and VO<sup>2+</sup> have high positive charge to generate stronger electrostatic attraction to sulfonate. Although VO<sup>2+</sup> has lower apparent charge number than V<sup>3+</sup>, VO<sup>2+</sup> can still have similar affinity to V<sup>3+</sup>, because it

has a vanadium atom with +4 valence in the oxo complex. The affinity of  $\text{VO}^{2+}$  for sulfonate can be due to the high positive charge on vanadium atom in it.

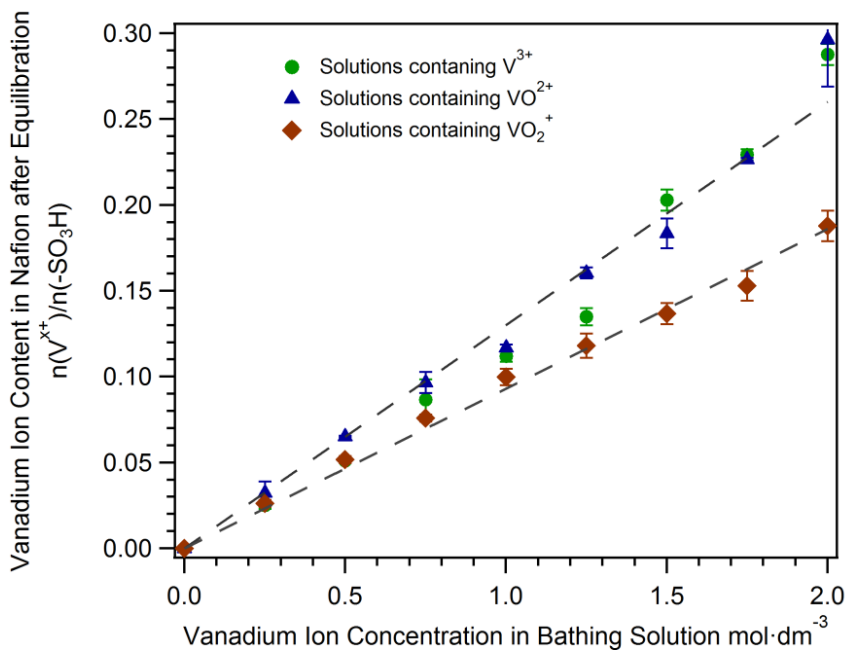


Figure 5–6. Vanadium ion content in Nafion being equilibrated in concentrated electrolyte solutions with  $\text{V}^{3+}$ ,  $\text{VO}^{2+}$  or  $\text{VO}_2^+$ .  $\text{V}^{3+}$  and  $\text{VO}^{2+}$  have stronger partitioning in Nafion than  $\text{VO}_2^+$ .

### 5.3.5 Analysis of Nafion Conductivity in Concentrated Equilibration Scenario

Vanadium ion in Nafion is the main reason for membrane conductivity loss after being equilibrated in the concentrated electrolyte. Nafion conductivity is comprehensively influenced by interaction among polymer and all electrolyte species. Nafion conductivity is highly determined by its water content, because proton transport is

favored by abundant water as a mediator.<sup>84,85,121,238</sup> With acid presence in the membrane, the proton concentration can be enhanced by dissociation of acid.<sup>30,200,201,203</sup> Cations in the membrane can simply reduce proton concentration, or even interfere with proton transport.<sup>211,212,239</sup> Since the equilibrium in Nafion with concentrated electrolyte solutions includes all these factors (water, acid and cations) the analysis of Nafion conductivity in concentrated electrolyte is complicated.

Vanadium uptake in Nafion can reduce the amount of proton and water content available for proton transport intermediation. It has been demonstrated that sulfuric acid and sulfonic acid in Nafion can fully dissociate<sup>30</sup>, so the charge balance is:

$$n_{H^+} + z_{V^{x+}}n_{V^{x+}} = n_{H_2SO_4} + n_{-SO_3H} \quad (5-5)$$

Vanadium ions in Nafion can reduce the content of protons for charge transport. The relative proton concentration  $n_{H^+}/n_{-SO_3H}$  is presented in Figure 5-7.

Water content in Nafion equilibrated in the concentrated solution scenario is corrected by vanadium hydration coordination and extra sulfuric acid. Because of the hydration of vanadium ions, it is assumed that water molecules in the first hydration shell of vanadium ions cannot take part in proton transfer. Water content available for proton transport is reduced:  $n'_{H_2O} = n_{H_2O} - n_{V^{x+}} \times n_{V^{x+}}^{hydration}$ . Here  $n_{V^{x+}}^{hydration}$  is the hydration number of vanadium ions in their first hydration shells; its value is 6,5,3 for  $V^{3+}$ ,  $VO^{2+}$  and  $VO_2^+$  respectively.<sup>138,234</sup> Because of high hydrophobicity of bisulfate, we assume water can be similarly coordinated by sulfonate and bisulfate in ionic domain in membrane. The corrected water content is symbolized as  $\lambda'$  and shown in Figure 5-7:

$$\lambda' = \left( \lambda - n_{V^{x+}}^{hydration} \frac{n_{V^{x+}}}{n_{-SO_3H}} \right) / \left( 1 + \frac{n_{H_2SO_4}}{n_{-SO_3H}} \right) \quad (5-6)$$

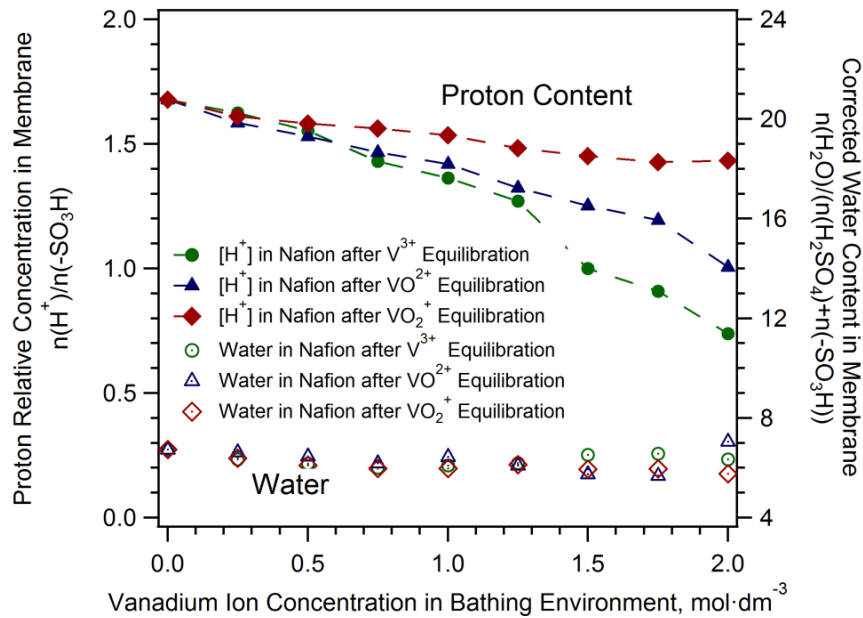


Figure 5–7. Proton content and corrected water content in Nafion after equilibration. Proton is provided by sulfuric and sulfonic acid dissociation and reduced by vanadium replacement. Water content is corrected by vanadium aqua-coordination and extra sulfuric acid.

In the presence of sulfuric acid,  $VO_2^+$  and  $VO_2^+$  can influence proton transport in Nafion, while  $V^{3+}$  does not interfere with proton mobility. One modeling analysis was carried out by assuming that proton mobility does not change in the presence of vanadium. It has been shown that proton mobility is a linear function of water content in Nafion equilibrated with sulfuric acid.<sup>30</sup> One empirical function is fitted from the proton mobility dependence on water content:

$$u_{H^+} = (6.88\lambda' - 12.5) \times 10^{-5} \text{ cm}^2 \cdot \text{V}^{-1} \cdot \text{s}^{-1} \quad (5-7)$$

The proton transference number can be calculated by the modeled proton mobility:

$$t_{H^+} = \frac{F c_{H^+} u_{H^+}}{\sigma_{measured}} = \frac{F \cdot c_{-SO_3H} u_{H^+}}{\sigma_{measured}} \left( \frac{n_{H^+}}{n_{-SO_3H}} \right) \quad (5-8)$$

$c_{-SO_3H}$  is the sulfonate concentration in Nafion equilibrated in 5 mol·dm<sup>-3</sup> sulfuric acid solution.  $c_{-SO_3H}$  equals  $1.39 \times 10^{-3} \text{ mol} \cdot \text{cm}^{-3}$ , according to the Nafion density measurement.<sup>30</sup>  $c_{-SO_3H}$  is assumed to be constant over the entire vanadium concentration range in the experiment. The calculated proton transference numbers are presented in Figure 5-8. Clearly, with no-cation-interference assumption, proton coexisting with V<sup>3+</sup> has a decreasing transference number lower than one. This suggests that in the concentrated electrolyte scenario, V<sup>3+</sup> in Nafion does not influence proton transfer, similar to that in the dilute electrolyte equilibration case. The V<sup>3+</sup> mobility can be calculated,  $(6.30 \pm 0.8) \times 10^{-5} \text{ cm}^2 \cdot \text{V}^{-1} \cdot \text{s}^{-1}$ , with the assumption that anion transference number in Nafion is negligible.<sup>30,200,201</sup> The V<sup>3+</sup> mobility is very close to V<sup>3+</sup> mobility in the dilute electrolyte equilibration case. However, the proton transference number exceeds unity when it is coexisting in the membrane with VO<sup>2+</sup> or VO<sub>2</sub><sup>+</sup>. This means that proton's mobility was overestimated with no-vanadium-interference assumption or that the no-interference assumption is only valid for V<sup>3+</sup>. Like the VO<sup>2+</sup> influence on proton mobility in dilute electrolyte equilibrium,<sup>30</sup> VO<sup>2+</sup> and VO<sub>2</sub><sup>+</sup> can reduce proton mobility by their presence in Nafion.

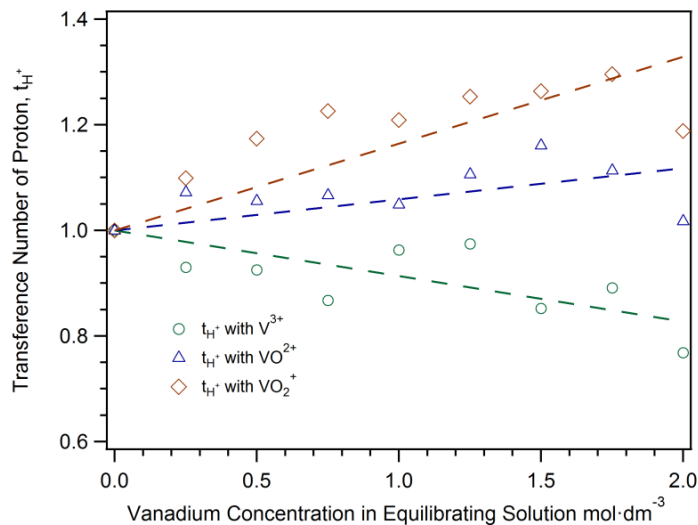


Figure 5–8. Proton transference number in Nafion with coexistence of vanadium ions ( $V^{3+}$ ,  $VO^{2+}$  or  $VO_2^+$ ) in concentrated electrolyte equilibration. The proton mobility is assumed to be only dependent on membrane's corrected water content.<sup>30</sup>

$VO_2^+$  has a decelerating effect on proton that is stronger than  $VO^{2+}$ . Since  $V^{3+}$  has the very similar mobility in Nafion equilibrated with dilute or concentrated electrolyte, in this case, we presume  $VO^{2+}$  has mobility,  $6.28 \times 10^{-5} \text{ cm}^2 \cdot \text{s}^{-1} \cdot \text{V}^{-1}$ , identical to its mobility in the dilute electrolyte equilibrated Nafion. Concerning the mobility of  $VO_2^+$  in Nafion, there is no literature report yet. So we assume that vanadium ions' mobility and diffusivity satisfy Einstein-Smoluchowski equation<sup>240</sup>:  $u_j \propto |z_j| D_j$ . The mobility of  $VO_2^+$  can be derived from the diffusivities of vanadium ions reported in literature<sup>89</sup>. The derived mobility of  $VO_2^+$  is  $3.0 \times 10^{-5} \text{ cm}^2 \cdot \text{s}^{-1} \cdot \text{V}^{-1}$ . Proton mobility can be calculated by the relation between conductivity and mobility:

$$u_{H^+} = \frac{(\sigma - Fz_V x + c_V x + u_V x)}{F c_{H^+}} \quad (5-9)$$

The calculated proton mobility is dependent on the  $VO^{2+}$  or  $VO_2^+$  content in Nafion, as is presented in Figure 5-9. Obviously, the decelerating effect of  $VO_2^+$  is stronger than that of  $VO^{2+}$ . As has been discussed above, proton mobility loss due to  $VO^{2+}$  or  $VO_2^+$  can be caused by water motion constraint by cations in their hydration shells, primarily the water molecules beyond the first hydration shell. Because,  $VO_2^+$  has higher valence on the vanadium atom, it can have stronger H-bond restriction in its hydration shells<sup>241</sup>. So,  $VO_2^+$  exhibits a stronger retarding influence on proton transport.

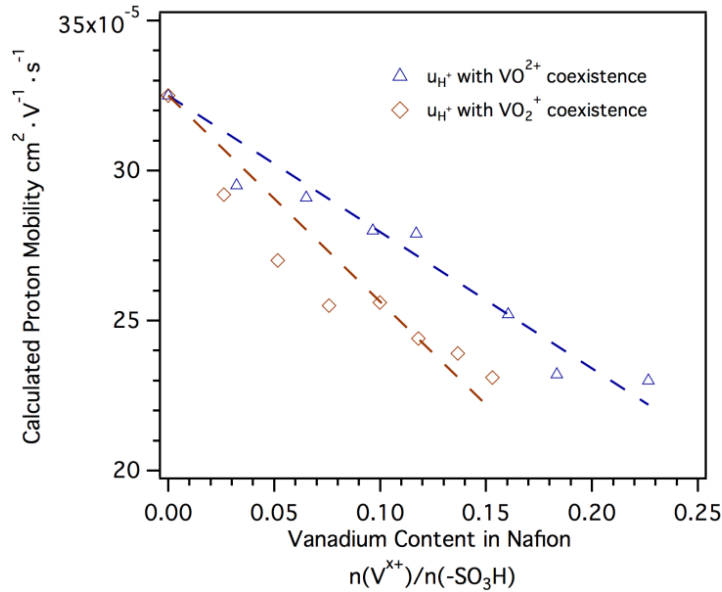


Figure 5–9.  $VO^{2+}$  and  $VO_2^+$  can retard proton transfer in Nafion.  $VO_2^+$  has a stronger interference than  $VO^{2+}$  on proton motion.



## 5.4 Conclusion

Nafion ionic conduction and properties in polymer-electrolyte solution equilibrium have been investigated. In equilibration with vanadium/sulfuric acid electrolyte solutions, the membrane behaves a strong affinity to  $V^{3+}$  ion, similar to that for  $VO^{2+}$ . This can be a result of strong electrostatic attraction between  $V^{3+}$  and sulfonate because of higher valence on vanadium. Because  $V^{3+}$  has a mobility,  $6.36 \times 10^{-5} cm^2 \cdot V^{-1} \cdot s^{-1}$ , much slower than that of proton  $8.23 \times 10^{-4} cm^2 \cdot V^{-1} \cdot s^{-1}$ , Nafion containing  $V^{3+}$  loses conductivity due to reduced proton content.  $VO^{2+}$  and  $VO_2^+$  can cause proton mobility loss in membrane with equilibration in concentrated vanadium/sulfuric acid electrolyte. However, the mechanism of proton mobility loss in coexistence with  $VO^{2+}$  and  $VO_2^+$  has not been definitively determined.

**CHAPTER 6**

**SULFONATED DIELS ALDER POLY(PHENYLENE) MEMBRANE**

**CHARACTERIZATION AS ELECTROLYTE SEPARATOR FOR VANADIUM**

**REDOX FLOW BATTERY**

**6.1 Introduction**

Hydrocarbon aromatic cation exchange membranes are attracting attention from VRFB researchers because their performance is comparable to Nafion in electrochemical devices.<sup>117,118</sup> Aromatic cation exchange membranes are generally developed from thermoplastics by sulfonation, resulting in high chemical/thermal stability, good mechanical properties and low cost.<sup>119–121</sup> Several cation exchange membranes have been synthesized and tested in flow battery setups; sulfonated poly(ether ether ketone) (SPEEK),<sup>99,120</sup> sulfonated poly(phenylsulfone) (S-Radel),<sup>95,96,242</sup> sulfonated poly(thioether ketone) series (SPTK or SPTKK)<sup>127</sup> and sulfonated Diels Alder poly(phenylene) (SDAPP)<sup>100</sup>.

Sulfonated Diels Alder poly(phenylene) (SDAPP) was initially synthesized as a proton exchange membrane for PEM fuel cells.<sup>243</sup> SDAPP performance as a fuel cell membrane has been studied as has SDAPPs conductivity, permeability and water uptake properties.<sup>244</sup> A preliminary investigation has been done on SDAPP as an electrolyte separator in VRFBs.<sup>100</sup> The SDAPP membrane can achieve very high ionic selectivity to provide comparable conductivity to Nafion and also lower  $\text{VO}^{2+}$  permeability.

Membranes with higher IEC had higher ionic conductivity, but lower durability in both battery environment and electrolyte solutions.

In this chapter, acid and water uptake by SDAPP were examined to determine its impact on the membrane ionic transport properties as it relates in VRFBs. As a reference, Nafion 117 was tested in parallel. The molecular formulas of SDAPP and Nafion are displayed in Figure 6-1. The sulfuric acid and water uptake properties of SDAPP were quantitatively measured after equilibration in sulfuric acid solutions with concentration ranging between 0 to 17.4 mol·kg<sup>-1</sup>. After equilibration, the membrane conductivity was also measured to investigate the electrolyte-polymer equilibrium influence on the membrane ion transport. Vanadium permeation in SDAPP was measured under different conditions (acid concentration or temperature) to study the influence of these conditions on vanadium transport. Transmission electron microscopy work was carried out to study the morphology of SDAPP and ionic domain distribution and sizing.

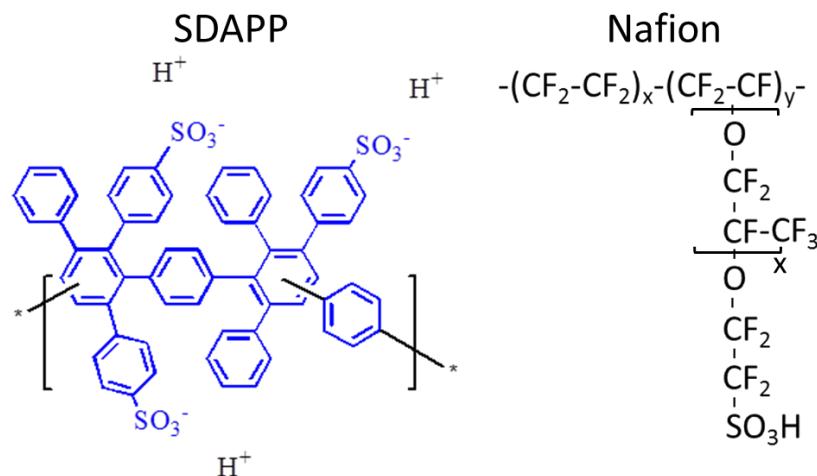


Figure 6–1. The molecular structures of SDAPP and Nafion. SDAPP is a short side-chained sulfonated poly(phenylene); Nafion is a long side-chained sulfonated tetrafluoroethylene based copolymer.

## 6.2 Experimental

### 6.2.1 Membrane Preparation and Characterization

Sulfonated Diels Alder poly(phenylene) (SDAPP) membranes at various ion exchange capacities were synthesized as reported previously.<sup>243</sup> The ion exchange capacity (IEC) of the SDAPP polymer was tuned by the stoichiometry of the sulfonating agent (chlorosulfuric acid) of Diels Alder poly(phenylene). The membranes were cast from a solution of 5 wt.% polymer in dimethylacetamide (DMAc) onto a bordered glass plate. After synthesis and protonation, the membranes were stored in deionized water (Milli Q, 18.0 MΩ) for future characterization and measurement. Ion exchange capacity (IEC) of the SDAPP membranes was determined by the back titration method reported in

literature.<sup>243</sup> Membrane density,  $\rho$  was calculated from membrane weight measurement and membrane dimensions:

$$\rho = \frac{m}{a^2\delta} \quad (6-1)$$

$m$  is measured membrane weight;  $a$  is the length of edge of membrane;  $\delta$  is the thickness of membrane.

Nafion 117 was purchased from Ion Power Inc. and was characterized in parallel for comparison. Before being testing Nafion 117 was conditioned by pretreated in 3% H<sub>2</sub>O<sub>2</sub> (Fisher Scientific), DI water, 1 mol·dm<sup>-3</sup> H<sub>2</sub>SO<sub>4</sub> (Alfa Aesar) and DI water for 1 hour at 85°C to remove residual organic and metallic impurity. Pretreated Nafion samples were then kept in DI water until future use.

### ***6.2.2 Acid and Water Uptake after Equilibration in Aqueous Sulfuric Acid***

Sulfuric acid and water uptake in SDAPP and Nafion were measured after equilibration in sulfuric acid solutions of different concentrations. Pretreated proton forms of SDAPP and Nafion were first soaked in aqueous sulfuric acid solutions with concentrations ranging from 0 to 17.4 mol·kg<sup>-1</sup> for 72 hours to reach solution-polymer equilibrium. After equilibration, membrane samples were taken out of solution and their saturated weight was measured as  $m_{total}$ . Saturated membrane samples were then boiled in DI water to transfer all sulfuric acid into the aqueous phase. The sulfuric acid content in water was titrated by a Mettler Toledo DL15 autotitrator with 0.1 mol·dm<sup>-3</sup> NaOH titrant. Each membrane dry weight was measured after the boiled membrane was

dehydrated in a vacuum oven for 3 hours at 90°C. Water content in membrane after equilibration in sulfuric acid can be calculated by:

$$m_{\text{H}_2\text{O}} = m_{\text{total}} - m_{\text{H}_2\text{SO}_4} - m_{\text{membrane,dry}} \quad (6-2)$$

The water content in pure water-equilibrated membranes was indexed as the molar ratio of water to sulfonic acid groups in membrane, symbolized as  $\lambda = n_{\text{H}_2\text{O}}/n_{-\text{SO}_3\text{H}}$ .<sup>84</sup>

### 6.2.3 Membrane Conductivity in Acidic Electrolyte

Before conductivity measurements, membrane samples were equilibrated in sulfuric acid solutions using the same protocol as described previous section. The membrane conductivity was measured by electrochemical impedance spectroscopy on a four electrode conductivity cell.<sup>30,243,244</sup> Before measurement, the membrane sample was taken out from the soaking solution, wiped to remove all liquid droplets on the membrane surface and mounted on the conductivity cell. The membrane resistance between two detecting electrodes was equal to the high frequency resistance. The high frequency resistance was determined by the intersection of the impedance spectrum with the real impedance axis in EIS. The membrane conductivity was calculated from the measured membrane resistance and its corresponding dimensions:

$$\sigma = \frac{L}{R \cdot w \cdot \delta} \quad (6-3)$$

Here,  $L$  is the length between two detecting electrodes;  $w$  is the width of membrane samples;  $\delta$  is membrane thickness. Membrane width and thickness were respectively

measured by a Fisherbrand digital calipers and Mitutoyo 543-696 micrometer.

#### **6.2.4 VO<sup>2+</sup> Permeation as a Function of Sulfuric Acid Concentration**

To mimic the actual electrolyte in VRFB, and understand the role of sulfuric acid concentration in impacting VO<sup>2+</sup> permeability across the SDAPP membrane, VO<sup>2+</sup> permeability was measured in the presence of sulfuric acid. The principle of this measurement has been reported in elsewhere.<sup>32,245</sup> VO<sup>2+</sup> permeability was measured using electron paramagnetic resonance (EPR) by flowing solution from a 5 cm<sup>2</sup> cross sectional area battery hardware (Fuel Cell Technology) with an empty flow field through the ESR cavity. During the measurement, VO<sup>2+</sup> rich solution was placed on one side of the battery, while a receiving solution of the same volume with no VO<sup>2+</sup> was circulated on the other side of the separator. The volume of the solutions on both sides was 20 mL. The temperature of the cell was stabilized at 30°C by a cartridge heater. The cavity of a Magnettech Miniscope ESR (Berlin, Germany) was built in the tubing line on the receiving side to monitor VO<sup>2+</sup> accumulation caused by its crossover from the rich side. The concentration ratio of VO<sup>2+</sup> and H<sub>2</sub>SO<sub>4</sub> in the given solution was controlled at 1:5 and the acid concentration on both sides ranged 0.5 to 5 mol·dm<sup>-3</sup>. The governing equation of mass balance in this diffusion process is:

$$V \frac{dc_{receiving}}{dt} = PA \left( \frac{c_{giving} - c_{receiving}}{\delta} \right) \quad (6-4)$$

The permeability  $P$  can be calculated by:

$$P = -\frac{V\delta}{2At} \ln\left(\frac{c_{giving}^{t=0} - 2c_{receiving}^t}{c_{giving}^{t=0}}\right) \quad (6-5)$$

Where  $P$  is the measured membrane permeability;  $V$  is the volume of solution on either side of the battery;  $A$  is the cross sectional area of the battery hardware,  $5 \text{ cm}^2$ ;  $\delta$  is the thickness of the membrane;  $t$  is time the concentration is allowed to equilibrate.

### **6.2.5 $\text{VO}^{2+}$ Permeation as a Function of Temperature**

$\text{VO}^{2+}$  diffusivity in SDAPP was also measured in a PermeGear counter diffusion cell at various temperatures, sketched in Figure 6-2. On the rich side of the cell, the solution contains  $1 \text{ mol}\cdot\text{dm}^{-3}$   $\text{VO}^{2+}$  and  $4 \text{ mol}\cdot\text{dm}^{-3}$   $\text{H}_2\text{SO}_4$ . On the receiving side,  $5 \text{ mol}\cdot\text{dm}^{-3}$   $\text{H}_2\text{SO}_4$  was used to balance acid strength. The  $\text{VO}^{2+}$  concentration on the receiving side was monitored by circulating the solution through a UV-Vis flow cell coupled with an ALS-Japan SEC 2000 portable UV-Vis spectrometer. The temperature of the system was maintained by water circulation in the water jacket of the diffusion cells with a refrigeration water circulator (Fisher Scientific Isotemp 3016D). During the measurement, the solutions were mixed by magnetic stirrers to minimize the influence of vanadium distribution on membrane surface. The volume of each cell chamber is 50 mL. The concentration of  $\text{VO}^{2+}$  in the receiving side can be calculated by Beer-Lambert law. The  $\text{VO}^{2+}$  mass balance in this measurement can also be expressed as equation 6-4. The diffusivity of  $\text{VO}^{2+}$  across membrane can be calculated from equation 6-5.



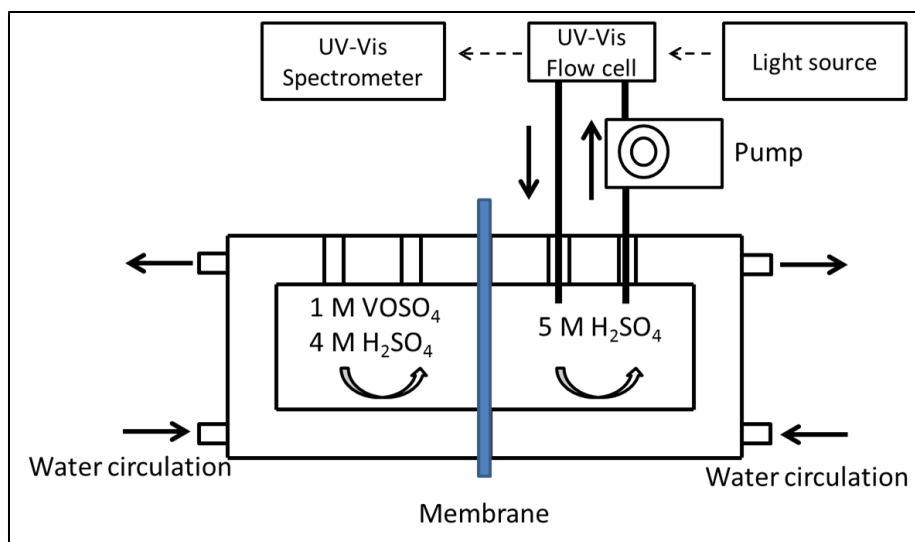


Figure 6–2. Sketch of VO<sup>2+</sup> diffusion across membrane monitored by UV-Vis spectrometer with temperature control.

### 6.2.6 Transmission Electron Microscopy

To study the morphology and sulfonic acid group distribution of the SDAPP membrane, micrographs were taken using transmission electron microscopy. To better image the sulfonic acid, the membrane was exchanged into the Cs<sup>+</sup> form to provide higher electron contrast.<sup>246</sup> SDAPP and Nafion samples were first soaked in 0.1 mol·dm<sup>-3</sup> Cs<sub>2</sub>SO<sub>4</sub> solutions for seven days to reach complete Cs<sup>+</sup> exchange. Then film samples were embedded in a low viscosity epoxy resin (Ted Pella) and microtomed into 70-nm-thick slices. TEM results were collected using a Zeiss Libra 120 at 120kV with an emission current of 7μA and a minimum dose condition in order to largely mitigate the electron-beam-induced polymer damage.

## 6.3 Results and Discussion

### 6.3.1 Membrane Characterization

SDAPP membranes with different ion exchange capacities were synthesized and the IEC was determined by back titration. Membranes with IECs of 1.4, 1.8 and 2.3 meq/g were obtained by varying the stoichiometry of chlorosulfuric acid used during sulfonation. From here on forward we label the SDAPP membranes as SDAPP 1.4, SDAPP 1.8 and SDAPP 2.3, according to their IEC. Membrane density and water content under a fully hydrated state are presented in Table 6-1, with comparison to Nafion 117.<sup>30</sup> Sulfonic acid group concentration in the membrane under fully hydrated conditions can be calculated by:

$$C_{-\text{SO}_3\text{H}}^{\text{hydrated}} = \frac{EW+18\lambda}{\rho_{\text{hydrated}}} \quad (6-6)$$

The equivalent weight of the membranes ( $EW$ ), were 714, 555 and 434 grams per mole sulfonate for SDAPP 1.4, 1.8 and 2.3 respectively.  $\lambda$  is the water content in pure water equilibrated membrane.  $\rho_{\text{hydrated}}$  is the membrane density under fully hydrated conditions. The calculated sulfonic acid concentration in the membranes is presented in Table 6-1. Because SDAPP and Nafion are compositionally variant, (hydrocarbon vs. fluorocarbon) the concentration of sulfonic acid group can better represent acid group distribution than IEC. Although SDAPP polymers have significantly higher IEC than Nafion 117, its densities are much lower than Nafion because the SDAPP backbone is formed primarily by C-H bonds while Nafion is composed of heavier C-F bonds. The

higher IEC in SDAPP is traded off by the membrane density, leading to very similar sulfonic acid group concentrations in SDAPPs, especially SDAPP 2.3, and Nafion 1100.

Table 6-1. Density and water content in SDAPP and Nafion membranes at fully hydrated state, and calculated sulfonate concentration.

	SDAPP 1.4	SDAPP 1.8	SDAPP 2.3	Nafion 117 <sup>30</sup>
Hydrated density (g·cm <sup>-3</sup> )	1.2	1.2	1.1	1.8
$\lambda$	20.4	20.9	24.1	21.6
Sulfonate concentration (mol·cm <sup>-3</sup> )	$1.11 \times 10^{-3}$	$1.27 \times 10^{-3}$	$1.29 \times 10^{-3}$	$1.24 \times 10^{-3}$

### ***6.3.2 Impact of Acid and Water Uptake after Equilibration***

The sulfuric acid and water contents in SDAPP membranes are presented in Figure 6-3, with respect to Nafion. Within the experimental sulfuric acid concentration range, sulfuric acid can overcome Donnan exclusion from the polymer and enter membrane micropores. Sulfuric acid content in the membrane is characterized as the mole ratio of free sulfuric acid to sulfonic acid groups attached in membrane. As is shown in Figure 6-3(a), the free sulfuric acid content in SDAPP films with various IECs are similar over the entire sulfuric acid concentration range. This consistency means that the sulfonic acid group in SDAPP has similar ability to exclude or coordinate free anions, regardless of membrane IEC. Although the SDAPP membranes have higher ion exchange capacities than Nafion, SDAPP membranes can take more sulfuric acid per attached acid than Nafion. This could be a result of weaker Donnan exclusion from the aromatic sulfonic acid groups in SDAPP than the fluorosulfonic acid group in Nafion. Sulfuric acid content

in SDAPP does not level off as seen in Nafion, where acid content remains constant after  $6 \text{ mol kg}^{-1}$  at 0.7. This can be attributed to less deswelling in SDAPP than Nafion in the concentrated sulfuric acid environment. As has been proven, Nafion can deswell and cause reduced internal porous space for imbibed species in low water activity environments.<sup>30,204</sup> Because the sulfonic acid groups in Nafion are attached via a long side chain, it has more flexible ionic cluster channel structure that can deswell substantially in acid solutions.<sup>247</sup> SDAPP has an aromatic backbone with side chains only one benzene ring in length, resulting in a stiff molecular structure to resist deswelling. So, SDAPP polymer can suffer less deswelling than Nafion at high sulfuric acid concentration to take up more sulfuric acid and water, as is presented in Figure 6-3.

As shown in Figure 6-3(b), membrane water content is reduced by increasing the bathing sulfuric acid concentration. Since the sulfuric acid in the membrane can be hydrated, in addition to the polymer-bound sulfonic acid group, the water content in membrane has to be corrected by incorporating the effects of sulfuric acid. The corrected water content is defined as the mole ratio of water to the total amount of sulfonic acid groups and sulfuric acid,  $\lambda' = n_{\text{H}_2\text{O}} / (n_{-\text{SO}_3\text{H}} + n_{\text{H}_2\text{SO}_4})$ <sup>30</sup>. In Figure 6-4, the corrected water content  $\lambda'$  in SDAPP and Nafion is shown to decrease with increasing concentration of sulfuric acid or lower water activity of the system. The water content in the membranes is independent of IEC or backbone type (hydrocarbon or fluoropolymer). This suggests that the sulfonic acid groups in Nafion and SDAPP have similar hydration properties, not influenced by polymer morphology. The consistent water content also suggests that the sulfuric acid in the membrane's ionic domain might have similar

hydration behavior regardless of the sulfonic acid groups in SDAPP or Nafion.

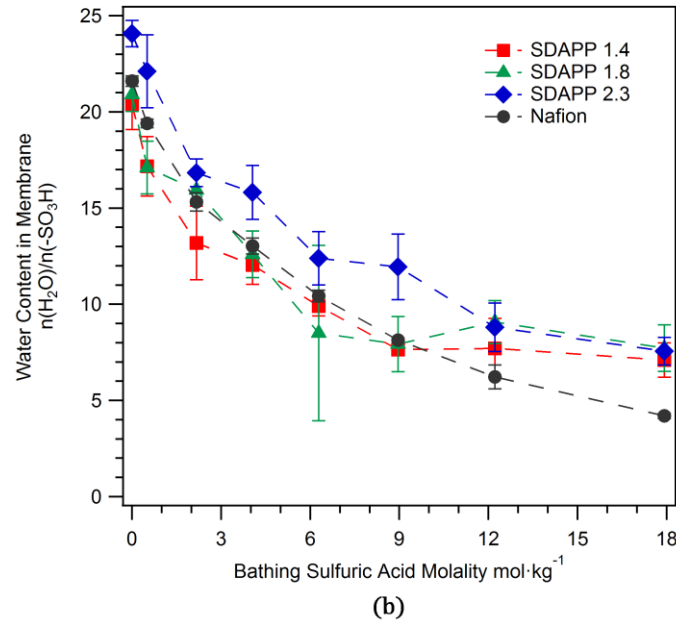
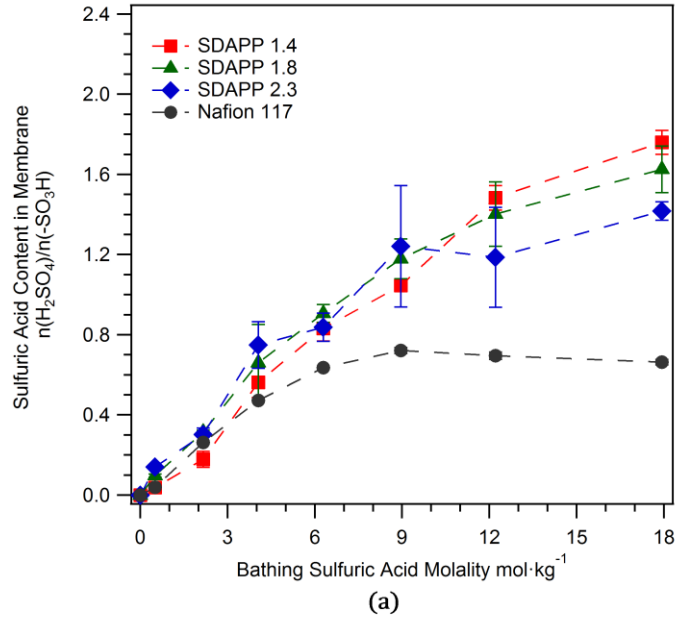


Figure 6–3. Sulfuric acid (a) and water (b) contents in SDAPP membranes compared to Nafion 117. SDAPP membranes have both significantly higher sulfuric acid and water contents than Nafion in concentrated sulfuric acid environment.

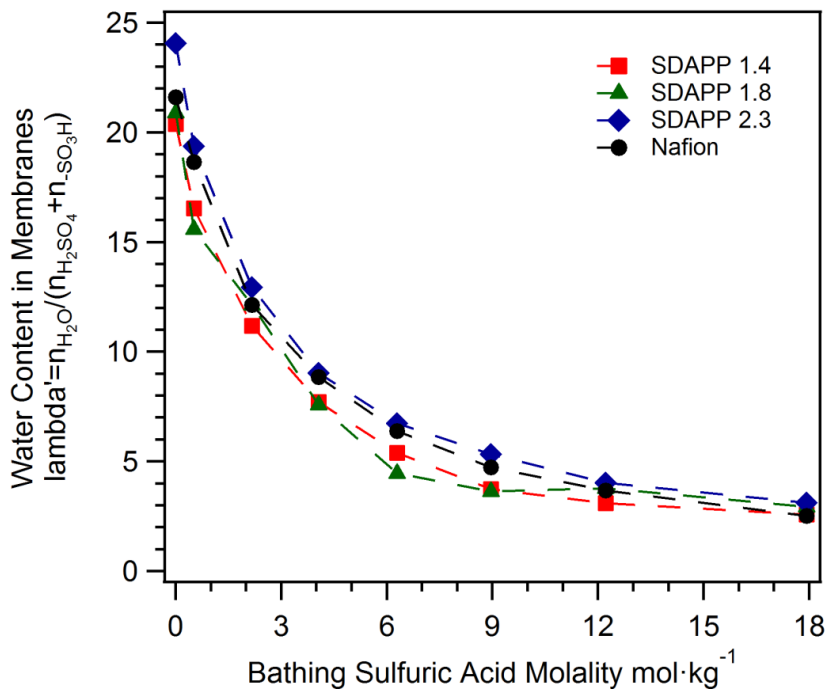


Figure 6–4. SDAPP and Nafion have close water content after being equilibrated in sulfuric acid solutions. Sulfuric acid in the membrane ionic domain has similar hydration behavior to sulfonic acid group in SDAPP and Nafion.

The Donnan exclusion strength in SDAPP is related to the membrane ion exchange capacity. The molality of sulfuric acid in the membrane micropore is presented in Figure 6-5. The molality of sulfuric acid in the membrane phase is calculated from membrane sulfuric acid and water content:

$$m_{H_2SO_4} = \frac{n_{H_2SO_4}}{(18\lambda/1000)} \quad (6-7)$$

The calculated sulfuric acid molality in SDAPP increases with decreasing IEC. The reason for this trend is that at higher IECs, more sulfonic acid groups are present and

dissociate to ions and form a stronger potential barrier to exclude sulfuric acid. When comparing SDAPP with aromatic acid groups with fluorosulfonic acid groups in Nafion at equivalent sulfonic acid concentration (SDAPP 2.3,  $1.29 \times 10^{-3}$ ; Nafion,  $1.24 \times 10^{-3}$  mol·cm<sup>-3</sup> respectively in Table 1), SDAPP has a higher sulfuric acid molality than Nafion, which suggests that Nafion has a stronger Donnan effect. As is presented in Figure 6-6, the different strength of the Donnan exclusion effect in SDAPP and Nafion can be attributed to sulfonic acid group clustering differences in SDAPP and Nafion as an additional factor. Sulfonic acid groups in SDAPP are evenly distributed throughout the matrix, while sulfonic acid groups cluster in Nafion.<sup>119,244,247</sup> Since sulfonic acid group concentrations in SDAPP and Nafion are similar, the sulfonate clustering in Nafion can locally condense sulfonate in the ionic channel to exclude anions. On the other hand, the less agglomerated sulfonic acid group in SDAPP can generate a weaker potential barrier to sulfuric acid than that in Nafion.

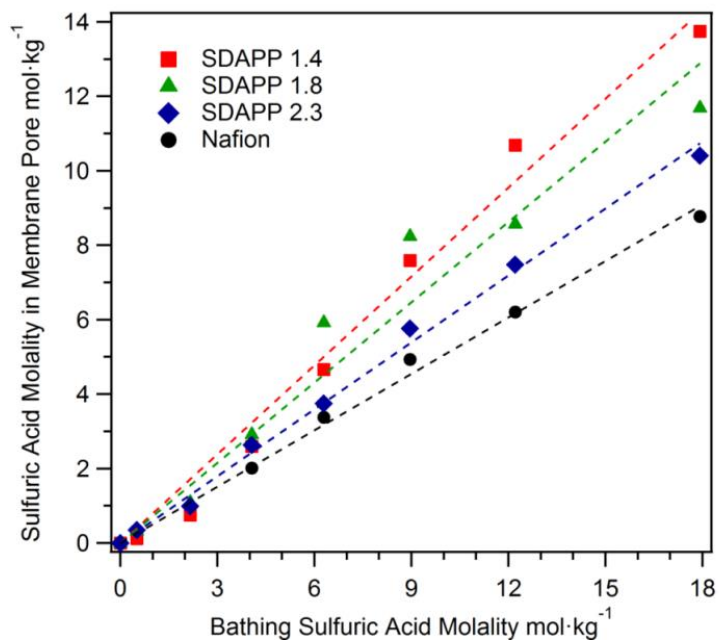


Figure 6–5. Calculated sulfuric acid molality in membrane phase. Sulfuric acid can be more effectively excluded by Nafion than SDAPP. Donnan exclusion in SDAPP membrane is consistent with membrane ion exchange capacity.



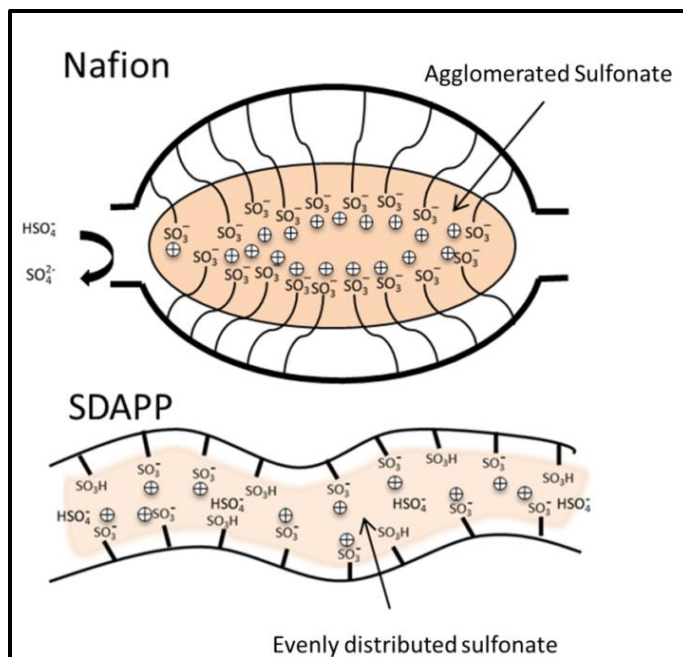


Figure 6–6. Sulfuric acid uptake behavior in membrane is controlled by the degree of sulfonic acid group agglomeration and acidity (or dissociation). Nafion has high sulfonic acid group agglomeration and higher acidity; SDAPP has an even sulfonic acid group distribution and lower acidity.

### 6.3.3 Sulfuric Acid Influence on Membrane Conductivity

To understand the influence of sulfuric acid concentration on membrane conductivity, conductivities of membranes were measured after being equilibrated in aqueous sulfuric acid with concentrations that ranged between 0 to  $17.4 \text{ mol}\cdot\text{kg}^{-1}$  (Figure 6-7). SDAPP 2.3 had the highest conductivity among all three SDAPP membranes, while SDAPP 1.4 has the lowest, which is consistent with the general finding that higher IECs display higher conductivity. Generally, membranes with higher IEC possess higher conductivity because they have more sulfonic acid groups to maintain higher proton

concentration to carry charge.<sup>244,248,249</sup> As shown in Figure 6-3(a), since a considerable amount of sulfuric acid can be present in the membranes, extra protons can be provided as charge carriers. Both SDAPP and Nafion membranes displayed higher conductivity after equilibrating in aqueous sulfuric acid, between 0-3 mol·kg<sup>-1</sup>. However, increasing concentrations of sulfuric acid (>3mol·kg<sup>-1</sup>) causes a constant decrease in conductivity. This trend is due to the trade-off between increasing proton concentration in the presence of more acid and proton mobility loss due to reduced water content in the membrane.<sup>30,200</sup>

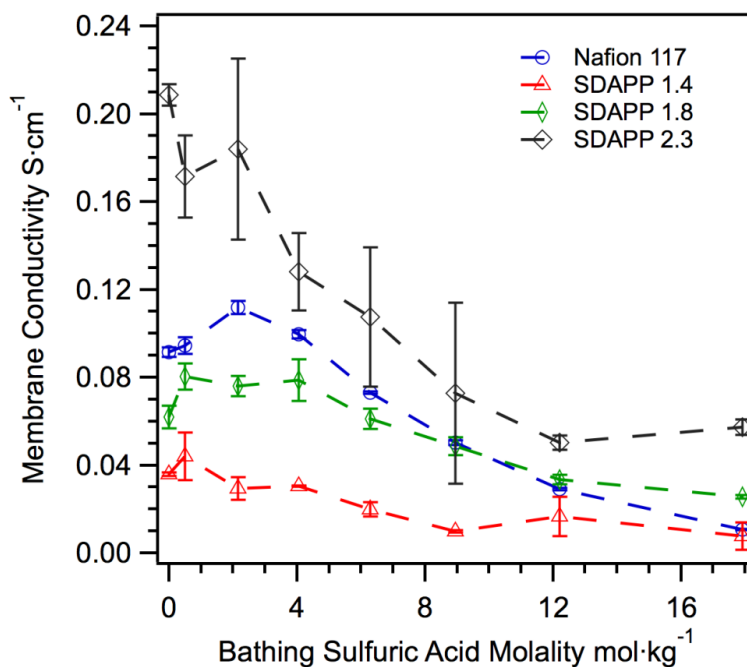


Figure 6–7. Conductivity of SDAPP membranes after being equilibrated in sulfuric acid solutions with varying concentration. SDAPP membrane with higher IEC has higher conductivity.

To analyze proton mobility in the SDAPP membrane, a modeling study was carried out based on membrane water uptake and conductivity measurements. The modeling analysis is analogous to the proton transport study on Nafion with sulfuric acid equilibration.<sup>30</sup> At first, it is assumed that the conductivity of electrolyte is a function of all mobile charged species in the electrolyte:

$$\sigma = F \sum z_i c_i u_i \quad (6-8)$$

Here,  $F$  is the Faraday constant,  $96500 \text{ C}\cdot\text{mol}^{-1}$ ;  $z_i$ ,  $c_i$  and  $u_i$  are charge number, ion concentration and mobility of the ion  $i$ ; the mobile ionic species include proton, bisulfate and sulfate in the SDAPP membranes. Because SDAPP is a cation exchange membrane, anion motion in SDAPP is largely hindered by the negative electrostatic force arising from sulfonate in the polymer. Generally anion transference numbers are much lower than those of protons in cation exchange membranes equilibrated in acids.<sup>200,201</sup> Thus, it is reasonable to approximate that protons are the only charge carrying species in SDAPP membrane by assuming anion transfer number is negligible. Therefore equation 6-8 can be simplified to:

$$\sigma = F c_{\text{H}^+} u_{\text{H}^+} \quad (6-9)$$

Proton concentration in the membrane can be calculated from the overall acid (sulfuric acid and sulfonic acid group) concentration in the membrane and acid dissociation. Measured densities of the SDAPP membrane with varying IEC are presented in Table 6-1. Due to the strong acidity of sulfuric acid ( $\text{pK}_a=-3.0$ ) and sulfonic acid group ( $\text{pK}_a=-2.8$  for benzenesulfonic acid)<sup>250</sup>, it is assumed that all sulfuric acid and

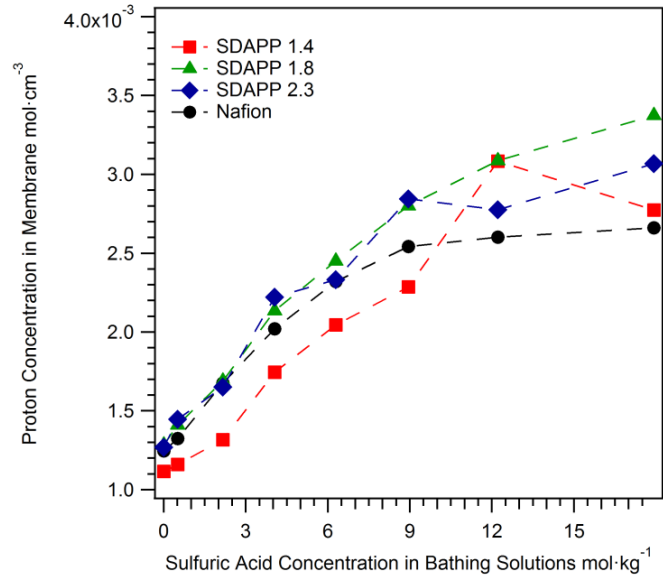
sulfonic acid groups in membrane can dissociate into bisulfate or sulfonate over the entire sulfuric acid concentration range.<sup>222</sup> It also has been shown that the dissociation of bisulfate can be fully suppressed by the abundance of protons provided by sulfuric and sulfonic acid groups.<sup>30</sup> The amount of protons in the membrane then is equal to the total amount of sulfuric and sulfonic acid groups. Because SDAPP's sulfuric acid uptake behavior suggests it has a low deswelling effect in sulfuric acid solutions, we assume that the sulfonate concentration in SDAPP does not change when varying the concentration of the sulfuric acid solution. Proton concentration in the membrane can be calculated by following equation:

$$c_{H^+} = \left(1 + \frac{n_{H_2SO_4}}{n_{-SO_3H}}\right) c_{-SO_3H}^{hydrated} \quad (6-10)$$

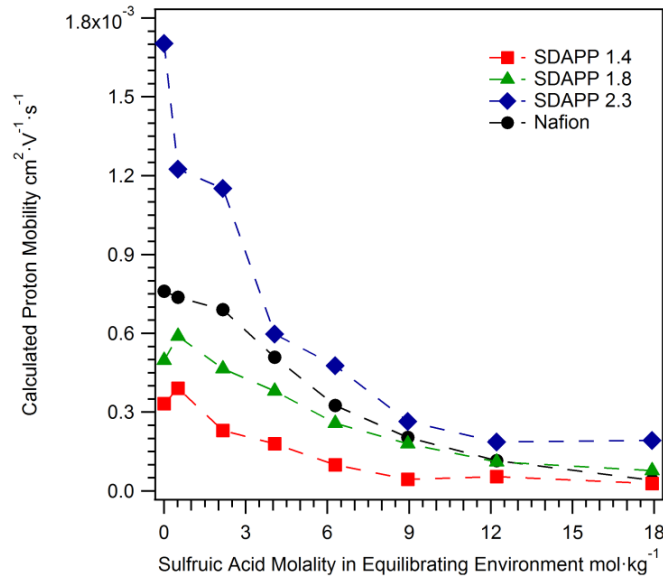
The calculated proton concentration is presented in Figure 6-8(a). As expected, increasing the concentration of the sulfuric acid bathing solution also increases the proton concentration in the membranes.

Proton mobility in the membrane is then calculated from equation 6-8 with membrane conductivity and proton concentration. Although there is an increase in proton concentration in both SDAPP and Nafion membranes with increasing sulfuric acid bathing solution, there is also a reduction in the calculated proton mobility as shown in Figure 6-8(b). The bathing sulfuric acid solution can influence the membrane conductivity by raising the proton content and lowering proton mobility. At relatively low sulfuric acid concentration, the conductivity enhancement is caused by an increase in proton concentration due to the uptake of sulfuric acid. In more concentrated sulfuric acid

solutions, the conductivity loss is mainly due to severe proton mobility loss caused by severe water content loss.



(a) Proton Concentration



(b) Proton Mobility

Figure 6–8. Proton concentration (a) and mobility (b) in SDAPP membranes and Nafion with respect to the sulfuric acid concentration in the bathing environment.

Proton mobility in SDAPP is highly favored by the membrane's IEC and water content in the membrane. As is shown in Figure 6-9, at any hydration level in the membrane, SDAPP 2.3 has the highest proton mobility followed by SDAPP 1.8 and then SDAPP 1.4. Apparently, proton transport in the SDAPP membrane is favored by a high degree of sulfonation, because higher IEC results in higher concentration of anionic groups in ionic domains. As is presented in Table 1, SDAPP with higher IEC has higher sulfonate group concentration, so it should also have shorter average inter-sulfonate distance. The shorter distance among sulfonate groups can ease proton transport by increasing the probability of proton transfer from one sulfonate to another. In addition, it is clear that proton mobility in SDAPP is dependent on water content in a way similar to what is observed in Nafion.<sup>84</sup> In hydrated cation exchange membranes, proton transport is favored at high water contents in the membrane because it is facilitated by proton 'hopping' across more condensed water media.<sup>84,85,244</sup>

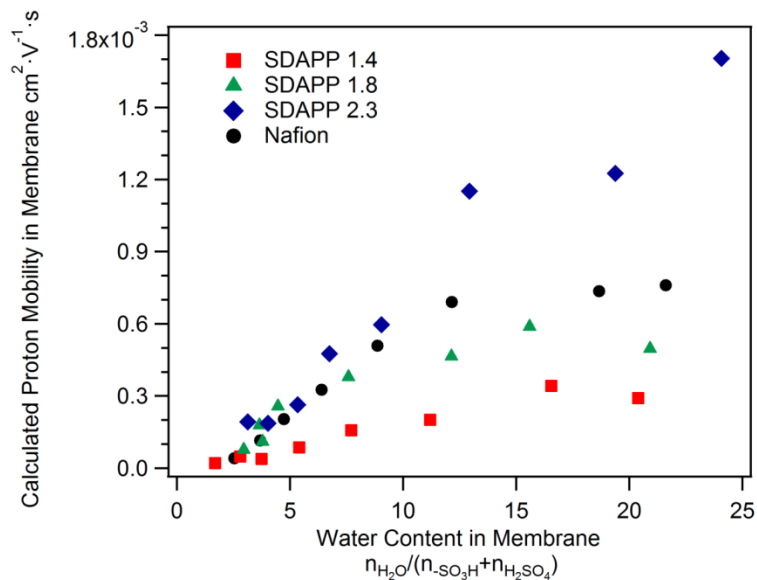


Figure 6–9. Proton mobility in SDAPP is highly dependent on water content in membranes. Proton transport in SDAPP is favored by high availability of water molecules to serve as transport mediator.

### 6.3.4 VO<sup>2+</sup> Permeation across SDAPP Membranes

VO<sup>2+</sup> diffusion in SDAPP is consistent with the ion exchange capacity of the membrane; higher IEC results in higher VO<sup>2+</sup> diffusivity. As is shown in Figures 6-10 and 6-11, SDAPP 2.3 displays the highest VO<sup>2+</sup> diffusivity and SDAPP 1.4 has the lowest, regardless of temperature or acid concentration. Generally, cation diffusivity in cation exchange membranes is highly consistent with the membrane ion exchange capacity.<sup>99,113</sup> As was just discussed, in membranes with higher IEC, higher amounts of sulfonic acid groups have shorter inter-anion distances to allow higher possibility for cations to successfully transfer from one sulfonate group to another. Also, cation

transport can be favored by larger ionic domain pathways, since the higher sulfonate concentrations increase the domain size. Finally, and probably most importantly, higher IEC leads to higher water content and thus lower local viscosity.

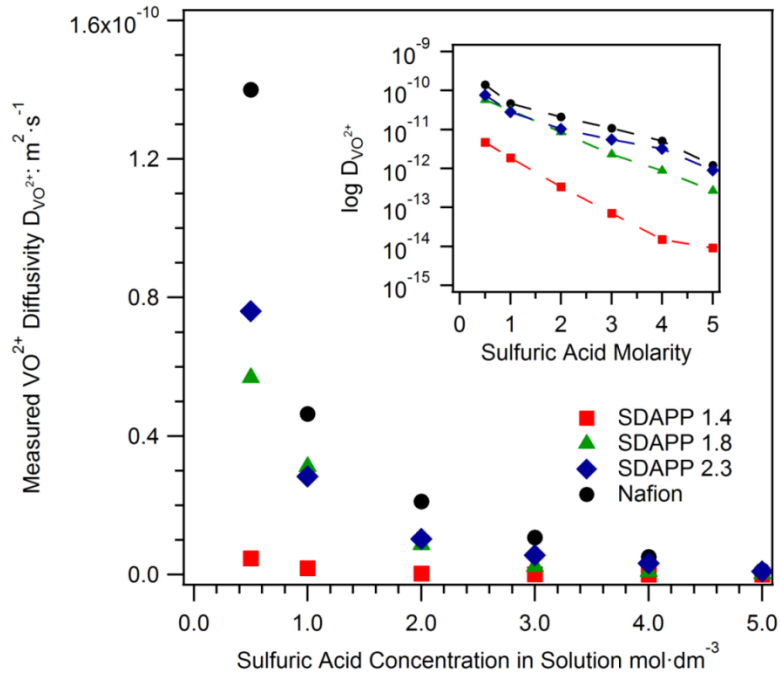


Figure 6–10. Vanadium permeability across SDAPP membranes is sharply reduced by high sulfuric acid concentration in electrolyte environment.

Besides membrane IEC, vanadium transport is a function of the concentration of acid in the electrolyte solution. As is shown in Figure 6-10, vanadium permeability across SDAPP membranes and Nafion is sharply reduced with increasing sulfuric acid concentrations.<sup>32</sup> Figure 6-3(a) displays that as the concentration of sulfuric acid in electrolyte increases the amount of sulfuric acid absorbed by the membrane also increases. As has been pointed out, the process of cation permeation in membrane consists of cation



partitioning into the polymer and then diffusion through the polymer matrix.<sup>251,252</sup> In concentrated electrolyte solutions, the partitioning of VO<sup>2+</sup> into the membrane is reduced by the presence of sulfuric acid in the membrane.<sup>253</sup> Moreover, the dynamics of VO<sup>2+</sup> transport in the membrane can be slowed by the presence of sulfuric acid in membrane.<sup>32</sup> The diffusive medium in the membrane consists of sulfuric acid and water, and the viscosity of the solution increases with sulfuric acid concentration. According to the Stokes-Einstein equation, ionic diffusivity is inversely related to the viscosity of diffusion medium  $\eta$ :

$$D = \frac{k_B T}{6\pi\eta r} \quad (6-11)$$

Here,  $k_B$  is Boltzmann constant;  $r$  is ionic radius;  $T$  is absolute temperature. While VO<sup>2+</sup> is diffusing within the ionic cluster channel, its motion can be restricted by the viscous friction caused by its interaction with stagnant or slower species in the diffusion media. A higher viscosity of the diffusion medium will result in lower VO<sup>2+</sup> transport due to a stronger frictional resistance.

VO<sup>2+</sup> diffusion in SDAPP is also dependent on temperature. According to classical Arrhenius kinetics theory, the diffusivity is exponentially dependent on temperature:

$$D = D_0 \exp(-E_a/RT) \quad (7-12)$$

In Figure 6-11, it is shown that the logarithm of VO<sup>2+</sup> diffusivity is linearly dependent on the reciprocal of temperature, in the range of 10 to 50°C. The pre-

exponential factors and activation energies for the SDAPP membranes and Nafion are fitted and listed in Table 6-2. The activation energy for  $\text{VO}^{2+}$  diffusion is fairly similar in all SDAPP membranes and Nafion regardless of their IEC. This consistency means that  $\text{VO}^{2+}$  encounters a similar energy barrier for diffusion among sulfonic acid groups in these membranes, and this implies a similar diffusion mechanism. The consistent activation energy of  $\text{VO}^{2+}$  diffusion in membranes might be due to the similar acidic environment inside the membrane. In SDAPP membranes, the activation energy decrease slightly with IEC increase. This means SDAPP membrane with higher IEC has lower energy barrier for  $\text{VO}^{2+}$  transfer. The activation energy of  $\text{VO}^{2+}$ ,  $\sim 20 \text{ kJ}\cdot\text{mol}^{-1}$ , is much higher than that of proton in Nafion,  $\sim 10 \text{ kJ}\cdot\text{mol}^{-1}$ .<sup>254</sup> The  $E_a$  difference between  $\text{VO}^{2+}$  and proton suggests that  $\text{VO}^{2+}$  diffusion across membrane is much more difficult than proton.

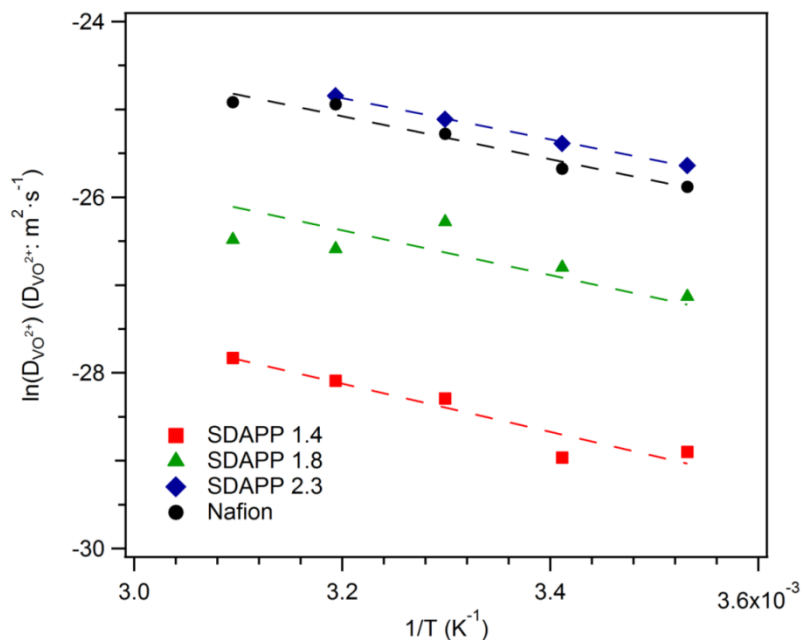


Figure 6–11. The logarithm of vanadyl diffusivity in SDAPP and Nafion is linearly dependent on  $1/T$ . The vanadyl diffusion in cation exchange membrane obeys classical Arrhenius kinetics.

Table 6-2. The pre-exponential factor and activation energy for SDAPP membranes and Nafion in Arrhenius kinetics theory.

	SDAPP 1.4	SDAPP 1.8	SDAPP 2.3	Nafion
$D_0$ (cm <sup>2</sup> ·s <sup>-1</sup> )	$4.03 \times 10^{-9}$	$1.23 \times 10^{-8}$	$2.98 \times 10^{-8}$	$2.69 \times 10^{-8}$
$E_a$ (kJ·mol <sup>-1</sup> )	22.8	21.2	19.6	20.3

### 6.3.5 Morphology of SDAPP by TEM

In comparison with Nafion, SDAPP has a more homogeneous morphology with less phase separation and a more tortuous structure. The TEM micrographs of SDAPP are

presented in Figure 6-12 and 6-13, with comparison to Nafion 117 at different magnification respectively. In these images, bright regions represent hydrophilic domain with  $\text{Cs}^+$  stain. Although the state of the film during examination is not equivalent to conditions of a working flow battery, (presence of  $\text{Cs}^+$  and dehydrated film held under vacuum), the TEM micrographs can still give us important information about the microstructure and morphology of the membranes. In Figure 6-12, a clear contrast between SDAPP membranes and Nafion 117 is revealed by the TEM imaging at the relatively lower magnification. In contrast to an obvious phase separation in Nafion, SDAPP possesses a more homogeneous appearance regardless of its ion exchange capacity. In Nafion, because the sulfonic acid group is attached on a flexible side chain and the entire polymer is more flexible, the sulfonic acid group can agglomerate and phase separation between hydrophilic ionic cluster and hydrophobic polymer backbone.<sup>255</sup> The ionic clusters in Nafion are well connected to establish a reticulated ionic network, as can be seen in Figure 6-12. The featured width or diameter of hydrophilic and hydrophobic phases is about 5 nm. For SDAPP, the sulfonic acid group is attached on a short side chain to the backbone and this structural feature may not be flexible enough to support a considerable amount of sulfonic acid group agglomeration as large as that in Nafion. As a result, no well-organized hydrophilic channel network can be observed in the SDAPP polymer in Figure 6-12.

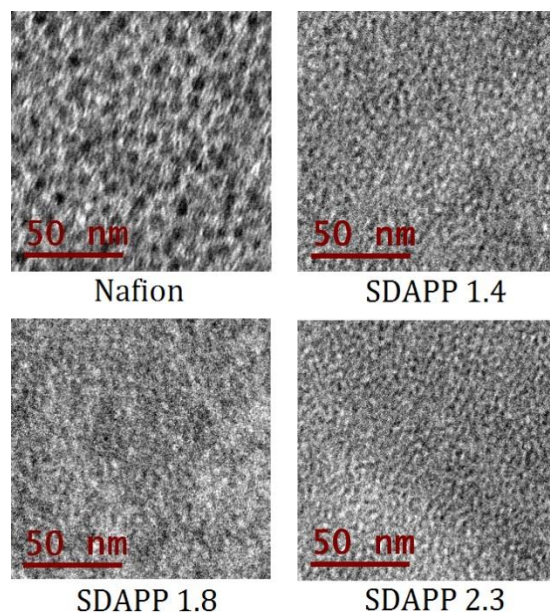


Figure 6–12. Cs<sup>+</sup> stained TEM micrographs of SDAPP and Nafion 117 at 50 nm magnification. More homogeneous sulfonic acid group distribution is presented in SDAPP membranes with varying ion exchange capacity.

The size and distribution of the ionic domain in SDAPP membranes is illustrated at a higher magnification in Figure 6-13. In these images of SDAPP, there are obvious bright and dark areas representing hydrophilic region and hydrophobic segments of the backbone, respectively. The featured width or diameter of hydrophilic and hydrophobic segments in SDAPP is around 0.5 nm. Considering the C-C distance in benzene is about 0.14 nm<sup>256</sup>, this feature suggests that sulfonic acid group is not agglomerated but evenly distributed along polymer backbone. The diameter of the ionic channel in SDAPP is much smaller in size than the ionic channel in Nafion. Since the ionic channel is formed by organizing sulfonic acid groups along polymer backbone, high tortuosity of ionic

channels can be developed by a torturous polymer backbone, as can be seen in micrographs. With a higher IEC in SDAPP, brighter and wider ionic domain presented in TEM image means the membrane contains more condensed sulfonic acid groups surrounding the ionic channel.

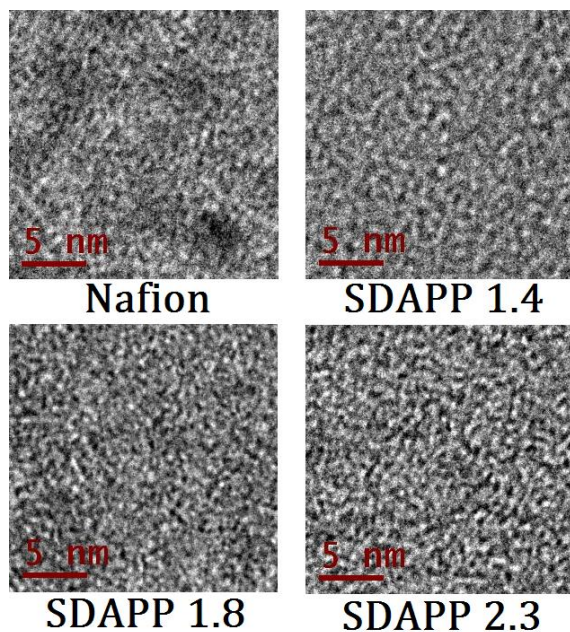


Figure 6–13.  $\text{Cs}^+$  stained TEM micrograph of SDAPP and Nafion 117 at 5 nm magnification. The structure of SDAPP is highly homogeneous and the sulfonic acid group is evenly distributed in the polymer.

Sulfonated Diels Alder poly(phenylene) membrane ion transport properties in sulfuric acid solution and its microstructure of ionic domain were investigated to evaluate its potential as electrolyte separator for vanadium redox flow battery. With microscopy, it is found that SDAPP is a more homogeneous polymer without strong phase contrast

brought about by sulfonic acid group agglomeration. In SDAPP, the dispersed sulfonate group distribution and tortuous ionic pathway reduces proton mobility, but more importantly, causes lower vanadyl permeation as well. SDAPP can achieve comparable conductivity to Nafion but much lower vanadium permeation. SDAPP has higher conductivity to vanadyl diffusivity ratio, as is presented in Table 6-3. This suggests that SDAPP membranes have selectivity to conduct ionic transport and suppress the unwanted vanadium crossover.

Table 6-3. Conductivity and  $\text{VO}^{2+}$  permeability comparison among SDAPPs and Nafion around 20°C. Membranes have been equilibrated in 5 mol·dm<sup>-3</sup> H<sub>2</sub>SO<sub>4</sub>/sulfate solutions. SDAPPs have better conductivity to  $\text{VO}^{2+}$  permeability ratio than Nafion.

Membrane	SDAPP 1.4	SDAPP 1.8	SDAPP 2.3	Nafion 117
$\sigma \text{ S}\cdot\text{cm}^{-1}$ at 22°C	0.020	0.061	0.107	0.073
$D(\text{VO}^{2+}) \text{ cm}^2\cdot\text{s}^{-1}$ at 20°C	$2.64\times 10^{-9}$	$2.30\times 10^{-8}$	$9.45\times 10^{-8}$	$7.07\times 10^{-8}$
$\sigma/D \text{ S}\cdot\text{cm}^{-3}\cdot\text{s}$	$7.58\times 10^6$	$2.65\times 10^6$	$1.13\times 10^6$	$1.03\times 10^6$

## 6.4 Conclusion

In this work, the proton and  $\text{VO}^{2+}$  transport in sulfonated Diels Alder poly(phenylene) membrane with various ion exchange capacities have been studied in light of the potential utilization of the membrane in a vanadium redox flow battery. The sulfuric acid equilibrium in SDAPP and its impact on conductivity have been studied based on membrane uptake analysis and conductivity tests. It is shown that SDAPP has higher sulfuric acid uptake than Nafion, possibly because it has weaker Donnan exclusion

to sulfuric acid than Nafion. Sulfuric acid and sulfonic acid groups in SDAPP have similar hydration ability to those in Nafion. With a higher ion exchange capacity, SDAPP can achieve comparable conductivity to Nafion 117. SDAPP can have a higher conductivity to vanadium permeability ratio than Nafion. SDAPP is therefore a suitable membrane to be used as electrolyte separator for VRFB.

The intrinsically slower ionic transport in SDAPP is due to its homogeneous morphology. Since sulfonic acid groups in SDAPP are attached on the short side chains, the lack of distance between the backbone and acid moiety cannot support the agglomeration of the sulfonate group to form a hydrophilic phase with a considerable size. The ionic domain in SDAPP is much smaller in radius and is highly tortuous. This structural feature can be more selective to the larger  $\text{VO}^{2+}$  ion than to proton.. The tortuosity in the membrane is unhelpful for both proton and vanadium transport because it leads to a longer pathway for ionic diffusion. For future ion exchange membrane development, it is critical to control the sizing of ionic domains in membranes to enhance ionic selectivity and reduce tortuosity of the ionic channel to improve proton transport.



## CHAPTER 7

### RECOMMENDATION FOR FUTURE WORK

1. Systematic characterization and diagnostic techniques are needed to evaluate the performance of VRFB system and components.

Despite the long history of VRFB development, the development of characterization methods for VRFB is still insufficient to support the performance improvement of VRFB, in contrast to diagnostic methods system of proton exchange membrane fuel cell<sup>147,148</sup> which shares many features with the VRFB. Due to the similarity between VRFB and PEM fuel cells, the performance diagnostic methods for PEMFC are highly compatible with VRFB, as shown in this thesis for the polarization curve<sup>33,34,169</sup> and electrochemical impedance spectroscopy<sup>170</sup>. As has been mentioned in chapter 2, the performance loss in VRFB system can be roughly sorted as activation loss, ohmic loss and mass transport loss. The sources of activation loss are the overpotential losses on each electrode surface during battery operation. The ohmic loss is caused by the electronic resistance of the electrode, contact resistance at interfaces between cell components, and ionic resistance of electrolyte separator. The mass transport loss is related to the active vanadium ionic transport resistance within the porous electrode and on electrode surface.

Recently, polarization curve and EIS measurements with hydrogen dynamic reference electrode were effectively applied to VRFB kinetics research<sup>169,170</sup>. The activation losses contributed by positive and negative electrodes were respectively quantified. The results suggested that any future catalyst development should focus

mainly on the negative electrode which contributes most of the activation loss. The ex-situ membrane conductivity measurement suggested membrane resistance is the primary part of the area specific resistance in non-gap battery cell configuration. However, the exact membrane resistance in operating cells has not been reported yet. The fine in-situ membrane measurement or battery internal resistance diagnostic method is needed to clarify the sources of internal resistance in VRFB. The current interrupt is a good candidate for this measurement. The understanding of mass transport loss is also of critical importance for VRFB. The mass transport loss can be directly reflected in the whole cell polarization curve at varying flow rate. And for each electrode, the mass transport loss can be clarified by EIS measurement. However, the detailed relation between mass transport loss and transport conditions (flow rate and flow field) has not yet been clarified. So both experimental and modeling works are needed to help to understand the sources of mass transport loss.

2. The detailed reaction mechanism for each vanadium redox couples and its relation with the property of electrode surface and electrolyte composition.

Understanding of reaction process for each vanadium redox couple is critical to guide the development of catalyst for each electrode. As has been reviewed in chapter 1, the surface modification of carbon electrode can obviously improve battery performance. Some additives in the electrolyte solution can also catalyze vanadium redox reactions in battery. Actually, these two methods provide two strategies to develop catalysts for vanadium redox flow battery. One is to develop catalysts using solid state catalysts which can be loaded on carbon electrode surface. Another one is to develop a soluble catalytic

additive to be loaded in electrolyte solution. The detailed reaction mechanism is still not available yet for such developments. The observation that  $V^{4+}/V^{5+}$  and  $V^{2+}/V^{3+}$  redox couples have very different kinetics on SGL 10AA carbon paper suggests that these two reactions might have very distinct reaction pathways. In addition, the UV-Vis spectroscopy work testified to the existence of complex ion  $V_2O_3^{3+}$  in the positive electrolyte. The complex ion might be able to serve as an intermediate in  $VO_2^+/VO^{2+}$  redox reaction. Based on this, the detailed reaction mechanism is critical to guide the development of new catalyst for vanadium redox flow battery.

### 3. Practical state of charge monitor based on UV-Vis spectroscopy

A more practical state of charge monitor can be developed based on the electrolyte spectrum analysis developed in the chapter 3. The analysis presented in chapter 3 gave an effective methodology to accurately estimate state of charge in positive and negative electrolyte solutions. The effectiveness of spectral analysis to calculate state of charge improves the feasibility to instantly monitor state of charge in electrolyte with the UV-Vis technique. A practical SoC monitor can be developed using an industrial UV-Vis detector with automatic signal processing circuit. The instant SoC monitoring can effectively enhance the management of battery system.

### 4. Understanding the polymer-sulfuric acid equilibrium influence on ionic transport in cation exchange electrolyte separator.

Due to the partitioning of sulfuric acid and vanadium ions in the polymer, a dynamic equilibrium in the separator can be established among electrolyte species and the polymer

membrane. As has been proved in previous sections, the acid and vanadium ions can have strong effects on the ion transport in the separator. However, the origin of factors controlling partitioning of sulfuric acid and vanadium ions into separator, for example Nafion, has not yet been clarified. The electrolyte species entering the polymer matrix in the separator can alter the microenvironment, especially the properties of water, for the proton transport.

The electrolyte-polymer equilibrium can be reached in a membrane immersed in electrolyte. Due to the anionic character of cation exchange membranes, the Donnan potential generated by the sulfonic acid group can exclude sulfuric acid from the electrolyte solutions. At practical electrolyte concentration level, the Donnan potential in membrane is not strong enough to completely prevent sulfuric acid from entering micropores in membrane. An acidic balance between sulfuric acid (electrolyte) and sulfonic acid group (polymer) can be established by the breaking through of potential barrier. The equilibrium should mostly be driven by the thermodynamic strength (acid strength or chemical potential) difference between the bathing electrolyte and separator. Currently the acid partitioning behavior in membrane cannot be predicted by membrane and electrolyte conditions. More accurate measurement is needed to determine the sulfuric acid uptake dependence on the electrolyte acid concentration and membrane properties (ion exchange capacity, polymer structure). Moreover, a rigorous mathematical model should be established based on thermodynamic theory to explain the acid uptake process into membrane. The correlation between electrolyte equilibrium in membrane and electrolyte properties is a precondition to predict the electrolyte influence on

membrane conductivity.

Since proton is the most efficient mobile ion in cation exchange membrane for conducting current, its concentration and mobility can largely determine membrane conductivity. The sulfuric acid presence in membrane can deteriorate proton mobility, although the acid dissociation can provide excess proton in some extent to enhance current transfer. The sulfuric acid in electrolyte can remarkably reduce membrane water content which is the most important factor for proton transfer in cation exchange membranes. Since the acid can reduce membrane conductivity in practical vanadium/sulfuric acid electrolytes, it is critical to understand the mechanism of proton mobility loss caused by water content reduction in membrane. Experimental measurements such as nuclear magnetic resonance (NMR) of proton mobility in Nafion membrane should be carried out to verify the proton mobility dependence on water state with equilibration with varying sulfuric acid concentrations. Understanding of the proton mobility loss would be helpful to provide support for electrolyte composition optimization and new polymer separator selection.

5. Understanding on vanadium-oxo ions influence on ionic transport in cation exchange membrane.

More thorough research is needed to understand the vanadium-oxo ion ( $\text{VO}^{2+}$  and  $\text{VO}_2^+$ ) interference on proton motion. The detailed mechanism of vanadium-oxo ions impedance of proton transport in membrane is required to better understand membrane conducting behavior during battery operation. Membrane conductivity is reduced by

vanadium-oxo ions reducing both concentration and mobility of proton. It is important to understand the direct cause of proton mobility loss in coexistence with  $\text{VO}^{2+}$  or  $\text{VO}_2^+$ . To reduce retarding effects from vanadium-oxo ions can effectively improve proton transfer efficiency and enhance membrane conductivity.

However, the cation interaction with proton has not been well clarified. Although both  $\text{VO}^{2+}$  and  $\text{VO}_2^+$  can reduce proton mobility while  $\text{V}^{3+}$  has no such ability, the proton motion restriction effect is not necessarily related to the oxo structure in these ions because  $\text{Fe}^{3+}$  also was observed to decelerate proton motion as well<sup>212</sup>. One reasonable explanation of this effect is that proton motion was indirectly slowed down by the presence of cations due to their restriction of water dynamics in their hydration shells. It has been demonstrated that multivalent cations ( $\text{Mg}^{2+}$  and  $\text{Al}^{3+}$ ) can form more condensed secondary hydration shells by hydrogen bonding between the primary hydration shell and outer hydration shells.<sup>237</sup> The cation with higher charge density tends to hold water molecules in outer hydration shells more tightly, leading to a shorter H-bond length and higher density in hydration shell. The molecular motion of water in the outer hydration shell can be substantially restricted by the H-bond among the water molecules. This effect is more obvious in the solution with high cation concentration,<sup>257</sup> which is analogous to the membrane equilibrated with vanadium-sulfuric acid electrolyte solutions. Future work can focus on the water motion within the secondary hydration shell of vanadium ions. It is necessary to evaluate the hydration shell structure (hydrogen bonding length and strength) of vanadium ions ( $\text{V}^{3+}$ ,  $\text{VO}^{2+}$  and  $\text{VO}_2^+$ ), and the water mobility around vanadium ions.

6. More comprehensive investigation on performance of SDAPP in vanadium-sulfuric acid electrolyte.

Due to the essential difference between SDAPP and Nafion, the comparison of performance between these two membranes can provide researchers more insight into membrane transport properties and their dependence on membrane structure and morphology. Since SDAPP is an aromatic polymer backbone membrane, it is essentially different from Nafion, a perfluorinated sulfonic acid polymer electrolyte, which is commonly used as VRFB separator. Its behavior as an electrolyte separator in the VRFB is of great importance to clarify the ionic transport performance dependence on membrane properties. Ionic transport and equilibrium is highly reliant on membrane properties, but most of current membrane development work for VRFB just focuses on the new membrane fabrication without serious investigation of the fundamental aspects of membrane performance.

Since protons are the most efficient mobile ion for carrying current, the polymer improvement should exclusively target facilitating proton transport. It is critical to illustrate the state of water in membrane-electrolyte equilibrium with respect to membrane morphology, ion exchange capacity and side chain structure. As has been pointed out, proton transport in the membrane is highly favored by high water content or activity in membrane<sup>30</sup>. A clear correlation between membrane structure and water content can largely favor the development of a high performance separator for VRFB. Also, since concentrated acid uptake and vanadium ion partitioning in membrane can reduce membrane conductivity, membrane structure should be optimized to limit acid and

vanadium presence in membrane in electrolyte conditions. A more organized and well separated membrane morphology with less branched structure can also improve proton transport.<sup>119</sup>



## Reference

- (1) Chen, H.; Cong, T. N.; Yang, W.; Tan, C.; Li, Y.; Ding, Y. *Prog. Nat. Sci.* **2009**, *19*, 291–312.
- (2) Yang, Z.; Zhang, J.; Kintner-Meyer, M. C. W.; Lu, X.; Choi, D.; Lemmon, J. P.; Liu, J. *Chem. Rev.* **2011**, *111*, 3577–613.
- (3) Dunn, B.; Kamath, H.; Tarascon, J. M. *Science* **2011**, *334*, 928–35.
- (4) Carta, J. A. In *Comprehensive Renewable Energy*; Elsevier Ltd., 2012; Vol. 2, pp. 569–622.
- (5) Dell, R. M.; Rand, D. A. J. *J. Power Sources* **2001**, *100*, 2–17.
- (6) Ge, B.; Wang, W.; Bi, D.; Rogers, C. B.; Peng, F. Z.; de Almeida, A. T.; Abu-Rub, H. *Int. J. Electr. Power Energy Syst.* **2013**, *44*, 115–122.
- (7) Leadbetter, J.; Swan, L. G. *J. Power Sources* **2012**, *216*, 376–386.
- (8) Nair, N. K. C.; Garimella, N. *Energy Build.* **2010**, *42*, 2124–2130.
- (9) McDowall, J. *J. Power Sources* **2006**, *162*, 959–964.
- (10) Skyllas-Kazacos, M.; Menictas, C. In *19th International Telecommunications Energy Conference*; 1997; pp. 463 – 471.
- (11) Joerissen, L.; Garche, J.; Fabjan, C.; Tomazic, G. *J. Power Sources* **2004**, *127*, 98–104.
- (12) Wade, N. S.; Taylor, P. C.; Lang, P. D.; Jones, P. R. *Energy Policy* **2010**, *38*, 7180–7188.
- (13) Vazquez, S.; Lukic, S. M.; Galvan, E.; Franquelo, L. G.; Carrasco, J. M. *IEEE Trans. Ind. Electron.* **2010**, *57*, 3881–3895.
- (14) Ibrahim, H.; Ilinca, a; Perron, J. *Renew. Sustain. Energy Rev.* **2008**, *12*, 1221–1250.
- (15) Skyllas-Kazacos, M.; Chakrabarti, M. H.; Hajimolana, S. A.; Mjalli, F. S.; Saleem, M. *J. Electrochem. Soc.* **2011**, *158*, R55.
- (16) Ding, C.; Zhang, H.; Li, X.; Liu, T.; Xing, F. *J. Phys. Chem. Lett.* **2013**, *4*, 1281–1294.
- (17) Skyllas-kazacos, M.; Kazacos, G.; Poon, G.; Verseema, H. *Int. J. Energy Res.* **2010**, *34*, 182–189.

- (18) Kear, G.; Shah, A. A.; Walsh, F. C. *Int. J. Energy Res.* **2012**, *36*, 1105–1120.
- (19) Shibata, T.; Kumamoto, T.; Nagaoka, Y.; Kawase, K. *SEI Tech. Rev.* **2013**, *76*, 14–22.
- (20) Tokuda, N.; Kanno, T.; Hara, T.; Shigematsu, T.; Tsutsui, Y.; Ikeuchi, A.; Itou, T.; Kumamoto, T. *SEI Tech. Rev.* **2000**, *50*, 88–94.
- (21) Watt-Smith, M. J.; Ridley, P.; Wills, R. G. a.; Shah, A. A.; Walsh, F. C. *J. Chem. Technol. Biotechnol.* **2013**, *88*, 126–138.
- (22) Moore, M.; Watson, J. S.; Zawodzinski, T. A.; Zhang, M.; Counce, R. M. *ECS Trans.* **2012**, *41*, 1–19.
- (23) Zhang, M.; Moore, M.; Watson, J. S.; Zawodzinski, T. A.; Counce, R. M. *J. Electrochem. Soc.* **2012**, *159*, A1183–A1188.
- (24) Skyllas-Kazacos, M.; Grossmith, F. *J. Electrochem. Soc.* **1987**, *134*, 2950–2953.
- (25) Rychcik, M.; Skyllas-Kazacos, M. *J. Power Sources* **1988**, *22*, 59–67.
- (26) Bartolozzi, M. *J. Power Sources* **1989**, *27*, 219–234.
- (27) Skyllas-kazacos, M.; Kasherman, D.; Hong, D. R.; Kazacos, M. *J. Power Sources* **1991**, *35*, 399–404.
- (28) Zaffou, R.; Li, W. N.; Perry, M. L. In *Polymers for Energy Storage and Delivery Polyelectrolytes for Batteries and Fuel Cells*; 2012; pp. 107–127.
- (29) Zhao, P.; Zhang, H.; Zhou, H.; Chen, J.; Gao, S.; Yi, B. *J. Power Sources* **2006**, *162*, 1416–1420.
- (30) Tang, Z.; Svoboda, R.; Lawton, J. S.; Aaron, D. S.; Papandrew, A. B.; Zawodzinski, T. A. *J. Electrochem. Soc.* **2013**, *160*, F1040–F1047.
- (31) Tang, Z.; Keith, R.; Aaron, D. S.; Lawton, J. S.; Papandrew, A. B.; Zawodzinski Jr., T. A. *ECS Trans.* **2012**, *41*, 25–34.
- (32) Lawton, J. S.; Jones, A.; Zawodzinski, T. A. *J. Electrochem. Soc.* **2013**, *160*, A697–A702.
- (33) Aaron, D. S.; Tang, Z.; Papandrew, A. B.; Zawodzinski, T. A. *J. Appl. Electrochem.* **2011**, *41*, 1175–1182.

- (34) Aaron, D. S.; Liu, Q.; Tang, Z.; Grim, G. M.; Papandrew, A. B.; Turhan, A.; Zawodzinski, T. A.; Mench, M. M. *J. Power Sources* **2012**, *206*, 450–453.
- (35) Rahman, F.; Skyllas-Kazacos, M. *J. Power Sources* **2009**, *189*, 1212–1219.
- (36) Zhang, J.; Li, L.; Nie, Z.; Chen, B.; Vijayakumar, M.; Kim, S.; Wang, W.; Schwenzer, B.; Liu, J.; Yang, Z. *J. Appl. Electrochem.* **2011**, *41*, 1215–1221.
- (37) Liang, X.; Peng, S.; Lei, Y.; Gao, C.; Wang, N.; Liu, S.; Fang, D. *Electrochim. Acta* **2013**, *95*, 80–86.
- (38) Sum, E.; Skyllas-Kazacos, M. *J. Power Sources* **1985**, *15*, 179–190.
- (39) Skyllas-Kazacos, M.; Rychcik, M.; Robins, R. G.; Fane, A. G. *J. Electrochem. Soc.* **1986**, *133*, 1057–1058.
- (40) Hawkins, J. M.; Robbins, T. P. In *IEEE 23rd International Telecommunication Conference*; 2001; pp. 652–656.
- (41) Kim, S.; Thomsen, E.; Xia, G.; Nie, Z.; Bao, J.; Recknagle, K.; Wang, W.; Viswanathan, V.; Luo, Q.; Wei, X.; Crawford, A.; Coffey, G.; Maupin, G.; Sprenkle, V. *J. Power Sources* **2013**, *237*, 300–309.
- (42) Shibata, A.; Sato, K. *Power Eng. J.* **1999**, *13*, 130–135.
- (43) Huang, K.; Li, X.; Liu, S.; Tan, N.; Chen, L. *Renew. Energy* **2008**, *33*, 186–192.
- (44) Hamelin, J.; Agbossou, K.; Laperri , A.; Laurencelle, F.; Bose, T. K. *Int. J. Hydrogen Energy* **2001**, *26*, 625–629.
- (45) Tu, Z.; Zhang, H.; Luo, Z.; Liu, J.; Wan, Z.; Pan, M. *J. Power Sources* **2013**, *222*, 277–281.
- (46) Wang, L.; Husar, A.; Zhou, T.; Liu, H. *Int. J. Hydrogen Energy* **2003**, *28*, 1263–1272.
- (47) Shyu, J. C.; Hsueh, K. L.; Tsau, F. *Energy Convers. Manag.* **2011**, *52*, 3415–3424.
- (48) Cooper, K. R.; Smith, M. *J. Power Sources* **2006**, *160*, 1088–1095.
- (49) Liu, Q. H.; Grim, G. M.; Papandrew, A. B.; Turhan, A.; Zawodzinski, T. A.; Mench, M. M. *J. Electrochem. Soc.* **2012**, *159*, A1246–A1252.
- (50) Manahan, M. P.; Liu, Q. H.; Gross, M. L.; Mench, M. M. *J. Power Sources* **2013**, *222*, 498–502.

- (51) Sun, C. N.; Tang, Z.; Belcher, C.; Zawodzinski, T. A.; Fujimoto, C. *Electrochem. Commun.*
- (52) Wang, W.; Luo, Q.; Li, B.; Wei, X.; Li, L.; Yang, Z. *Adv. Funct. Mater.* **2013**, *23*, 970–986.
- (53) Friedrich, J. M.; Ponce-de-León, C.; Reade, G. W.; Walsh, F. C. *J. Electroanal. Chem.* **2004**, *561*, 203–217.
- (54) Rychcik, M.; Skyllas-Kazacos, M. *J. Power Sources* **1987**, *19*, 45–54.
- (55) Qiu, G.; Dennison, C. R.; Knehr, K. W.; Kumbur, E. C.; Sun, Y. *J. Power Sources* **2012**, *219*, 223–234.
- (56) Kaneko, H.; Nozaki, K.; Wada, Y.; Aoki, T.; Negishi, A.; Kamimoto, M. *Electrochim. Acta* **1991**, *36*, 1191–1196.
- (57) Inoue, M.; Tsuzuki, Y.; Iizuka, Y.; Shimada, M. *J. Electrochem. Soc.* **1987**, *134*, 756–757.
- (58) Sun, B.; Skyllas-Kazacos, M. *Electrochim. Acta* **1992**, *37*, 2459–2465.
- (59) Sun, B.; Skyllas-Kazacos, M. *Electrochim. Acta* **1992**, *37*, 1253–1260.
- (60) Kim, K. J.; Kim, Y.-J.; Kim, J.-H.; Park, M.-S. *Mater. Chem. Phys.* **2011**, *131*, 547–553.
- (61) Flox, C.; Skoumal, M.; Rubio-Garcia, J.; Andreu, T.; Morante, J. R. *Appl. Energy* **2013**, *109*, 344–351.
- (62) Zhang, W.; Xi, J.; Li, Z.; Zhou, H.; Liu, L.; Wu, Z.; Qiu, X. *Electrochim. Acta* **2013**, *89*, 429–435.
- (63) Di Blasi, A.; Di Blasi, O.; Briguglio, N.; Aricò, A. S.; Sebastián, D.; Lázaro, M. J.; Monforte, G.; Antonucci, V. *J. Power Sources* **2013**, *227*, 15–23.
- (64) Pezeshki, A. M.; Clement, J. T.; Liu, Q. H.; Manahan, M. P.; Papandrew, A. B.; Turhan, A.; Zawodzinski, T. A.; Mench, M. M. In *222nd ECS Meeting*; Honolulu, Hawaii, 2012; p. October.
- (65) Shao, Y.; Wang, X.; Engelhard, M.; Wang, C.; Dai, S.; Liu, J.; Yang, Z.; Lin, Y. *J. Power Sources* **2010**, *195*, 4375–4379.
- (66) Wu, T.; Huang, K.; Liu, S.; Zhuang, S.; Fang, D.; Li, S.; Lu, D.; Su, A. *J. Solid State Electrochem.* **2011**, *16*, 579–585.

- (67) He, Z.; Su, A.; Gao, C.; Zhou, Z.; Pan, C.; Liu, S. *Ionics* **2012**, *19*, 1021–1026.
- (68) Flox, C.; Rubio-García, J.; Skoumal, M.; Andreu, T.; Morante, J. R. *Carbon* **2013**, *60*, 280–288.
- (69) Jin, J.; Fu, X.; Liu, Q.; Liu, Y.; Wei, Z.; Niu, K.; Zhang, J. *ACS Nano* **2013**, *7*, 4764–4773.
- (70) Gao, C.; Wang, N.; Peng, S.; Liu, S.; Lei, Y.; Liang, X.; Zeng, S.; Zi, H. *Electrochim. Acta* **2013**, *88*, 193–202.
- (71) Li, W.; Liu, J.; Yan, C. *Carbon* **2013**, *55*, 313–320.
- (72) Sun, B.; Skyllas-Kazacos, M. *Electrochim. Acta* **1991**, *36*, 513–517.
- (73) Wang, W. H.; Wang, X. D. *Electrochim. Acta* **2007**, *52*, 6755–6762.
- (74) Tsai, H.-M.; Yang, S.-J.; Ma, C.-C. M.; Xie, X. *Electrochim. Acta* **2012**, *77*, 232–236.
- (75) Chandrabose Raghu, S.; Ulaganathan, M.; Lim, T. M.; Skyllas Kazacos, M. *J. Power Sources* **2013**, *238*, 103–108.
- (76) Yao, C.; Zhang, H.; Liu, T.; Li, X.; Liu, Z. *J. Power Sources* **2012**, *218*, 455–461.
- (77) Yao, C.; Zhang, H.; Liu, T.; Li, X.; Liu, Z. *J. Power Sources* **2013**, *237*, 19–25.
- (78) González, Z.; Sánchez, A.; Blanco, C.; Granda, M.; Menéndez, R.; Santamaría, R. *Electrochem. Commun.* **2011**, *13*, 1379–1382.
- (79) Li, B.; Gu, M.; Nie, Z.; Shao, Y.; Luo, Q.; Wei, X.; Li, X.; Xiao, J.; Wang, C.; Sprenkle, V.; Wang, W. *Nano Lett.* **2013**, *13*, 1330–5.
- (80) Kim, K. J.; Park, M. S.; Kim, J. H.; Hwang, U.; Lee, N. J.; Jeong, G.; Kim, Y. J. *Chem. Commun.* **2012**, *48*, 5455–7.
- (81) Flox, C.; Rubio-Garcia, J.; Nafria, R.; Zamani, R.; Skoumal, M.; Andreu, T.; Arbiol, J.; Cabot, A.; Morante, J. R. *Carbon* **2012**, *50*, 2372–2374.
- (82) Prifti, H.; Parasuraman, A.; Winardi, S.; Lim, T. M.; Skyllas-Kazacos, M. *Membranes for Redox Flow Battery Applications*, 2012, Vol. 2, pp. 275–306.
- (83) Li, X.; Zhang, H.; Mai, Z.; Zhang, H.; Vankelecom, I. *Energy Environ. Sci.* **2011**, *4*, 1147.

- (84) Zawodzinski, T. A.; Derouin, C.; Radzinski, S.; Sherman, R. J.; Smith, V. T.; Springer, T. E.; Gottesfeld, S. *J. Electrochem. Soc.* **1993**, *140*, 1041.
- (85) Hickner, M. A. *J. Polym. Sci. Part B Polym. Phys.* **2012**, *50*, 9–20.
- (86) Pei, P.; Yuan, X.; Chao, P.; Wang, X. *Int. J. Hydrogen Energy* **2010**, *35*, 3147–3151.
- (87) Du, H. Y.; Wang, C. H.; Hsu, H. C.; Chang, S. T.; Yen, S. C.; Chen, L. C.; Viswanathan, B.; Chen, K. H. *J. Mater. Chem.* **2011**, *21*, 2512.
- (88) Chaparro, A. M.; Ferreira-Aparicio, P.; Folgado, M. A.; Martín, A. J.; Daza, L. *J. Power Sources* **2011**, *196*, 4200–4208.
- (89) Sun, C.; Chen, J.; Zhang, H.; Han, X.; Luo, Q. *J. Power Sources* **2010**, *195*, 890–897.
- (90) Tang, A.; Bao, J.; Skyllas-Kazacos, M. *J. Power Sources* **2011**, *196*, 10737–10747.
- (91) Luo, Q.; Li, L.; Wang, W.; Nie, Z.; Wei, X.; Li, B.; Chen, B.; Yang, Z.; Sprenkle, V. *ChemSusChem* **2013**, *6*, 268–74.
- (92) Xie, G.; Okada, T. *J. Electrochem. Soc.* **1995**, *142*, 3057.
- (93) Chen, D.; Kim, S.; Sprenkle, V.; Hickner, M. A. *J. Power Sources* **2013**, *231*, 301–306.
- (94) Chen, D.; Hickner, M. A. *Phys. Chem. Chem. Phys.* **2013**, *15*, 11299–305.
- (95) Kim, S.; Yan, J.; Schwenzler, B.; Zhang, J.; Li, L.; Liu, J.; Gary, Z.; Hickner, M. A. *Electrochem. Commun.* **2010**, *12*, 1650–1653.
- (96) Kim, S.; Tighe, T. B.; Schwenzler, B.; Yan, J.; Zhang, J.; Liu, J.; Yang, Z.; Hickner, M. A. *J. Appl. Electrochem.* **2011**, *41*, 1201–1213.
- (97) Mohammadi, T.; Kazacos, M. S. *J. Appl. Electrochem.* **1997**, *27*, 153–160.
- (98) Sukkar, T.; Skyllas-Kazacos, M. *J. Appl. Electrochem.* **2004**, *34*, 137–145.
- (99) Mai, Z.; Zhang, H.; Li, X.; Bi, C.; Dai, H. *J. Power Sources* **2010**, *196*, 482–487.
- (100) Fujimoto, C.; Kim, S.; Stains, R.; Wei, X.; Li, L.; Yang, Z. G. *Electrochem. Commun.* **2012**, *20*, 48–51.

- (101) Chen, D.; Hickner, M. A.; Wang, S.; Pan, J.; Xiao, M.; Meng, Y. *J. Memb. Sci.* **2012**, *415-416*, 139–144.
- (102) Luo, Q.; Zhang, H.; Chen, J.; You, D.; Sun, C.; Zhang, Y. *J. Memb. Sci.* **2008**, *325*, 553–558.
- (103) Luo, Q.; Zhang, H.; Chen, J.; Qian, P.; Zhai, Y. *J. Memb. Sci.* **2008**, *311*, 98–103.
- (104) Xi, J.; Wu, Z.; Teng, X.; Zhao, Y.; Chen, L.; Qiu, X. *J. Mater. Chem.* **2008**, *18*, 1232.
- (105) Teng, X.; Zhao, Y.; Xi, J.; Wu, Z.; Qiu, X.; Chen, L. *J. Memb. Sci.* **2009**, *341*, 149–154.
- (106) Hwang, G.; Ohya, H. *J. Memb. Sci.* **1997**, *132*, 55–61.
- (107) Xing, D.; Zhang, S.; Yin, C.; Zhang, B.; Jian, X. *J. Memb. Sci.* **2010**, *354*, 68–73.
- (108) Xi, J.; Wu, Z.; Qiu, X.; Chen, L. *J. Power Sources* **2007**, *166*, 531–536.
- (109) Mauritz, K. A.; Warren, R. M. *Macromolecules* **1989**, *22*, 1730–1734.
- (110) Trogadas, P.; Pinot, E.; Fuller, T. F. *Electrochem. Solid-State Lett.* **2012**, *15*, A5.
- (111) Vijayakumar, M.; Schwenzer, B.; Kim, S.; Yang, Z.; Thevuthasan, S.; Liu, J.; Graff, G. L.; Hu, J. *Solid State Nucl. Magn. Reson.* **2011**, *42*, 71–80.
- (112) Zeng, J.; Jiang, C.; Wang, Y.; Chen, J.; Zhu, S.; Zhao, B.; Wang, R. *Electrochem. Commun.* **2008**, *10*, 372–375.
- (113) Luo, X.; Lu, Z.; Xi, J.; Wu, Z.; Zhu, W.; Chen, L. *J. Phys. Chem. B* **2005**, *109*, 20310–20314.
- (114) Ma, J.; Wang, Y.; Peng, J.; Qiu, J.; Xu, L.; Li, J.; Zhai, M. *J. Memb. Sci.* **2012**, *1*–8.
- (115) Qiu, J.; Li, M.; Ni, J.; Zhai, M.; Peng, J.; Xu, L.; Zhou, H.; Li, J.; Wei, G. *J. Memb. Sci.* **2007**, *297*, 174–180.
- (116) Tian, B.; Yan, C. .; Wang, F. . *J. Memb. Sci.* **2004**, *234*, 51–54.
- (117) Kreuer, K. D. In *Handbook of Fuel Cells – Fundamentals, Technology and Applications*; 2010; pp. 1–16.
- (118) Rikukawa, M.; Sanui, K. *Prog. Polym. Sci.* **2000**, *25*, 1463–1502.



- (119) Kreuer, K. D. *J. Memb. Sci.* **2001**, *185*, 29–39.
- (120) Xing, P.; Robertson, G. P.; Guiver, M. D.; Mikhailenko, S. D.; Wang, K.; Kaliaguine, S. *J. Memb. Sci.* **2004**, *229*, 95–106.
- (121) Hickner, M. A. *Transport and Structure in Fuel Cell Proton Exchange Membranes*, Virginia Polytechnic Institute and State University, 2003.
- (122) Wei, W.; Zhang, H.; Li, X.; Mai, Z.; Zhang, H. *J. Power Sources* **2012**, *208*, 421–425.
- (123) Jia, C.; Liu, J.; Yan, C. *J. Power Sources* **2010**, *195*, 4380–4383.
- (124) Jia, C.; Liu, J.; Yan, C. *J. Power Sources* **2012**, *203*, 190–194.
- (125) Chen, D.; Wang, S.; Xiao, M.; Han, D.; Meng, Y. *J. Power Sources* **2010**, *195*, 7701–7708.
- (126) Chen, D.; Wang, S.; Xiao, M.; Meng, Y. *J. Power Sources* **2010**, *195*, 2089–2095.
- (127) Chen, D.; Wang, S.; Xiao, M.; Meng, Y. *Energy Environ. Sci.* **2010**, *3*, 622.
- (128) Chen, D.; Hickner, M. A.; Agar, E.; Kumbur, E. C. *Electrochem. Commun.* **2013**, *26*, 37–40.
- (129) Jung, M. J.; Parrondo, J.; Arges, C. G.; Ramani, V. *J. Mater. Chem. A* **2013**, *1*, 10458.
- (130) Zhang, S.; Yin, C.; Xing, D.; Yang, D.; Jian, X. *J. Memb. Sci.* **2010**, *363*, 243–249.
- (131) Zhang, B.; Zhang, S.; Xing, D.; Han, R.; Yin, C.; Jian, X. *J. Power Sources* **2012**, *217*, 296–302.
- (132) Wang, Y.; Qiu, J.; Peng, J.; Xu, L.; Li, J.; Zhai, M. *J. Memb. Sci.* **2011**, *376*, 70–77.
- (133) Qiu, J.; Zhai, M.; Chen, J.; Wang, Y.; Peng, J.; Xu, L.; Li, J.; Wei, G. *J. Memb. Sci.* **2009**, *342*, 215–220.
- (134) Chen, D.; Hickner, M. A.; Agar, E.; Kumbur, E. C. *ACS Appl. Mater. Interfaces* **2013**, *5*, 7559–66.
- (135) Wen, Y.; Xu, Y.; Cheng, J.; Cao, G.; Yang, Y. *Electrochim. Acta* **2013**, *96*, 268–273.

- (136) Kausar, N.; Howe, R.; Skyllas-Kazakos, M. *J. Appl. Electrochem.* **2001**, *31*, 1327–1332.
- (137) Vijayakumar, M.; Burton, S. D.; Huang, C.; Li, L.; Yang, Z.; Graff, G. L.; Liu, J.; Hu, J.; Skyllas-kazacos, M. *J. Power Sources* **2010**, *195*, 7709–7717.
- (138) Vijayakumar, M.; Li, L.; Graff, G.; Liu, J.; Zhang, H.; Yang, Z.; Hu, J. Z. *J. Power Sources* **2011**, *196*, 3669–3672.
- (139) Vijayakumar, M.; Li, L.; Nie, Z.; Yang, Z.; Hu, J. *Phys. Chem. Chem. Phys.* **2012**, *14*, 10233–42.
- (140) Vijayakumar, M.; Wang, W.; Nie, Z.; Sprenkle, V.; Hu, J. *J. Power Sources* **2013**, *241*, 173–177.
- (141) Chang, F.; Hu, C.; Liu, X.; Liu, L.; Zhang, J. *Electrochim. Acta* **2012**, *60*, 334–338.
- (142) Wu, X.; Liu, S.; Wang, N.; Peng, S.; He, Z. *Electrochim. Acta* **2012**, *78*, 475–482.
- (143) He, Z.; Liu, J.; Han, H.; Chen, Y.; Zhou, Z.; Zheng, S.; Lu, W.; Liu, S.; He, Z. *Electrochim. Acta* **2013**, *106*, 556–562.
- (144) Jia, Z.; Wang, B.; Song, S.; Chen, X. *J. Electrochem. Soc.* **2012**, *159*, A843.
- (145) Weber, A. Z.; Mench, M. M.; Meyers, J. P.; Ross, P. N.; Gostick, J. T.; Liu, Q. *J. Appl. Electrochem.* **2011**, *41*, 1137–1164.
- (146) Ponce de Leon, C.; Frias-Ferrer, A.; Gonzalez-Garcia, J.; Szanto, D. .; Walsh, F. C. *J. Power Sources* **2006**, *160*, 716–732.
- (147) Wu, J.; Yuan, X.; Wang, H.; Blanco, M.; Martin, J.; Zhang, J. *Int. J. Hydrogen Energy* **2008**, *33*, 1735–1746.
- (148) Wu, J.; Ziyuan, X.; Wang, H.; Blanco, M.; Martin, J.; Zhang, J. *Int. J. Hydrogen Energy* **2008**, *33*, 1747–1757.
- (149) Yuan, X.; Wang, H.; Colinsun, J.; Zhang, J. *Int. J. Hydrogen Energy* **2007**, *32*, 4365–4380.
- (150) Williams, M. V.; Kunz, H. R.; Fenton, J. M. *J. Electrochem. Soc.* **2005**, *152*, A635.
- (151) Santarelli, M. G.; Torchio, M. F.; Cochis, P. *J. Power Sources* **2006**, *159*, 824–835.
- (152) Pisani, L.; Murgia, G.; Valentini, M.; D’Aguanno, B. *J. Power Sources* **2002**, *108*, 192–203.

- (153) Stern, M.; Geary, A. L. *J. Electrochem. Soc.* **1957**, *104*, 56–63.
- (154) Riessa, I.; Giidickemeierb, M.; Gaucklerb, L. J. *Solid State Ionics* **1996**, *90*, 91–104.
- (155) Zhao, F.; Virkar, A. V. *J. Power Sources* **2005**, *141*, 79–95.
- (156) Wruck, W. J.; Machado, R. M.; Chapman, T. W. *J. Electrochem. Soc.* **1987**, *134*, 539–546.
- (157) Song, J. M.; Cha, S. Y.; Lee, W. M. *J. Power Sources* **2001**, *94*, 78–84.
- (158) Springer, E.; Zawodzinski, A.; Wilson, M. S.; Golfesfeld, S. *J. Electrochem. Soc.* **1996**, *143*, 587–599.
- (159) Kong, C. S.; Kim, D.; Lee, H.; Shul, Y.; Lee, T. *J. Power Sources* **2002**, *108*, 185–191.
- (160) Turhan, A.; Heller, K.; Brenizer, J. S.; Mench, M. M. *J. Power Sources* **2006**, *160*, 1195–1203.
- (161) Turhan, A.; Heller, K.; Brenizer, J. S.; Mench, M. M. *J. Power Sources* **2008**, *180*, 773–783.
- (162) Kowal, J. J.; Turhan, A.; Heller, K.; Brenizer, J.; Mench, M. M. *J. Electrochem. Soc.* **2006**, *153*, A1971.
- (163) Yoon, Y. G.; Lee, W. Y.; Yang, T. H.; Park, G. G.; Kim, C. S. *J. Power Sources* **2003**, *118*, 193–199.
- (164) Noponen, M.; Mennola, T.; Mikkola, M.; Hottinen, T.; Lund, P. *J. Power Sources* **2002**, *106*, 304–312.
- (165) Ghosh, P. C.; Wüster, T.; Dohle, H.; Kimiaie, N.; Mergel, J.; Stolten, D. *J. Power Sources* **2006**, *154*, 184–191.
- (166) Mench, M. M.; Wang, C. Y. *J. Electrochem. Soc.* **2003**, *150*, A79.
- (167) Hickner, M. A.; Ghassemi, H.; Kim, Y. S.; Einsla, B. R.; McGrath, J. E. *Chem. Rev.* **2004**, *104*, 4587–611.
- (168) Aaron, D. S.; Tang, Z.; Lawton, J. S.; Papandrew, A. P.; Zawodzinski Jr., T. A. *ECS Trans.* **2012**, *41*, 43–51.

- (169) Aaron, D.; Sun, C. N.; Bright, M.; Papandrew, A. B.; Mench, M. M.; Zawodzinski, T. A. *ECS Electrochem. Lett.* **2013**, *2*, A29–A31.
- (170) Sun, C. N.; Delnick, F. M.; Aaron, D. S.; Papandrew, A. B.; Mench, M. M.; Zawodzinski, T. A. *ECS Electrochem. Lett.* **2013**, *2*, A43–A45.
- (171) Wang, C. Y. *Chem. Rev.* **2004**, *104*, 4727–65.
- (172) Shah, A. A.; Tangirala, R.; Singh, R.; Wills, R. G. A.; Walsh, F. C. *J. Electrochem. Soc.* **2011**, *158*, A671.
- (173) Al-Fetlawi, H.; Shah, A. A.; Walsh, F. C. *Electrochim. Acta* **2009**, *55*, 78–89.
- (174) Feser, J. P.; Prasad, A. K.; Advani, S. G. *J. Power Sources* **2006**, *161*, 404–412.
- (175) Wang, Y.; Wang, C. Y. *J. Power Sources* **2005**, *147*, 148–161.
- (176) Fishman, J. Z. Investigation of Surface Properties and Heterogeneity in Gas Diffusion Layers for Polymer Electrolyte Membrane Fuel Cells by Investigation of Surface Properties and Heterogeneity in Gas Diffusion Layers for Polymer Electrolyte Membrane Fuel Cells, University of Toronto, 2010.
- (177) Skyllas-Kazacos, M.; Kazacos, M. *J. Power Sources* **2011**, *196*, 8822–8827.
- (178) Shah, A. A.; Al-Fetlawi, H.; Walsh, F. C. *Electrochim. Acta* **2010**, *55*, 1125–1139.
- (179) Liu, H.; Xu, Q.; Yan, C.; Qiao, Y. *Electrochim. Acta* **2011**, *56*, 8783–8790.
- (180) Liu, H.; Xu, Q.; Yan, C. *Electrochem. Commun.* **2013**, *28*, 58–62.
- (181) Huet, F. *J. Power Sources* **1998**, *70*, 59–69.
- (182) Piller, S.; Perrin, M.; Jossen, A. *J. Power Sources* **2001**, *96*, 113–120.
- (183) Rodrigues, S.; Munichandraiah, N.; Shukla, A. K. *J. Power Sources* **2000**, *87*, 12–20.
- (184) Zhang, J.; Lee, J. *J. Power Sources* **2011**, *196*, 6007–6014.
- (185) Salkind, A. J.; Fennie, C.; Singh, P.; Atwater, T.; Reisner, D. E. *J. Power Sources* **1999**, *80*, 293–300.
- (186) Lee, S.; Kim, J.; Lee, J.; Cho, B. H. *J. Power Sources* **2008**, *185*, 1367–1373.
- (187) Charkhgard, M.; Farrokhi, M. *IEEE Trans. Ind. Electron.* **2010**, *57*, 4178–4187.

- (188) Mohamed, M. R.; Ahmad, H.; Seman, M. N. A.; Razali, S.; Najib, M. S. *J. Power Sources* **2013**, *239*, 284–293.
- (189) Martin, E. L.; Bentley, K. E. *Anal. Chem.* **1962**, *34*, 354–358.
- (190) Liu, L.; Xi, J.; Wu, Z.; Zhang, W.; Zhou, H.; Li, W.; Qiu, X. *J. Appl. Electrochem.* **2012**, *42*, 1025–1031.
- (191) Liu, L.; Xi, J.; Wu, Z.; Zhang, W.; Zhou, H.; Li, W.; He, Y. *J. Spectrosc.* **2013**, *2013*, 1–8.
- (192) Heintz, A.; Illenberger, C. *Berichte der Bunsen-Gesellschaft* **1998**, *102*, 1401–1409.
- (193) Gao, X.; Lynch, R. P.; Leahy, M. J.; Buckley, D. N. *ECS Trans.* **2013**, *45*, 25–36.
- (194) Tang, Z.; Aaron, D. S.; Papandrew, A. B.; Zawodzinski Jr., T. A. *ECS Trans.* **2012**, *41*, 1–9.
- (195) Blanc, P.; Madic, C.; Launay, J. P. *Inorg. Chem.* **1982**, *21*, 2923–2928.
- (196) Okamoto, K.; Woo-Sik, J.; Tomiyasu, H.; Fukutomi, H. *Inorganica Chim. Acta* **1988**, *143*, 217–221.
- (197) Mohamed, M. R.; Ahmad, H.; Abu Seman, M. N. *Elektron. IR ELEKTROTEHNIKA* **2013**, *19*, 37–42.
- (198) Kazacos, M.; Skyllas-Kazacos, M. *J. Electrochem. Soc.* **1989**, *136*, 2759–2760.
- (199) Smitha, B.; Sridhar, S.; Khan, A. A. *J. Memb. Sci.* **2005**, *259*, 10–26.
- (200) Pourcelly, G.; Lindheimer, A.; Gavach, C.; Hurwitz, H. D. *J. Electroanal. Chem.* **1991**, *305*, 97–113.
- (201) Pourcelly, G. G.; Lindheimer, A. A.; Pamboutzoglou, G.; Gavach, C. *J. Electroanal. Chem.* **1989**, *259*, 113–125.
- (202) Donnan, F. G. *Chem. Rev.* **1924**, *1*, 73–90.
- (203) Pivovar, B. S.; Smyrl, W. H.; Cussler, E. L. *J. Electrochem. Soc.* **2005**, *152*, A53.
- (204) Verbrugge, M. W.; Hill, R. F. *J. Phys. Chem.* **1988**, *92*, 6778.
- (205) Verbrugge, M. W.; Hill, R. F. *J. Electrochem. Soc.* **1990**, *137*, 893–899.

- (206) Verbrugge, M. W.; Schneider, E. W.; Conell, R. S.; Hill, R. F. *J. Electrochem. Soc.* **1992**, *139*, 3421.
- (207) Tuan, L. X.; Verbanck, M.; Buess-Herman, C.; Hurwitz, H. D. *J. Memb. Sci.* **2006**, *284*, 67–78.
- (208) Cheng, X.; Shi, Z.; Glass, N.; Zhang, L.; Zhang, J.; Song, D.; Liu, Z. S.; Wang, H.; Shen, J. *J. Power Sources* **2007**, *165*, 739–756.
- (209) Kelly, M.; Egger, B.; Fafilek, G.; Besenhard, J.; Kronberger, H.; Nauer, G. *Solid State Ionics* **2005**, *176*, 2111–2114.
- (210) Okada, T.; Xie, G.; Gorseth, O.; Kjelstrup, S.; Nakamura, N.; Arimura, T. *Electrochim. Acta* **1998**, *43*, 3741–3747.
- (211) Okada, T.; Satou, H.; Okuno, M.; Yuasa, M. *J. Phys. Chem. B* **2002**, *106*, 1267–1273.
- (212) Okada, T.; Ayato, Y.; Yuasa, M.; Sekine, I. *J. Phys. Chem. B* **1999**, *103*, 3315–3322.
- (213) Yeager, H. L.; Steck, A. *J. Electrochem. Soc.* **1981**, *128*, 1880–1884.
- (214) Jalani, N. H.; Datta, R. *J. Memb. Sci.* **2005**, *264*, 167–175.
- (215) Viana, M.; Jouannin, P.; Pontier, C.; Chulia, D. *Talanta* **2002**, *57*, 583–593.
- (216) Paddison, S. J. *Annu. Rev. Mater. Res.* **2003**, *33*, 289–319.
- (217) Schroeder, P. *Z. Phys. Chem.* **1903**, *45*, 75.
- (218) Gates, C. M.; Newman, J. *AIChE J.* **2000**, *46*, 2076–2085.
- (219) Bontha, J. R.; Pintauro, P. N. *Chem. Eng. Sci.* **1994**, *49*, 3835–3851.
- (220) Tandon, R.; Pintauro, P. . *J. Memb. Sci.* **1997**, *136*, 207–219.
- (221) Pintauro, P. N.; Tandon, R.; Chao, L.; Xu, W.; Evilia, R. *J. Phys. Chem.* **1995**, *99*, 12915–12924.
- (222) Walrafen, G. E.; Dodd, D. M. *Trans. Faraday Soc.* **1961**, *57*, 1286–1296.
- (223) Lund Myhre, C. E.; Christensen, D. H.; Nicolaisen, F. M.; Nielsen, C. J. *J. Phys. Chem. A* **2003**, *107*, 1979–1991.

- (224) Ludvigsson, M.; Lindgren, J.; Tegenfeldt, J. *Electrochim. Acta* **2000**, *45*, 2267–2271.
- (225) Michigan State University Ionization Constants of Inorganic Polyprotic Acids  
<http://www.cem.msu.edu/~reusch/OrgPage/acidity.htm>.
- (226) Kreuer, K. D. *Chem. Mater.* **1996**, *8*, 610–641.
- (227) Staples, B. R. *J. Phys. Chem. Ref. Data* **1981**, *10*, 779–798.
- (228) Sone, Y.; Ekdunge, P.; Simonsson, D. *J. Electrochem. Soc.* **1996**, *143*, 1254.
- (229) Choi, P.; Jalani, N. H.; Datta, R. *J. Electrochem. Soc.* **2005**, *152*, E123.
- (230) Palomo, J.; Pintauro, P. N. *J. Memb. Sci.* **2003**, *215*, 103–114.
- (231) Huang, K.-L.; Holsen, T. M.; Selman, J. . *J. Memb. Sci.* **2002**, *210*, 137–145.
- (232) Okada, T.; Nakamura, N.; Yuasa, M.; Sekine, I. *J. Electrochem. Soc.* **1997**, *144*, 2744–2750.
- (233) Marcus, Y. *Biophys. Chem.* **1994**, *51*, 111–127.
- (234) Helm, L.; Merbach, A. E. *Chem. Rev.* **2005**, *105*, 1923–59.
- (235) Stangret, J.; Gampe, T. *J. Phys. Chem. A* **2002**, *106*, 5393–5402.
- (236) Bergstrom, P. A.; Lindgren, J.; Read, M.; Sandstrom, M. *J. Phys. Chem.* **1991**, *95*, 7650–7655.
- (237) Waluyo, I.; Huang, C.; Nordlund, D.; Bergmann, U.; Weiss, T. M.; Pettersson, L. G. M.; Nilsson, A. *J. Chem. Phys.* **2011**, *134*, 064513–1 : 064513–10.
- (238) Zawodzinski, T. A.; Springer, T. E.; Davey, J.; Jestel, R.; Lopez, C.; Valeria, J.; Gottesfeld, S. *J. Electrochem. Soc.* **1993**, *140*.
- (239) Lehmani, A.; Turq, P.; Michelle, P.; Jacques, P.; Simonin, J. *J. Electroanal. Chem.* **1997**, *428*, 81–89.
- (240) Koryta, J.; Dvorak, J.; Kavan, L. *Principles of Electrochemistry (Second Edition)*; 1987; p. John Wiley & Sons.
- (241) Chen, C.; Huang, C.; Waluyo, I.; Nordlund, D.; Weng, T.-C.; Sokaras, D.; Weiss, T.; Bergmann, U.; Pettersson, L. G. M.; Nilsson, A. *J. Chem. Phys.* **2013**, *138*, 154506.

- (242) Chen, D.; Wang, S.; Xiao, M.; Meng, Y. *Energy Convers. Manag.* **2010**, *51*, 2816–2824.
- (243) Fujimoto, C. H.; Hickner, M. A.; Cornelius, C. J.; Loy, D. A. *Macromolecules* **2005**, *38*, 5010–5016.
- (244) Hickner, M. A.; Fujimoto, C. H.; Cornelius, C. J. *Polymer* **2006**, *47*, 4238–4244.
- (245) Lawton, J. S.; Aaron, D. S.; Tang, Z.; Zawodzinski, T. A. *J. Memb. Sci.* **2013**, *428*, 38–45.
- (246) Rieberer, S.; Norian, K. H. *Ultramicroscopy* **1992**, *41*, 225–233.
- (247) Mauritz, K. A.; Moore, R. B. *Chem. Rev.* **2004**, *104*, 4535–4585.
- (248) Fontanella, J. J.; Edmondson, C. A.; Wintersgill, M. C.; Wu, Y.; Greenbaum, S. G. *Macromolecular* **1996**, *29*, 4944–4951.
- (249) Hamrock, S. J.; Yandrasits, M. A. *J. Macromol. Sci. Part C Polym. Rev.* **2006**, *46*, 219–244.
- (250) Guthrie, J. P. *Can. J. Chem.* **1978**, *56*, 2342–2354.
- (251) Crank, J. *The Mathematics of Diffusion*; Oxford University Press: New York, 1977.
- (252) Tong, J.; Anderson, J. L. *Biophys. J.* **1996**, *70*, 1505–1513.
- (253) Tang, Z.; Bright, M.; Zawodzinski, T. A. In *223rd ECS Meeting*; 2013.
- (254) Costamagna, P.; Yang, C.; Bocarsly, A. B.; Srinivasan, S. *Electrochim. Acta* **2002**, *47*, 1023–1033.
- (255) Hsu, W. Y.; Gierke, T. D. *J. Memb. Sci.* **1983**, *13*, 307–326.
- (256) Tamagawa, K.; Iijima, T.; Kimura, M. *J. Mol. Struct.* **1976**, *30*, 243–253.
- (257) Stirnemann, G.; Wernersson, E.; Jungwirth, P.; Laage, D. *J. Am. Chem. Soc.* **2013**, *135*, 11824–31.



## VITA

Zhijiang Tang was born in small town named Aopin near the city of Pengzhou in Sichuan Province, China. He attended schools in Pengzhou before entering Sichuan University in Chengdu. During the final year in college, Zhijiang took part in a research program lead by Prof. Yunxiang Zhang to develop a manufacturing protocol for sulphoaluminate cement. Zhijiang earned his Bachelor of Engineering degree in Chemical Engineering from Sichuan University in 2007. Then Zhijiang joined the Structural Mechanics Research Section in Southwest Jiaotong University to conduct study on elastic and plastic structural analysis of concrete-steel hybrid structure in seismic conditions till July 2009, under the supervision of Prof. Junsheng Peng. Zhijiang was granted his Master of Engineering in Civil Engineering by Jiaotong University in 2010. In 2009, Zhijiang went to the University of Tennessee as graduate student, and then joined the research group of Governor's Chair Professor Dr. Thomas Zawodzinski in Department of Chemical and Biomolecular Engineering. He is currently a Ph.D. candidate in Chemical Engineering in UT.